EPFL

Coincidence imaging spectroscopy of extreme-ultraviolet photoionisation processes in molecules and clusters

Andrew Daniel Bonnar CLARK

École
polytechnique
fédérale
de Lausanne

2021

"I put your quote in my thesis but I do not think I will get a quote in your thesis."
- Verónica Oliver Álvarez de Lara, Lausanne, 2019

To Grandma Jean

Résumé

Les expériences de photoionisation sur des molécules et des amas en phase gazeuse produisent toujours des multiples particules chargées. L'ionisation simple produit toujours un photoélectron et un photoion, tandis que l'ionisation d'ordre supérieur peut en produire un plus grand nombre des deux types de particules. Les techniques de spectroscopie par coïncidence concernent la détection de deux ou plusieurs de ces particules en coïncidence afin que des corrélations puissent être établies entre leurs propriétés diverses. Filtrer l'ensemble des données expérimentales en fonction des paramètres souhaités permet de séparer et de démêler les diverses contributions concurrentes au signal expérimental, ce qui permet de récupérer plus d'informations. Présenté ici est la conception, la construction et la mise en service d'une machine de spectroscopie d'imagerie par coïncidence couplée à la source de photons dans l'ultraviolet extrême : Harmonium high-harmonic generation (HHG) au Lausanne Center for Ultrafast Science.

La machine est capable d'enregistrer des coïncidences photoélectron-photoion (PEPICO), des coïncidences photoion-photoion (PIPICO) et des coïncidences photoélectron-photoion-photoion (PEPIPICO) des constituants du faisceau moléculaire photoionisé par imagerie de carte de vitesse sur un détecteur delay-line (« DLD-VMI »). Le DLD-VMI ne peut détecter qu'un maximum d'un électron par tir laser, de sorte que les coïncidences photoélectron-photoélectron (PEPECO) ne peuvent actuellement pas être mesurées. La machine peut fonctionner de trois manières générales : les potentiels d'électrode sont maintenus à des valeurs négatives fixes pour détecter les photoélectrons ; les potentiels sont maintenus à des valeurs positives pour détecter les photoions, ce qui permet d'observer les coïncidences PIPICO ; ou les potentiels sont initialement maintenus à des valeurs négatives pour obtenir une image des photoélectrons, puis rapidement commutés après détection pour obtenir une image des ions sur le même détecteur, ce qui permet d'observer les coïncidences PEPICO et PEPIPICO. Le dispositif de détection fournit des informations concernant rapport masse-à-charge (m/z) des ions, l'énergie cinétique et les informations angulaires pour les ions et les électrons. La machine contient également une deuxième configuration d'imagerie de carte de vitesse identique avec une plaque à micro canaux et un détecteur au phosphore avec une caméra à dispositif à couplage de charge (« CCD-VMI ») qui peut être utilisée pour obtenir des images de photoélectrons et de photoions, mais pas par coïncidence.

Les photoélectrons peuvent être détectés sur le CCD-VMI avec la résolution full-width-at-half-maximum (FWHM) augmentant linéairement de 0,1 eV à 1 eV d'énergie cinétique à 0,4 eV à 15 eV d'énergie cinétique, et sur le DLD-VMI de 0,2 eV à 1 eV d'énergie cinétique à 0,7 eV à 15 eV d'énergie cinétique. La détection de photoions avec les électrodes maintenues à des potentiels fixes a donné une résolution FWHM de TOF variant de 1500 à 4500, et une focalisation spatiale de 150 μm à 380 μm selon le m/z des ions et le schéma de voltage exact utilisé. La commutation des potentiels d'électrode pour obtenir une image de l'ensemble les électrons et des ions créés produit des grandes perturbations, dépendantes de la masse et de la charge, aux trajectoires ioniques. Ceci nécessite l'optimisation des potentiels d'imagerie ionique pour un ion d'intérêt particulier. La résolution TOF, déterminée pour des ions compris entre m/z 18 et m/z 92, peut varier de 200 à 2800. La résolution spatiale pour ces ions varie de 200 μm à 14000 μm. L'enregistrement efficace des ions en coïncidence avec les électrons nécessite donc un examen attentif des ions particuliers d'intérêt et une optimisation des conditions expérimentales en fonction de leur rapport masse-à-charge.

Les premières expériences d'essai ont été réalisées en analysant les coïncidences PEPICO de la double photoionisation du toluène. L'ionisation et double ionisation du toluène a été largement étudiée par les techniques d'ionisation par impact électronique et de photoionisation. Les spectres partiels de double photoionisation en coïncidence avec le dication du toluène suggèrent que le potentiel de double ionisation est d'environ 23,8 eV, ce qui est en accord avec les études précédentes de synchrotron et de coïncidence

électron-électron. Des dications métastables du toluène ont été observées, ainsi que d'autres dications correspondant à la perte de H et H_2 et une fragmentation métastable de l'ion déshydrogéné $C_7H_6^{2+}$ en $C_2H_3^+$ et $C_5H_3^+$. Des monocations métastables d'un fragment de toluène, ainsi que le monomère et le dimère ont également été observés. De nombreuses paires d'ions correspondant à des explosions coulombiennes du dication parentale ont été observées, ainsi que celle d'un dication tétramère.

Des expériences de double photoionisation sur des monomères 2-propanol ont été réalisées. Les spectres de photoionisation partielle de ces coïncidences estiment le potentiel de double photoionisation à environ 28 eV, ce qui est une limite supérieure pour cette valeur. Le mécanisme exact de l'ionisation n'est pas clair d'après les données électroniques ; cependant, il est suggéré à partir des données de coïncidence ion-ion que l'émission du deuxième électron a lieu avant que la molécule ne se dissocie. Une double photoionisation a également été observée pour des amas de 2-propanol au moins aussi large que le tétramère. L'analyse des coïncidences ion-ion de ces clusters suggère que les deux charges positives créées par la double ionisation naissent sur des unités monomères différentes. De nombreuses voies de fragmentation métastables de monomères et d'agrégats de 2-propanol ionisés individuellement ont également été observées dans les spectres de coïncidence TOF-TOF, où les ions parents se dissocient en un fragment chargé et un neutre à divers points le long de la trajectoire de vol vers le détecteur. Un modèle a été développé pour déterminer la relation entre la durée de vie des parents et le TOF des fragments détectés. Cependant, les hypothèses utilisées pour créer le modèle ont entraîné des valeurs de durée de vie incorrectes par rapport aux simulations électrostatiques. Malgré cela, le modèle a reproduit avec succès les formes des signatures métastables sur les spectres de coïncidence TOF-TOF et a permis d'isoler les coïncidences correspondant à ces voies pour donner un schéma qualitatif de la variation du signal par rapport à la durée de vie.

Mots-clés : spectroscopie d'imagerie par coïncidence, imagerie vitesse-carte, photoélectron, photoion, double photoionisation, amas, métastable, PEPICO, PEPIPICO, PIPICO, toluène, 2-propanol

Abstract

Photoionisation experiments on gas-phase molecules and clusters always produces multiple charged particles. Single ionisation produces a photoelectron and a photoion, while higher-order ionisation can produce greater numbers of both types of particles. Coincidence spectroscopic techniques concern the detection of two or more of these particles in coincidence so that correlations can be drawn between their various properties. Being able to filter the experimental dataset according to the desired parameters enables the separation and disentangling of various competing contributions to the experimental signal, allowing for more information to be retrieved. Presented here is the design, construction and commissioning of a coincidence imaging spectroscopy endstation coupled to the Harmonium high-harmonic generation (HHG) extreme-ultraviolet photon source at the Lausanne Centre for Ultrafast Science.

The endstation is capable of recording photoelectron-photoion coincidences (PEPICO), photoion-photoion coincidences (PIPICO), and photoelectron-photoion-photoion coincidences (PEPIPICO) of photoionised molecular beam constituents using velocity-map imaging onto a delay-line detector ("DLD-VMI"). The DLD-VMI can only detect a maximum of one electron per laser shot, so photoelectron-photoelectron coincidences (PEPECO) cannot currently be measured. The endstation can function in three general ways: Electrode potentials are held at fixed negative values to image detect photoelectrons; the potentials are held at positive values to image detect photoions, which allows PIPICO coincidences to be observed; or the potentials are initially held at negative values to image photoelectrons, then quickly switched after detection to image the ions onto the same detector, which allows PEPICO and PEPIPICO coincidences to be observed. The detection setup provides information concerning the mass-to-charge ratio (m/z) of ions, and kinetic energy and angular information for both ions and electrons. The endstation also contains a second, identical velocity-map imaging setup with a microchannel plate and phosphor screen detector with a charge-coupled device camera ("CCD-VMI") which can be used to obtain photoelectron and photoion images, although not in coincidence.

Photoelectrons can be detected on the CCD-VMI with the full-width-at-half-maximum (FWHM) resolution increasing linearly from 0.1 eV at 1 eV kinetic energy to 0.4 eV at 15 eV kinetic energy, and on the DLD-VMI from 0.2 eV at 1 eV kinetic energy to 0.7 eV at 15 eV kinetic energy. Detecting photoions with the electrodes held at fixed potentials gave TOF FWHM resolution ranging from 1500 to 4500, and spatial focusing from 150 μm to 380 μm depending on the m/z of the ions and the exact voltage scheme used. Switching the electrode potentials to image both electrons and ions results in large, mass- and charge-dependent perturbations to the ion trajectories, requiring the ion-imaging potentials to be optimised for a particular ion of interest. The TOF resolution, determined for ions between m/z 18 and m/z 92, can vary from 200 to 2800. The spatial resolution for these ions varies from 200 μm to 14000 μm. Effectively recording ions in coincidence with electrons therefore requires careful consideration of the particular ions of interest and for the experimental conditions to be optimised for their mass-to-charge ratio.

Initial trial experiments were performed by analysing PEPICO coincidences of the double photoionisation of toluene. The partial double photoionisation spectra in coincidence with the toluene dication suggest the double ionisation potential is approximately 23.8 eV, which agrees with previous synchrotron and electron-electron coincidence studies. Metastable toluene dications were observed, along with other dications corresponding to H and H_2 loss and a metastable fragmentation of the dehydrogenated ion $C_7H_6^{2+}$ to $C_2H_3^+$ and $C_5H_3^+$. Metastable monocations of a toluene fragment, as well as the monomer and dimer were also observed. Numerous ion pairs corresponding to Coulomb explosions of the parent dication were observed, as well as that of a tetramer dication.

Double photoionisation experiments on 2-propanol monomers were performed. The partial double photoionisation spectra from these coincidences estimate the double photoionisation potential at approximately 28 eV, which is an upper bound for the value. The exact mechanism of ionisation is not clear from the electron data; however, it is suggested from ion-ion coincidence data that emission of the second electron takes place before the molecule dissociates. Double photoionisation was also observed for 2-propanol clusters at least as large as the tetramer. Analysis of the ion-ion coincidences from these clusters suggest that the two positive charges created by double ionisation are born on different monomer units. Numerous metastable fragmentation pathways of singly-ionised 2-propanol monomers and clusters were also observed in TOF-TOF coincidence spectra, where the parent ions dissociate into a charged and neutral fragment at various points along the flight path to the detector. A model was developed to determine the relationship between the parent lifetime and the TOF of the detected fragments. However, the assumptions used to create the model were found to result in incorrect lifetime values when compared with electrostatic simulations. Despite this, the model successfully reproduced the shapes of the metastable signatures on the TOF-TOF coincidence spectra and allowed isolation of the coincidences corresponding to these pathways to give a qualitative scheme of the signal variation with lifetime.

Contents

1 Introduction

Electronically-exciting and ionising radiation incident on molecular biological systems can induce numerous processes, such as photoionisation and fragmentation. The photophysics and photochemistry of biological molecules is directly linked to their surrounding environment. The native state of many biomolecules is typically either in solution or solid state and this is where their biological function is determined. However, gas-phase studies are required to separate intrinsic effects and properties of the molecule from those that come from interaction with the surrounding solvent. Understanding of the innate electronic structure and spectroscopy of these molecules is also important in determining their biological function [1]–[3]. Solvents often affect the spectroscopy of their solute species, as interactions between the analyte and the surrounding solvent can stabilise or destabilise electronic states, resulting in spectral shifts of transition peaks. More solvent-specific effects can take place such as acting as a thermal bath for dissipation of excess energy [4] and hydrogen bonding [5]. Solvent clusters represent an intermediate case, as they can be doped with selected analyte systems, and their size can be controlled using molecular beam techniques [6]. This allows control of the degree of solvation of the analyte system and changes in dynamical processes from isolated molecular systems to solvated systems to be gradually followed with increasing cluster size.

These processes are typically tracked by time-resolved photoelectron spectroscopy (TR-PES), a powerful technique in which a particular process in a molecule is initiated with a "pump" laser pulse and allowed to proceed for a determined time before a second "probe" laser pulse ionises the molecule. The electronic and vibrational changes are tracked by analysing the kinetic energy of the emitted electron. Photoelectron spectroscopy is particularly powerful as photoionisation is always an allowed process, resulting in no dark states. Electronic and vibrational dynamics can also lead to photodissociation of molecules, resulting in the production of smaller fragments. These processes can also be followed by detection and mass analysis of the photoionised fragments. These techniques can be made more powerful when combined and all charged particles detected and analysed in coincidence.

1.1 Coincidence imaging spectroscopy

A photoionisation event on a gas-phase molecule will always produce at least two charged particles, a negatively-charged photoelectron and a positively-charged photoion. More can be produced in higher orders of ionisation. Coincidence spectroscopy refers to the detection of two or more of these products with the ability to correlate them. It may exist in numerous forms depending on the particular particles involved, including photoelectron-photoion coincidence spectroscopy (PEPICO), photoion-photoion (PIPICO), photoelectron-photoelectron (PEPECO) or higher order combinations of these. There also exist coincidence methods involving detection of a fluorescent photon [7], neutral particles [8] or negative ions [9].

The photoelectrons are typically kinetic energy-analysed, while the photoions are at least mass analysed and may be also kinetic energy-analysed. Mass and kinetic energy analysis is often performed using time-of-flight (TOF) techniques although coincidence spectroscopy techniques are often combined with methods which allow imaging of velocity and momentum distributions such as velocity-map imaging (VMI). VMI [10] is an improvement upon the existing charged-particle imaging techniques [11] in which cylindrical electrostatic lenses are used to shape an electric field in way such that charged particles created with the identical momentum vectors are imaged onto the same spot on a 2D detector. These "coincidence imaging spectroscopy" (CIS) techniques combine the kinetic energy and mass analysis with that of VMI which allows simultaneous angle-resolved studies. Such charged particle imaging spectrometers are a powerful and common technique in studying reaction dynamics of gas-phase systems as they allow the full 3D momentum

distribution of all charged fragment products to be determined. The angles in which photoelectrons are emitted relative to the laser polarisation axis, photoelectron angular distributions (PADs), are sensitive to the symmetry of the electronic states they are ionised from and provide additional information on the system dynamics.

1.2 Double photoionisation

Double photoionisation (DPI) is the process of removing two electrons from an atom or molecule, resulting in formation of either a doubly-charged dication or two singly-charged cations. It requires high energy which results in it being observed comparatively rarely compared to other processes. However, it is a common process for systems in situations where there is sufficient energy [12]. Examples of this include in interstellar clouds [13] and upper atmospheres [14], [15] subject to extreme-ultraviolet (XUV) radiation. When dications fragment they often do so with high kinetic energies due to the Coulomb repulsion of the positive charges. These processes may therefore be important in determining how atmospheric species can escape the gravity well of planetary bodies into space. Many mass spectra of molecules are recorded by electron impact ionisation (EI) at incident energies of approximately 70 eV, which is sufficient to doubly ionise many species. Aromatic molecules featuring π orbitals with delocalised electrons and have relatively high stability due to being able to delocalise positive charges over multiple atomic sites, meaning they don't easily fragment after double ionisation compared to other molecules [16]. Ionic signatures of double ionisation, such as dications and fast monocations, therefore appear in the mass spectra of many molecules.

DPI specifically refers to the process of emitting two electrons with a single photon. The frozen orbital approximation assumes that the orbitals of an ion are the same as those in a neutral molecule. Under this approximation such a one-photon-two-electron interaction is forbidden and the process therefore must proceed by either an indirect multi-step mechanism or involve interactions between electrons in a direct process. The observed occurrence of direct DPI in atoms and molecules is therefore a signature of electron correlation and has been claimed to provide a basic probe into this phenomenon.

Coulomb repulsion in the final dication product is important to consider in determining double ionisation potentials (DIPs) and differences in similar molecules can be interpreted based on where the positive charges are located. An empirical rule-of-thumb [17] for estimating the DIPs in molecules is

$$DIP = 2.20 \times IP + \frac{11.5}{r_{12}}$$
1.1

where r_{12} is the distance between electron vacancies in Å and IP is the single ionisation potential in eV. This rule uses vertical ionisation potentials because the molecular geometry can evolve greatly after DPI. The vertical ionisation energy is the photon energy required to induce the DPI process. The adiabatic ionisation energy is the energy difference between the ground electronic state of the cation and the ground electronic state of the neutral molecule.

1.2.1 Double ionisation mechanisms

The mechanism by which DPI proceeds is researched alongside determination of the relevant thresholds. Different mechanisms will be present in different systems and at different ionising energies. The different types of mechanisms can be grouped as either direct or indirect

1.2.1.1 Direct mechanisms

Direct processes are single-step and described by the scheme

$$M + h\nu \rightarrow M^{2+} + 2e^-$$
1.2

In DPI both electrons must escape the positive ion core. There is Coulomb attraction between each electron and the ion core that must be overcome by kinetic energy. There is also Coulomb repulsion between the two electrons which causes electron correlation. This correlation strongly affects the escape process. The physical principles of electron correlation were first discussed in comparison to EI [18], where incident electrons of sufficient kinetic energy on a sample will inelastically scatter further electrons, leading to ionisation

$$He + e^- \rightarrow He^+ + e^- + e^-$$
1.3

A single photon can bring about the ejection of two electrons in a direct process in two different ways, the knock-out (KO) and shake-off (SO) mechanisms. In the KO, the photon ejects one electron that then inelastically collides with a second electron, leading to transfer of some the first electrons excess kinetic energy and the escape of both electrons. At less than 100 eV above the DIP, direct DPI processes are dominated by the knock-out mechanism [19]. Many details and signatures of this mechanism are shared with that of EI of singly-charged ions, and the cross-section varies in a similar way according to the Wannier law [20]:

$$\sigma_{total} = \sigma_0 E_x^{1.056}.$$
1.4

where σ_0 is a proportionality constant and E_x is the excess energy above the DIP. In SO, fast ionisation of a core electron leads to the Coulomb potential of the system suddenly changing due to different screening of the nuclear charge. This results in rapid rearrangement of orbital energies which electrons must relax into. In some cases, the electrons relax into unbound states of the new Hamiltonian which leads to ejection of further electrons. SO dominates at very high photon energies (100s of eV above the DPI) and becomes significant at photon energies approaching the inner-shell threshold of carbon. In these processes, the mechanisms appear to involve electron correlation of a system that is either ionised or very nearly so. The extent to which they can be said to be exemplify electron correlation in neutral systems is therefore contentious [21].

The total excess energy $E_x = E_1 + E_2$ of a direct process is shared between the two outgoing electrons. Electron pair distributions show the signal intensity varying with the energy fraction of E/E_x that the electrons have. In direct processes at lower photon energies where the knock-out mechanism is dominant, this distribution is flat, indicating that all combinations of E_1 and E_2 are equally likely. At higher photon energies where the shake-off mechanism becomes more significant this distribution becomes "hollow", or U-shaped, indicating that pairs where one electron takes almost all of the available kinetic energy, leaving the other as a threshold electron, are more likely [19].

1.2.1.2 Indirect mechanisms

Indirect processes are multi-step mechanisms, where a singly-charged cation is formed upon photoionisation as an intermediate. There are two general indirect mechanisms. One is Auger-Meitner decay where an electron is initially ionised from an inner-valence or core orbital. This hole usually has a lifetime of a few femtoseconds before another electron decays from a higher energy orbital. The energy released then allows the emission of another electron, leading to a doubly-charged ion:

$$A + h\nu \rightarrow A^{*+} + e_1^-$$
$$A^{*+} \rightarrow A^{2+} + e_2^-$$
1.5

The short lifetime of the intermediate states means that electron peaks are usually very broad from Auger-Meitner processes. One of the electrons (the Auger-Meitner electron) has kinetic energy that is independent of the photon energy (as long as the photon energy is sufficient to induce the Auger-Meitner process), while the primary photoelectron kinetic energy varies directly with kinetic energy. This should manifest in an electron-electron coincidence spectrum as a discrete (albeit potentially broad) peak where the location on one axis does not vary with photon energy. Variations of this mechanism include situations where the initial ionisation is from either a core or inner-valence orbital or when the intermediate state is a 2h-1p (two-hole-one-particle) state. A 2h-1p state corresponds to the existence of two electron vacancies in orbitals which would normally be occupied and an electron in a higher-energy orbital that would normally be unoccupied. The other indirect mechanism involves the singly-charged intermediate ion fragmenting into a charged and neutral fragment. The dissociation generates the neutral fragment in an excited state which then autoionises to create a second ionic fragment:

$$AB^+ + h\nu \rightarrow AB^+ + e_1^-$$
$$AB^+ \rightarrow A^+ + B^*$$
$$B^* \rightarrow B^+ + e_2^-$$

1.6

The second emitted electron usually has a well-defined energy, at least when the autoionizing species is an atom. For a molecule, broadening is likely to occur due to vibrational structure. This is most likely to occur for molecules with terminal oxygen atoms, although it remains unclear why [21]. This mechanism is notable as it is possible to lead to DPI at photon energies below the DIP of the parent molecule [19]. Since many dications are unstable, it is more energetically favourable to generate two singly-charged cations and this can proceed by pathways below the threshold for generating the dication.

If the photoelectron and Auger-Meitner electron kinetic energies are similar, they be impossible to separate in the spectrum and may participate in post-collision interactions (PCI) [22]. If the Auger-Meitner electron is faster than the photoelectron, it may overtake the photoelectron despite being emitted later. The electrons can potentially exchange energy as the faster electron benefits from having the slower one screen the positive charge of the core, resulting in the slower electron losing energy and the faster electron gaining energy.

Indirect mechanisms allow dications to be formed in geometries or vibrational states with very little Franck-Condon overlap with the neutral ground state. The lowest energy state of the dication might be far outside the Franck Condon zone, and possibly behind a potential barrier but still be accessible by indirect ionisation. Therefore, appearance potentials of dications or fast monocations as often determined by EI are not always reliable for determining DIPs.

Direct processes are the only possible mechanism for helium and other two-electron systems i.e. where the dication has no electrons. They are present in more complex species but are comparatively weak compared to indirect processes, particularly at ionising energies close to the threshold. This is because they require electron correlation to occur and when there is little excess energy to share between the electrons it must occur in specific ways. The electrons must have approximately equal energy and opposite trajectories to escape the positive ion core. Indirect processes have larger cross sections at these energies as the multi-step processes mean that the basic interaction is between one photon and one electron. Even in cases where this is not the case, such as autoionisation via the 2h-1p states, it remains common due to a larger number of Rydberg states which the intermediate ion can occupy.

1.2.2 Experimental methods

The simplest method to study DPI is to detect dications on photoionisation with TOF analysis. A possible disadvantage is that molecular dications may have the same mass-to-charge ratio as monocation fragments, although selectively deuterating the molecule can overcome this. Detection of stable dications is possible for atoms and aromatic molecules, however fragmentation of many other molecular dications makes detection difficult in those cases as the Coulomb repulsion of the positive charges often leads to fragmentation. Coincidence techniques for DPI are necessary for any in-depth study as they result in generation of multiple products between which energy is shared. Two electrons are always liberated and extensive fragmentation often leads to multiple charged and neutral molecular fragments.

Threshold photoelectrons coincidence spectroscopy (TPEsCO) involves scanning the photon energy and specifically only counting events where two electrons near zero (<10 meV) kinetic energy, so-called "threshold" electrons, are detected. Like other threshold techniques, this method offers very high resolution. The low electron speeds mean that electron correlation becomes important. Peaks in the TPEsCO spectra therefore correspond to electronic and vibrational states of the dication. The best method to accurately determine DIPs and mechanisms is to measure the kinetic energy of both electrons in coincidence in a PEPECO experiment. Typically, a magnetic bottle TOF spectrometer is used to energy-analyse both electrons however it is also possible with COLTRIMS techniques [23], [24]. In cases where only one electron is detected an energy analysed, COLTRIMS and similar techniques such as imaging of PEPIPICO coincidences can be used to determine the missing electron's kinetic energy by momentum conservation. Analysing a single electron's kinetic energy can provide partial information. If the energy-sharing profile of the two electrons are known to be concave then detecting and energy-analysing a single electron can provide a reasonable estimate of the DIP. Detecting a single threshold electron in a TPEPICO or TPEPIPICO experiment and scanning the photon energy can provide the shape of the DPI cross-section [25]. Detecting photoions in coincidence using PIPICO or PEPIPICO experiments can determine the fragmentation channels of the generated dications and the charge separation dynamics [26].

1.3 High-harmonic generation

High-harmonic generation (HHG) has become a popular method for generating ultrashort XUV pulses. HHG can produce XUV light with high brilliance levels at high repetition rates (10^{11} photons s^{-1} at 36 eV and 6000 s^{-1}) [27], while avoiding the difficulties of using facility-based methods such as synchrotrons and free-electron lasers. In HHG [28], an intense, ultrashort infrared (IR) laser pulse is incident on a noble gas, most commonly argon or neon. The intense electric field of the pulse distorts the potential energy well of the target atom, resulting in tunnel ionisation and acceleration of the electron away from atomic nucleus. When the polarisation of the electric field changes, the electron is driven back towards the nucleus at high kinetic energy where it recombines and emits a high-energy photon. HHG is a promising candidate as an intense, flexible light source for studying DPI. However, there have been few such studies performed with it due to a previous lack of sufficient intensity caused by the need to monochromatise the pulses in order to improve their energy resolution and remove unwanted harmonics [19].

The main laboratory-based alternatives for generating high-energy incident light include 4-wave mixing with plasma filamentation, stimulated Raman shifting (SRS) and gas-discharge lamps, while electron impact ionisation can be used for many multi-ionisation studies with coincident techniques. Compared to HHG, 4-wave mixing techniques and SRS both generally have lower flux levels and energy limits. 4-wave mixing coupled with plasma filamentation has achieved photon energies up to approximately 9 eV at 3×10^9 photons pulse^{-1} at 1000 s^{-1} [29] and tandem third harmonic generation (3 x 3ω) of a Ti:sapphire output has been used to generate 14 eV photons at (9×10^{10} photons pulse^{-1} at 1000 s^{-1}) [29], [30]. SRS-based

techniques have been shown to generate energies up to 7 eV [31]. Sum-frequency mixing techniques have also produced energies up to 10 eV [12], [13], [14]. It is generally desired to ionise the molecule in a single probe pulse, for which these techniques are mostly only suitable as a probe in pump-probe experiments involving the sample already being UV excited in the pump process. The energies available are also inadequate for any DPI investigations conducted here, where photon energies are usually required to be above approximately 25 eV. Additionally, the low sample density of gas-phase molecular beams, compared to condensed matter phases for which these techniques are usually used, requires higher photon fluxes than is available from these sources.

EI is extremely advantageous with respect to other methods in that one can easily generate an intense beam of electrons of almost any energy. It has therefore been commonly used in multiple-ionisation studies. However, there are disadvantages: the incident electron beam can easily be deflected by stray electric or magnetic fields, which would make it difficult to use with coincidence techniques or a detection technique like VMI. This requires the use of extremely fast electrons (larger than 500 eV) which may result in the contributions from higher orders of ionisation than desired. It is possible to circumvent issues of distortion by the electric fields for TOF or VMI detection of the cations by pulsing the voltages after the electrons have ionised the sample and cleared the interaction region [35]. Compared to photoionisation, EI is also not state selective. A photon can transfer an exact amount of energy $h\nu$ to a system, while impact electrons can carry off some of their initial kinetic energy when scattered, meaning that comprehensive energy analysis requires the scattering electron to be detected and diagnosed in coincidence with any products, including secondary electrons and cations. Reliable detection of higher-order coincidences therefore becomes more difficult. Polarised light also provides a reference axis in the laboratory frame, something which EI methods lack, allowing for examination of symmetries. Additionally, space-charge effects can limit the pulse length of an electron bunch which can decrease resolution in time-of-flight based methods.

Apart from the above-mentioned laboratory-based methods, other available sources for such experiments are synchrotron sources and x-ray free electron laser (XFEL) facilities. Both sources provide almost free choice of XUV energies at high flux levels. However, there are inherent difficulties of using facility-based methods such as beamtime constraints and availability of a suitable endstation at a suitable light source. Synchrotrons offer an extremely high repetition rate, which is suitable for PEPICO experiments in particular, but synchronising the endstation to the electron bunches is difficult. This means that PEPICO collection cannot be reliably triggered for each light pulse, making false coincidences in the datasets a significant problem and generally doing pump-probe experiments with a table-top laser are a challenge. While FELs can be synchronised with, the low repetition rate (tens of s^{-1}) of most XFELs to date make this unworkable for acquiring PEPICO data as well as the poor shot-to-shot stability of unseeded XFELs. However, this is likely to change with the recent and upcoming commissioning of high-repetition rate XFELs such as European XFEL and LCLS-II [36].

1.4 Motivation and outline

The initial motivation for this thesis was the development of an experimental setup would be used to perform time-resolved photoelectron-photoion coincidence spectroscopy on molecules doped in size-controlled solvent clusters. This thesis primarily concerns the design, construction and commissioning of a coincidence imaging spectroscopy (CIS) apparatus with velocity-map imaging (VMI) capabilities with a molecular beam source. This apparatus would be used with XUV light generated by the Harmonium HHG [27] facility at the Lausanne Centre for Ultrafast Science (LACUS) to investigate the effects of solvation for a range of solvents on the excited state dynamics of a range of molecular species. Functionality for creating the doped clusters and performing pump-probe experiments was not achieved in this work, and the XUV light and coincidence techniques were used to perform DPI experiments on small hydrocarbons and their clusters.

The thesis is organized as follows: Chapter 2 describes the general experimental description of the endstation and hardware involved. Chapter 3 describes experimental and simulation attempts to calibrate and characterise the performance of the endstation. Chapter 4 describes results obtained from trial commissioning experiments with the Harmonium HHG source performed on the XUV photoionisation of toluene and comparison of the results to existing literature. Chapter 5 describes results obtained from XUV photoionisation experiments on 2-propanol monomers and clusters. The thesis work is summarised and concluded in Chapter 6.

All work presented here was performed collaboratively with and supervised by Prof. Marcel Drabbels. The CIS endstation, including the vacuum chambers, molecular beam source and charged particle optics, was designed, simulated and assembled by me. The vacuum chambers were fabricated by *Pfeiffer Vacuum* and many other custom parts were fabricated by the mechanical and electronic workshops at EPFL ISIC. A data acquisition program for coincidence operation of the delay-line detector was written by Dr. Achim Czasch of Universität Frankfurt and *Roentdek Handels*. Other data acquisition and endstation-operation programs were written by Prof. Drabbels. The constructed endstation was first coupled to the Harmonium HHG facility by myself and LSU postdoctoral researcher Dr. Michele Puppin. A program for quickly reconstructing velocity maps from raw images was generously provided by Prof. Dr. Bernhard Dick of Universität Regensburg. This was incorporated as a subroutine into a program for fast coincidence analysis of the large output files from CIS experiments written by Prof. Drabbels and modified by me. The calibration experiments and simulations in Chapter 3 were performed and the data analysed by me. The XUV photoionisation experiments of toluene and 2-propanol in Chapters 4 and 5 were performed by me in collaboration with LSU postdoctoral researchers Dr. Rebecca Ingle and Dr. Thomas Barillot. Hartree-Fock calculations on 2-propanol were provided by Dr. Ingle. The data analysis was performed by me.

2 Experimental setup - hardware

A significant portion of the work in this thesis involved the design, construction and commissioning of the experimental setup. This chapter describes the hardware and designs. Description of the experimental methods performed and their calibration and characterisation details are described in Chapter 3.

The molecular beam coincidence imaging spectroscopy (CIS) setup (Figure 2.1) consists of a series of differentially-pumped vacuum chambers. Gas-phase molecules and clusters are generated in a continuous-wave (CW) molecular beam (a pulsed molecular beam source can also be installed) in the first chamber before passing through two further chambers into the final chamber. The molecules are then irradiated with laser light to produce charged photoproducts, some or all of which are extracted by electrostatic lenses and detected in one of two available velocity-map imaging schemes. The CIS setup features two opposite-facing velocity-map imaging (VMI) setups, one with a microchannel plate (MCP) and delay-line detector (DLD) configuration installed at the end of the flight tube ("DLD-VMI") and the other with an MCP and phosphor screen assembly with charge-coupled device (CCD) camera configuration ("CCD-VMI").

The original design plan for the project was to feature a cryogenic beam source capable of generating size-controlled nanodroplets of superfluid helium (as achieved previously in this research group). It would also generate clusters and nanodroplets of other molecules. These clusters and nanodroplets would function as potential microsolvation matrices. The machine would additionally allow doping of these clusters and nanodroplets by the pickup method before being irradiated in a time-resolved pump-probe photoionisation scheme. The photoelectron(s) and photoion(s) would be extracted in opposite directions in the electrode source and hit opposite detectors. The signals from each detector would then be correlated to give coincidence information.

The apparatus geometry was therefore designed with these goals in mind, but full functionality as described above was not achieved within the project of this thesis. The cryogenic source for large clusters and droplets was not constructed; instead a room-temperature or heated molecular beam source for use on gas-phase monomers and small clusters was used. Subsequently the crucible oven for cluster doping was not constructed. MCP detectors are typically able to read out TOF information by decoupling the signal current from the phosphor screen and displaying it on an oscilloscope via an amplifier. This was not achieved here, because the amplifier would blow immediately due to arcing in an undetermined location, rendering it useless for coincidence purposes. The CCD-VMI is then only used for creating photoelectron spectra of the entire chemical ensemble in the molecular beam accessible by the ionisation scheme utilised. The DLD-VMI was therefore used for detecting both the photoelectrons and photoions generated from the photoionisation events in coincidence.
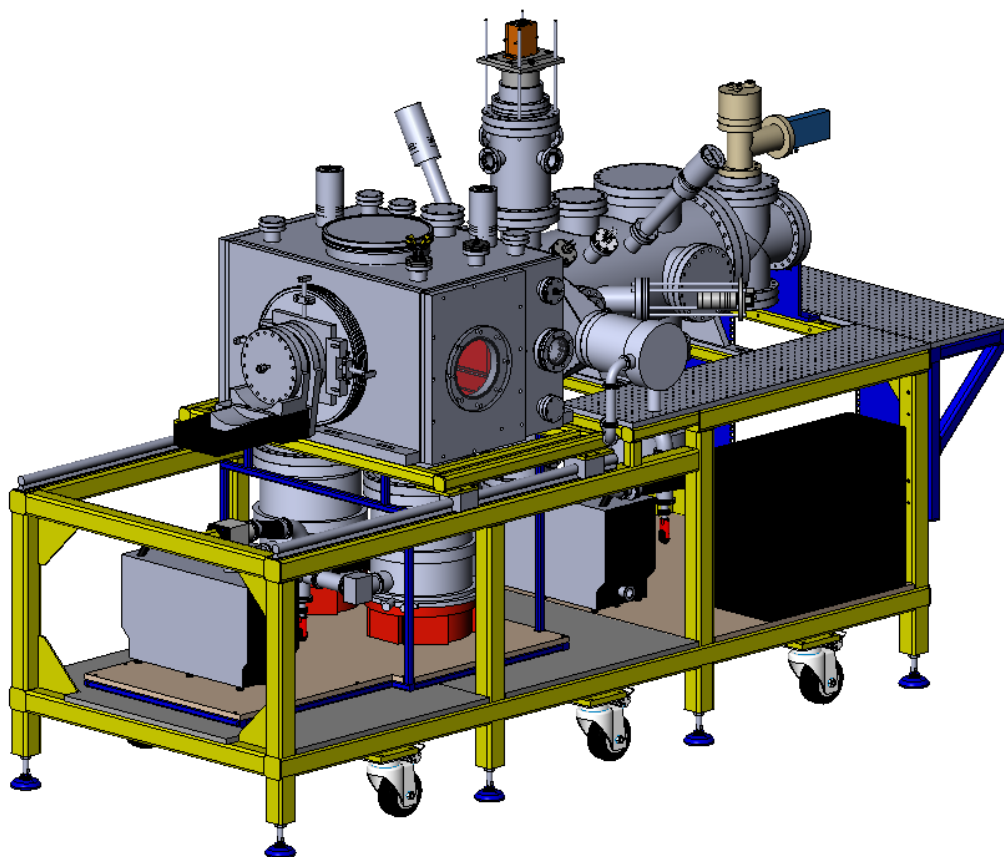
Figure 2.1: Dimetric view of a Solidworks computer-aided design (CAD) model of the entire CIS apparatus on its supporting frame.

2.1 Vacuum chamber apparatus

2.1.1 Overall frame

The endstation consists of four consecutive differentially-pumped vacuum chambers (Figure 2.2); the source chamber, doping chamber, differential chamber and detection chamber, arranged coaxially along the molecular beam axis. They are custom-manufactured as part of the TrinosLine by *Pfeiffer Vacuum* in AISI 304L stainless steel. The interior surfaces of all the chambers are electrochemically polished for vacuum quality, and the exterior surfaces are glass-bead blasted. The vacuum chambers' design and build were based on previous designs of a helium nanodroplet beam machine with velocity-map imaging built by Dr. Andreas Braun [37] and upgraded by Dr. Evgeniy Loginov [38]; and the Low Density Matter (LDM) endstation at the FERMI Free Electron Laser (FEL) at Elettra Sincrotone Trieste [39]. The entire assembly is mounted onto a single, portable, stainless-steel frame, which allows transport of the apparatus between laboratories with minimal disassembling. The source and doping chambers are additionally mounted on a linear rail system (S3025-SET and T9725B, *AMSLER & CO*) along the molecular beam axis with 565 mm range. This allows the machine to be opened and the source unit to be pulled away to allow access to the chamber interior, or to add additional intermediate chambers later. The machine can be opened either between the doping and differential

chambers or between the differential and detection chambers to allow work to be done in the doping or detection chamber respectively.
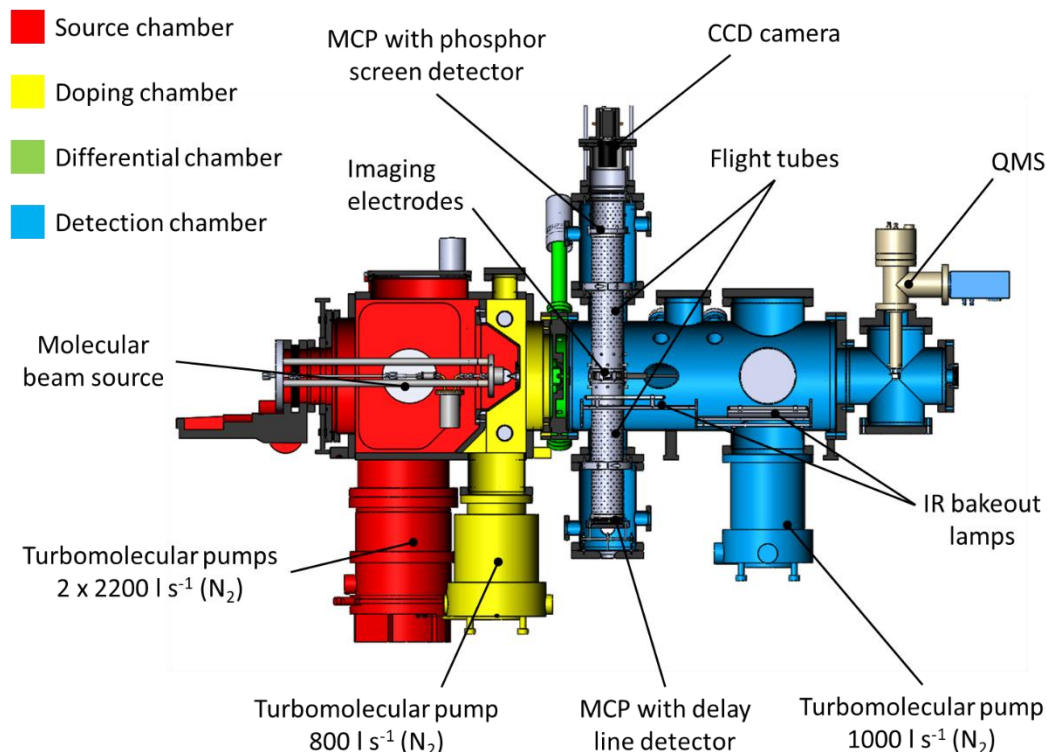
Figure 2.2: Vertical cross-section of the coincidence imaging spectrometer, viewed from the side, with the individual differentially-pumped chambers colour coded. The molecular beam travels horizontally from the source chamber to the detection chamber. The laser enters the chamber perpendicular to the plane of the page and crosses the molecular beam at the point of the imaging electrodes. The turbomolecular pump for the differential chamber, the fore-vacuum connections, the support frame and some vacuum components are omitted from the cross-section for clarity.

2.1.2 Source and doping chambers

The Harmonium HHG source has a low photon flux. It is therefore necessary for the cluster beam to have as high a flux into the detection chamber as possible. To facilitate this, the distance between the source chamber skimmer and the point of interaction between the sample and laser in the detection chamber is shortened as much as possible.

The source chamber and the doping chamber are housed within the same overall stainless-steel chamber, and separated from each other by an internal partition. The source and doping chamber turbomolecular pumps are jointly pumped by a single dry-vacuum backing pump (PDV500-GB, *Ebara*), which is connected to an uninterruptible power supply (UPS) (2000 VA 1200 W, *König Electronic*). This allows vacuum to be maintained for up to ten minutes in case of power outages.

On the front face of the source chamber, the gas line for the molecular beam is mounted on a heavy duty z-axis linear translator (UL160.100short, *Metallic Flex*) with a 100 mm-range manual hand wheel. The translator is then mounted on a custom built xy-translatable DN 320 ISO-K flange. Manipulation in the xy-plane is achieved by adjusting four M12 screws (two for each axis, one in each direction) that move a DN 160 CF flange on the surface of the DN 320 ISO-K flange over an FKM o-ring seal.

In the original cryogenic source design, high backing pressure and cryogenic temperatures would be necessary to generate the superfluid helium nanodroplets. This would introduce large gas loads into the source chamber. The source chamber is therefore pumped by two large turbo pumps, each with a nominal N_2 pumping speed of 2200 ls^{-1} (STPiXR2206 DN 250 CF, *Edwards Vacuum*). The chambers are designed to reach a base pressure below 10^{-7} mbar.

To accommodate both pumps in a vertical position underneath the chamber, the source chamber is a cuboid design, with the pumps attached underneath. Because the chamber walls are flat, they are made 20 mm thick to prevent flexing under the pressure difference.

Approximately 10 mm from the nozzle a skimmer (0.29 mm orifice diameter, Model 2, *Beam Dynamics, Inc.*) is mounted on a wall separating the source chamber from the doping chamber. Because different species will be used in the beam and because the source can be changed between CW and pulsed options, it is necessary that this distance is also easily adjustable, hence the provision of the *z*-translator onto which the source is mounted.

Between the source chamber and doping chamber, a partition is mounted onto an FKM o-ring seal. The partition is removable to allow work to be done on the doping chamber from the source chamber side. Borosilicate glass windows are mounted on the sides to directly view the gap between the source nozzle and the skimmer for visual assessment of the molecular beam alignment.

On the other side of the wall-mounted skimmer is the doping chamber. The doping chamber is pumped by an 800 l s^{-1} vacuum pump (STPA803 DN 160 CF, *Edwards Vacuum*) and is designed to reach base pressures below 10^{-8} mbar. The doping chamber was designed to introduce selected molecules as dopants into the nanodroplets. This would be achieved via the "pickup" process by using either an oven capable of vaporising solid samples or an adjustable leak valve system to fill the chamber with gas-phase samples. Since the nanodroplet/large cluster cryogenic source was never constructed, the oven and leak valve system were never implemented and this chamber is currently empty and only functions as a differential pumping stage.

2.1.3 Differential and detection chambers

A differential pumping chamber is added in between the doping chamber and detection chamber. This was originally installed to minimise leaking of dopant molecules from the doping chamber into the detection chamber to help reach ultra-high vacuum in the detection chamber. It is pumped by a 300 l s^{-1} turbomolecular vacuum pump (STP301 DN 100 CF, *Edwards Vacuum*) and is designed to reach pressures below 10^{-8} mbar.

To allow space above and below the chamber for the VMI setups, the pumping port of the differential chamber is rotated 90° to a horizontal position, jutting out at the right side of the chamber. The pump might need to be removed when transporting the apparatus between laboratories.

On the exterior of the cylindrical face are four angularly-spaced DN 40 CF flanges and a DN 16 CF flange. A Pirani/cold cathode full-range pressure gauge (PKR 251, *Pfeiffer Vacuum*) is attached to a DN 40 CF flange, with the others being left available for later modifications. A linear-motion feedthrough (SBLM-133-2, *MDC Vacuum*) is attached to the DN 16 CF flange. This was intended to adjust the opening of a thin-blade gate valve which was ultimately not installed. The gate valve was meant to close off the differential and detection chambers separately from the source and doping chambers to allow the source and doping chambers to be vented and worked on without having to vent the detection chamber, which requires much longer pump-down times.

The detection chamber is structured around a DN 300 CF tube which is 752 mm long. The molecular beam follows the tube axis. The chamber is designed to reach pressures below 10^{-9} mbar. Close to the connection

with the differential chamber are four DN 100 CF flanges, arranged around the axis of the tube at 90° angles. The intersection of all of the axes of these flanges is the interaction region of the experiment, where the molecules are irradiated by the laser beam. The top and bottom DN 100 CF flanges are attached to the CCD-VMI and DLD-VMI respectively. The left and right DN 100 CF flanges are the laser input and output ports. When the setup is operated with the Harmonium facility (Figure 2.3), the input port is attached, via a manual gate valve (Mini UHV gate valve 01032-CE01, *VAT Group*), to the vacuum-sealed beamline. The beamline is pumped by a 66 l s⁻¹ turbomolecular vacuum pump (EXT75DX, *Edwards Vacuum*). The terminating XUV beam can emit photoelectrons from the chamber surface after scattering from the output glass port. To prevent these secondary photoelectrons from entering the imaging setup and contaminating the experimental signal, the output glass port is attached to a 1 m long DN 63 CF arm that terminates the XUV beam at a large distance from the charged particle optics. Windows are mounted at approximate 65° angles to decrease reflections of the incident light back into the chamber. The HHG beam dump has two mounts where apertures of various sizes can be mounted, to allow the HHG beam to pass through and block back-scattered light from reaching the charged particle optics. In this work the removable apertures were not used and their holding brackets effectively functioned apertures of 20 mm diameter. The HHG beam dump is also pumped by a 66 l s⁻¹ turbomolecular vacuum pump (EXT75DX, *Edwards Vacuum*). The HHG beamline and HHG beam dump turbomolecular pumps are jointly pumped by the same backing dry scroll pump (nXDS15i, *Edwards Vacuum*). When performing experiments using optical lasers, the beamline and beam dumps are simply replaced with glass windows at 65° angle to decrease reflections.
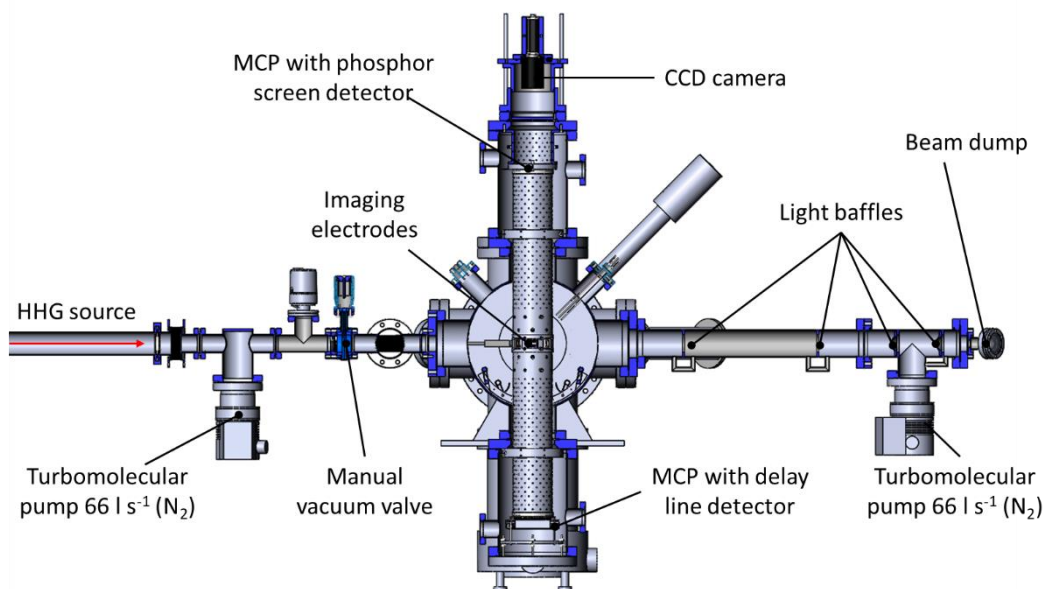
Figure 2.3: Vertical cross section of the detection chamber, viewed from the direction of the molecular beam source, with the relevant connections for the installation on the Harmonium beamline. The molecular beam travels into the plane of the page and enters at the point of the imaging electrodes. The beamline and beam dump turbomolecular pumps share a fore-vacuum, which is omitted from the cross section as is the support frame for clarity.

Two DN 63 CF flanges are horizontally attached at a 45° angle to the molecular beam axis of the chamber. Attached to one of these is a linear motion feedthrough (BLM-275-6, *MDC Vacuum*) mounted with a Ce:YAG crystal that is specially treated for XUV light (*Crytur*). When in the path of the laser beam, the Ce:YAG crystal's fluorescence is observed through a glass viewport on the other DN 63 CF flange, and recorded with a CCD camera (Ace acA1300-200um, *Basler*) (Figure 2.4). This setup is used to check the alignment of the laser into the interaction region of the detection chamber. As long as the camera is rigidly fixed in place and not displaced, the pixel reading of the fluorescence spot can be used as an alignment reference.
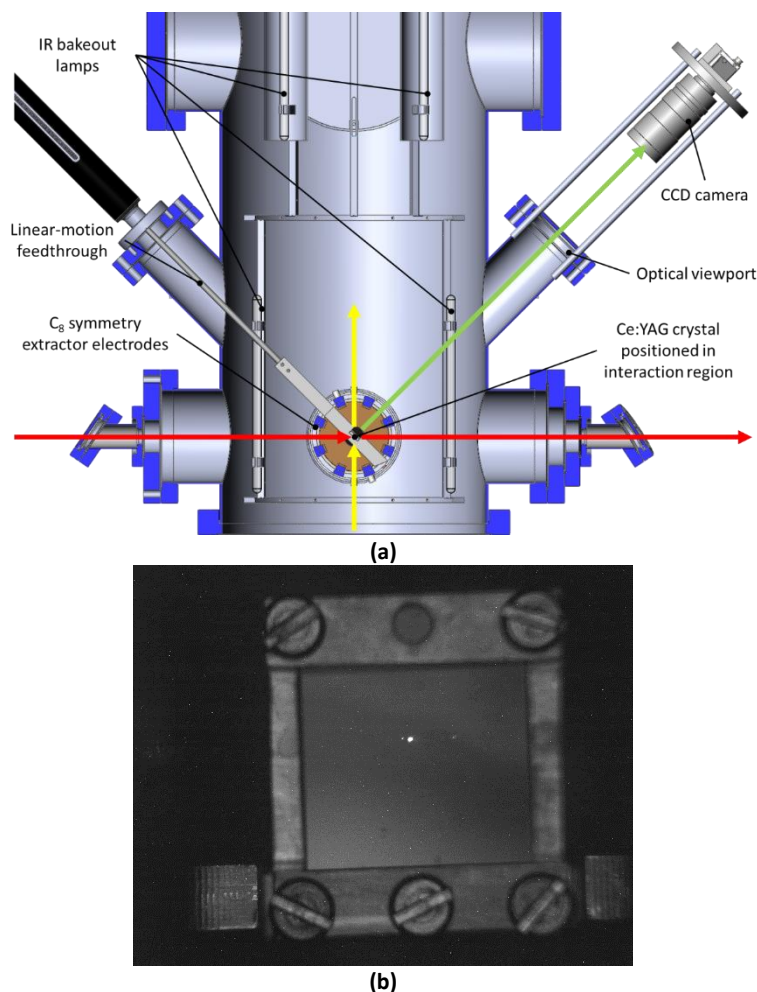
(a)

(b)

Figure 2.4: (a) Horizontal cross-section, viewed from above, of the detection chamber showing the IR bakeout lamps and the Ce:YAG crystal extended into the interaction region. Coloured arrows show the nominal directions of the laser (red), molecular beam (yellow), and fluorescence (green) from Ce:YAG crystal when irradiated by the laser. The presence of the crystal in the interaction region blocks the molecular beam and laser from passing all the way through the interaction region. The arrows are included to highlight the exit points in the C_8 symmetry of the extractor electrode. (b) Picture of the Ce:YAG crystal taken with the CCD camera. The bright spot is fluorescence due to excitation by incident 24.8 eV light from the HHG laser (Section 2.4.1).

Six DN 40 CF flanges are also arranged, three each side, normal to the linear axis and at 45° to the horizontal plane, of the chamber. Attached are a cold cathode pressure gauge (IKR 270, *Pfeiffer Vacuum*) and feedthroughs for internal components. The cold cathode pressure gauges are surrounded by mu-metal shields to minimise the effect of stray magnetic fields on electron trajectories.

A removable framework was designed, built and installed to support a system of infrared-emitting tungsten filament lamps (Noblelight Infrared Emitter Group 02, *Heraeus*) inside the detection chamber. The four lamps are arranged in two sets of two lamps in series, heating the front and back of the chamber. They have a combined heating power of 2 kW and are inserted into the detection chamber to provide heating for a more efficient bakeout than heating the chamber exterior would provide. The temperatures of the interior chamber surface and VMI tube are measured with Type K thermocouples. The chamber is usually baked to approximately 200°C for at least one day after pumping down. The MCPs and electrodes can be safely operated with high voltage about eight hours after stopping bakeout for cooling down. After bakeout, the detection chamber is currently able to reach pressures down to 5 x 10^{-10} mbar. The heating provided by the

infrared lamps is supplement by heating tape wrapped around the exterior chamber surfaces. The entire bakeout process is controlled by a home-built bakeout controller with a timer and kill switch in case the temperature or chamber pressures exceed set limits.

At the back end of the detection chamber on the underside is attached the magnetically-levitated 1000 l s^{-1} turbomolecular vacuum pump (STPA1003 DN 200 CF, *Edwards Vacuum*). Two DN 160 CF flanges at the back allow the chamber to be opened and worked on. On the top surface, a DN 100 CF and DN 200 CF are linearly arranged along the beam axis. These are left available for later modifications.

The molecular beam is terminated in a separate chamber at the back end of the detection chamber. A four-way DN 160 CF standard cross (C-0800S, *Kurt J. Lesker Company*) is attached by reducer flange to the back end of the detection chamber. On the top flange of the cross is a quadrupole mass spectrometer (QMS) with cross beam ion source (PT Q16 31 310, *Pfeiffer Vacuum*). On the bottom an 800 ls^{-1} sized magnetically levitated vacuum pump is intended to be installed. An aperture designed to just fit the diameter of the molecular beam will be attached to the DN 300 to 160 CF reducer flange. This allows the cluster beam to travel into the cavity of the DN 160 CF cross to be mass-analysed and pumped away with minimal scattering of the clusters back into the detection chamber. On the far side DN 160 CF flange of the cross, a DN 40 CF viewport is attached to allow viewing along the beam axis in order to check alignment of the chambers. The weight on the cross due to the QMS and the vacuum pump mean that a support piece will be needed on the end flange to reduce strain at the reducer. A steel support to attach the framework is made for the appropriate height to support the cross.

The differential and detection chambers are jointly pumped by the same dry vacuum backing pump (PDV500-GB, *Ebara*) which is also connected to the UPS.

2.2 Molecular beam source

For studies of gas-phase molecules and small molecular clusters, a simple, heated, molecular beam source was constructed (Figure 2.5). The source consists of a bored aluminium chassis with a 30 μm platinum-iridium nozzle (*Frey*) mounted on the output with an indium foil gasket 0.127 mm thick. The nozzle is compressed into the gasket and fixed in place by a stainless-steel cover on the front. Just behind the chassis, an aluminium reservoir for liquid-phase samples is joined via Swagelok connections and copper tubing. Both the reservoir and chassis can be heated with individual heating cartridges (RS PRO 860-7135, *RS Components*) using AC power supplies (RS PRO 890-2793, *RS Components*), while the copper tube between them is wrapped and heated with resistance wire. The heating can be used to increase the vapour pressure of liquid-phase species, therefore increasing their presence in the molecular beam and subsequent ionisation signals. The temperatures of each component are monitored with Type K thermocouples. The system can ostensibly be heated up to 156.6°C, the melting point of the indium gasket, but is usually kept below 100°C. The placement of the heated reservoir directly behind the nozzle means that the source chamber must be vented when changing or refilling the reservoir contents. There is another reservoir on the molecular beam, situated outside the chamber, which can be used and filled without breaking vacuum. However, the long distance of gas flow to the nozzle means it can only be used at room temperature. Two 0.5 μm particle filters are used to prevent blockages in the nozzle. The molecular beam source is mounted by three aluminium rods onto a DN 160 CF flange on the source chamber linear translator. The molecular beam travels approximately 291 mm to the interaction region. Based on the skimmer diameters and their positions relative to the molecular beam source and interaction region, the width of the molecular beam in the interaction region is estimated to be 2.8 mm.
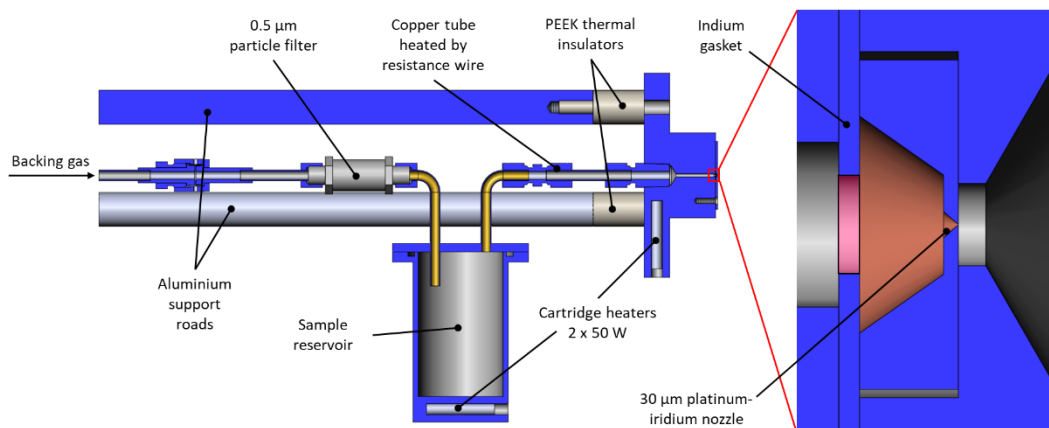
Figure 2.5: Vertical cross-section, viewed from the side, of the heated molecular beam source, and a zoomed-in section of the aperture. A second sample reservoir is situated earlier in the gas line, outside the vacuum chamber, which can be used for room temperature samples and refilled without breaking vacuum.

2.3 Detection setup

2.3.1 Detectors

The detectors used in the experiments are two-dimensional, position-sensitive detectors (PSDs). For the CCD-VMI, the detector assembly consists of two chevron-stacked MCPs with a P43 phosphor screen (APD 2 PS 75/32/25/12 I 60:1 NR CT P43, *Photonis*) and a CCD camera (Pilot piA1000-48gc, *Basler*). The MCPs have a 75 mm effective diameter.

The delay-line detector assembly consists of two chevron-stacked MCPs with 75 mm effective diameter (75/32/25/8 D 60:1 NR, *Photonis*) and an anode of crossed delay-line wires (DLD80, *RoentDek Handels*). Potentials are applied to the various components of the assembly by a high-voltage power supply (NDT1471, *CAEN*) via a voltage divider (HVZ12, *RoentDek Handels*). The delay-line detector provides spatial and time-of-flight information in the form of electronic pulses emerging from both ends of two sets of crossed wires for the x- and y- coordinates. The coordinates are calculated from the difference between the arrival times of the pulses at each end of the wire. The signal pulses are decoupled from the applied potentials with an airside decoupling circuit (FT12TP, *RoentDek Handels*) and sent through an amplifier ((D)FAMP6, *RoentDek Handels*). To improve timing, and therefore spatial, resolution, the signal pulses are converted to digital NIM pulses with a constant faction discriminator (CFD7x, *RoentDek Handels*).

2.3.2 Charged-particle optics

The charged-particle optics of the coincidence imaging setup were designed through simulations with SIMION 8.1 software. The operation is based on the setup built by Prof. Maurice Janssen at the Vrije Universiteit Amsterdam [40]–[42]. The coincidence detector is intended to measure the three-dimensional momentum distributions of correlated electrons and ions in an ionisation experiment. It was designed with the goal of maximising spatial (and therefore) energy resolution of photoelectron with kinetic energies from 0 eV to approximately 25 eV. See Chapter 3 for details on the simulation and performance of the charged-particle optics and detectors.

To have optimal settings to image both electrons and ions, the electrode potentials are operated in a pulsed mode at the repetition rate of the experiment. Because of the much faster flight time for electrons compared to ions, the lens voltages are initially set negative values to image electrons. A certain amount of time after the electron has been detected, the lens voltages are switched to map the coincident ion to the detector. The lenses remain at these voltages for a set time to allow ions of all masses to be detected before switching back to the electron imaging settings in time for the next laser pulse.

The charged particle optics setup was custom built (Figure 2.6, Figure 2.7). The electrodes and flight tube structure are nominally geometrically identical in both directions to each detector. There are six electrodes (three at each end) made from zinc-free phosphorous bronze $CuSn_8$. The electrodes are labelled α, β and γ depending on their position in the stack relative to the interaction region (α is the closest) followed by a subscript C or D if they are on the CCD or DLD side respectively. For example, the β_D electrode is the second electrode from the interaction region on the DLD side. The electrodes are housed in a polyether ethyl ketone (PEEK) chassis, and are separated from each other by 2mm thick cylindrical PEEK spacers. The distance from the interaction region to both detector surfaces is approximately 400 mm. All electrodes are 2 mm thick. The α electrode surface is 11 mm from the interaction region, the β electrode surface is 30 mm from the interaction region and the γ electrode surfaces are 60 mm from the interaction region. The diameters of the bore holes of the α, β and γ electrodes are 23 mm, 30 mm and 40 mm respectively. To reduce the possibility of performance being affected by electrostatic charging of the insulating material, the electrodes have a brim which blocks most of the PEEK material. The flight tubes are made from aluminium and in direct electrical contact with the respective γ electrodes. The flight tubes can theoretically operate at an applied potential, but they are kept grounded via the γ electrodes in this work. The upper flight tube, which is used for the CCD-VMI, is split into two overlapping pieces to better allow assembly of the detection setup and access to the electrodes for work.
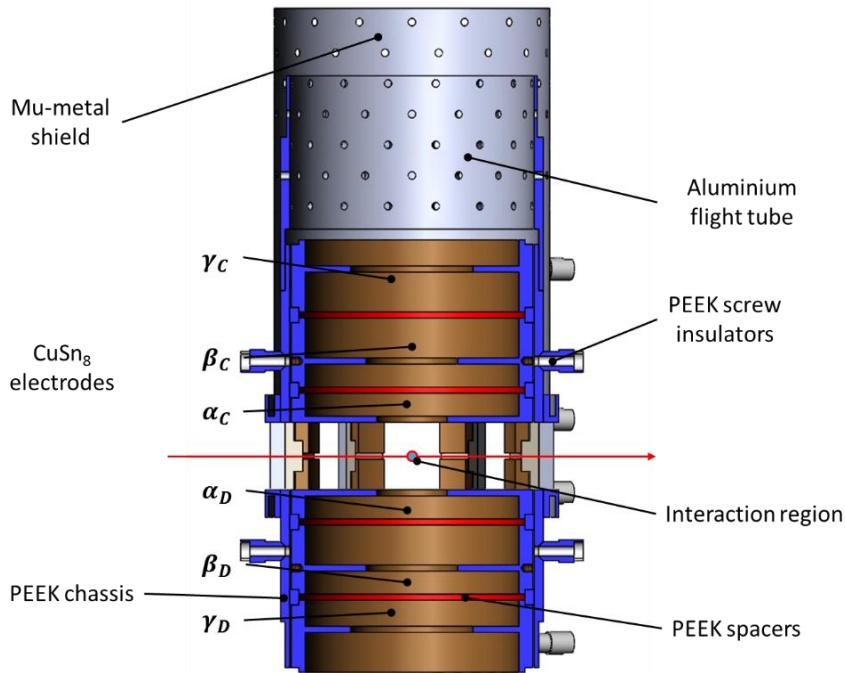
Figure 2.6: Vertical cross-section of the electrode setup. The flight tube and mu-metal shield in the DLD-VMI direction (towards the bottom) are omitted for clarity.
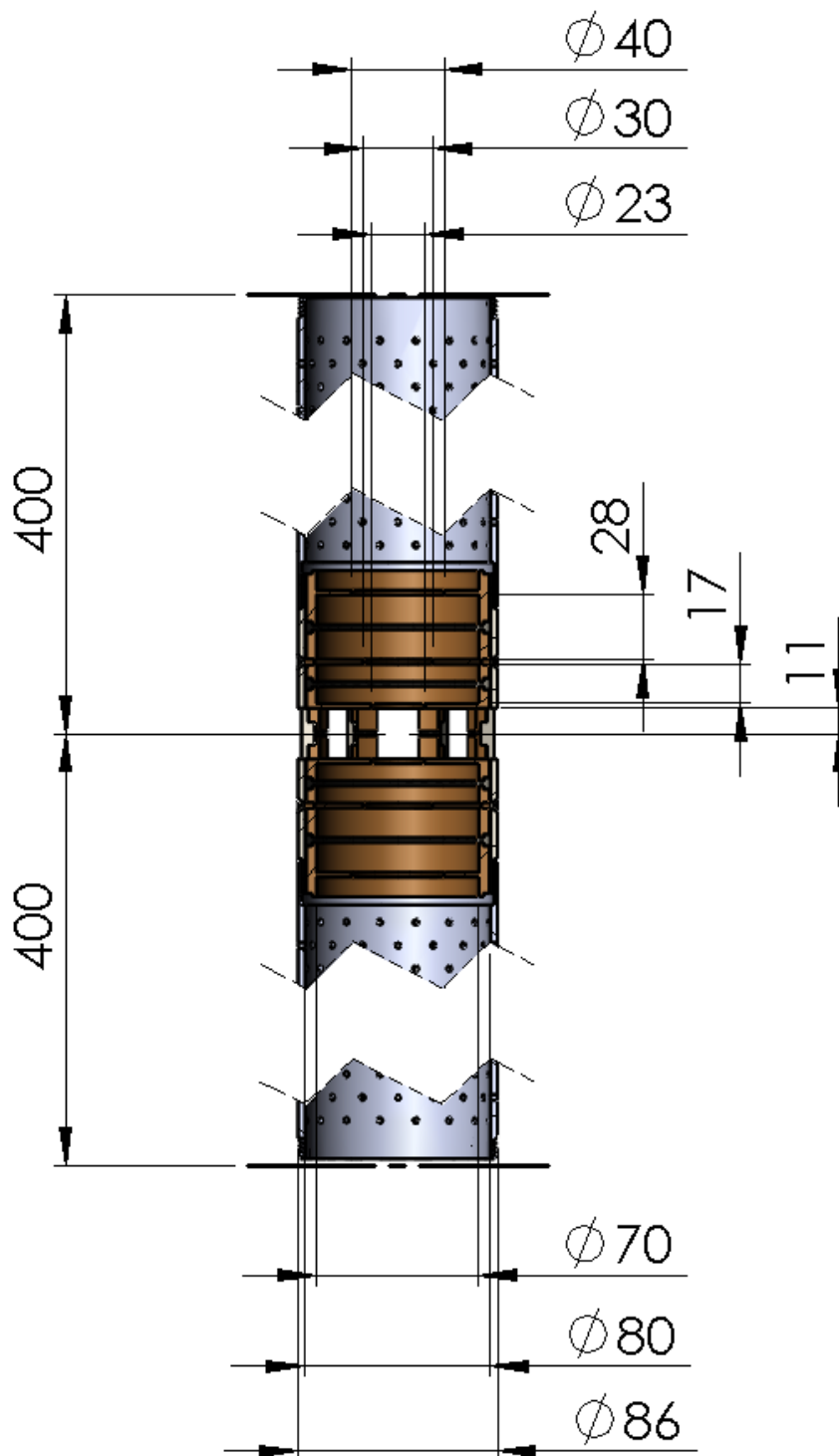
Figure 2.7: Vertical cross-section of the imaging setup with dimensions shown. The PEEK and mu-metal parts are omitted for clarity. The distance to each detector surface is nominally 400 mm, with the flight tubes being a few mm shorter to avoid contact and damaging the MCPs. The central parts of all the electrodes are 2 mm thick. The longitudinal distances between the electrodes shown are the face-to-face distances of the central parts.

Within the electrode setup, the system is cylindrically symmetrical except for the extractor electrodes, which have C_8 symmetry. This is to allow room for the molecular beam and laser beams to enter and exit the interaction region; to allow the Ce:YAG crystal to extend into the interaction region and be monitored with a CCD camera; and to increase pumping speed in this area. Mu-metal shields are placed around the flight tubes and electrode chassis to reduce the effect of stray magnetic fields on the electron trajectories. The mu-metal shields are explicitly grounded. Both the flight tube and mu metal shields have holes in an 8-fold symmetry pattern to allow for increased pumping speed within the VMI system.

Voltages are applied to the extractor through DN 40 CF electrical feedthroughs (MHV-5 or SHV-10, *Kurt J. Lesker Company*). The electrical connections within the vacuum system comprise copper wire coated with poly(4,4'-oxydiphenylene-pyromellitimide) (Kapton). They are further insulated within polytetrafluoroethylene (PTFE) tubes. The cables are fixed to the electrodes with M3 screws, through holes in the PEEK chassis and mu metal. The live cables and screws are protected from arcing to the mu-metal shield by PEEK insulator rings that surround the screws. The voltages are provided by four HV power supplies (HCP 140-6500, *FUG*) with a range up to 6 kV voltage and 20 mA current.

The ion optics can be operated in 2-, 3- or 4-electrode modes (Figure 2.8), with subsequent changes in resolution and kinetic energy range (See Chapter 3).

- 2-electrode mode: only the α electrodes are used; one as a repeller with voltage V_R and the other as an extractor with voltage V_E.
- 3-electrode mode: an α electrode and the β electrode on the same side are both operated as repeller electrodes at the same voltage V_R. This is to generate a more uniform repelling voltage which more closely resembles that which would be provided by a uniform repeller electrode without a bore hole. The other α electrode is again operated as an extractor at V_E.
- 4-electrode mode: similar to 3-electrode mode, but the second β electrode is also operated as a focusing lens at V_L. This increases the maximum kinetic energy range of particles that can reach the detector.
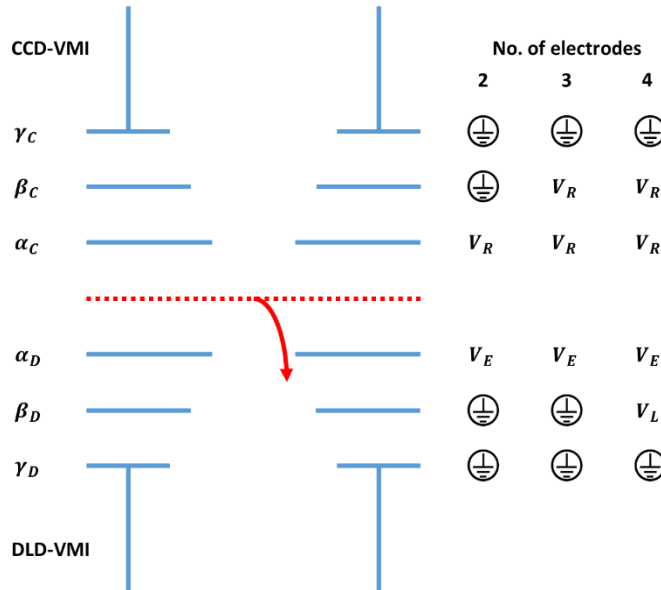
Figure 2.8: Schematic showing the electrode labelling and the voltage schemes used for each VMI mode of operation when using the DLD-VMI side. The columns on the right indicate whether the electrode is operated at ground, as a repeller (V_R), as an extractor (V_E) or as a lens (V_L). When using the CCD-VMI in the corresponding modes the opposite electrodes are used. The V_E/V_R ratios are not the same between different modes.

The available number of power supplies with sufficiently high current ratings means that only 2- or 3-electrode modes can be used to image both electrons and ions onto the same detector ("PEPICO operation" or "switched voltages" operation, see next Chapter) (Figure 2.9). 2-electrode mode is operated by connecting the two power supplies supplying positive and negative voltages to a fast, high-voltage push-pull switch (HTS 111-06-GSM, *Behlke*) whose output is connected to the repeller and connecting the other two power supplies to another HV switch connected to the extractor. The switches have a rise of time of approximately 20 ns and can switch between voltage differences up to 11 kV with 60 A current. 3-electrode mode is operated by having the output from the switch connected to the repeller be split into two channels close to the vacuum feedthrough, which go to the α and β electrodes that jointly form the "uniform repeller." Since both electrodes are operated at the same voltage, they can be powered by the same power supply.
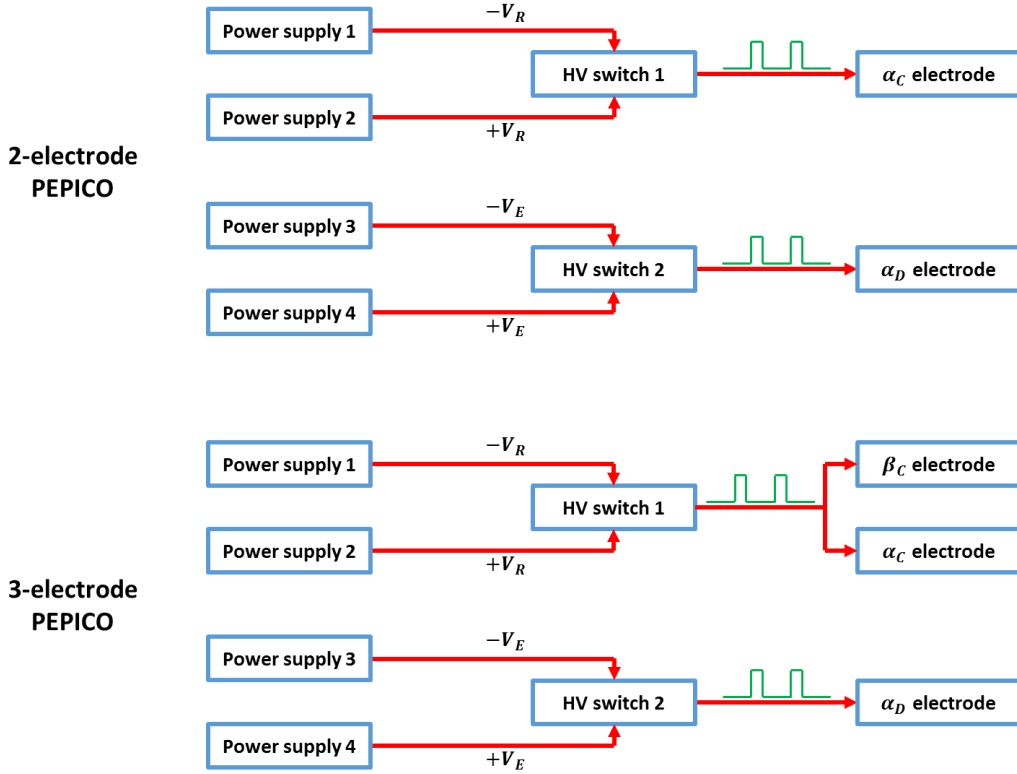
Figure 2.9: Schematic layout of the connections for supplying the switched voltages to the electrodes when performing PEPICO with two or three electrodes. In PEPICO mode, both electrons and ions are imaged to the delay line.

2.4 Lasers

2.4.1 Harmonium high-harmonic generation source

The XUV ionisation experiments were performed in the Harmonium facility [27], [43], [44] (Figure 2.10), the HHG XUV source constructed in the Lausanne Centre for Ultrafast Science (LACUS). Harmonium delivers femtosecond XUV pulses to three experimental endstations installed within the facility. The light is directed towards the endstations and focused with toroidal mirrors. To select a specific harmonic, four monochromator gratings are available (Figure 2.11). The grating used in this work has a groove density of 200 gr mm^{-1} and in combination with a 100 μm wide slit allows photon energies to be selected in the range 20 –

40 eV, with FWHM energy resolution of approximately 0.5 eV and FWHM time resolution around 50 fs. The photon flux at these conditions is estimated to be 2 x 10^{11} photons s[-1] at 6000 s^{-1} repetition rate [27].

The XUV light is directed by two sequential toroidal mirrors along vacuum-sealed tubes directly into the CIS endstation. The second toroidal mirror focuses the light into the interaction region and can be adjusted to control the angular direction of the XUV beam into the chamber. However, there is no available translational degree of freedom, requiring the entire endstation to be positioned precisely along the beam path. The focusing path from the second mirror is approximately 3.9 m long.
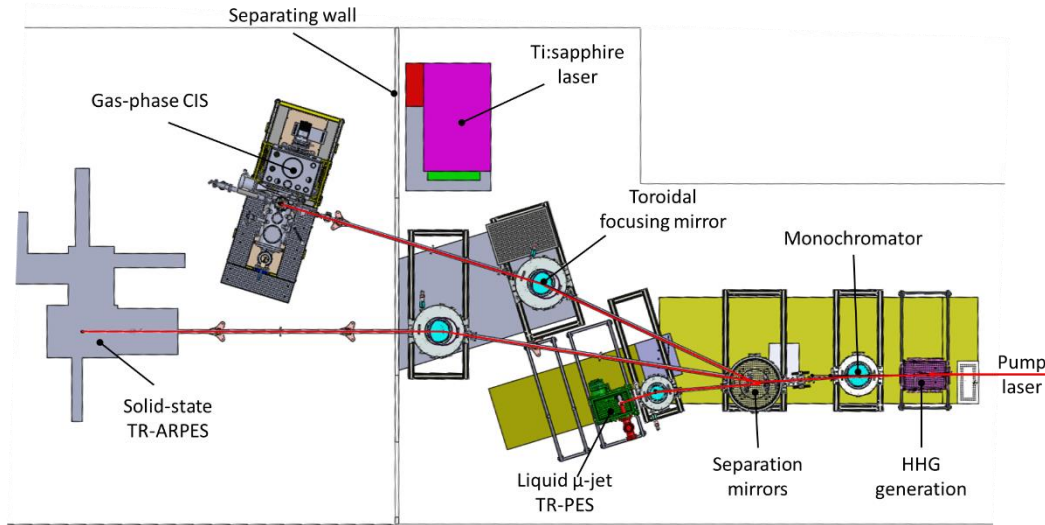
Figure 2.10: Top view of a Solidworks model of the entire Harmonium facility at LACUS. The separation chamber allows steering of the XUV beam to one of the three pictured endstations at a time. Also pictured is the femtosecond Ti:sapphire laser (Astrella, *Coherent*) used for some of the optical characterisation experiments.
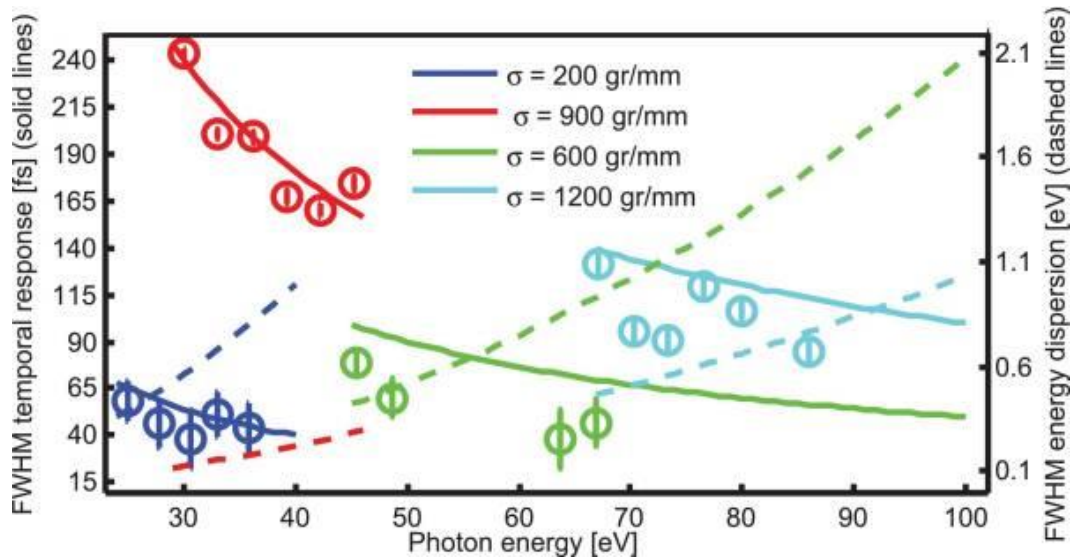
Figure 2.11: Time response and energy bandwidth of the four different gratings in the monochromator. Colours correspond to different groove densities, which are shown in the legend. Solid lines, left vertical axis: calculated temporal response by ray-tracing. Dashed line, right vertical axis: FWHM energy dispersion calculated assuming an XUV source spot size of 100 μm. Open circles: retrieved XUV pulse duration by laser-assisted photoemission (LAPE) experiments. The error bars in the retrieved temporal response are from the uncertainty in the IR pulse duration. Reprinted from Ref. [27].

2.4.2 Optical measurements

Many of the calibrations and setup measurements detailed in the next chapter were performed using multiphoton ionisation (MPI) or above-threshold ionisation (ATI) with infrared femtosecond pulses from either another laser based in the Harmonium facility or from a laser in the LCPM facility.

The LCPM laser is a system with a mode-locked Ti:sapphire oscillator (NJA-5, *Clark-MXR*) pumped by a continuous-wave argon ion laser (Innova 300, *Coherent*) which produces 780 nm pulses at 80 MHz. The alignment of the argon laser into the Ti:sapphire is maintained by a piezo steering mirror (Pointmaster, *Clark-MXR*). The pulses are amplified by a chirped-pulse amplifier (CPA-1000, *Clark-MXR*) consisting of a pulse stretcher, a regenerative amplifier (TRA-1000, *Clark-MXR*) pumped by the 532 nm output from a neodymium-doped yttrium aluminium garnet (Nd:YAG) laser (ORC-1000, *Clark-MXR*), and a pulse compressor. The system operates at 2000 s^{-1}, and delivers 780 nm pulses with energies up to 700 μJ and an estimated pulse duration of 100 fs.

The Harmonium infrared laser (Astrella, *Coherent*) is a one-box system. It features an integrated Ti:sapphire oscillator laser (Vitara, *Coherent*) seeding a Ti:sapphire regenerative amplifier (STAR, *Coherent*) pumped by the 527 nm output of a diode-pumped, neodymium-doped yttrium lithium fluoride (Nd:YLF) laser (Revolution, *Coherent*). The system operates at 6000 s^{-1} and delivers 800 nm pulses that are 30 fs long with energies up to 1 mJ.

In both cases, the laser light is focused about 400 mm from the interaction region. Pulse energies of approximately 70 μJ were used to provide approximately $10^{14} - 10^{15}$ W cm^{-2} peak power density which was usually sufficient to non-resonantly ionise the species used in the calibration, while keeping the ionisation rate low enough to avoid saturating the DLD.

3 Experimental setup – calibration and characterisation

In this chapter, the techniques performed using the endstation are described and various modes of operation of are characterised and calibrated. The two main techniques that are used and combined in this work are time-of-flight mass spectrometry (TOF-MS) and VMI. TOF-MS allows mass analysis of ions and VMI can determine the 3D momentum vectors of ions and electrons. Information can often be acquired from both techniques simultaneously. The TOF-MS gives a TOF spectrum corresponding to the ion mass-to-charge ratio (m/z) distribution, for which it must be calibrated and the resolution characterised. TOF-MS information on the CCD-VMI was not able to be achieved in this work, so this is only performed on the DLD-VMI. VMI information gives the kinetic energy distributions (Section 3.2) in 2D images (often 1000 pixels x 1000 pixels). The VMI must be calibrated to extract the particle kinetic energies from their pixel position and to characterise the setup in terms of the kinetic energy resolution. This is done on images acquired with both the CCD-VMI and DLD-VMI detectors. The DLD-VMI images can be generated only for those particles with the desired TOF, allowing many dark counts and other noise signals to be filtered out. The CCD-VMI currently cannot do this, and the images include both the electron signal and all dark counts accumulated in the acquisition time. For the ions, both VMI and TOF information can be acquired.

The spectrometer can function in two ways. The simplest operating mode, "static voltages", is performed by fixing the electrode voltages and keeping them constant throughout the data acquisition. This mode can record either electrons (using negative voltages) or ions (using positive potentials) at any one time. Under static voltages, the VMI image calibration functions the same for both electrons and ions, it is simply a matter of reversing the voltage polarity. Therefore the "static" ion images do not need to be calibrated separately from the electrons.

The other operating mode, "switched voltages", involves first setting negative electrode voltages before the laser pulse arrives and ionises the species of interest. The electron is then imaged very quickly to the detector before the heavier ion can move too far from the interaction region. The voltages are then switched to positive values to image the photoion to the detector. The voltages are held at positive values long enough for the heaviest ions to be detected (usually several 10s of μs) before switching back to negative values before the next laser shot. This technique allows electron-ion coincidences recorded on one detector. The time between laser shots is at least 167 μs for a 6000 s^{-1} repetition rate, the highest duty cycle used in this work. The later the voltages are switched, the more distance the ion travels from the interaction region before being imaged. This increases the likelihood of the ion being lost and/or the static VMI and TOF conditions breaking down. The potentials are therefore switched as early as possible without being early enough to perturb the electron trajectories. This value is found experimentally to be approximately 85 ns after ionisation (Figure 3.1). The voltage switching has a rise time of approximately 25 ns. In this operating mode, the electron VMI functions the same as it does under static voltages since the switching happens after the electrons are detected. Therefore, the electron VMI under switched voltages can be treated the same as under static voltages. For the ions, the switching-induced changes to the VMI and TOF conditions from static voltages must be calibrated and characterised. Because electrons are very light, it is not possible to detect them after switching, as they are either imaged or lost very quickly from the pre-switch voltages. Switched-voltage ion calibration data must therefore be recorded for both the VMI and TOF modes. For switched VMI, images must be recorded for ions generated in a process where they are released with a known kinetic energy. For the switched-voltages TOF, the calibration and characterisation are similar to the static voltages. Switched-voltage experiments are only performed on the DLD-VMI.
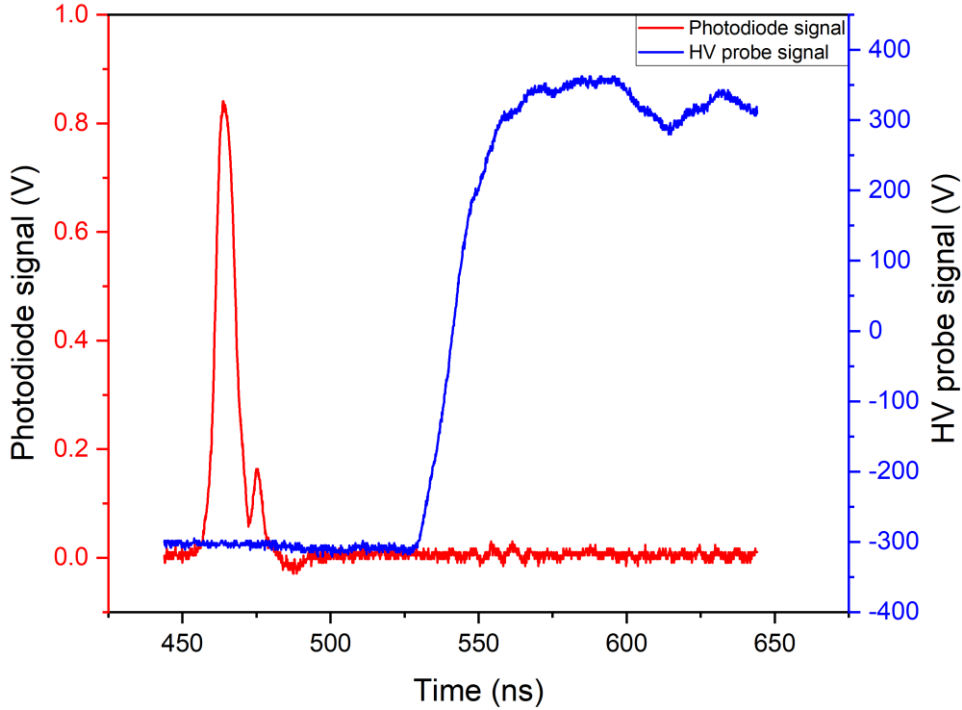
Figure 3.1: Oscilloscope traces showing the photodiode signal of the laser pulse on exiting the vacuum chamber (red) and the HV probe signal of the voltage going to the repeller voltages at the point of the vacuum chamber feedthroughs. The operating range of the HV probe limited the voltage values that could be measured. The timing trigger for the oscilloscope comes from the laser.

The calibration and characterisation sections presented here are organised by their concept: TOF operation of ions is presented first for static voltages, then the idea is expanded on to incorporate switched voltages. VMI imaging of ions and photoelectrons is then derived using concepts from the static voltages TOF setup then expanded upon into the switching operation for ions from Coulomb explosions. The photoelectron and Coulomb explosion VMI measurements were performed during an HHG beamtime in the Harmonium laboratory. The other experiments were performed later using an IR laser in the LCPM laboratory. In between these two experiments, an arcing incident occurred in the electrode setup which required repair of the electrode setup. The endstation was also disassembled, moved between the labs, and reconstructed. These events might have resulted in small geometrical changes to the electrode setup, which in turn could have caused some performance discrepancies between the two datasets, such as which voltage ratios were used.

3.1   Time-of-flight mass spectrometry

Mass analysis of ions is performed by recording TOF information. Here, an attempt is made to determine the relationship between m/z of an ion and its TOF for both the static and switched voltage cases. The static voltages model is based on the Wiley-McLaren configuration [45], [46] and the same basic principles are used to try to expand it to the switched voltages case. The particle is assumed to begin with zero initial velocity u_0 along the TOF axis, as the molecular beam travels perpendicular to this axis and transverse spread is minimal. All electric fields are approximated to be uniform and defined only by the two most local electrode potentials. In switched voltage mode, the voltage switching is assumed to be instantaneous with no significant rise time. More detailed derivations for both models are in Appendix A. The relationship is evaluated with comparison to calibration experiments and SIMION simulations.

3.1.1 Static voltages ion time-of-flight

The TOF detector has three types of components (Figure 3.2). The extraction region, labelled $n = 0$, is where the charged particles are first generated and accelerated towards the detector. The intermediate acceleration region(s) are where particles continue to be accelerated. The total number of intermediate acceleration regions present is designated N, with each successive region labelled $n = 1,2,3, \dots , N$. The final region is the field-free drift tube, where the particles travel towards the detector with a constant final velocity. Depending on whether a lens electrode is used in this current setup, there can be one or two intermediate acceleration regions, with the effective length of the drift tube changing accordingly.

4-electrode mode

2- and 3-electrode modes
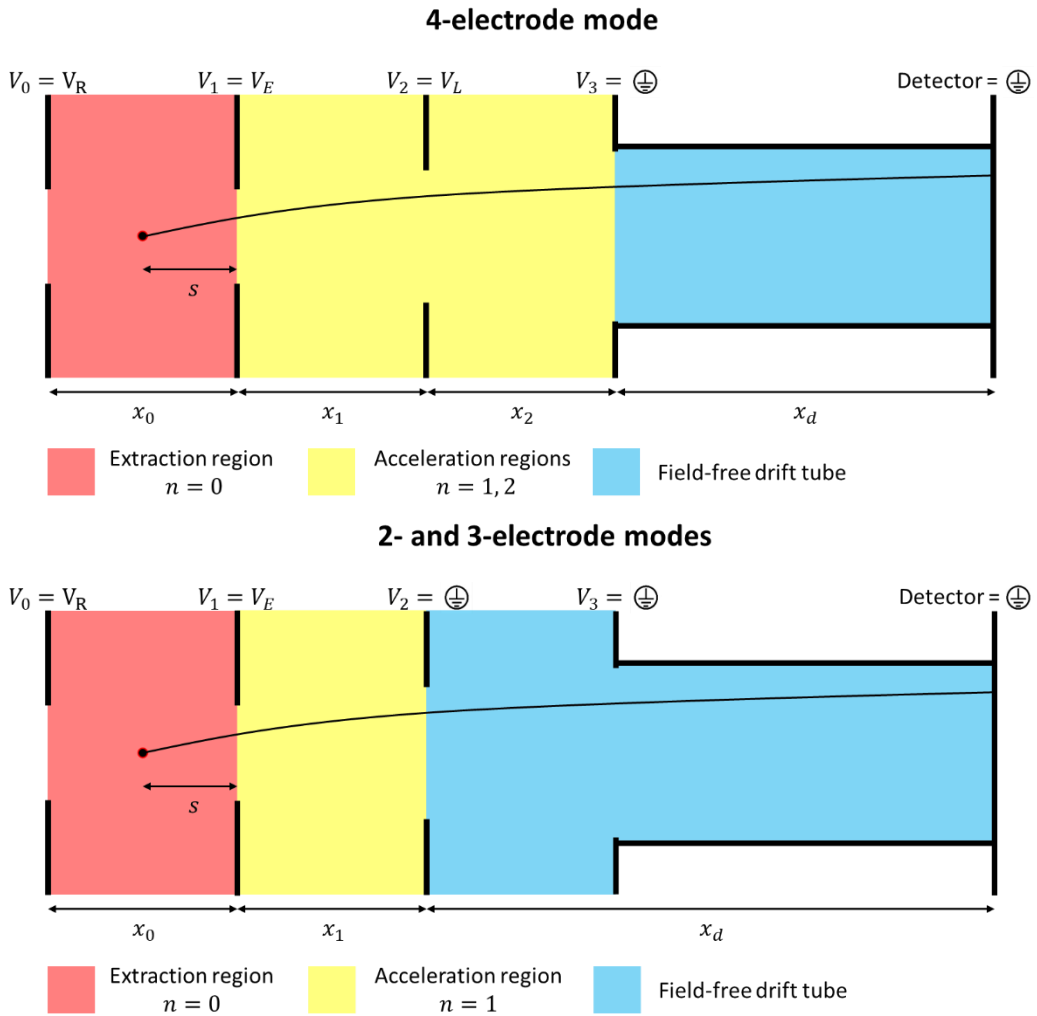
Figure 3.2: Schematic of the TOF operation on the DLD-VMI for static voltages showing the flight path of the ions or electrons. Top: 4-electrode mode, where there are two intermediate acceleration regions. Bottom: 2- and 3-electrode modes, where there is one acceleration region due to the lens electrode being grounded and the effective length of the field-free drift tube x_d is increased. The θ_C repeller electrode (Figure 2.8) is omitted for simplicity.

The TOF t of a charged particle detected with static voltages is given by:

$$t = \sqrt{2\frac{m}{z}}\left(\sqrt{\frac{x_0 s}{\Delta V_0}} + \sum_{n=1}^{N}\frac{x_n}{\Delta V_n}\left(\sqrt{\frac{\Delta V_0 s}{x_0} + \sum_{i=1}^{n}\Delta V_i} - \sqrt{\frac{\Delta V_0 s}{x_0} + \sum_{i=1}^{n-1}\Delta V_i}\right) + \frac{x_d}{2\sqrt{\frac{\Delta V_0 s}{x_0} + \sum_{n=1}^{N}\Delta V_n}}\right)$$
$$\times \sqrt{\frac{amu}{e}}. \qquad 3.1$$

where z is the particle's charge in units of fundamental charge e (1.602 x 10^{-19} C), m is the particle's mass in atomic mass units amu (1.661 x 10^{-27} kg), ΔV_n is the voltage difference across the region n in volts, x_n is the length of the region n along the TOF axis in metres, and s is the distance travelled by the particle through the extraction region from its origin point where the photoionisation occurs.

This describes the TOF of a charged particle from the moment of ionisation. In a typical experiment, the timing trigger for the acquisition will be offset from the exact moment of ionisation creating an additional term t'. The above relationship is linear with $\sqrt{m/z}$, so the geometry and voltage parameters can be more simply expressed as a single collective parameter k, simplifying the relationship to

$$t = k\sqrt{\frac{m}{z}} + t', \qquad 3.2$$

This is the relationship on which the static TOF spectra are calibrated. The instrumental parameter k is different for 2-, 3- and 4-electrode operations. In converting from TOF spectra to mass spectra, the signal must be modified according to particle conservation, which states that

$$\sigma(m/z)d(m/z) = \sigma(t)dt, \qquad 3.3$$

where $\sigma(m/z)$ and $\sigma(t)$ are the signal variations of the mass spectrum and TOF spectrum respectively. The TOF spectrum signal can therefore be converted from to mass spectrum by multiplying the signal by the relevant Jacobian factor [47]:

$$\sigma(m/z) \propto \frac{\sigma(t)}{\sqrt{m/z}}. \qquad 3.4$$

The m/z resolution is related to the TOF resolution by

$$\frac{m/z}{\Delta(m/z)} = \frac{1}{2}\frac{t}{\Delta t}, \qquad 3.5$$

where $\Delta(m/z)$ and Δt are the full width at half maximum (FWHM) values of the peak located at m/z and t respectively.

3.1.1.1 Voltage calibration

The determined relationship between TOF and m/z is experimentally calibrated and the m/z-dependence of the resolution characterised. A gas-phase molecular beam mixture was created that was composed of a synthetic air carrier gas (containing oxygen O_2 (IP = 12.1 eV, mass = 32 amu)) seeded with water H_2O (IP = 12.6 eV, mass = 18 amu), 2-propanol C_3H_8O (IP = 10.2 eV, mass = 60 amu) and toluene C_7H_8 (IP = 8.8 eV, mass = 92 amu). The water was stored in the heated molecular beam reservoir behind the nozzle (Section 2.2) and heated to approximately 80°C to increase its presence in the molecular beam and therefore its ionisation

yield. A solution of 10% toluene in 2-propanol by volume was stored at room temperature in another reservoir further back in the gas line leading to the molecular beam source. The gas mixture was singly photoionised using 780 nm femtosecond pulses in an above threshold ionisation (ATI) scheme. The laser pulses of energy approximately 250 μJ and pulse length ~100 fs were focused on the molecular beam in the interaction region at approximately 400 mm focal distance. The molecular beam mixture was made in this way to try to get all the above species ionised by the laser and detected in sufficient quantities for analysis without letting the most easily-detected species (toluene) saturate the detector. Nitrogen (IP = 15.6 eV, mass = 28 amu) was also present in the molecular beam as a carrier gas but was not easily ionised in this laser scheme and therefore not detected in a significant quantity.

The setup is also reconstructed in a SIMION 8.1 simulation to attempt to guide and evaluate the hardware design and performance. The electrodes, flight tube and detector surfaces are created as "electrodes" in a geometry file, where the flight tube and detector potentials are fixed at 0 V and the electrode potentials varied. The simulated grid unit density is 0.25 mm gu^{-1}. The simulation is setup with two planes of mirror symmetry along the molecular beam (z-axis) and laser beam (y-axis) axes. The x-axis is the TOF axis. The ionisation volume defined in the simulations is estimated based on the molecular beam and laser parameters in Chapter 2. The PEEK electrode chassis is not modelled in the simulations. The molecular beam width is estimated to be 2.8 mm and the laser diameter is taken from the HHG values and conservatively rounded up to 200 μm. This creates a cylinder with 200 μm diameter and 2.8 mm length along the y-axis. Singly-charged ions of variable mass are defined around the surface of this cylinder with 800 m s^{-1} velocity in the direction of the molecular beam. This number is taken as a rough estimate of the molecular beam speed with the heated source and mixture of chemical species.

Experimental voltage ratios are found by fixing V_R and varying V_E. The ion images are examined which show a spot corresponding to each mass in the molecular beam. This indicates velocity-map imaging (described in more detail in Section 3.2), where all ions with the same mass and velocity vector are imaged onto the same spot on the detector. The length of the spot along the molecular beam axis depends on the velocity distribution in the beam, and the width depends on the angular spread and spatial distribution in the ionisation region. V_E is varied until the spot width is minimised, indicating the tightest possible velocity focusing of the setup (Figure 3.3). In the 4-electrode operation, fixing V_R gives two degrees of freedom to vary: V_E and V_L. In this case V_E is fixed to a chosen ratio with V_R while V_L is varied. The voltage ratios are found for VMI performance in the static case (Table 3.1).

The m/z-dependence of the voltage ratios in the SIMION simulations is very small and corresponds to less than 1 V difference in V_E or V_L when operating in the V_R range 0 to 5000 V. This difference is even harder to perceive in the experiment, so the static voltage ratios are taken to be independent of m/z in this range. Examining very large ions such as clusters or droplets with large m/z values, or using much higher voltages than in this work may make these differences become more significant.
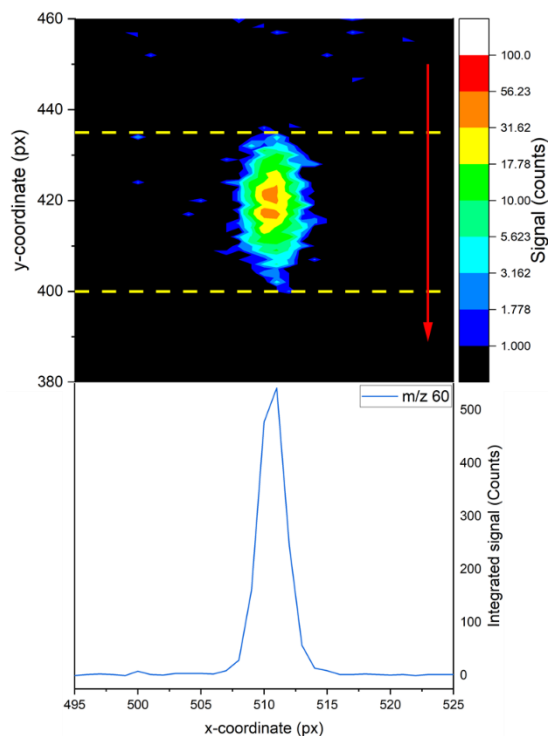
Figure 3.3: (top) VMI image of 2-propanol, recorded using 3-electrode mode with V_R = 4000 V. The red arrow denotes the direction of the molecular beam. (bottom) Signal of the spot integrated along the direction of the molecular beam, between the limits of the yellow lines. The full velocity-map image is plotted as a 1000 x 1000 px image. Each pixel is 75 μm width.

Number of electrodes used	Optimised m/z	V_X/V_R			
		SIMION		Experiment	
		DLD-VMI	CCD-VMI	DLD-VMI	CCD-VMI
2	18	0.51158(2)	0.51226(2)		
	32	0.51160(2)	0.51226(2)	0.512(2)	0.507(2)
	60	0.51160(2)	0.51226(2)		
	92	0.51162(2)	0.51226(2)		
3	18	0.63346(2)	0.63380(2)		
	32	0.63346(2)	0.63380(2)	0.640(2)	0.631(2)
	60	0.63344(2)	0.63378(2)		
	92	0.63344(2)	0.63378(2)		
4	18	0.61858(2)	0.61404(2)		
	32	0.61860(2)	0.61404(2)	0.612(2)	0.623(2)
	60	0.61864(2)	0.61406(2)		
	92	0.61868(2)	0.61412(2)		

Table 3.1: Voltage ratios used for velocity-map imaging conditions. The standard errors are shown in brackets. The ratios are held the same even if the absolute voltage values are changed. V_X in the table heading corresponds to V_E for 2- and 3-electrode modes and V_L for 4-electrode mode. In 4-electrode operation, V_E/V_R is fixed at 0.8 and V_L/V_R varied instead. V_L is not used in 2- and 3-electrode operation and kept at ground.

The voltage ratios are fairly similar between the SIMION simulations and experiment, but do not overlap considering their errors. The errors are estimated by the voltage step size when searching for the minimum width. In the simulations (and nominally in the instrument design) the CCD-VMI and DLD-VMI only differ by 1 mm in their TOF axis distances. This gives very minimal differences in the voltage ratios (6 parts in 10,000) for 2- and 3-electrode modes but slightly more in 4-electrode mode (4 parts in 1000). This would be expected to

translate to the experiment having almost the same ratios for both detectors in 2- and 3-electrode modes and a slightly lower ratio for the CCD-VMI in 4-electrode mode. Reasons for the differences between experiment and simulation may be due to the ionisation region not being in the VMI centre if the laser or molecular beam are pointing wrongly, or other small geometrical differences between the nominal design and the actual instrument that may arise when assembling the instrument in the lab. Over the course of the construction and commissioning of the instrument, there were several times when there were large electrical discharges between the electrodes and nearby grounded parts that required disassembly and cleaning of the traces left before reassembling. These operations may have resulted in some geometrical differences, such as flight path or inter-electrode distances, from the original design that may cause the voltage differences between experiment and simulation.

3.1.1.2 Mass-to-charge ratio calibration

The TOF spectra are recorded in each mode at V_R values of 1000 V, 2000 V, 3000 V, and 4000 V; with their corresponding values of V_E and V_L. An example spectrum is shown (Figure 3.4). Many of the small peaks are known photofragments of 2-propanol, which allow calibration using many m/z values in the spectrum. Gaussian distribution fits to the peaks determine the TOF values and obtain the TOF variation with m/z for each voltage (Figure 3.5 (a)). Fitting Equation 3.2 to the $\sqrt{m/z}$-TOF variation gives the calibration parameters k. The relationship between k and V_R is then examined. The expression

$$ k = \frac{k'}{\sqrt{V_R}} $$

3.6

fits the k-V_R observed variation very well for both simulation and experiment (Figure 3.5 (b)) and gives k' as an instrument parameter that only varies with the number of electrodes. The TOF can then be calibrated for any voltage settings, not just those used here, using the "electrode mode" parameters k' (Table 3.2).
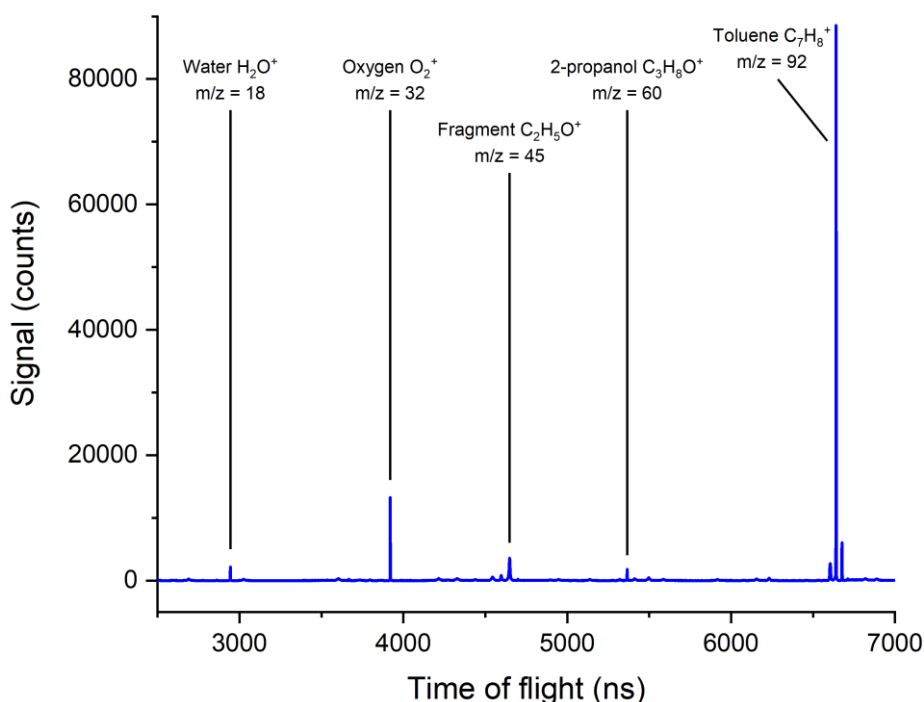
Figure 3.4: TOF spectrum of the molecular beam mixture recorded in 4-electrode mode with V_R = 4000 V. The fragment at $m/z = 45$ is the dominant fragment of 2-propanol.

(a)

(b)
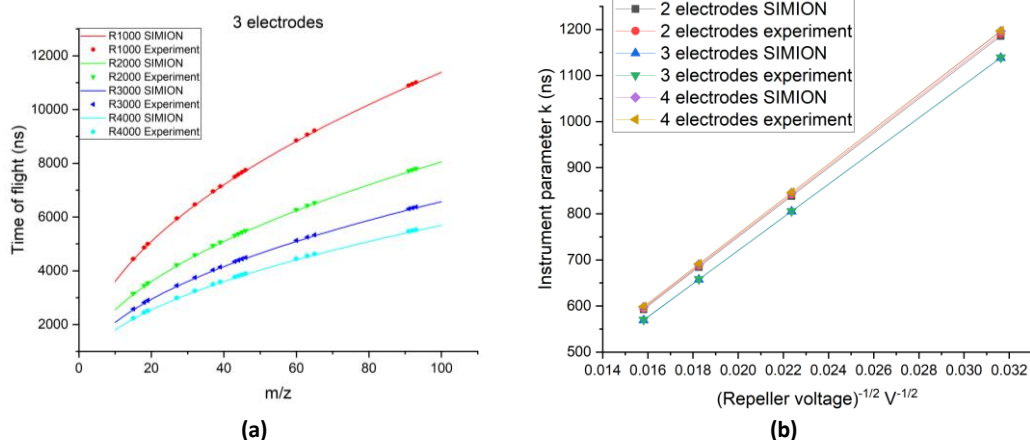
Figure 3.5: (a) Ion TOF as a function of m/z for various voltages in 3-electrode mode. V_R given in the figure, the corresponding V_E and V_L are then determined from Table 3.1. The corresponding curves for the 2- and 4-electrode modes are very similar in appearance. (b) The instrument parameter k', obtained from fitting Equation 3.2 to the data in (a), as a function of V_R for 2-, 3- and 4-electrode modes for both the SIMION and experimental data.

Number of electrodes used	k' (ns V$^{1/2}$)	
	SIMION	**Experiment**
2	37492.9(8)	37652(4)
3	35995.2(10)	36050(7)
4	37817.4(7)	37856(4)

Table 3.2: Instrument parameters k' for each voltage mode in the SIMION simulations and the experiment. These parameters can be used with Equation 3.6 and any chosen V_R value to convert the TOF spectrum to a mass spectrum.

3.1.1.3 Time-of-flight resolution

The experimental TOF resolutions $t/\Delta t$ are determined using the TOF and FWHM values determined from Gaussian fits of the TOF spectra peaks. Only the species already present in the molecular beam are used since fragments can be released with kinetic energies in different directions and after different delays, resulting in peak broadening and obscuring of the instrument's native resolution. The simulated TOF resolutions are calculated by filling the ionisation volume defined previously with 1000 ions in a random uniform distribution and then flown with the initial "molecular beam" velocity. The mean and standard deviation σ of the sample TOFs are calculated. The distribution is assumed to be Gaussian so that the calculated Δt is $FWHM = 2\sqrt{2\ln 2}\,\sigma$. m/z values between 10 and 100 are simulated.

The TOF resolution of each molecular beam species is presented for each voltage setting. The simulations show that the resolution improves with the number of electrodes used. 4-electrode mode is substantially better than 2- and 3-electrode modes, giving resolutions of approximately 9600. It is also independent of voltage and m/z in the ranges sampled. This is only partially reproduced in the experimental data. The experimental resolutions also improve with the number of electrodes. For the 2-electrode mode, the experimental resolution is better than the simulations. The 3-electrode mode experimental resolutions are also better than the simulated values in most cases. The 4-electrode mode resolutions are worse than the simulations but still improved over the 2- and 3-electrode modes. The experiments deviate from the simulations significantly in m/z-dependence. In every case, resolution appears to improve with increasing m/z. In the 3-electrode mode, the resolutions at low m/z values diverge significantly for different V_R values, while in 2-electrode mode, they do so at high m/z values. The reason for the difference in trends is unknown.
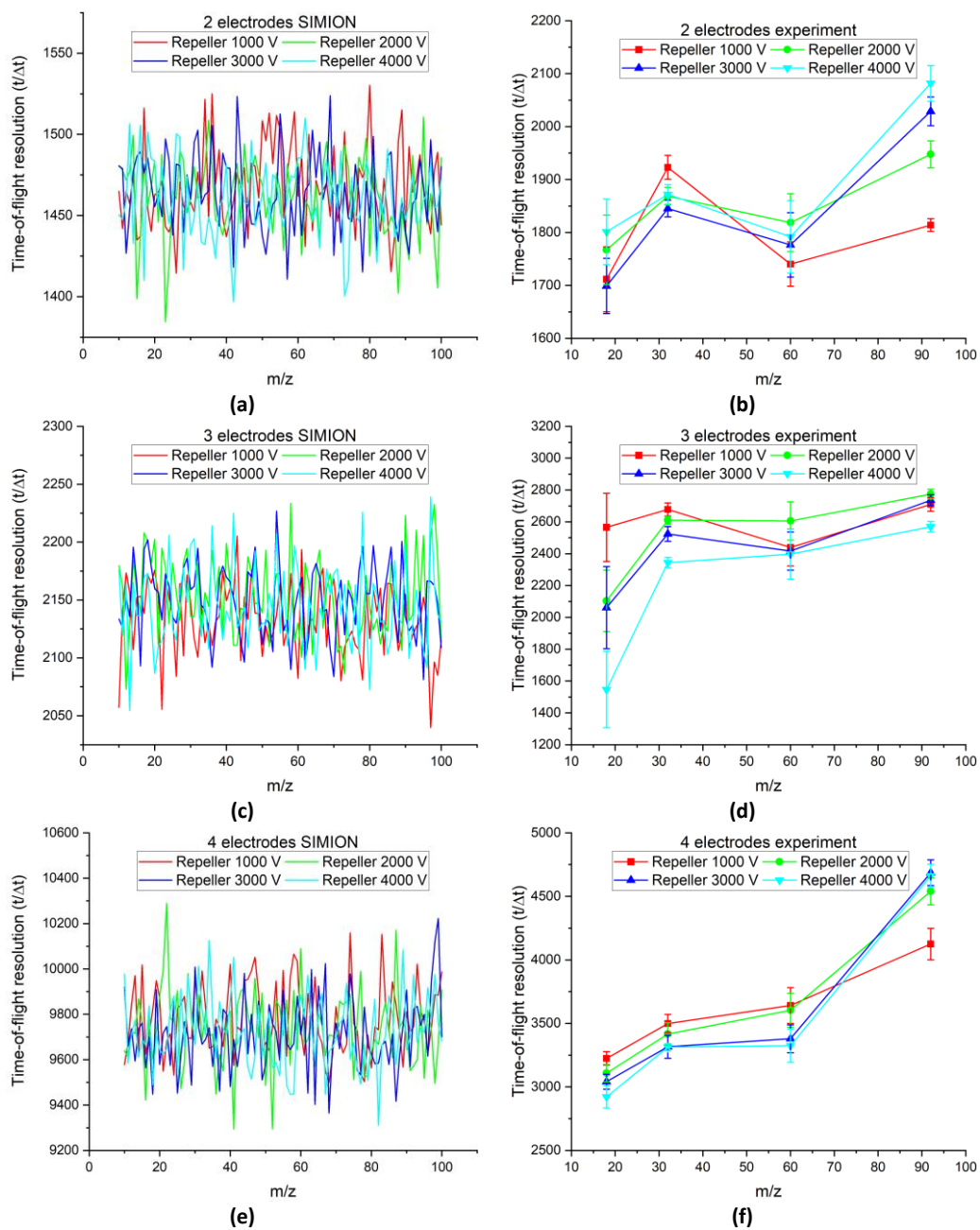
Figure 3.6: TOF resolutions, defined by Equation 3.5, as a function of m/z. The left-hand figures (a), (c) and (e) show the SIMION simulation results for 2-, 3- and 4-electrode mode respectively and the right-hand figures (b), (d) and (f) show the corresponding experimental results.

3.1.2 Switched voltages ion time-of-flight

When performing PEPICO, the voltages are first set to image electrons onto the DLD. For the duration that the voltages are set this way, the ions will move away from the detector before the voltages are switched to image them ions (Figure 3.7). Between ionisation and switching, lighter ions will move farther from the interaction region than heavier ions, resulting in a longer flight distance and different m/z-dependence of the TOF. They could also move too far for the ion potentials to successfully recover and be lost. These factors are more significant when imaging fast electrons which require strong negative voltages. The voltage switching limit introduces a cap on how strong the positive field can be. This limit is set by the maximum current (20 mA) of the HV power supplies. Ions in a strong negative field travel far in the wrong direction and must be recovered by a comparatively weak positive field. Conversely, slow electrons can be imaged by a weak negative field which perturbs the ions less, and a strong positive field can overcome the distortion. The latter case is more likely to resemble static-voltages operation. Therefore, the TOF-m/z relationship might differ from that of static-voltages operation and may also vary significantly between different switched voltages.
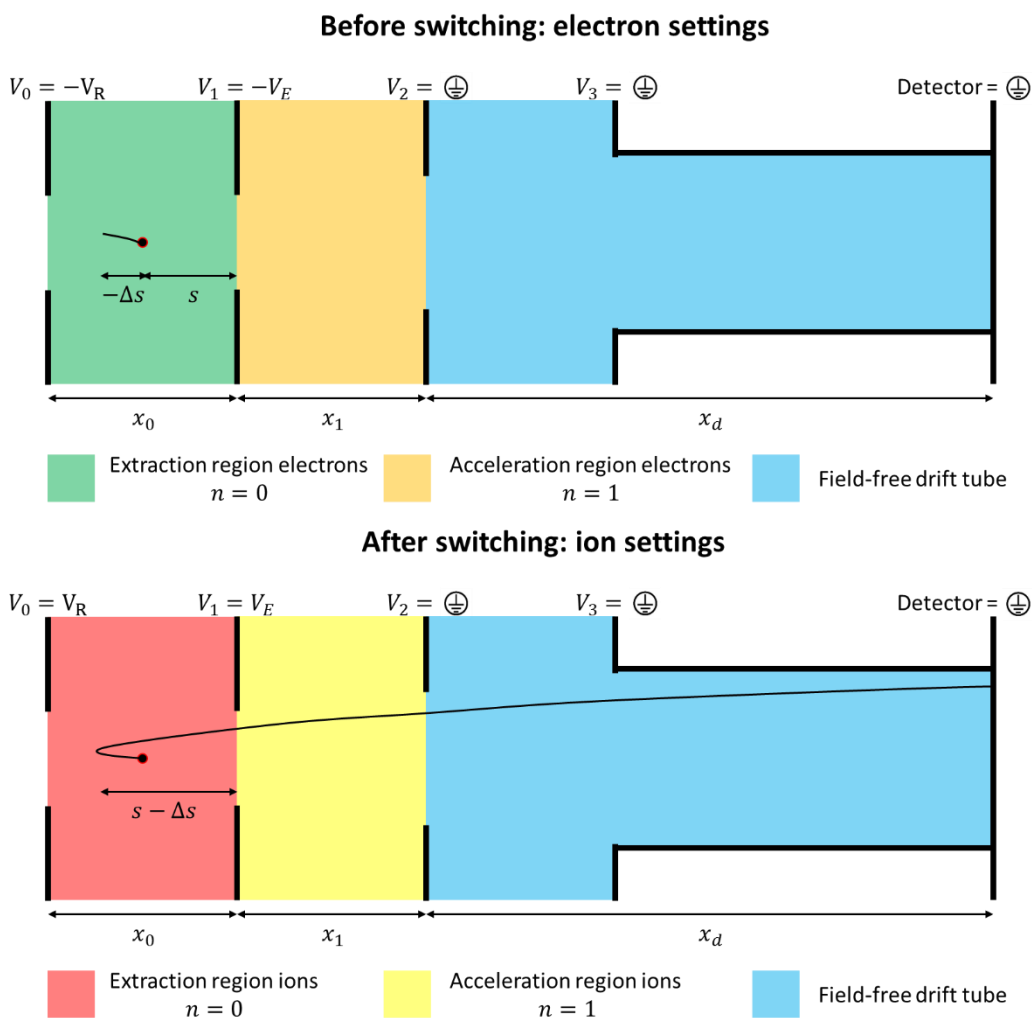
Figure 3.7: Switched-voltages TOF schematic on the DLD-VMI. Only the ion flight path is shown. Top: trajectory when voltages are negative to image electrons. s and Δs are displacement vectors from the origin with the positive direction towards the detector. Bottom: trajectory after switching to positive voltages to image ions. Only 2- or 3-electrode modes are used when switching, so there is one acceleration region. The β_C electrode (Figure 2.8) is omitted for simplicity.

The TOF t of a charged particle detected with switched voltages is given by:

$$t = \sqrt{\frac{(\Delta V_{el}^2 - \Delta V_{el}\Delta V_{ion})t_s^2}{\Delta V_{ion}^2} + 2\frac{m}{z}\frac{x_0 s}{\Delta V_{ion}}},$$

$$+ \frac{x_1}{\Delta V_1}\left(\sqrt{\frac{(\Delta V_{el}^2 - \Delta V_{el}\Delta V_{ion})t_s^2}{x_0^2} + 2\frac{m}{z}\left(\frac{\Delta V_{ion}}{x_0}s + \Delta V_1\right)}\right.$$

$$\left. - \sqrt{\frac{(\Delta V_{el}^2 - \Delta V_{el}\Delta V_{ion})t_s^2}{x_0^2} + 2\frac{m}{z}\frac{\Delta V_{ion}}{x_0}s}\right)$$

$$+ \frac{m}{z}\frac{x_d}{\sqrt{\frac{(\Delta V_{el}^2 - \Delta V_{el}\Delta V_{ion})t_s^2}{x_0^2} + 2\frac{m}{z}\left(\frac{\Delta V_{ion}}{x_0}s + \Delta V_1\right)}} + t_s\left(1 - \frac{\Delta V_{el}}{\Delta V_{ion}}\right).$$

3.7

where ΔV_{el} is the extraction region voltage difference when imaging electrons in volts V, ΔV_{ion} is the extraction region voltage difference when imaging ions in volts V, and t_s is the switching time in s.

3.1.2.1 Voltage calibration

Optimal switched voltages are found similarly to those for the static mode. 3-electrode mode is chosen for the switching experiments. In the simulations, the switch time was set at 85 ns with a 25 ns rise time. The rise time was modelled as a simple linear increase. The ion deviations pre-switch results in m/z-dependencies on the optimised voltage. Switching between different electron and ion voltage allows for many combinations to choose for a given experiment. Different switching settings are given the labels "A-B MX switching," where A is the absolute V_R in kV used to image the electrons; B is the absolute V_R value in kV used to image the ions and X is the specific value of m/z for which the voltages have been optimised for spatial imaging. The value of V_E corresponding to A is known from Table 3.1 for static voltages and the value of V_E corresponding to B from Table 3.3 for a given m/z. For example: "3-3 M18 switching" means using V_R = -3 kV for the electrons (so V_E = -1900 V from Table 3.1) and V_R = 3 kV for the ions. $M18$ means that the ion V_E is optimised for spatial imaging of m/z = 18, so V_E = 1794 V from Table 3.3. In the experiments performed here, the voltages were restricted due to arcing risk. The absolute voltage would be less than 4000 V and the voltage switching difference would be less than 6000 V. Three settings were explored:

- 1-4 switching. Considered as a "best-case" scenario for the ions that would minimise distortions in the ion trajectories due to the weak electron-imaging field and strong ion-imaging field. Most likely
- 3-3 switching. Used as a likely candidate for operating in HHG experiments for its ability to image fairly fast electrons (up to approximately 12 eV) and reliably recover the ions
- 4-1 switching. Considered as a "worst-case" scenario for the ions that would maximise distortions in the ion trajectories due to the strong electron-imaging field and weak ion-imaging field.

Optimised m/z	V_E/V_R					
	SIMION			Experiment		
	1-4	3-3	4-1	1-4	3-3	4-1
18	0.6315(5)	0.6143(5)	0.4460(5)	0.621(2)	0.598(2)	0.346(2)
32	0.6325(5)	0.6257(5)	0.5720(5)	0.623(2)	0.614(2)	0.527(2)
60	0.6330(5)	0.6300(5)	0.6140(5)	0.624(2)	0.616(2)	0.597(2)
92	0.6330(5)	0.6317(5)	0.6230(5)	0.628(2)	0.623(2)	0.614(2)

Table 3.3: Voltage ratios used for optimal VMI conditions of ions in switched-voltages mode. Standard errors are in brackets.

Optimised m/z	k (ns)					
	SIMION			Experiment		
	1-4	3-3	4-1	1-4	3-3	4-1
18	569.69(2)	660.84(6)	1187(2)	584.60(8)	683.40(9)	1307(2)
32	569.60(2)	659.52(4)	1149(2)	584.40(8)	681.52(10)	1228.8(10)
60	569.56(2)	659.03(4)	1139(2)	584.31(9)	681.17(9)	1204.6(12)
92	569.56(2)	658.83(4)	1137(2)	584.06(8)	680.36(9)	1198.9(6)

Optimised m/z	t' (ns)					
	SIMION			Experiment		
	1-4	3-3	4-1	1-4	3-3	4-1
18	100.90(15)	139.7(4)	112(9)	132.9(6)	184.9(7)	-40(1)
32	101.02(15)	144.9(3)	300(13)	133.4(6)	193.1(9)	302(7)
60	101.05(15)	146.9(2)	370(13)	133.6(7)	193.7(7)	467(9)
92	101.05(15)	147.7(2)	386(13)	134.0(6)	197.3(8)	514(6)

Table 3.4: Calibration parameters for the switched-voltages TOF spectra using the static-voltage TOF Equation 3.2. (Top) the instrument parameter k'. (Bottom) the offset t'. t' includes both the trigger delay and effects of voltage switching.

Like in the static operation, the voltage ratios differ quite significantly between experiment and simulation. In all cases the experimental ratio is lower than the simulation. In the setup, the VMI voltage ratio is usually lower when the particle is further from the detector, suggesting either the laser/molecular beam is pointing too high or the switching takes longer than previously estimated, allowing the photoion to move further in the wrong direction before being recovered. This assumes there are none of the other previously hypothesised geometrical differences between the simulated and real instrument setups.

3.1.2.2   Mass-to-charge ratio calibration

Equation 3.7 is a complex function of m/z with many fitting parameters and there is no analytical solution to find m/z in terms of the TOF. The static-voltages Equation 3.2 is therefore fitted to the switched-voltages TOFs as an approximation and evaluated. The calibration parameters from the fit are shown (Table 3.4). t_0 now includes effects from the switching and the trigger delay. In all cases, k' decreases and t_0 increases with increasing optimised m/z. This is due to the change in V_E. Heavier masses have a higher optimal V_E (Table 3.3). This results in a weaker extraction-region electric field which takes longer to turn the ions around from their initial pre-switch trajectory, increasing the offset t_0. However, the longer turn-around time allows the ions to travel closer to the high-potential repeller. The ion therefore gains a higher kinetic energy along its flight path, and travels to the detector faster which is reflected in the decreased value of k'.

The suitability of Equation 3.2 to describe the switched-voltages TOF-m/z relationship is evaluated by examining the mass residuals. The mass residuals are calculated by using the determined TOF parameters (Table 3.4) to find the theoretical mass that would be at a given TOF peak using Equation 3.2 and taking the difference from the nominal mass of the ion signal located at that peak:

$$Residual = Calculated\ mass - Nominal\ mass \tag{3.8}$$

The mass residuals (Figure 3.8) in all cases are extremely small, less than half a unit of m/z. The residuals are smallest for 1-4 switching and greatest for 4-1 switching. At higher values of m/z, the absolute residuals appear to monotonically increase as m/z increases, suggesting a different fit would be necessary for large masses. The residuals are small enough in the sampled range that adjacent mass peaks would not be confused, the linear approximation is deemed sufficient for the type of experiments performed in this work.
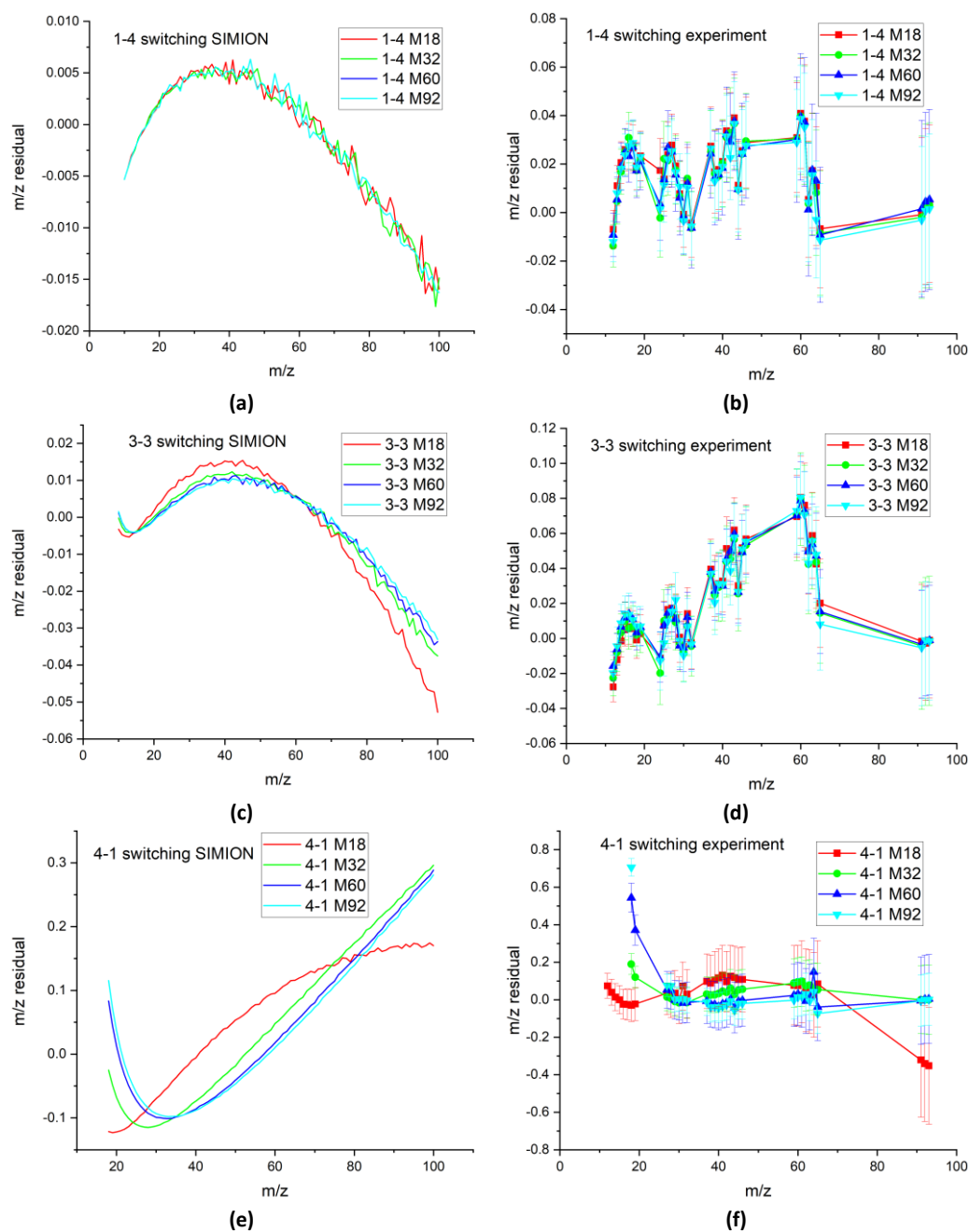
Figure 3.8: Mass residuals for the voltage switching modes. The left-hand figures (a), (c) and (e) show the SIMION simulation results for 1-4, 3-3 and 4-1 switching modes respectively and the right-hand figures (b), (d) and (f) show the corresponding experimental results.

3.1.2.3   Time-of-flight resolution

The experimental and simulated TOF resolutions of the switched-voltage modes are obtained in a very similar way as they were for the static-voltage modes. The SIMION simulations also incorporate the voltage switching at 85 ns delay with a linear ramp of 25 ns rise time. In both simulations and experiments (Figure 3.9), 1-4 switching gives the highest resolution and 4-1 switching the lowest. However, they disagree strongly on the trends they follow with m/z. For 1-4 and 3-3 switching, the simulations show that the TOF resolution decreases with increasing m/z before beginning to level off at high masses. This is due to heavier masses not being significantly perturbed by the switching and therefore more closely resembling the static-voltages case (Figure 3.6). In the experiment, the opposite behaviour is shown: the TOF resolution begins to rapidly increase with increasing m/z. For 4-1 switching, the simulated TOF resolutions show a maximum resolution at a lower m/z than the optimised m/z. For example, the experimental $M32$ curve has a local maximum at m/z = 32, although the simulation shows it occurring at m/z = 18. The experimental $M18$ curve monotonically decreases with m/z and appears to agree well with simulations. The experimental $M60$ and $M92$ curves are both monotonically increasing over the range, and begin levelling off at the high m/z limit. The local maxima shown in the simulation for these curves might appear at an m/z value not sampled in the experiment. Similar to the TOF resolution behaviour of the static voltage mode, these trends do not change with any small change to the simulation conditions that might be reflected in the experimental conditions, such as moving the ionisation spot vertically, changing the simulated time step or altering the voltage ramping in the switching process. The reason for these discrepancies is therefore not known. In some cases, the TOF resolution is better in the switched tests than in the static, which might imply the ions are being turned around in a region closer to the time focus.
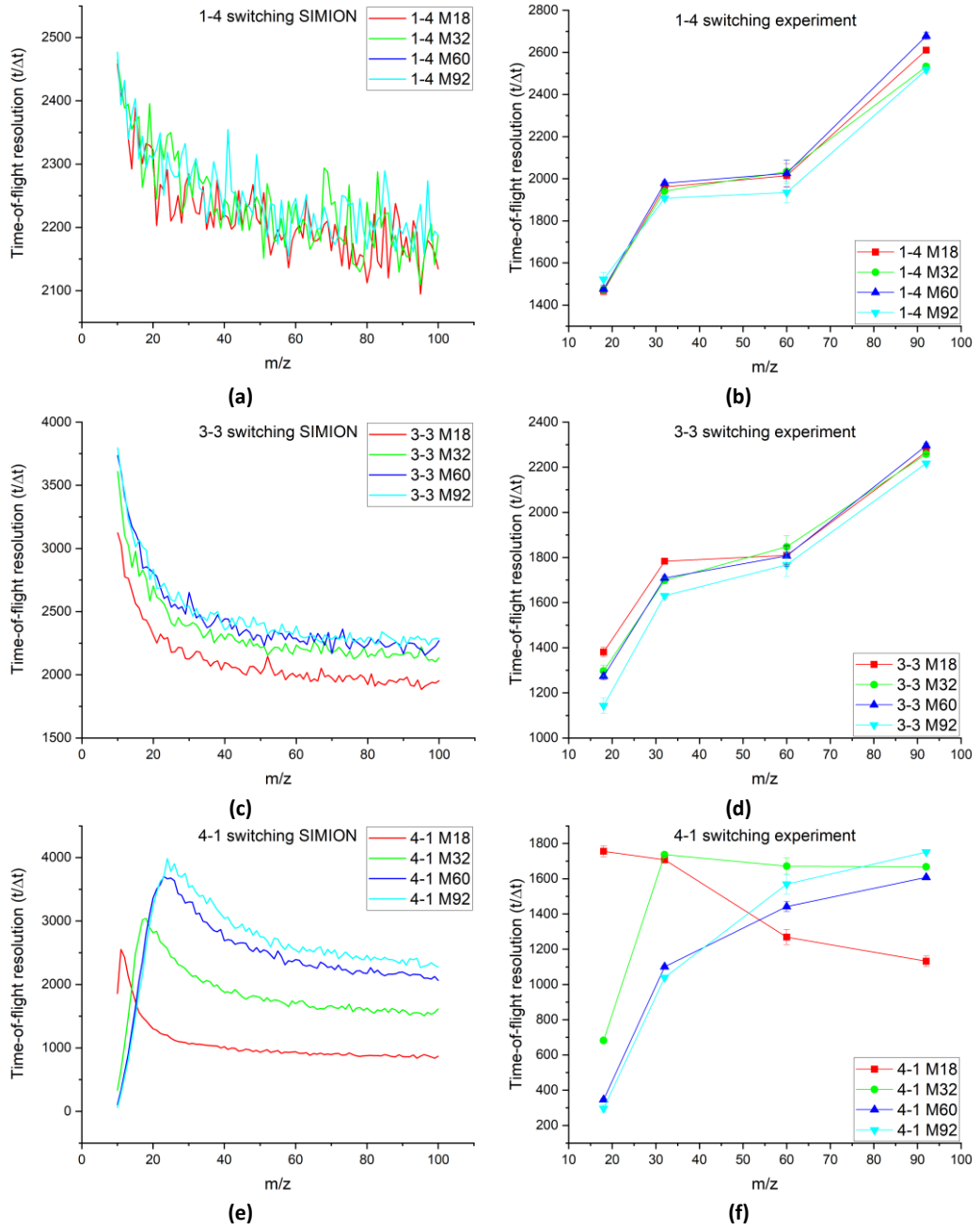
Figure 3.9: TOF resolutions, defined by Equation 3.5, as a function of m/z. The left-hand figures (a), (c) and (e) show the SIMION simulation results for 1-4, 3-3 and 4-1 switching modes respectively and the right-hand figures (b), (d) and (f) show the corresponding experimental results.

3.1.2.4 Switching-induced ion loss

Switched-voltages mode risks losing some ions if the switching is too late or takes too long, or if the electron settings are too high and the ion voltage settings too low. This should be more significant for lighter ions, which travel further in the wrong direction before the switching, and those released with significant kinetic energies in dissociation processes. The signal loss is evaluated by comparing the m/z-dependent signal level between switched-voltage and static-voltage TOF datasets. No ions are expected to be lost when using static voltages. While recording the switched TOF datasets, static TOF spectra were recorded as references immediately afterwards in order to try keep the experimental conditions as consistent as possible.

For the featured ions, the relative signal levels from each switched voltage setting for each mass is determined by taking the area of the Gaussian fits of the TOF peaks and comparing them to those recorded in the static reference spectrum with the same repeller voltage. For example, 3-3 switching data is compared to static-voltage data recorded with 3 electrodes using V_R = 3000 V. Each TOF is normalised to its acquisition time and the relative signals of each mass are compared (Figure 3.10). The relative intensity I is calculated as:

$$I = \frac{\sigma_{switch}(m/z)}{\sigma_{static}(m/z)},$$

3.9

where $\sigma_{switch}(m/z)$ is the intensity of a given m/z peak in a switched-voltage dataset, and $\sigma_{static}(m/z)$ is the corresponding intensity in the relevant static-voltage dataset. SIMION data for light masses shows what fraction of the ions of each mass successfully reach the detector. 1-4 switching shows that ions of all masses are recovered fully and none are lost in the switching process (only the $M18$ curve is shown, but the other settings give the same result). For 3-3 switching m/z 1 and 2 will be lost, but all other ions are detected, meaning this setting cannot perform coincidence experiments on hydrogen atoms (again, the other settings give the same result as the $M18$ curve). For 4-1 switching, optimising the $M18$ voltages allows all ions to be detected down to m/z 8; $M32$ voltages allow detection down to m/z 9; and $M60$ and $M92$ (curve not shown) voltages allow detection down to m/z 10. In all cases, the detection curves proceed as step functions, where all the ions in the source volume are detected or none are at all.

(a)   **(b)**
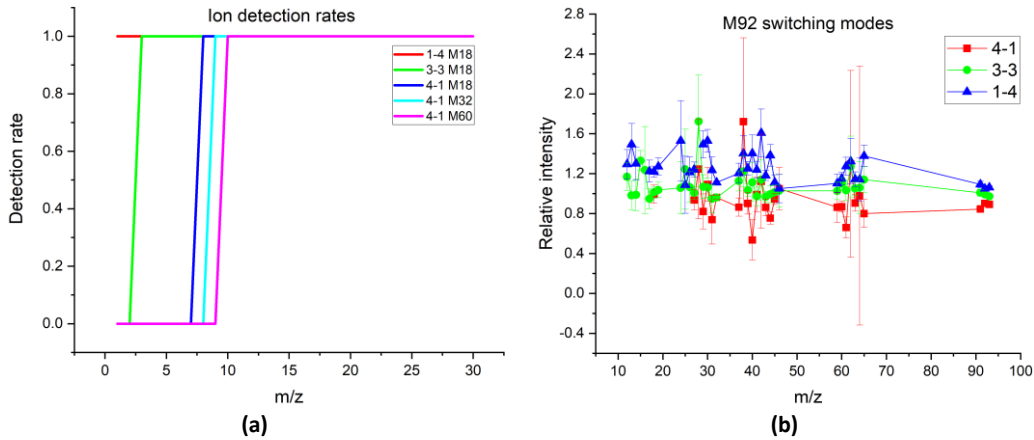
Figure 3.10: (a) SIMION results for ion detection rates against m/z. The rates are calculated as the fraction of ions reaching the detector from those originally flown (1000). (b) Relative intensities against m/z for $M92$ switched voltages.

The experimental results are shown for $M92$ voltages. Datasets from other MX voltages were disqualified for this analysis due to large laser power instabilities during the experiments. The fluctuations are also present in the $M92$ datasets but to a lesser degree. There are significant fluctuations in the relative m/z intensities, although the largest outlying values tend to have large uncertainties. The results show relative intensities

around 1.0, suggesting ions are lost by the voltage switching. However, in many cases the intensity is higher than 1.0. This would suggest that more ions are detected in the switching experiments than the corresponding static experiments, which should only be possible if this dataset is contaminated by power instabilities. One possibility is that ions in the switching experiments could be detected with higher final velocities due to being accelerated closer to the repeller electrodes pre-switch (as discussed in 3.1.2.2). MCPs will more efficiently detect particles with higher velocity, however the gain in signal due to this particular effect is expected to be negligible. The lowest m/z value recorded for the 3-3 and 1-4 voltage settings was 12 (a ^{12}C atomic fragment of 2-propanol) so the experimental dataset was unable to probe to the values of m/z that the simulations predict will be lost. This is also likely to be the lowest m/z value of interest for many of the experiments expected to be performed with the instrument. For the 4-1 experiments, the lowest m/z value fitted was 18 because the lower values did not appear in high enough intensities to reliably fit a Gaussian peak or discriminate between adjacent m/z values. This may suggest that these fragments are lost to a significant degree and the "step function" predicted by the simulations occurs just before m/z 18. Figure 3.9 (f) shows that optimising the voltages for spatial imaging of a high m/z (92) will decrease the TOF resolution of the lighter ions significantly. The m/z 18 peak originates in the molecular beam so it's TOF resolution is still acceptable, but the smaller m/z values are ions formed from fragmentation for which the deterioration of the TOF resolution is more pronounced, resulting in the peaks washing out and overlapping (Figure 3.11). Optimising the 4-1 switching voltages for m/z 18, however shows light masses detected in abundance with good resolution. The simulations predict that the step function location will increase with optimised m/z value, which may be reflected here and that the threshold is simply higher than predicted by the simulations while the behaviour remains similar. The simulations show that ions below m/z 10 are lost, and it is plausible to consider that this value may be slightly higher in the experiment, particularly if the ionisation point is high or that the switching takes longer than expected, as has been speculated previously (Section 3.1.1.1 and 3.1.2.1).

The datasets therefore do not offer conclusive evidence about the signal loss in the lowest masses due to the laser power fluctuations and loss of TOF resolution. However, one can tentatively assume that using 3-3 switching or better will reliably detect ions down to m/z = 12. If using 4-1 switching, for example when needing to image fast electrons, care should be taken regarding the light ions. If probing a system that requires detecting fast electrons in coincidence with ions over a large range of m/z such that a 4-1 scheme or similar is required, it would be therefore recommended to record multiple datasets with switching voltages optimised for several m/z values covering the range of interest.
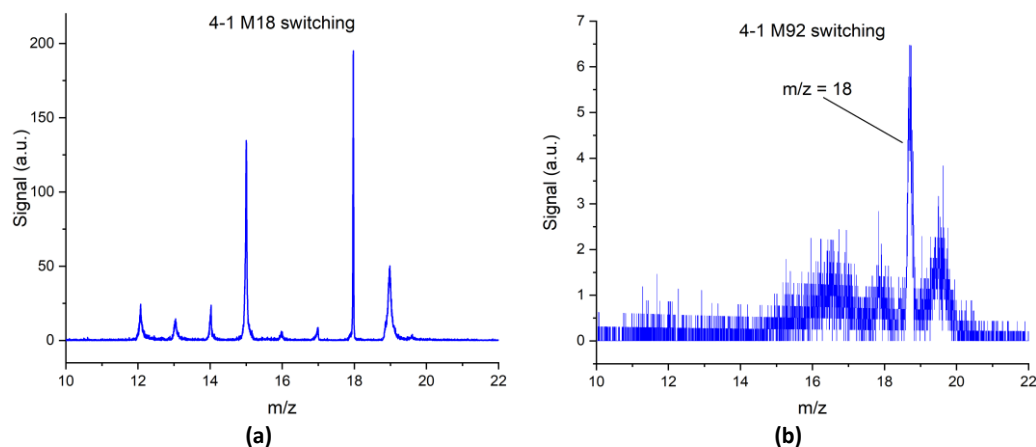
Figure 3.11: Mass spectra in the range m/z 10 to 22 using 4-1 switching voltages optimised for the spatial imaging of m/z 18 (a) and m/z 92 (b). The m/z 18 peak is noticeably displaced along the x-axis in (b) as determined in Figure 3.8 (f).

3.1.3 Coincidence time-of-flight

The DLD-VMI has the ability to register the TOFs and spatial coordinates of multiple particles created in a laser pulse. This allows for the recording of electron-ion coincidences where typically an electron kinetic energy spectrum is plotted that is in coincidence with a given TOF interval of an ion. It also allows recording of ion-ion coincidences, also known as a "pairs" spectrum, typically given as a 2D histogram with each axis representing the ion TOFs or m/z values. Ion-ion coincidences can be seen when a molecule is multiply-ionised and dissociates into two charged fragments. Alternatively, ion-neutral coincidences can be seen when a metastable parent ion lives long enough in the electric field to acquire a sufficient velocity before fragmenting into a charged fragment and a neutral fragment that retains this velocity and can be detected. A correlation between two particles is represented by a peak in the coincidence TOF map at the coordinates (t_1, t_2) where t_1 and t_2 are the TOFs of the first and second ions respectively.

The potential processes for fragmentations that can lead to these coincidences also manifest in specific signatures in the coincidence map. Multiply-charged ions that fragment into several smaller charged fragments often do so with significant energy release, typically several eV, in a Coulomb explosion. This will cause recoil in the fragments that may have a component along the TOF axis, resulting in one fragment's TOF increasing relative to that of its nominal m/z value and the other having a decreased TOF relative to that of its nominal m/z value. This manifests as diagonal lines centred on the coordinates of the nominal TOFs, the length and gradient of which can reveal details on the fragmentation process. Peaks corresponding to fragmentation of metastable ions will vary in their position depending on the time of fragmentation. A distribution of parent ion lifetimes will therefore manifest as long tails of signal extending through the spectrum. The specific shape depends on whether the parent ion dissociates into two charged fragments, or a charged fragment and a neutral fragment.

The calibration of each dimension in the coincidence TOF spectrum to m/z is the same as that for the 1D TOFs given above, but the unique properties of the coincidence TOF signatures can be derived. Here an attempt is made to quantify the relationship between the mass-to-charge ratios involved in a metastable fragmentation and the observed coincidence TOF traces resulting from them. This method is very similar to a model given before [48], but attempts to calculate the lifetime explicitly from the observed traces. There is also an explanation on how peak shapes of Coulomb explosions reveal details of the fragmentation process.

3.1.3.1 Metastable fragmentations

Metastable ion fragmentation in simplified TOF
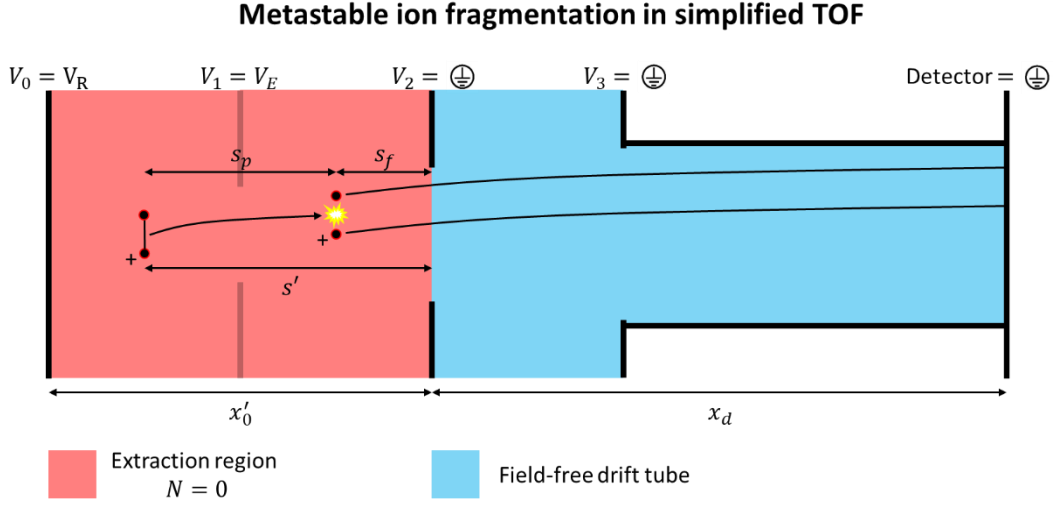
Figure 3.12: Schematic for the model to estimate TOFs of metastable ions based on a simplified version of the 3-electrode static-voltage model in Section 3.1.1. The electric field is defined only by the voltages and positions of the repeller electrode and the drift tube entrance. The extractor voltage is not considered in the model, but still applied in the experiment, so the electrodes are shown here faded out. The extraction region length x_0' and distance for the particle to travel s' are calculated from the quantities in Figure 3.2 as $x_0 + x_1$ and $s + x_1$ respectively.

The static TOF model used previously is simplified further here, where the extraction region and any intermediate acceleration regions are considered together as a single stage with a combined length of s' and a voltage difference $\Delta V = V_0 - V_2 = V_R$. Switched-voltage models for the metastable fragmentations would be too complex to give here. A parent molecule of mass-to-charge ratio m_p/z_p in the electric field E of the extraction region initially experiences a constant acceleration until it reaches the field-free drift tube. If it dissociates inside the extraction region to a fragment with mass-to-charge ratio m_f/z_f then the acceleration changes which affects the total TOF of the fragment. If it fragments in the field-free drift tube then it has already reached the maximum velocity which will be preserved and any fragments will arrive at the same time as an intact parent ion would. The linear TOF setup therefore has a limited range of parent ion lifetimes that can be sampled as given by

$$0 < t_p < \sqrt{2 \frac{m_p}{z_p} \frac{s'^2}{V_R}}$$

3.10

This suggests that the range of lifetimes that can be examined is longer for heavier parent ions and can be extended by using weaker electric fields. If the parent ion has a lifetime of t_p then it will fragment at the position s_p in the flight tube

$$s_p = \frac{1}{2} \frac{z_p}{m_p} \frac{V_R t_p^2}{s'}$$

3.11

The fragment must then traverse the remaining distance in the acceleration region $s_f = s' - s_p$ which takes the time t_f

$$t_f = \cfrac{2s' - \cfrac{z_p}{m_p}\cfrac{V_R}{s'}t_p^2}{\cfrac{z_p}{m_p}\cfrac{V_R}{s'}t_p + \sqrt{\cfrac{z_p}{m_p}\cfrac{V_R^2 t_p^2}{s'^2}\left(\cfrac{z_p}{m_p} - \cfrac{z_f}{m_f}\right) + 2V_R\cfrac{z_f}{m_f}}}$$

3.12

The time to traverse the drift tube t_d is given by:

$$t_d = \cfrac{x_d}{\sqrt{\cfrac{z_p}{m_p}\cfrac{V_R^2 t_p^2}{s'^2}\left(\cfrac{z_p}{m_p} - \cfrac{z_f}{m_f}\right) + 2V_R\cfrac{z_f}{m_f}}}$$

3.13

The total flight time is therefore the sum of the parent lifetime and the time for the fragments to travel the remaining distance in the extraction region and flight tube:

$$t_{metastable} = t_p + t_f + t_d$$

$$= t_p + \cfrac{2s' - \cfrac{z_p}{m_p}\cfrac{V_R}{s'}t_p^2}{\cfrac{z_p}{m_p}\cfrac{V_R}{s'}t_p + \sqrt{\cfrac{z_p}{m_p}\cfrac{V_R^2 t_p^2}{s'^2}\left(\cfrac{z_p}{m_p} - \cfrac{z_f}{m_f}\right) + 2V_R\cfrac{z_f}{m_f}}}$$

$$+ \cfrac{x_d}{\sqrt{\cfrac{z_p}{m_p}\cfrac{V_R^2 t_p^2}{s'^2}\left(\cfrac{z_p}{m_p} - \cfrac{z_f}{m_f}\right) + 2V_R\cfrac{z_f}{m_f}}}.$$

3.14

This gives a general expression for a parent ion of any m_p/z_p dissociating to any fragment with m_f/z_f. If the parent dissociates immediately at $t_p = 0$, Equation 3.14 reduces to the expression for the nominal flight time of the fragment m_f/z_f in a single stage TOF:

$$t_{t_p=0} = \sqrt{\frac{m_f}{z_f}}\left(\frac{2s' + x_d}{\sqrt{2V_R}}\right).$$

3.15

If the parent dissociates at the limit lifetime in Equation 3.10 (or later), then Equation 3.14 reduces to the nominal flight time of the parent ion m_p/z_p in a single stage TOF:

$$t_{t_p=limit} = \sqrt{\frac{m_p}{z_p}}\left(\frac{2s' + x_d}{\sqrt{2V_R}}\right).$$

3.16

If the fragment particle is neutral, then $z_f = 0$ and Equation 3.14 reduces to

$$t_{neutral} = \frac{t_p}{2} + \frac{m_p}{z_p}\frac{s'}{V_R t_p}(s' + x_d).$$

3.17

With these expressions, it can be seen that if a metastable ion dissociates, the TOF of a charged fragment will vary between the limits of the nominal TOF of the parent ion when it fragments in the drift tube, and the

nominal TOF of the fragment when fragmentation is immediate. The TOF of a neutral fragment will vary between the limits of the nominal TOF of the parent ion when it fragments in the drift tube, and infinity when fragmentation is immediate. Early fragmentation of the parent ion means there is less time for the parent ion to gain momentum towards the detector from the electrode potentials before the neutral fragment is created in the dissociation, resulting in increasingly slow longitudinal velocities of the neutral fragment as t_P approaches zero and therefore longer TOFs. Immediate fragmentation means the neutral fragment has no momentum component towards the detector and will never reach it, hence $t_{neutral}$ reaching an infinite value.

The range of observable parent ion lifetimes when detecting neutral particles is further limited by some additional experimental considerations. The MCP detection efficiency depends on the particle's incident velocity. The extremely slow longitudinal velocities of neutral particles generated from early dissociations will result in significantly lower detection efficiencies than for those generated from later dissociations, resulting in a lack of detected coincidences for the shortest parent lifetimes. Additionally, the transverse velocity added by the molecular beam means that slow neutral particles might hit the electrodes or the side of the flight tube before reaching the detector and therefore be lost. These two factors mean that coincidences relating to very short-lived parent ions are unlikely to be observed.

The model is compared to SIMION simulations (Figure 3.13) where the variation of fragment TOF with parent lifetime is shown for example fragmentations for metastable monocations and metastable dications. The settings shown are for 3-electrode static voltages with V_R = 3000 V. The variation of the electric potential and electric field along the particles path is also shown (Figure 3.13 (b)).

The monocation fragmentation (Figure 3.13 (a)) shown is for m/z 45 fragmenting to m/z 19 and the corresponding neutral with $m = 26$. This is a fragmentation signature which is present in spectra of 2-propanol and observed in Chapter 5. In Figure 3.13 (a) the TOFs of the neutral fragments only appear for parent lifetimes of 170 ns or more in the SIMION simulations. This is due to the molecular beam velocity resulting in slow neutral fragments hitting the electrodes or flight tube before the detector. Otherwise, the neutral fragments TOFs begin at very large values for short parent lifetimes. The charged fragments are a finite value, approximately 2900 ns, at zero parent lifetime. As the parent ion lifetime increases the neutral fragment TOFs decrease and the charged fragment TOFs increase until they become equal at an intermediate TOF value.

The dication fragmentation shown is for $m/z = 90/2 = 45$ fragmenting to monocations with $m/z = 27$ and $m/z = 63$. This is a fragmentation signature which is present in spectra of doubly-ionised toluene, which is the subject of Chapter 4. The model is an approximation that neglects any kinetic energy release in the fragmentation. For the dication this is unlikely to be accurate due to Coulomb repulsion, so SIMION simulations are also shown where there is a total kinetic energy release (TKER) of 4 eV for the cases where each fragment is facing the detector. By conservation of momentum and kinetic energy, the TKER of a two-body fragmentation is partitioned into the kinetic energy E_k of a given fragment according to the relative masses as

$$E_k(fragment) = \frac{m_f}{m_p} \times TKER,$$

3.18

Normally the $m/z = 27$ fragment, being lighter, will have a lower TOF than the $m/z = 63$ fragment. However, when the $m/z = 27$ fragment is facing away from the detector and the fragmentation happens in the drift tube, or near the entrance, then it is slowed down relative to the $m/z = 63$ fragment and arrives later due to a lack of sufficient further acceleration by the electric field. This is observed in Figure 3.13 (d). The red "+4 eV" curves, corresponding to a 4 eV Coulomb explosion with the lighter $m/z = 27$ fragment pointing

towards the detector, shows that the lighter fragment always has a lower TOF up until the maximum parent lifetime at 4410 ns, which is when the parent ion hits the detector and the fragment TOFs are effectively equal. The blue "-4 eV" curves, corresponding to a 4 eV Coulomb explosion with the heavier $m/z = 63$ fragment pointing towards the detector, show that the lighter ion has a shorter TOF up until a parent ion lifetime at 777 ns when the blue curves cross and the heavier ion has a shorter TOF. The fragment TOF values again become equal at 4410 ns when the parent ion hits the detector. The black "0 eV" curve shows the fragment TOFs converging earlier at approximately 1400 ns lifetime which is shortly after the parent ion enters the drift tube.

(a)

(b)

(c)

(d)
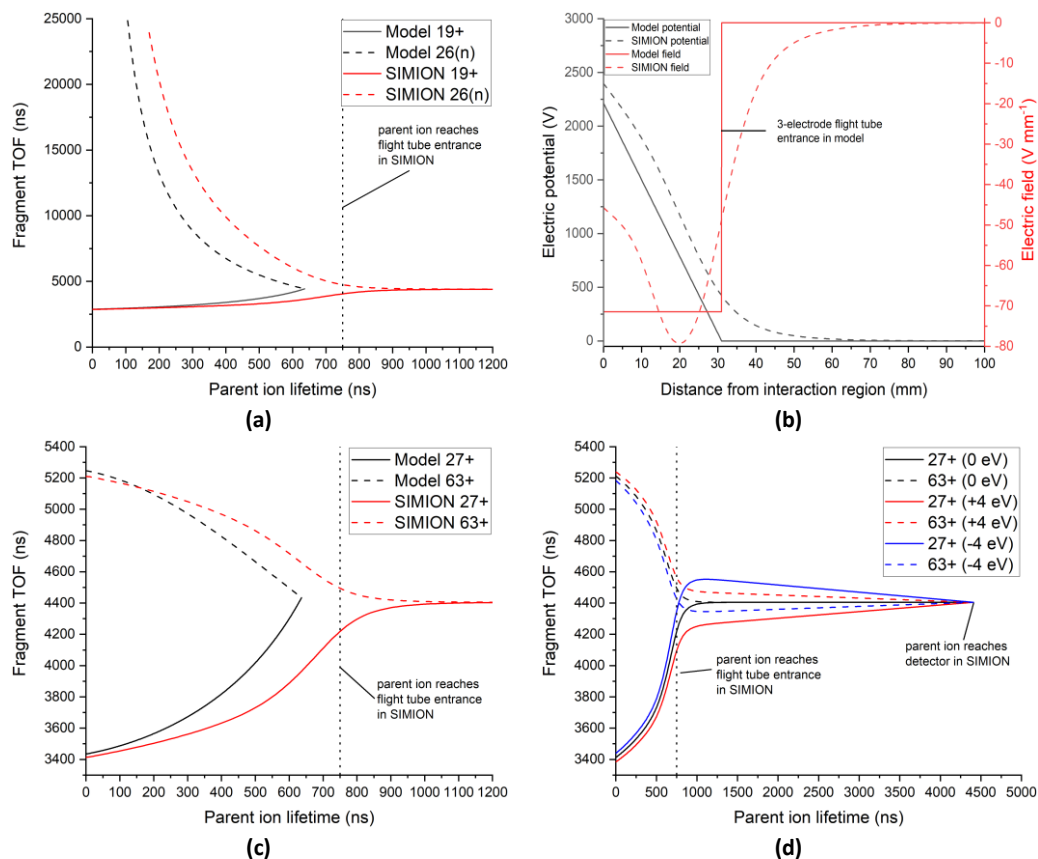
Figure 3.13: Comparison of metastable model with SIMION simulations, showing how the TOFs of the fragments vary with parent ion lifetime. (a) Monocation of m/z 45 fragmenting to an ion of m/z 19 and a neutral of $m = 26$ (b) Variations of electric field and electric potential with distance from the interaction region. (c) Dication of $m/z = 90/2 = 45$ fragmenting to monocations of m/z 27 and m/z 63 at 0 eV TKER. (d) SIMION simulations only of the dication fragmenting at several TKER values: 0 eV; "+4 eV" where the m/z 27 fragment is facing towards the detector; and "-4 eV" where the m/z 63 fragment is facing the towards detector. The calculations are performed for 3-electrode, static voltages with V_R = 3000 V.

The SIMION simulations show that the asymptotic TOFs appear in good agreement with the model, however the fragments do not converge until a later lifetime for both metastable monocations and dications. This might be attributed to approximating the extraction and acceleration regions as a single region of linear electric field. In reality when the voltages are set for VMI conditions, the extraction region has a weaker electric field than the acceleration region (Figure 3.13 (b)) in this setup which results in a longer overall time to reach the field-free drift tube. The model also has the uniform electric field end abruptly at the drift tube, while in reality the field penetrates into the drift tube at the entrance (31 mm along the x-axis of Figure 3.13 (b)) and gradually decreases with distance, meaning the TOFs of the two fragments will more gradually converge in the SIMION simulation than in the model. The SIMION results suggest that using the model on

the data as a method to directly observe the signal variation with parent ion lifetime would tend to underestimate any lifetime. However, it may still be useful as a method to select coincidences pertaining strictly to the metastable fragmentations from the datasets if it can reproduce the shapes of the traces in the coincidence TOF spectra well enough.

The information from the model and simulations for the monocations are recast as representations in the coincidence TOF spectra and compared to experimental results recorded with static voltages at 33.3 eV photon energy (Figure 3.14). The additional fragmentation m/z 45 to m/z 29 is also modelled and simulated for comparison. Both the model and the SIMION simulation can be seen to well replicate the experimental curve. The curve starts from the autocorrelation line for late fragmentations and extends upwards and asymptotically towards the nominal TOF of the charged fragment along the x-axis.

The agreement of the model to the experimental curves in the monocation coincidence TOF spectrum means that it can be used to specifically select for coincidences related to these metastable states. This is aided by the fact that for neutral fragments Equation 3.14 simplifies to Equation 3.17. The lifetime values derived will not be strictly accurate, but qualitative analysis might still be possible. Coincidences pertaining to the metastable signature can be searched for by solving Equation 3.17 for a neutral fragment to determine the lifetime of the parent ion, and then using that lifetime value to estimate the expected TOF of the ion fragment for a given m/z. Rearranging Equation 3.17 to find t_p gives two solutions:

$$t_p = TOF_{neutral} + \sqrt{TOF_{neutral}^2 - 2\frac{m_p}{z_p E}(s + x_d)},$$

$$t_p = TOF_{neutral} - \sqrt{TOF_{neutral}^2 - 2\frac{m_p}{z_p E}(s + x_d)}.$$

3.19

Only the second solution of Equation 3.19 is valid for the experiment as the first solution corresponds to a parent lifetime which is longer than the upper bound of the range over which the expressions are defined (Equation 3.10). The calculations of the lifetime in this model assume there is negligible kinetic energy release in the parent ion fragmentation. Under these conditions the acceleration of the neutral fragment can only be equal to or less than that of the charged fragment, meaning that the neutral fragment should almost always arrive second. This should only change if the parent ion fragments in the drift tube, or very close to the drift tube entrance, with the neutral fragment pointing towards the detector and the ion fragment pointing away. Coincidences of this nature correspond to fragmentations at or after the lifetime upper bound and manifest closely around the autocorrelation line. This is further explored in 2-propanol in Chapter 5.
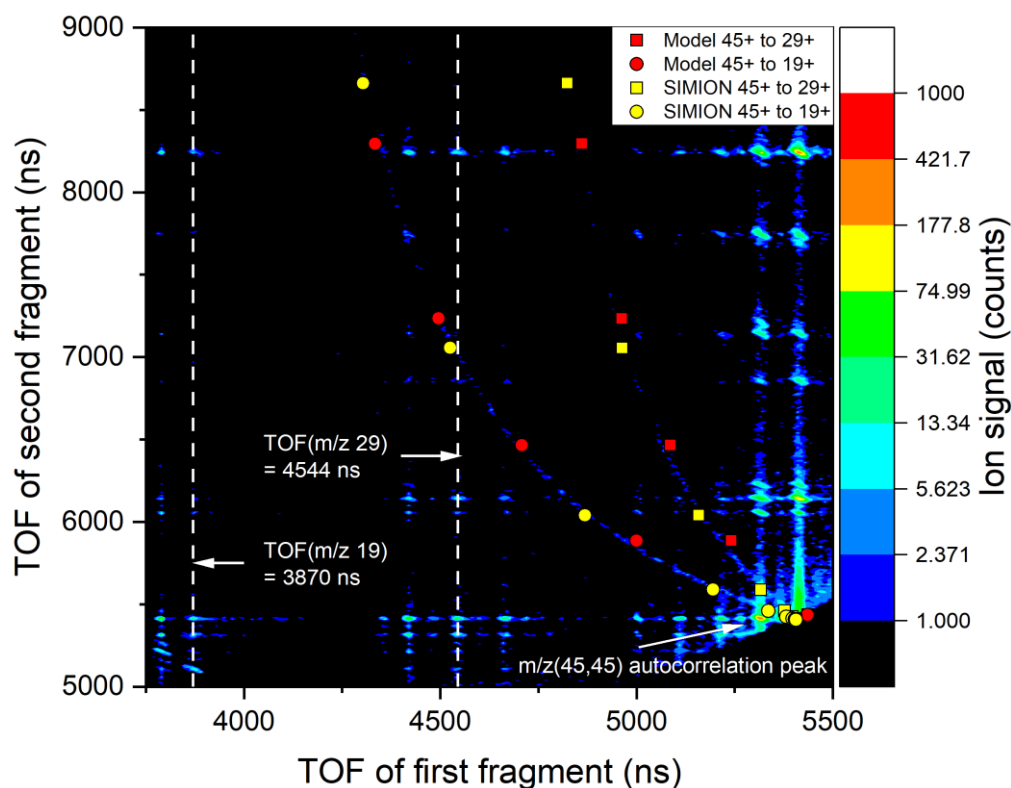
Figure 3.14: Comparison of CTOF traces from the metastable model and SIMION simulations with experiment. The monocation case for the fragmentations m/z 45 to m/z 19 and m/z 45 to m/z 29, featuring experimental data acquired on 2-propanol at 33.3 eV.

The dication figure (Figure 3.15 (a)) compares the model to the simulations for each TKER value in Figure 3.13 (d). It shows that the model slightly overestimates the TOF trace compared to SIMION. However, the shapes of the lines are very similar and they could be hypothetically "forced" to match simply by adjusting the TOF offset t'. The effect of the kinetic energy can be seen at the autocorrelation line where a "V" shape is formed corresponding to fragmentation in the drift tube. The upper arm of the V represents the heavier m/z 63 fragments recoiling towards the detector and arriving before the m/z 27 fragments. In all other cases where the lighter fragment faces the detector or there is no KER the coincidences from the metastable fragmentations follow the same trace between the autocorrelation line and the peak location for the immediate fragmentation into the fragments. For comparing the dication result to experiment, there is not a static voltage dataset available with the toluene metastable dication. However, there is a spectrum using 4-2 M 92 voltage switching. The model does not consider voltage switching as that would be too complex (imagine trying to combine Equation 3.7 and Equation 3.14), but nonetheless it is compared for static, 3-electrode mode with V_R = 2000 V to the spectrum obtained for toluene at 30.5 eV along with a 4-2 M 92 SIMION simulation with 0 eV TKER (Figure 3.15 (b)). The model is seen to underestimate the TOFs of the fragments, this time due to not incorporating the switching effect which temporarily drives the ions the wrong way in the flight tube. However, it again replicates the shape of the metastable curve very well and could be matched by adjusting t'. Unlike the neutral fragment in monocation case, Equation 3.14 does not simplify so it is not as simple a matter to use to isolate for coincidences.

(a)

(b)
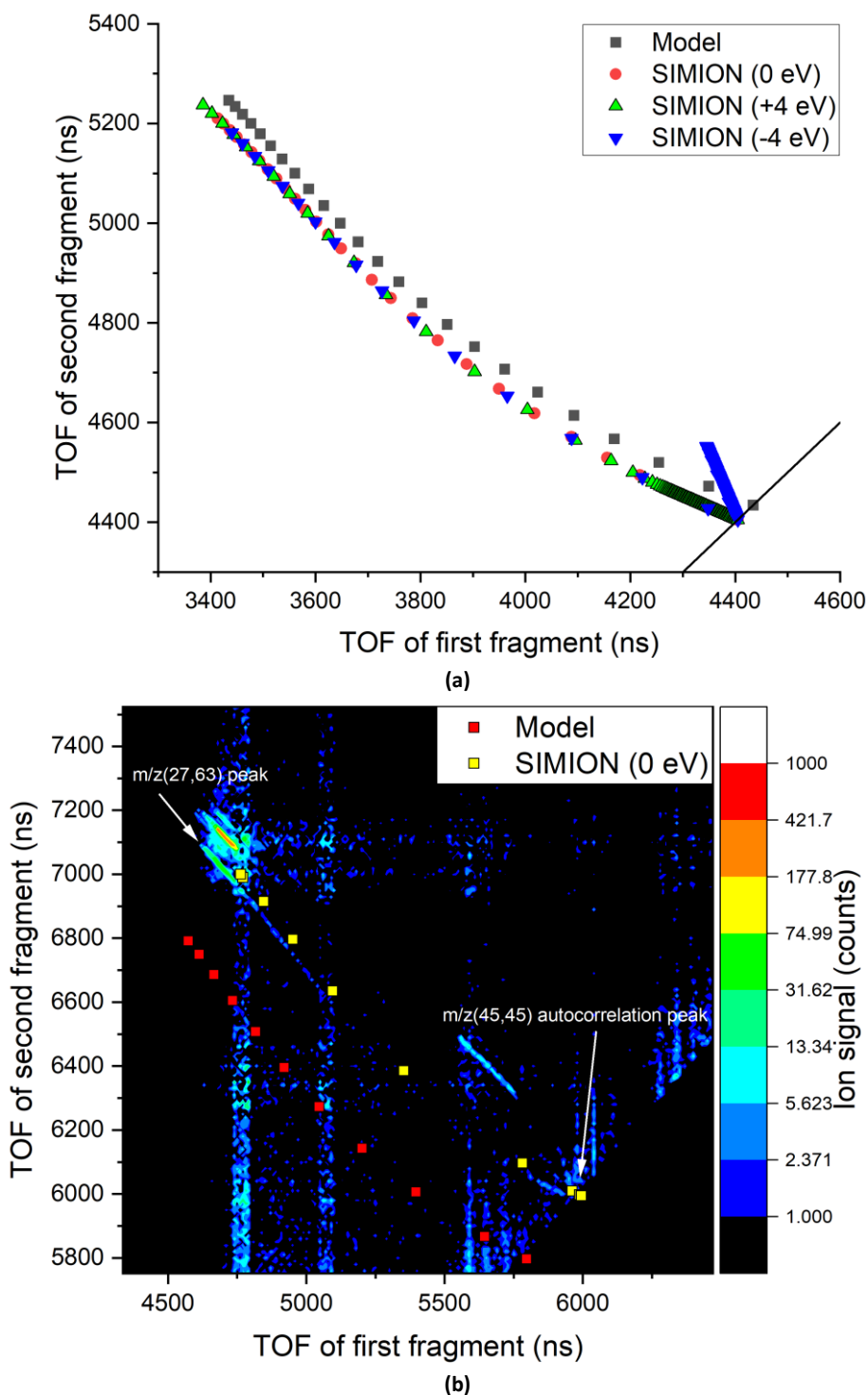
Figure 3.15: Comparison of the metastable model with SIMION simulations and experiment in coincidence TOF spectra. The dication case for the fragmentation m/z 45 to m/z 27 and m/z 63 (a) Model and SIMION at 3-electrode static voltages with V_R = 3000 V at 0 eV, "+4 eV" and "-4 eV" TKER. (b) Model with static 3-electrodes mode with V_R = 2000 V compared with experiment and SIMION both using 4-2 M92 switching and 0 eV TKER in the SIMION simulation.

3.1.3.2 Coulomb explosions

The TKER of a dication Coulomb explosion results in the fragment ion TOFs being distorted from the nominal value for fragments formed with no (or negligible) TKER. For immediate fragmentations after ionisation (i.e. not metastable), Equation 3.1 can be rewritten [45] for a fragment with initial kinetic energy E_k:

$$
t_{K_0} = \sqrt{2m} \left(\frac{x_0}{z\Delta V_0} \left(\sqrt{E_k + z\frac{\Delta V_0 s}{x_0}} \pm \sqrt{E_k} \right) + \frac{x_1}{z\Delta V_1} \left(\sqrt{E_k + z\left(\frac{\Delta V_0 s}{x_0} + \Delta V_1\right)} - \sqrt{E_k + z\frac{\Delta V_0 s}{x_0}} \right) \right.
$$
$$
\left. + \frac{x_d}{2\sqrt{E_k + z\left(\frac{\Delta V_0 s}{x_0} + \Delta V_1\right)}} \right),
$$

$\qquad\qquad$ 3.20

where the $\pm\sqrt{E_k}$ term is a dependence on whether the fragment velocity is towards or away from the detector. This means the TKER can be estimated from the broadening of 1D TOF peaks. In a two-body Coulomb explosion, the fragments recoil in opposite directions resulting in one fragment having an increased TOF and the other having a decreased TOF. If the particles are not aligned before ionisation then repeat measurements will give a TOF distribution depending on the exact angle. This shapes a coincidence TOF spectrum peak as a sloping line through the point (t_1, t_2) which corresponds to zero TKER along the TOF axis [12], [49], [50] (Figure 3.16). An approximation can be made [45] that for a particle with initial momentum p the TOF deviates from the nominal TOF for a particle at rest as:

$$
t_p = t + \frac{1}{zE_0}p\cos\theta,
$$

$\qquad\qquad$ 3.21

where θ is the angle between the momentum vector and the TOF axis. The gradient b of the peak is therefore

$$
b = \frac{t_{p,2} - t_2}{t_{p,1} - t_1} = \frac{p_2 \cos\theta_2\, z_1}{p_1 \cos\theta_1\, z_2}
$$

$\qquad\qquad$ 3.22

For a two-body fragmentation, momentum conservation requires $p_1 = -p_2$ and $\theta_1 = -\theta_2$. The simple case of a dication fragmenting to two monocations gives the gradient as -1. Three-body fragmentations of a dication into two monocations and a neutral fragment, where the neutral fragment is undetected, result in deviations from this gradient depending on the relative masses involved and whether the dissociation occurs in two sequential steps or a single step. If the fragmentation proceeds in a single step as

$$
m^{2+} \rightarrow m_1^+ + m_2^+ + m_3,
$$

$\qquad\qquad$ 3.23

and the neutral fragment does not gain significant kinetic energy or impede the trajectories of the charged fragments then the slope is -1. There are two possible sequential mechanisms for three-body dissociations and both are assumed to allow time for molecular rotation between steps. The first is initial charge separation (ICS), where the Coulomb explosion happens before one of the fragments loses a neutral fragment:

$$
m^{2+} \rightarrow m_1^+ + m_2^+,
$$
$$
m_2^+ \rightarrow m_3^+ + m_4.
$$

$\qquad\qquad$ 3.24

Here momentum conservation means $p_1 = -p_2$. Neglecting TKER in the second step means that

$$p_3 = \frac{m_3}{m_3 + m_4} p_2.$$

3.25

and $\theta_3 = \theta_2$. The two detected particles are m_1^+ and m_3^+, so the gradient of the line is either

$$b = -\frac{m_3}{m_3 + m_4} \text{ or } -\frac{m_3 + m_4}{m_3}$$

3.26

depending on whether the first ion detected is m_1 or m_3 respectively and assuming the first ion is plotted along the x-axis. The second sequential mechanism is deferred charge separation (DCS), where the parent dication first loses a neutral fragment before the Coulomb explosion:

$$m^{2+} \rightarrow m_1^{2+} + m_2,$$
$$m_2^{2+} \rightarrow m_3^+ + m_4^+.$$

3.27

Again, the TKER of the neutral fragment loss is assumed to be zero, so that the momentum of the detected fragments m_3^+ and m_4^+ primarily comes from the Coulomb explosion. This therefore more closely resembles a two-body dissociation and the observed peak gradient is again -1. In reality the TKER on loss of a neutral fragment is not zero, but significantly smaller than that of the Coulomb explosion. Assuming that each step in ICS and DCS is separated by enough time for the molecules to rotate, the loss of the neutral fragment adds a random velocity component to the relevant charged fragments. This results in a broadening of the width of the diagonal line. If the time between the steps is in fact shorter than a rotational period, then the mechanism begins to more closely resemble a single-step three-body process and the gradient of the line approaches -1.
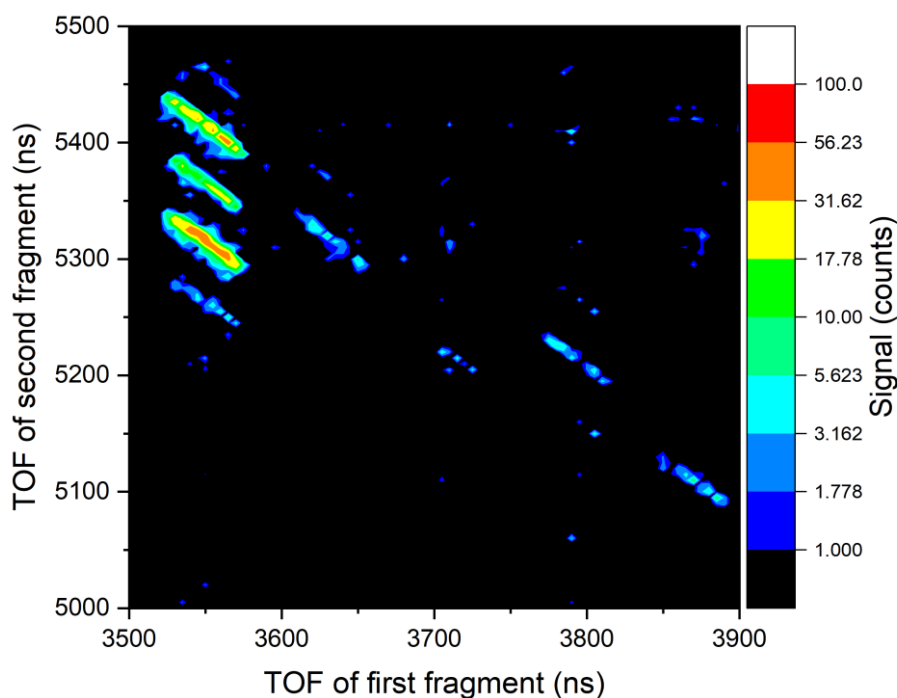
Figure 3.16: Example coincidence TOF spectrum showing Coulomb explosion of 2-propanol fragments when ionised at 33.3 eV. These peaks are analysed in more detail in Chapter 5.

3.2 Velocity-map imaging

VMI [10] is a technique used to image the energetics and directionality of charged particles from a chemical event. It has become a common and powerful tool in the field of charged-particle imaging, which was started by the spatial ion-imaging technique [11]. Electrode geometries and voltages are chosen to create an electrostatic field that can image charged particles onto a 2D detector in a way where the final position is dependent on the velocity vector that the particle was born with and not the particle's starting position (within a sufficiently small source region). Both electrons and ions can be imaged with opposite polarity voltages. VMI can reveal kinetic energy distributions and angular directionality for a range of processes in both electron spectroscopy and ion photodissociation studies.

Imaging a chemical process involves projecting a 3D spatial distribution onto the 2D detector surface, resulting in information loss. By using plane-polarised light parallel to the detector surface, electrons are emitted with cylindrical symmetry around the polarisation axis. This reduces the number of variables describing the velocity distribution from three to two in spherical coordinates as:

$$f(z, \theta, \phi) \to f(z, \theta) \qquad\qquad 3.28$$

This allows the initial 3D distribution to be reconstructed from the detected 2D distribution with an inverse Abel transform. Several methods exist for this reconstruction [51]–[55]. The method for reconstructing the 3D distribution used in this work is the Maximum Entropy Velocity Legendre Reconstruction (MEVELER) method [56]. In this method the image is not directly Abel-inverted, but an iterative process based on Bayesian statistics is used to find the distribution which would give the best match to the image when it undergoes the forward Abel transform. This method is very fast compared to others and accurate for low signal levels, which is advantageous when dealing with large datasets such as those from coincidence experiments.

VMI setups often have the molecular beam sample travel directly towards the detector centre. The velocity-mapping depends on the velocity component parallel to the detector surface so species that remain in the beam upon ionisation simply hit the detector centre. Any dissociation process that gives the ions a parallel velocity component will result in a distribution around the centre. Another setup (such as that developed here) involves the molecular beam initially travelling parallel to the detector surface. Particles are then only steered towards the detector after ionisation by the electrode voltages. The particles retain the velocity component from the molecular beam and therefore continue to travel in that direction while being imaged. Ions of species in the molecular beam will therefore manifest as narrow lines. The length of the line describes the velocity distribution in the beam and the position will be affected by m/z. Heavier ions have a longer TOF so they will travel further in this direction before detection. If a dissociation process adds an additional velocity component parallel to the detector, the distribution will be centred around the spot the particle would otherwise hit due to the molecular beam. Particles emitted in the plane of polarisation with the same kinetic energy will manifest as discrete rings on the detector. The molecular beam velocity is usually negligible compared to the velocity of a photoelectron and therefore the photoelectron distribution will still be distributed approximately around the VMI centre in the second VMI setup.

When performing VMI, the particles are detected at a distance R pixels (px) from the centre. R depends on the velocity component v_x parallel to the detector surface. R is then given by

$$R = C'v_x t,$$ (3.29)

where C' is an instrumental parameter in px m^{-1}, v_x is the parallel velocity component in m s^{-1} and t is the TOF in s. The TOF can be well-approximated to be inversely proportional with the square root of V_R (Figure 3.5) so that a TOF-m/z relationship can be used as:

$$t = k'\sqrt{\frac{m}{zV_R}}$$ (3.30)

Combining the above two equations gives the parallel kinetic energy component E_k of a charged particle in terms of the detected radius from the image centre. E_k is calculated in eV by

$$E_k = \frac{1}{2C'^2k'^2}zV_RR^2 = CzV_RR^2$$ (3.31)

where $C = (2C'^2k^2)^{-1}$ is an experimental constant in px^{-2}. Radially integrating an Abel-inverted image gives the signal per radial pixel. To convert the radial signal to a kinetic energy spectrum, the Jacobian is used:

$$\sigma(E_k) = \sigma(R)\frac{dR}{dE} = \frac{\sigma(R)}{2CzV_RR} \propto \frac{\sigma(R)}{R},$$ (3.32)

where $\sigma(E_k)$ is the signal variation with kinetic energy and $\sigma(R)$ is the signal variation with radius.

Assuming the absence of chromatic aberrations, where the focal length of the charged particles varies with E_k, the radial resolution ΔR would be approximately constant. The kinetic energy resolution ΔE_k would therefore be expected to get worse with increasing radius or kinetic energy as

$$\Delta E_k = 2CR\Delta R = 2\sqrt{E_kC}\Delta R$$ (3.33)

$$\Delta E_k \propto R \propto \sqrt{E_k}.$$ (3.34)

These relationships hold for both electrons and ions in static conditions.

3.2.1 Static voltages ion velocity-map imaging

3.2.1.1 Spatial resolution of species in the molecular beam

The spatial resolution of the molecular beam species is determined from the same datasets used for the TOF resolutions (Section 3.1.1). To determine the experimental spatial resolutions (Figure 3.17), ion images of selected m/z values are generated. The spot FWHM (Figure 3.3) is determined by integrating the spot along the molecular beam axis and fitting a Gaussian to the resulting peak. This is converted from px to μm based on the MCPs' nominal 75 mm effective diameter.

The simulations show that 2-electrode focusing should give the poorest spatial resolution and that it would be constant with m/z. The SIMION simulations for the 3- and 4- electrodes are quite strange compared to the 2-electrode results. Whereas the 2-electrode simulations give approximately constant resolution over the

mass range, the 3-electrode simulation results are quite bizarre, where different repeller settings give almost opposite trends in resolution against mass. However, the experiments suggest this is not the case, although the resolution decreases with increasing mass. The experimental results in all cases are significantly worse than simulation, and amount to widths of 2-4 pixels.
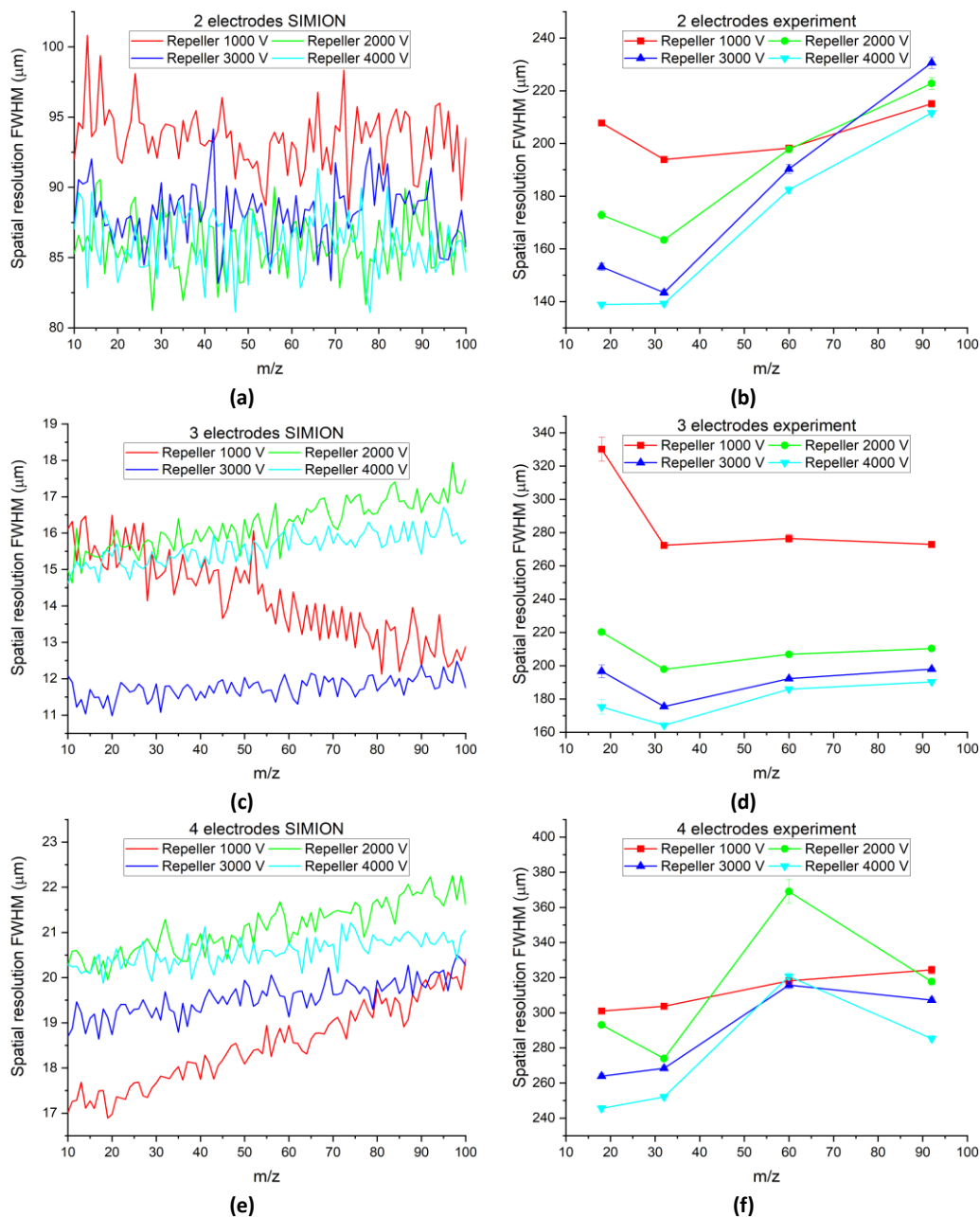
Figure 3.17: Spatial resolutions of the molecular beam species as a function of mass-to-charge ratio. The left-hand figures (a), (c) and (e) show the SIMION simulation results for 2-, 3- and 4-electrode mode respectively and the right-hand figures (b), (d) and (f) show the corresponding experimental results.

3.2.2 Static voltages electron velocity-map imaging

3.2.2.1 Kinetic energy calibration

To calibrate the VMI detector for measuring kinetic energy, photoelectron spectra of an atomic beam containing nominal molar concentrations of 80% helium (IP = 24.59 eV from the $1s$ orbital), 10% neon (IP = 22.6 eV from the $2p$ orbital) and 10% argon (IP = 15.76 eV from the $3p$ orbital and IP = 29.24 eV from the $3s$ orbital) [57] were recorded at various photon energies between 20 eV and 40 eV with the HHG source. Ionising argon and neon from the closed-shell p orbitals leave ions with a np^5 configuration, where n is the principal quantum number. This results in a ^2P state of the ion that can split via spin-orbit coupling into accessible $^2P_{3/2}$ and $^2P_{1/2}$ states. The argon $3p$ and neon $2p$ ionisation peaks therefore have additional peaks 0.18 eV and 0.10 eV below the main peak respectively. Due to relative degeneracies of the $^2P_{3/2}$ and $^2P_{1/2}$ states (4-fold to 2-fold), the lower-energy peaks have half the intensity of the main. With the current experimental resolution, these manifest as a lower-energy shoulder of the main peak which is accounted for in fitting. Spectra were recorded under static conditions for 3- and 4-electrode setups at various voltages on both the DLD-VMI and CCD-VMI (Figure 3.18). In the case of the DLD-VMI, the photoelectron images suffered from distortions that had to be repaired using a recircularisation process before calibration (see Section 3.2.2.2).

(a)   **(b)**
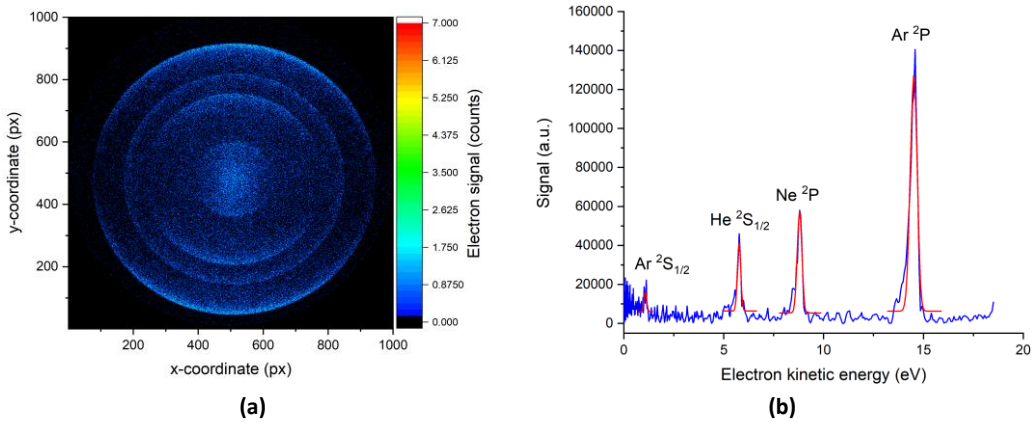
Figure 3.18: (a) Electron VMI image recorded with the CCD-VMI, 3 electrodes, V_R = 5000 V with 30.3 eV photon energy. (b) The resultant photoelectron spectrum after Abel inversion and kinetic energy calibration, along with Gaussian fits of the peaks in red. The peaks are labelled with the corresponding ionic state populated by the photoionisation event.

The E_k-R calibration was carried out by considering the difference in kinetic energies of the peaks and the difference in their radial positions.

$$E_2 - E_1 = CqV_R(R_2^2 - R_1^2)$$

3.35

This means the photon energy does not need to be explicitly known in advance which can improve the calibration. Otherwise the kinetic energy must be derived from knowledge of the photon energy, which may have its own calibration uncertainties. The difference in kinetic energies between two peaks only depends on the difference in the IPs of species being photoionised. These are very precisely known for the atomic species used. Equation 3.35 is fit to the data obtained from the spectrum in Figure 3.18 is shown (Figure 3.19). Nominal and calculated photon energies are shown in Table 3.5 for CCD-VMI spectra recorded with V_R = 5000 V at multiple photon energies. The experimental calibration constants C, which are determined from spectra recorded at multiple photon energies and V_R settings are shown in Table 3.6.

Equation	y = a + b*x
Plot	Radius squared difference
Weight	Instrumental (=1/ei^2)
Intercept	675.87254 ± 460.2483
Slope	12922.55571 ± 72.90163
Residual Sum of Squares	58.51592
Pearson's r	0.99987
R-Square (COD)	0.99975
Adj. R-Square	0.99971
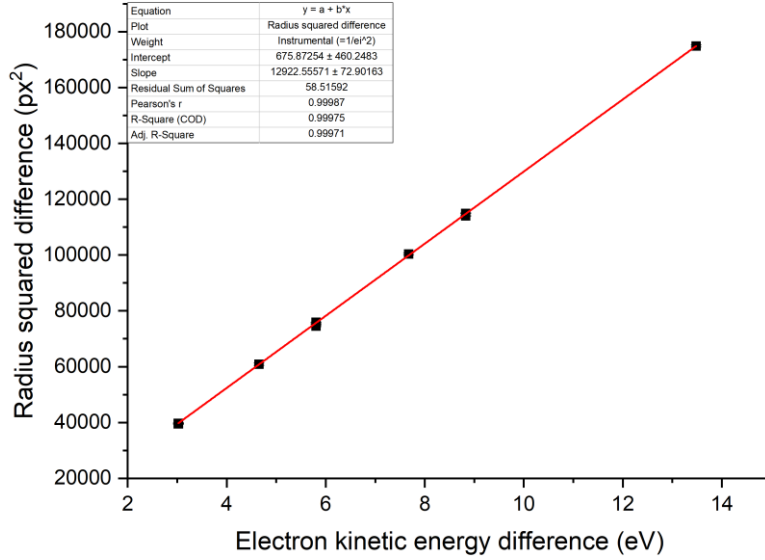
Figure 3.19: Calibration fit of the CCD-VMI based on the photoelectron spectrum in Figure 3.18.

Nominal photon energy (eV)	Calculated photon energy (eV)
23.9	23.959(18)
27.1	27.136(16)
30.3	30.30(4)

Table 3.5: Nominal and calculated photon energies based on CCD-VMI photoelectron spectra recorded with 3 electrodes, V_R = 5000 V.

No. of electrodes	C (px^{-2})	
	CCD-VMI	DLD-VMI
3	$1.540(2) \times 10^{-8}$	$1.657(8) \times 10^{-8}$
4	$1.927(6) \times 10^{-8}$	$2.063(7) \times 10^{-8}$

Table 3.6: Calibration constants of the radius-to-kinetic energy conversion for the 3- and 4-electrode static voltage modes. Obtained using photoelectron data at various kinetic energies and V_R values.

The kinetic energy resolution of the photoelectron VMI was investigated. SIMION simulations were performed by generating an isotropic photoelectron distribution perpendicular to the TOF axis from the volume in the VMI centre. The kinetic energies used are similar to those observed in the experiments, although spin-orbit coupling is neglected. The radial mean and standard deviations were measured and converted to kinetic energies using Equations 3.31 and 3.33. The FWHM resolution is determined by assuming a Gaussian. The simulations show that the resolution gets worse with increasing kinetic energy, going from below 10 meV for 1 eV electrons to approximately 160 meV for 14 eV electrons. Higher voltages slightly improve the resolution. There is very little variation between the DLD-VMI and CCD-VMI performances since geometric differences are very minor and little difference between the 3- and 4-electrode modes. The experimental resolutions are noticeably worse than the simulated ones. For the slowest electrons the resolution is above 100 meV. This might be the energy resolution of the HHG source which could be the limiting factor. The CCD-VMI has better experimental resolution than the DLD-VMI. The DLD-VMI ranges from 0.2 eV to 0.7 eV resolution and the CCD-VMI from 0.1 eV to 0.4 eV. The DLD images are not circular and the recircularisation process is imperfect, which might be a cause of the relative broadening. Recircularisation was not used on the CCD-VMI images as it had a negligible effect. Another explanation might be improperly chosen parameters on the CFD for the DLD or broadening induced by the magnetic fields of the turbomolecular pumps, which are next to the DLD-VMI.
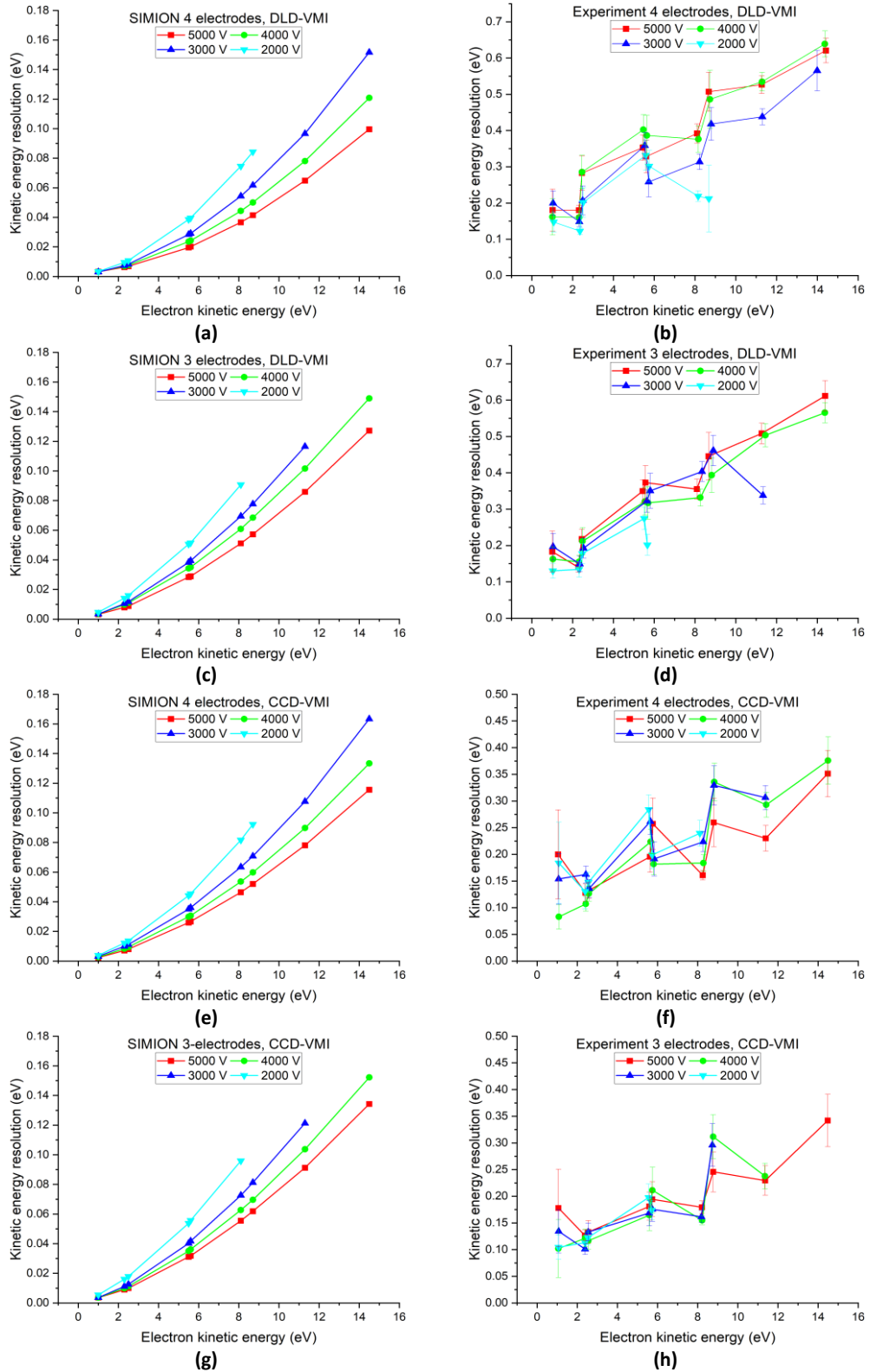
Figure 3.20: Kinetic energy resolution of photoelectrons as a function of the electron kinetic energy. The left-hand figures (a), (c), (e) and (g) show the SIMION simulation results for 4- and 3-electrode DLD-VMI and 4- and 3-electode CCD-VMI respectively. and the right-hand figures (b), (d), (f) and (h) show the corresponding experimental results.

3.2.2.2 Delay-line detector image recircularisation

Photoelectron peaks in VMI should resemble concentric rings centred on the spot where the ionisation event takes place. However, for the DLD images, there is a significant degree of deformation (Figure 3.21). This may result from stray magnetic or electrical fields penetrating the flight tube. Mu-metal tubes surround each of the flight paths, however holes were punched in them with the aim of increasing vacuum pumping speed inside the flight tube. It is possible these holes compromise the shielding effect sufficiently for stray magnetic fields to leak in. This would have a significant effect on the electron trajectories. Since ions are significantly heavier, they should be less distorted. The DLD-VMI is located underneath the detection chamber along with the magnetically-levitated turbopumps. It may also be an artefact due to the delay line detector itself. There is a gap of several millimetres between the back of the MCP stack and the delay line which is unshielded by mu-metal. Magnetic fields may distort the electron cloud from the MCPs on their path towards the delay lines. This would manifest as distorted images for both ions and electrons, since the electron cloud output from the MCPs is present for both types of signals. Another possible artefact would arise from the x- and y-lines having different propagation constants which could feasibly arise from the wires being different lengths in the anode geometry. The image distortions would then be elliptical in nature as the x and y-coordinates are amplified differently. None of these distortions were observed in the CCD-VMI photoelectron images.

Inspection of a polar plot of the images (Figure 3.21) shows that they are not elliptical (but may have elliptical contributions), suggesting that there is an effect present beyond just that of the wires having different propagation constants. The images are repaired using a circularisation method [58] and provided in the FITS Viewer and VMI Analysis program [59] where the centre of the image is initially guessed and a polar plot of the image derived, giving the signal variation I as a function of the radius r and angle θ. The polar plot is Abel inverted using a recursive method [60], [61]. The angular profiles of each photoelectron ring i are evaluated by fitting a Gaussian peak to the data as

$$I(r,\theta) = I(\phi)\exp\left(-\frac{\left(r - r_g(\theta)\right)^2}{2\sigma_i^2}\right) + c\,,$$ (3.36)

where σ_i is the standard deviation of the Gaussian of the ith peak, c is an intensity offset, $r_g(\theta)$ is the central position of the Gaussian peak at each angle θ and varies as

$$r_g(\theta) = r_i + \sum_{n=1}^{N} A_n^{(i)}\sin n\theta + B_n^{(i)}\cos n\theta\,.$$ (3.37)

r_i is the "true" centre of the Gaussian peak at all angles θ and is considered perturbed according to the trigonometric series in the sum term, where the number of terms N can be chosen as appropriate. $A_n^{(i)}$ and $B_n^{(i)}$ are coefficients that determine the magnitude of the perturbation by $\sin n\theta$ and $\cos n\theta$ respectively for the ith peak. The intensity $I(\phi)$ variation with angle from the polarisation vector $\phi = \pi/2 - \theta$ is

$$I(\phi) = I_0(1 + \frac{1}{2}\beta_i(3\cos^2\phi - 1)),$$ (3.38)

where β is the anisotropy parameter $-1 \leq \beta \leq 2$. The radial dependence of the trigonometric coefficients is determined by fitting numerous peaks ionised from each gas in the sample at multiple photon energies between 20 eV and 33 eV and is approximated here to be linear. The centre is found by iterating the process until the linear slope of the plots of $A_1\sin\theta$ and $B_1\sin\theta$ pass through the origin at $r = 0$ indicating that

radial deformations vanish at zero radius. The gradients of the linear fits of the coefficients $a_n = A_n(r)/r$ and $b_n = B_n(r)/r$ are used to determine a radial shift to correct the deformations:

$$\Delta r(r, \theta) = \sum_{n=1}^{N} a_n r \sin n\theta + b_n r \cos n\theta \, .$$

$$\text{3.39}$$

The corrected radius r_u is then determined as

$$r_u = \frac{r_g(\theta)}{1 + \Delta r(r, \theta)}.$$

$$\text{3.40}$$

This is then used to remove the deformations. The radial dependencies are determined for all of the photoelectron rings acquired (see the kinetic energy values present in Figure 3.20) in every voltage setting. Values are derived for every experimental condition under which the electrons are recorded on the DLD-VMI (number of electrodes, electrode voltage). These values are then kept and used to correct every subsequent experimental photoelectron image obtained under the same experimental conditions. An example (Figure 3.21) is shown for a photoelectron image taken at 30.4 eV with 4-electrode conditions at V_R = 5000 V. The effect of circularisation is clearly shown in the polar plots, where deformations that are particularly pronounced at θ = 0 - 180 degrees are transformed into straight lines. The coefficients A_n and B_n vary approximately linearly with radius, with the values being obtained by fitting the peaks of this image and other ones taken using the same electrode conditions with different photon energies. A constrained linear fit (the dashed lines in the plot) is used to determine the final gradient. The obtained circularisation constants are given in Appendix C.

(a)

(b)

(c)

(d)

(e)

(f)
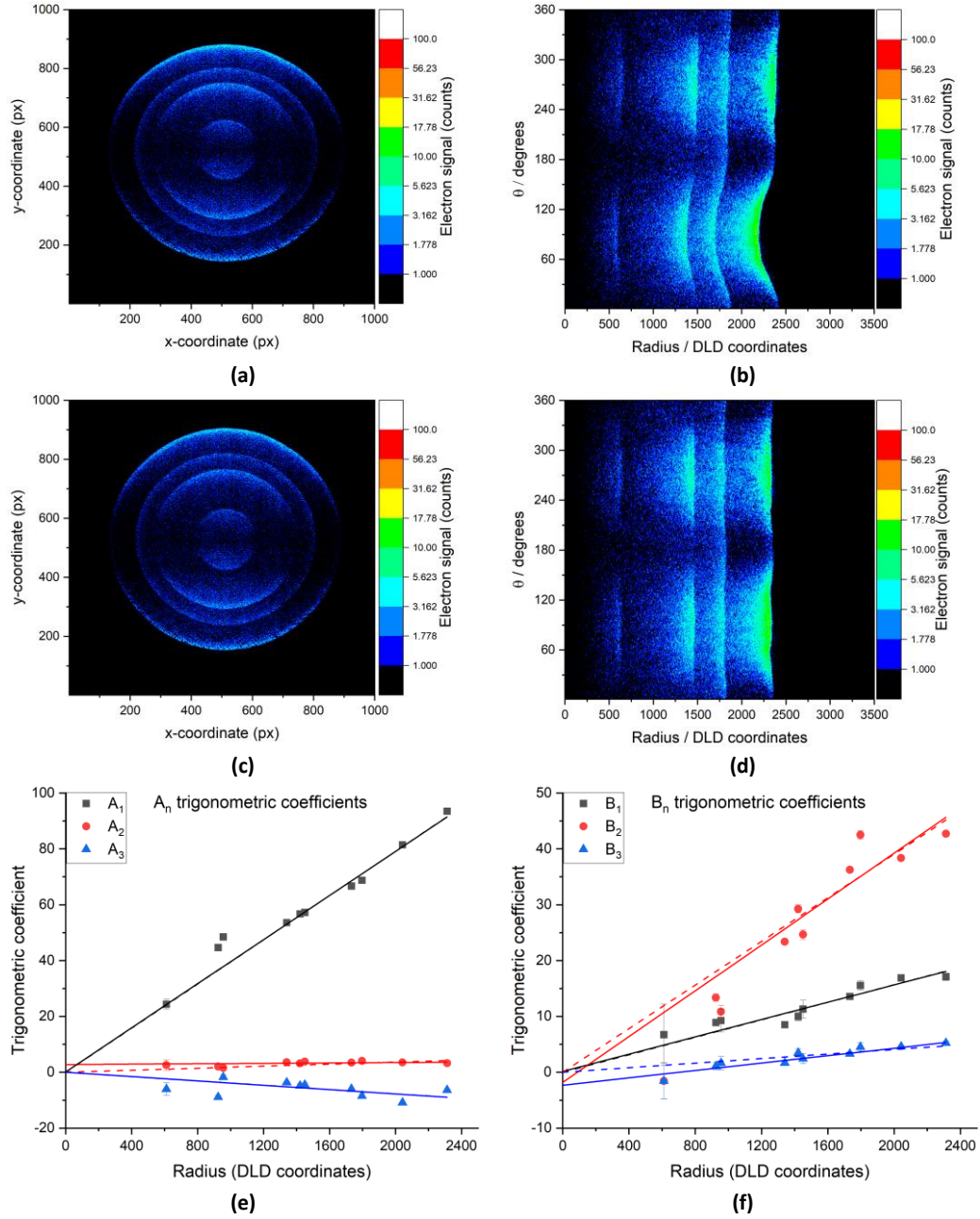
Figure 3.21: Photoelectron images with a logarithmic colour scale of the gas mixture recorded in 4-electrode mode with V_R = 5000 V using 30.4 eV photon energy before and after recircularisation. (a) Cartesian image before recircularisation; (b) polar image before recircularisation; (c) Cartesian image after recircularisation; (d) polar image after recircularisation; (e) the variation of the An trigonometric coefficients with radius; (f) the variation of B_n trigonometric coefficients with radius. Solid lines in (e) and (f) are linear fits, dashed lines are linear fits that are fixed at the origin. The photoelectron images used logarithmic colour scales to better show the weak signals.

3.2.3 Switched voltages ion velocity-map imaging

3.2.3.1 Spatial resolution of species in the molecular beam

The spatial resolution for the molecular beam ions (Figure 3.22) when using switched voltages is determined in the same way as the static voltage for both the SIMION simulations and the experiment. In this case distinctive trends appear: in the simulations it can be seen for every voltage setting that optimising for a given m/z produces a local minimum of the spot FWHM for that value of m/z. As m/z moves away from the optimised value, the spot size begins to increase. When going to higher m/z values the spot size increases and then begins to level off to become approximately constant as heavier ions are less influenced by the effects of the voltage switching. Going to lower m/z values than that optimised for results in a rapid increase in the spot FWHM, as lighter ions are significantly more perturbed by the voltage switching. Particularly when using 4-1 switching, optimising for VMI of m/z 92 results in the ion image of m/z 18 having extremely large spot widths and vice versa. The simulation trends are mostly well reproduced in the experiment, although the absolute FWHM values are higher in the experiment. The exception is when considering 1-4 switching. Optimising for m/z 60 results in it having the worst spatial resolution of the experimental masses. Optimising for m/z 32 shows the correct general trend, where it has the best spatial resolution, but the FWHM increases more sharply when going to high m/z than low m/z. The 1-4 experimental results suggest that even if m/z 60 is the primary value of interest, it may be more beneficial to optimise the voltages for m/z 32 if the lower values are also of interest, or for m/z 92 if the higher values are also of interest. If values on either side are also of interest to an equal extent, then optimising for m/z 60 may be appropriate.
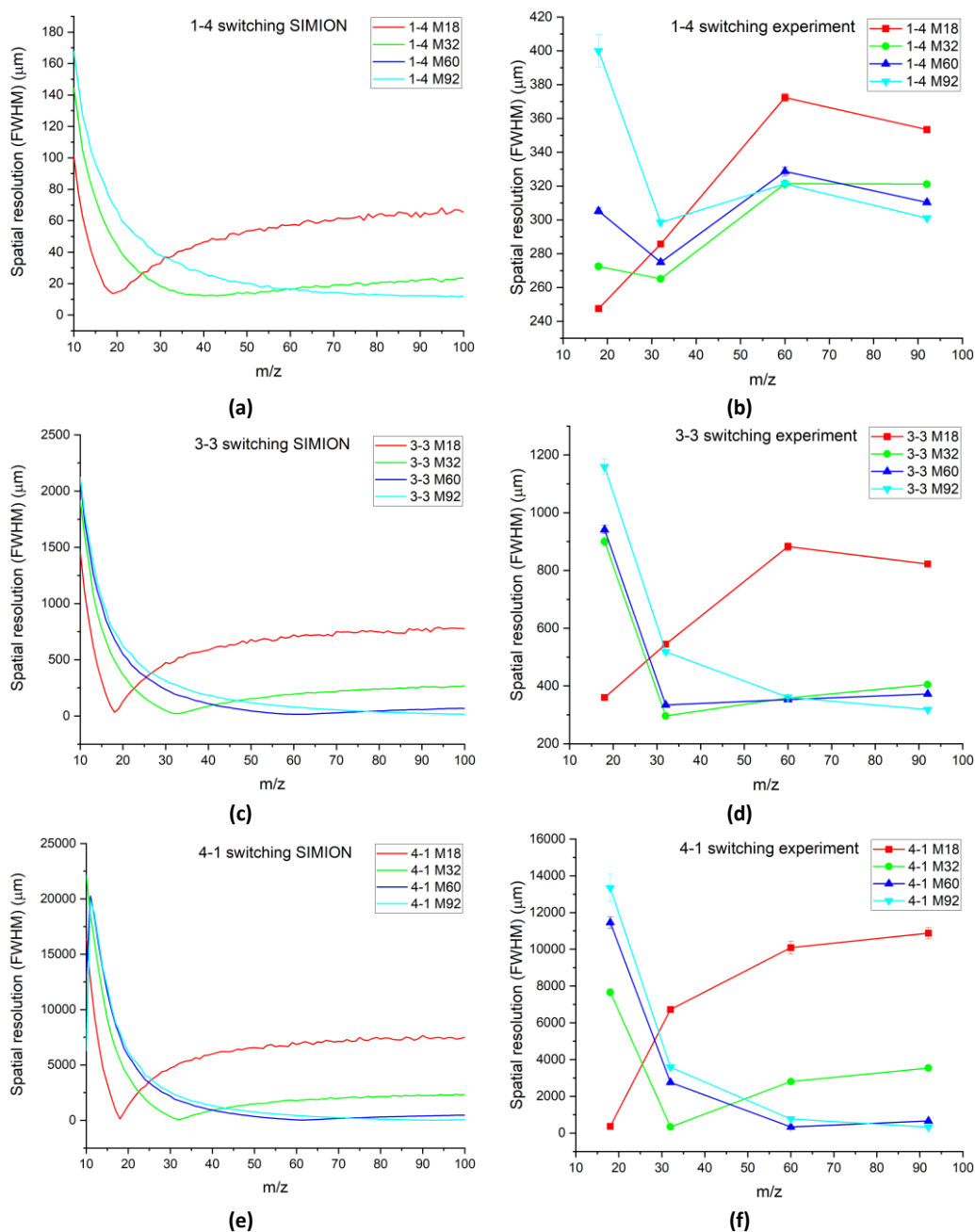
Figure 3.22: Spatial resolutions of the molecular beam species as a function of mass-to-charge ratio. The left-hand figures (a), (c) and (e) show the SIMION simulation results for 1-4, 3-3 and 4-1 switching modes respectively and the right-hand figures (b), (d) and (f) show the corresponding experimental results

3.2.3.2   Kinetic energy calibration

Obtaining a kinetic energy calibration for the ions when using the switched PEPICO mode is more challenging than the static case. Photoelectron spectra cannot be used because the electrons are quickly lost before the switch due to their light mass. It is therefore necessary to image a process where ions are produced with a defined kinetic energy, such as fast photodissociation or Coulomb explosion. HHG data of the double ionisation of 2-propanol is used here (spoiler alert for Chapter 5), as upon double ionisation the methyl

fragment CH_3^+ is observed with kinetic energies attributed to both processes. To obtain an expression for the calibration, it is again overly cumbersome to attempt to use the TOF equation for switched voltages in the same way as Equation 3.2 was used in the static mode to obtain Equation 3.31. Therefore, another approach is considered where Equation 3.31 is modified to include another factor $a(m/z)$ for a given MX switched voltage setting which is some function of m/z to account for a change in radius between static and switched modes where the repeller voltage is held constant:

$$E_k = CqV_R\big(R_{switched} \times a(m/z)\big) \qquad\qquad 3.41$$

To determine $a(m/z)$, the processes are observed in the ion images using both static and switched modes. Regardless of the operational mode, the kinetic energy of the fragments at the moment of the dissociation remains constant. $a(m/z)$ is the ratio between the radii of the peaks in each image:

$$a(m/z) = \frac{R_{static}}{R_{switched}}. \qquad\qquad 3.42$$

The geometric constant C determined by the photoelectron data can be used with Equation 3.31 to find the kinetic energy of the process in the static mode. Figure 3.23 shows ion images and radial distributions of CH_3 obtained at 33.3 eV photon energy on 2-propanol seeded in helium carrier gas. The images are acquired using V_R = 3000 V using static voltages and voltages that had been optimised for m/z = 40 (argon). At this photon energy double ionisation of 2-propanol occurs as well as single ionisation (see Chapter 5), and the m/z 15 signal contains two contributions. Slower CH_3^+ fragments come from fragmentation of singly-charged 2-propanol cations and faster CH_3^+ fragments come from a Coulomb explosion of the 2-propanol dication. The radial distributions therefore show two broad peaks of different kinetic energies. Gaussian fit data of the peaks are shown (Table 3.7).
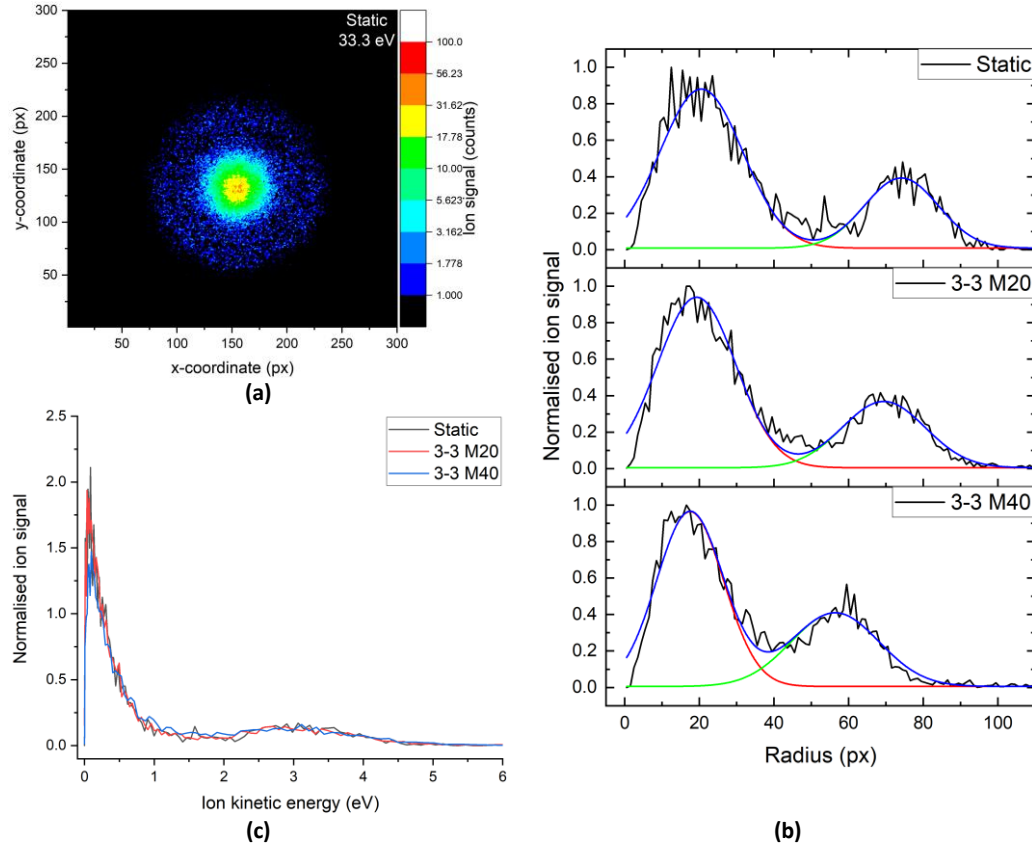
Figure 3.23: CH$_3^+$ fast dissociation and Coulomb explosion. (a) Ion velocity-map image using static voltages with V_R = 3000 V; (b) CH$_3^+$ radial distributions with Gaussian peak fitting acquired by Abel inverting (a) and corresponding images for 3-3 M20 and 3-3M40 voltage conditions; (c) CH$_3^+$ kinetic energy distributions of (b).

Property	Peak 1	Peak 2
Static voltages radius (px)	20.5(3)	74.1(7)
3-3 M20 radius (px)	19.3(2)	69.4(6)
3-3 M20 $a(m/z\ 15)$	1.07(2)	1.068(13)
3-3 M20 mean $a(m/z\ 15)$	1.067(11)	
3-3 M40 radius (px)	17.5(2)	56.4(6)
3-3 M40 $a(m/z\ 15)$	1.17(2)	1.315(18)
3-3 M40 mean $a(m/z\ 15)$	1.262(14)	

Table 3.7: Radial distribution data for the CH$_3$ Coulomb explosion when 2-propanol is double ionised at 34.5 eV using both static and switched voltages.

$a(m/z)$ is different for the two peaks. Therefore, it is possible that it is not just a function of mass-to-charge ratio but also of kinetic energy: $a(m/z, E_K)$. This would be due to higher kinetic energy particles being able to travel further from the VMI centre than lower kinetic energy particles before the switch, similar to how lighter masses travel further than heavier masses. However, SIMION simulations (Figure 3.24) suggest a is independent of E_k, with average values being 1.0347(7) and 1.0639(9) for 3-3 M20 and 3-3 M40 conditions respectively. The simulations do however show m/z-dependence, with $a(m/z)$ decreasing asymptotically with increasing m/z. This is due to heavier ions being comparatively unperturbed by the switching compared to light ions and having a trajectory that can be better approximated to the static voltages case. As with the other discrepancies between experiment and simulation for the switched voltage, the E_k-dependence could potentially be due to the ionisation taking place away from the VMI centre, or the voltage switching taking

longer than previously estimated. The kinetic energy distribution for the switched voltage in Figure 3.23 was obtained by using the weighted average of $a(m/z, E_k)$ as an approximation. The shortcomings of the approximation can be seen where the high energy peak (at approximately 2.7 eV) of the switched voltage distribution is skewed to a slightly lower energy than that of the static voltage distribution and the low energy peak is skewed oppositely. However, the kinetic energy distributions are very broad and over the given range it can suffice as an approximation. This may change if there is some process that can give ion distributions with two distinct kinetic energies that are very different from one another, as multiplying both peaks by an average factor might give very wrong results. It can also be argued that there is not a need to calculate very accurate ion kinetic energy distributions in the switched mode. If they must be determined accurately, this can be done using the static mode while the only added benefit (apart from reduced acquisition times) of the switched mode can be to determine threshold kinetic energy values with which to filter other particles coincident to those of the distribution in question. However, this approach may fall short if considering filtering the other way using coincident photoelectrons. For example, if the kinetic energy distribution of a given mass changes drastically when considering only those particles that are coincident with slow electrons such that a hidden peak or feature would appear. The static voltages do not detect electrons and so the data set can't be filtered to give the same distribution that could be acquired with switched voltages that detect electrons. The kinetic energy of the feature would have to be determined either approximately or with an accurately known value of $a(m/z, E_k)$.
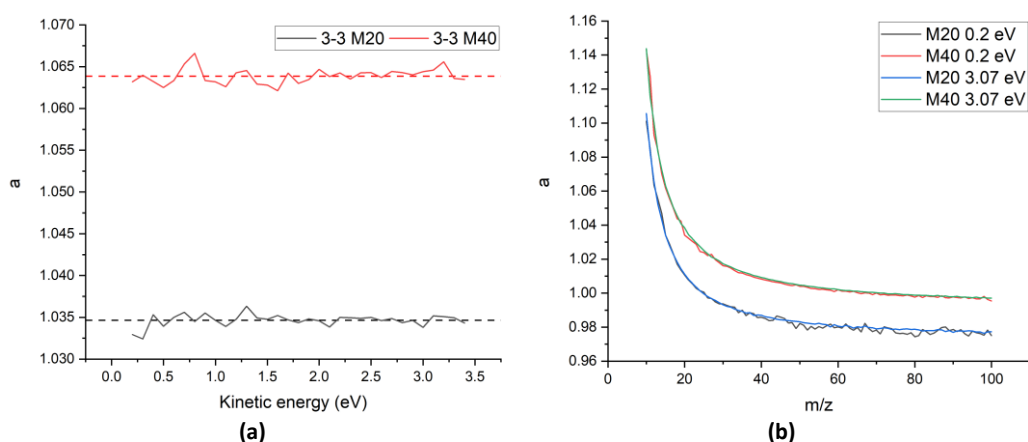
Figure 3.24: SIMION simulations of switched VMI of ions. (a) Variation of the ratio $a(m/z)$ with kinetic energy for m/z 15 with 3-3 M20 and 3-3 M40 voltage switching. (b) Variation of $a(m/z)$ with m/z for the kinetic energies 0.2 eV and 3.1 eV with 3-3 M20 and 3-3 M40 voltage switching.

3.3 False coincidences and detection efficiency

Doing coincidence experiments of photoionisation processes raises the issue of whether the coincidence events detected are true or false. This problem is made more complicated when considering multi-ionisation processes where varying numbers of charged particles may be detected and then more so again when considering the setup used here where only one electron per laser shot can be reliably detected. False coincidences are ubiquitous in coincidence experiments and there is treatment of them both in terms of minimising their original occurrence in the experiment [62] and in removing them from existing datasets [63]–[67]. They can arise from several causes, including high ionisation rates of the sample or secondary electrons emitted from the apparatus caused by scattered light. Their existence in coincidence data is entirely dependent on the limited detection efficiencies of the ions and electrons. If the detection efficiencies of either the electrons or ions were unity, any event containing more particles than should be possible for a single molecule under the ionisation scheme in question could be rejected from the analysis. However, with limited

detection efficiencies there is the chance that multiple molecules are ionised, and then some product fragments from each molecule are not detected, with the detected fragments from different molecules appearing to lead to a coincidence in the data.

There a several possibilities for what may lead to true or false events or coincidences in the data:

- A single molecule is ionised in a laser pulse, generating N_e electrons and N_i ions and all particles are detected in coincidence. This a true coincidence.
- A single molecule is ionised in a laser pulse, but the limited detection efficiency results in the loss of at least one particle. If the number of particles expected in the experiments is well known (e.g. in single ionisation) then the event can be rejected in the analysis. If there is some uncertainty in the number of particles to expect (e.g. a dication might dissociate or remain stable, or an ion might be either an intact monomer or a fragment from a cluster) then the event might not be discarded but assigned falsely.
- Multiple molecules are ionised in the laser pulse, leading to the detection of more particles than is possible for a single molecule ionisation. These events are rejected from the analysis.
- Multiple molecules are ionised in the laser pulse, but the limited detection efficiency leads to the appearance of the expected number of particles for ionisation of a single molecule. This event is included in the analysis as a false coincidence.

The most conceptually simple way to decrease their occurrence in an experiment is to lower the ionisation rate by either attenuating the laser power or the sample density. However, this may become unfeasible for certain experiments when considering the timescales required to obtain an appreciable signal.

False coincidence events have different characteristics for experiments where the ionisation source is pulsed or continuous. Many coincidence experiments are carried out at synchrotrons where the repetition rate of the photon source is far greater than the duty cycle of the detection method, so the synchrotron is considered to be quasi-continuous on this timescale. In continuous ionisation experiments, the trigger for recording the TOF of the cation cannot be easily linked to the ionisation source, so it is usually considered to be the detection of an electron, which has a much lower TOF that is almost instantaneous on the timescale of the ion TOF. An electron detection signal will trigger the opening of a timing window in which the detector can record ion arrivals. This leads to false coincidences in continuous experiments being largely independent of the TOF, and manifesting in the TOF spectrum as a constant background that might obscure weak signals [62]. When multiple ionisations take place in pulsed experiments, they do so almost at the same time during a given laser pulse. This results in the false coincidences being distributed in the TOF along with the true coincidences. In most cases in a pulsed experiment a given event cannot be designated true or false unless it violates known rules of the experiment. However, it might be possible in COLTRIMS experiments by applying momentum conservation to each particle in the coincidence [23], [24].

Methods for estimating the number of false coincidences in pulsed single ionisation PEPICO experiments have been made for stable [68] and noisy [69], [70] experimental conditions. The experimental stability was found to be much less influential on the false coincidence levels than the overall ionisation rate. Bayesian analysis methods have also been employed for removing false coincidences from pump-probe PEPICO data when subtracting pump- and probe-only background signals under both stable [63], [65] and noisy [64] conditions. Here the method from Stert *et al.* [68], which uses a magnetic bottle electron TOF spectrometer which can detect multiple electrons per laser shot, is modified to account for the limitations of the DLD in the case of single ionisation PEPICO coincidences. For double ionisation PEPICO, PIPICO and PEPIPICO coincidences, the extension of the model is given in Appendix B.

3.3.1 Single ionisation electron-ion coincidences

In an experiment with stable conditions and an average number of single ionisation events per laser shot $\bar{n}$, the probability $p(n)$ of singly ionising a number n of molecules in a laser pulse is described by a Poisson distribution:

$$p(n) = \frac{\bar{n}^n}{n!} e^{-\bar{n}}. \tag{3.43}$$

In n single ionisations, there are n photoelectrons and n photoions created. The probability $p_i(n,k)$ to successfully detect k photoions out of n is described by a binomial distribution

$$p_i(n,k) = \binom{n}{k} \xi_i^k (1-\xi_i)^{n-k}, \tag{3.44}$$

where ξ_i is the ion collection-detection efficiency and $0 < \xi_i < 1$, and $\binom{n}{k}$ is the binomial coefficient. When performing VMI of electrons with the DLD-VMI, all the electrons generated in an ionisation event will arrive at approximately the same time (within 1 ns). After detection of a particle, the DLD has a dead time of tens of nanoseconds and is therefore only capable of recording one particle when multiple arrive simultaneously. With the limitations of the DLD, even if multiple electrons are successfully "detected", only one will be recorded. The probability of recording one electron is therefore the probability of detecting any number of electrons that is not zero and the probability of recording more is negligible. The photoions are usually distributed over a larger range in time, so the instances where they might arrive simultaneously (e.g. if two ions have the same mass and momentum vector) are considered to be negligible here. Equation 3.44 is therefore rewritten for electrons as

$$p_e(n,k) = \begin{cases} \binom{n}{k} \xi_i^k (1-\xi_i)^{n-k}, & k = 0 \\ 1 - p_e(n,0), & k = 1 \\ 0, & k > 1 \end{cases}$$
$$= \begin{cases} (1-\xi_e)^n, & k = 0 \\ 1 - (1-\xi_e)^n, & k = 1 \\ 0, & k > 1 \end{cases} \tag{3.45}$$

where ξ_e is the electron collection-detection efficiency and $0 < \xi_e < 1$. The probability $p_{e(i)}(k)$ of detecting k particles (either electrons or ions) in a laser shot is

$$p_{e(i)}(k) = \sum_{n=0}^{\infty} p_{e(i)}(n,k)p(n) \tag{3.46}$$

The average number of particles $\omega_{e(i)}$ (either electrons or ions) detected per laser shot is:

$$\begin{aligned} \omega_{e(i)} &= \sum_{k=0}^{\infty} k \times p_{e(i)}(k) \\ &= \sum_{k=0}^{\infty} \left(k \times \sum_{n=0}^{\infty} p_{e(i)}(n,k)p(n) \right) \\ &= \sum_{n=0}^{\infty} \sum_{k=0}^{n} k p_{e(i)}(n,k)p(n) \end{aligned} \tag{3.47}$$

For electrons and ions this is

$$\omega_e = 1 - e^{-\xi_e \bar{n}},$$

3.48

$$\omega_i = \xi_i \bar{n}.$$

3.49

The electron-ion coincidence rate ω_{11} is the probability of detecting only one electron and one ion in a laser shot and is given by

$$\omega_{11} = \sum_{n=0}^{\infty} \left(1 - p_e(n, 0)\right) p_i(n, 1) p(n)$$
$$= \xi_i \bar{n} e^{-\xi_i \bar{n}} \left[1 - (1 - \xi_e) e^{-\xi_e(1 - \xi_i)\bar{n}}\right]$$

3.50

In a laser shot where n molecules are ionised the total number of possible coincidences N_{11} is the number of electrons multiplied by the number of ions (each of the n generated electrons has n ions available to correlate with):

$$N_{11} = n^2.$$

3.51

In this laser shot, each molecule ionised offers only one possible true coincidence, so the number of true coincidences $N_{11}^{(t)}$ is simply n:

$$N_{11}^{(t)} = n.$$

3.52

The true coincidence rate $\omega_{11}^{(t)}$ is therefore given by:

$$\omega_{11}^{(t)} = \sum_{n=0}^{\infty} \left(1 - p_e(n, 0)\right) p_i(n, 1) p(n) \times \frac{N_{11}^{(t)}}{N_{11}}$$
$$= \frac{\xi_i}{1 - \xi_i} e^{-\xi_i \bar{n}} \left[1 - e^{-\xi_e(1 - \xi_i)\bar{n}}\right]$$

3.53

ω_e, ω_i and ω_{11} can easily be measured in an experiment. It is not possible for a given coincidence in the dataset to be diagnosed as true or false, unless it violates certain rules known about the experiment (e.g. electron energetics, ion mass/element conservation). From these parameters, Equations 3.48, 3.49 and 3.50 form a system of three equations with three unknown variables ξ_e, ξ_i and $\bar{n}$ that can be determined and allows $\omega_{11}^{(t)}$ to be calculated. This method is compared with the original from Ref. [68] for example detection efficiencies of $\xi_e = 0.4$ and $\xi_i = 0.4$ (Figure 3.25). The total number of coincidences (true and false) is much higher for the DLD due to the increased probability of detecting a single electron using Equation 3.45. This is because Ref. [68] allows detection of multiple electrons, resulting in detection of higher-order coincidences that are then discarded. With the DLD, these potential higher-order coincidences are reduced to single-electron coincidences since only one electron can be registered. The chance for a coincidence to be rejected from DLD analysis for being too high-order therefore relies only on ion detection, while for Ref. [68] it depends on both electron and ion detection. Along with the limited ion detection efficiency, this increases the probability compared to Ref. [68] that for a given laser pulse with multiple ionisations, a single electron-ion coincidence will be registered. The disadvantage is that the false coincidence rate increases more rapidly with increasing $\bar{n}$ for the DLD, resulting in a lower fraction of coincidences which are true for the DLD.
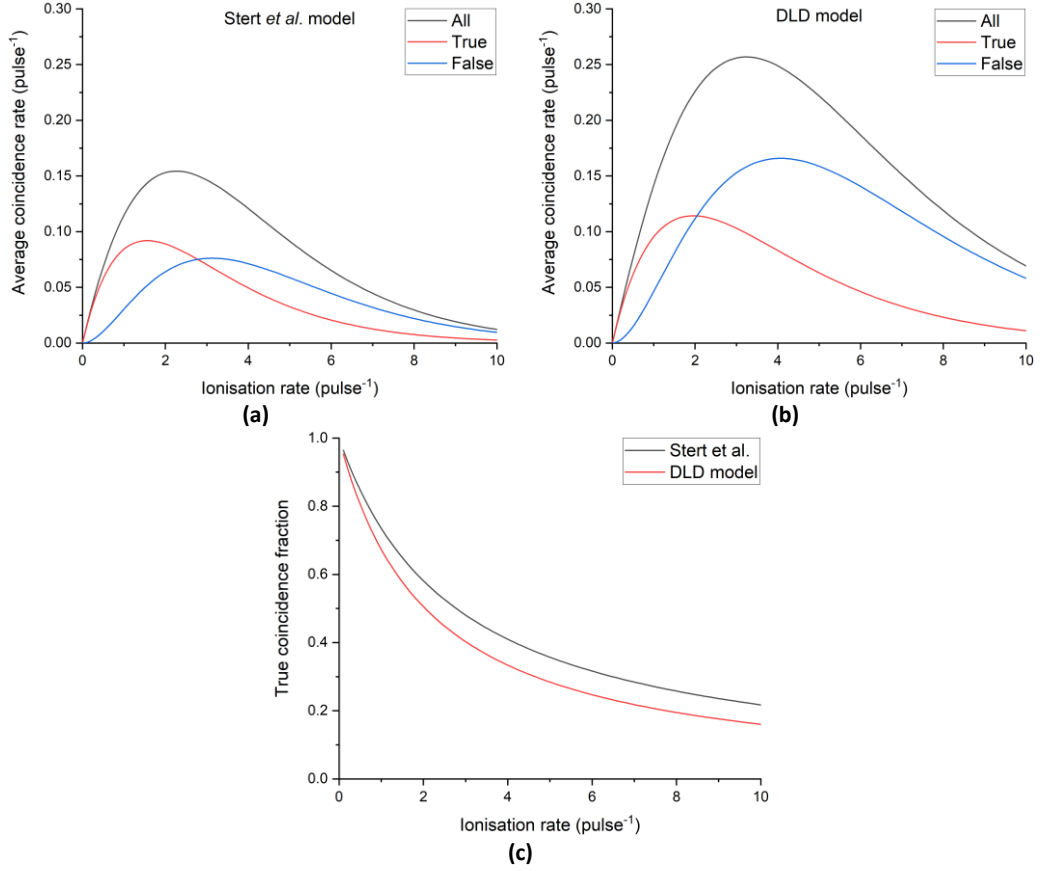
Figure 3.25: Coincidence rates as a function of the average ionisation rate for ξ_e = 0.4 and ξ_i = 0.4. (a) Total, true and false coincidences calculated using the method from Ref. [68]. (b) Total, true and false coincidences calculated for the DLD. (c) Comparison of the true coincidence fraction for each method.

3.3.2 Detection efficiency determination

The ion and electron detection efficiencies are important for determining false coincidence rates. They are also important for determining properties like total and partial ionisation cross-sections, which require knowledge of the numbers of particles being generated. If multiple ionisation events occur in a laser shot, a higher detection efficiency means that more particles are successfully detected and the event can be discarded for being too high-order. The system of equations described above allows determination of the electron and ion detection efficiencies. The total detection efficiency of the experiment is affected by the voltage switching factors as well as the MCP/DLD detection efficiencies. The MCP's ability to reliably detect a particle depends on the particle's longitudinal velocity. Additionally, lower voltage settings will reduce the velocity and therefore the efficiency. There is also the possibility to consider that ξ_e and ξ_i will have dependencies on E_k and m/z respectively. For ξ_e this is expected to only vary weakly: most of the electron's longitudinal velocity is gained from the electrode potentials. The detection efficiency should decrease only when the electrons are too fast to be steered on to the detector. For the ions there are two counteracting effects: the risk of losing light particles, at least if using harsh switching conditions, and the increased longitudinal velocities those light particles will have relative to the heavier ones on detection. The analysis gives the ion detection efficiency as an average over all the m/z values observed in the experiment. The model derived in the previous section is tested to try to determine the detection efficiency for electrons and ions under each voltage setting, so that false coincidences might be estimated in further datasets. The dataset used is the $M92$ dataset with the IR laser for the sample mixture described in Section 3.1.1.1. Figure 3.26 (a)

shows the repeller electrode settings of each data acquisition and (b) shows the measured count rates taken directly from the raw data. The electron count rate appears constant and is therefore independent of the repeller voltage within the ranges used. This is due to the electrons being light enough to easily have sufficient velocity to be detected. The ion count rate decreases with the repeller voltage. The electron-ion coincidence rate decreases in accordance with the reduced ion count. The results of the model are shown in (c) and (d). The ion detection efficiency decreases in agreement with its observed count rate, however the electron detection efficiency also decreases, despite the measured count rate being approximately constant across scans. Additionally, the ionisation rate appears to increase with each consecutive scan, again contrary to the observed count rates. The true coincidence fraction also increases with the ionisation rate which is completely contrary to the models shown in Figure 3.25 as well as how false coincidences generally work. This suggests that the model derived for the DLD does not work. This may be due to a misconception on how the DLD handles the simultaneous arrival of electrons, or it may be that the total detection efficiency is a convolution of that of the chevron stack MCP plates and the delay line anode itself. Otherwise the cause is not known.
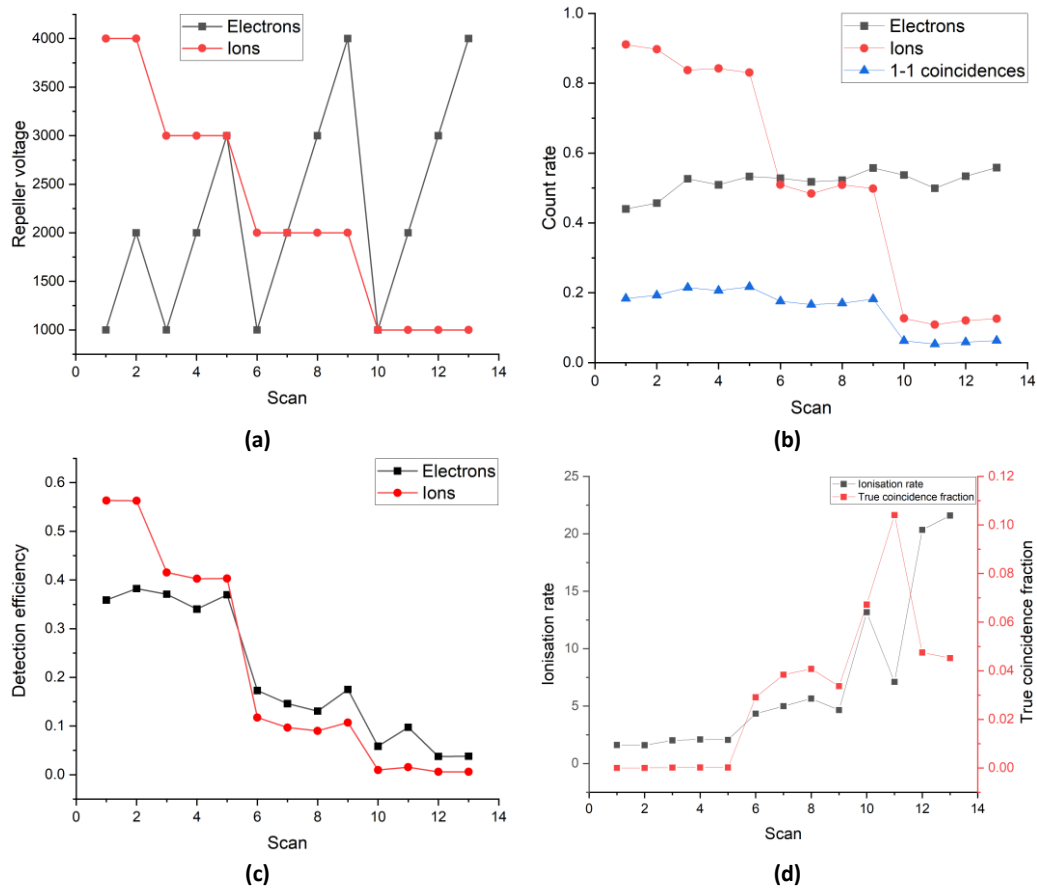
Figure 3.26: Analysis of the false coincidence model for various $M92$ data acquisitions acquired with the IR laser. (a) Repeller voltage for electrons and ions set for each data acquisition scan e.g. Scan 1 is 1-4 $M92$ switching. (b) Recorded count rate per laser shot for electrons, ions and PEPICO coincidences. (c) Calculated electron and ion detection efficiency. (d) Calculated ionisation rate and true coincidence fraction.

In light of this spectacular failure, a vastly simplified model that does not take into account whether the coincidences are true or not is used to try to acquire a rough estimate of the detection efficiency [12]. In a single ionisation experiment, there are n ionisations, leading to n photoelectrons and n photoions being created. If the detection efficiency is less than unity then only ω_e photoelectrons and ω_i photoions will be detected, so that the electron detection efficiency $\xi_e = \omega_e/n$ and the ion detection efficiency is $\xi_i = \omega_i/n$.

An electron and a partnering ion must both be detected to register a coincidence. The probability of detecting a coincidence ξ_c is therefore $\xi_c = \xi_e \xi_i$ and the number of coincidences ω_{11} recorded in an experiment is

$$\omega_{11} = n\xi_e\xi_i = \frac{\omega_e\omega_i}{n}.$$

3.54

The electron detection efficiency can therefore be expressed as:

$$\xi_e = \frac{\omega_e}{n} = \frac{\left(\frac{\omega_e\omega_i}{n}\right)}{\omega_i} = \frac{\text{No. of coincidences}}{\text{No. of single ions}}.$$

3.55

Likewise, the ion detection efficiency is

$$\xi_i = \frac{\omega_i}{n} = \frac{\left(\frac{\omega_e\omega_i}{n}\right)}{\omega_e} = \frac{\text{No. of coincidences}}{\text{No. of single electrons}}.$$

3.56

The electron and ion detection efficiencies can then be estimated by simply counting the number of electrons, ions and electron-ion coincidences in an experiment. This is possible in a general case even if there is more than one ionisation per shot. ω_{11} will simply equal the lower value of ω_e and ω_i. Only results from certain laser shots are considered: those that yield only one electron, only one ion or only one electron-ion coincidence. The results are shown for the same $M92$ datasets from the previous section (Figure 3.27).
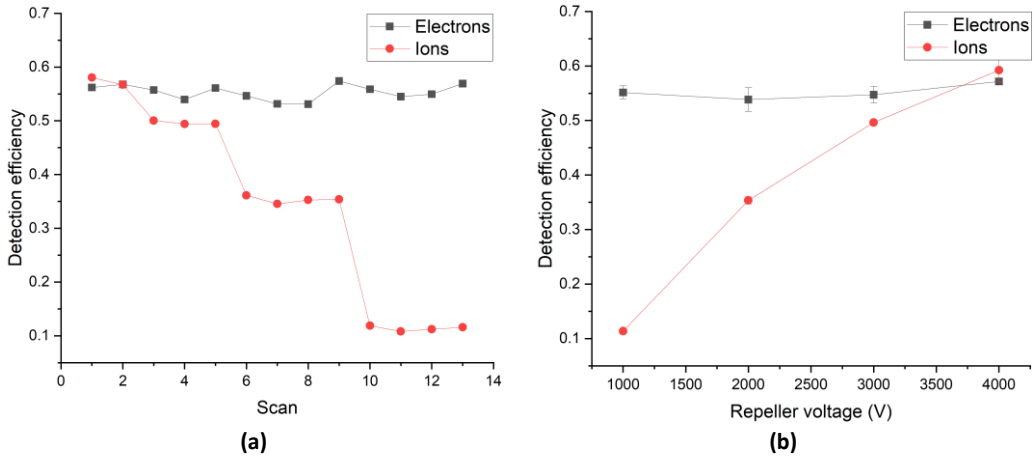
Figure 3.27: Estimated detection efficiencies of the DLD-VMI (a) Varying with each data acquisition scan as in Figure 3.26. (b) Averaged for each repeller voltage value.

The results are an average of multiple $M92$ switching experiments. The x-axis in Figure 3.27 (b) denotes the repeller voltage used for the scans of which the electron and ion efficiencies are shown, but the electron and ion results should be decoupled from each other when observing trends with repeller voltage. For example, the data point for electrons at V_R= 1000 V is an average for the electrons of every $M92$ dataset that used V_R = 1000 V for the electrons and does not mean that it is only from a 1-1 switching experiment. It should therefore not be considered in correlation with the ion data point at V_R = 1000 V. The electron detection efficiency is almost independent of V_R at approximately 55% due to their light mass. The ion efficiency increases with V_R from very low values up to approximately the same value as the electron detection efficiency. The analysis involved was limited by the DLD abilities, but if one considers that this would not be in place, more electrons would be detected, resulting in a higher electron detection efficiency. However, these results would not show in the subset used for the analysis as adding a second electron to a given laser shot

that already has an electron detected would invalidate it from the analysis for being a higher-order coincidence, and adding a first electron to a laser shot without any electrons would imply it had failed to be detected due to the limited MCP efficiency and not the DLD's inability to detect multiple electrons per shot. If one were to consider the other laser shots that were excluded from the calculation for having too many ions present: adding the second "phantom" electron would increase the number of electrons recorded as well as the number of coincidences recorded. However, the number of electrons would increase at a faster rate. Additionally, the number of ions would stay the same, therefore by Equations 3.55 and 3.56, the analysis curves suggest that this is a lower bound efficiency for the detected electrons and an upper bound efficiency for the ion.

3.3.3 False coincidence subtraction from coincidence time-of-flight spectra

False coincidences can be subtracted from coincidence TOF spectra with pulsed-ionisation sources using a method [35], [49], [50], [67] that is similar to one for continuous sources [71]. A coincidence TOF "pairs" spectrum has signal intensity corresponding to coincidences between TOFs T_1 and T_2 given by $P(t_1, t_2)$. The number of false coincidences between these TOFs is $F(t_1, t_2)$. The number of true coincidences between these TOFs $C(t_1, t_2)$ is

$$C(t_1, t_2) = P(t_1, t_2) - F(t_1, t_2). \hspace{2cm} 3.57$$

The false coincidences can be determined by considering that for an uncorrelated ion with TOF t_1, the probability of the second uncorrelated ion having TOF t_2 is given by the signal variation of uncorrelated ions over the whole dataset: the so-called "singles" spectrum S. S is a TOF spectrum with the same histogram bin widths as P of TOF values of ions from events where there is only one ion detected. $F(t_1, t_2)$ is therefore calculated as

$$F(t_1, t_2) = \alpha S(t_1)S(t_2), \hspace{2cm} 3.58$$

where α is a normalisation constant. An autocorrelation matrix of the singles spectrum can be found by $S \times S^T$ which will give the $S(t_1)S(t_2)$ values at all points in the spectrum. An example is shown for a coincidence TOF spectrum of 2-propanol ionised at 33.3 eV recorded with 3-electrode static voltages at $V_R =$ 3000 V (Figure 3.28). As discussed in Chapter 5, 33.3 eV is can doubly-ionise 2-propanol, which means the coincident TOF spectrum will have both true and false coincidences. α can be determined by finding a peak $P\left(t_1^{(f)}, t_2^{(f)}\right)$ in the pairs spectrum that is known to only contain false coincidences, such that $C\left(t_1^{(f)}, t_2^{(f)}\right) = 0$ and

$$\alpha = \frac{P\left(t_1^{(f)}, t_2^{(f)}\right)}{S\left(t_1^{(f)}\right)S\left(t_2^{(f)}\right)} \hspace{2cm} 3.59$$

α is then the ratio of the peak intensity in the pairs spectrum and the autocorrelation matrix. Suitable false coincidence peaks $\left(t_1^{(f)}, t_2^{(f)}\right)$ are those involving background gas ions or fragment pairs that would break mass/element conservation. In (Figure 3.28), α is found from a coincidence between the helium carrier gas at 2315 ns and the $C_2H_5O^+$ ion fragment at 5415 ns, the two most intense peaks in S, which gives $\alpha = 9.20 \times 10^{-9}$ counts^{-1}. The initial and corrected coincidence TOF spectra are shown (Figure 3.29). The difference can be seen in the absence of multiple "round" peaks from the true spectrum compared to the

total spectrum (around 5000 - 5500 ns on the y-axis). These are false as peaks in coincidence TOF spectra are normally short diagonal lines from Coulomb explosions or long tails from metastable fragmentations, as discussed previously. The colour scale is significantly reduced in the true spectrum due to the absence of the very intense He^+-$C_2H_5O^+$ peak.

(a)

(b)
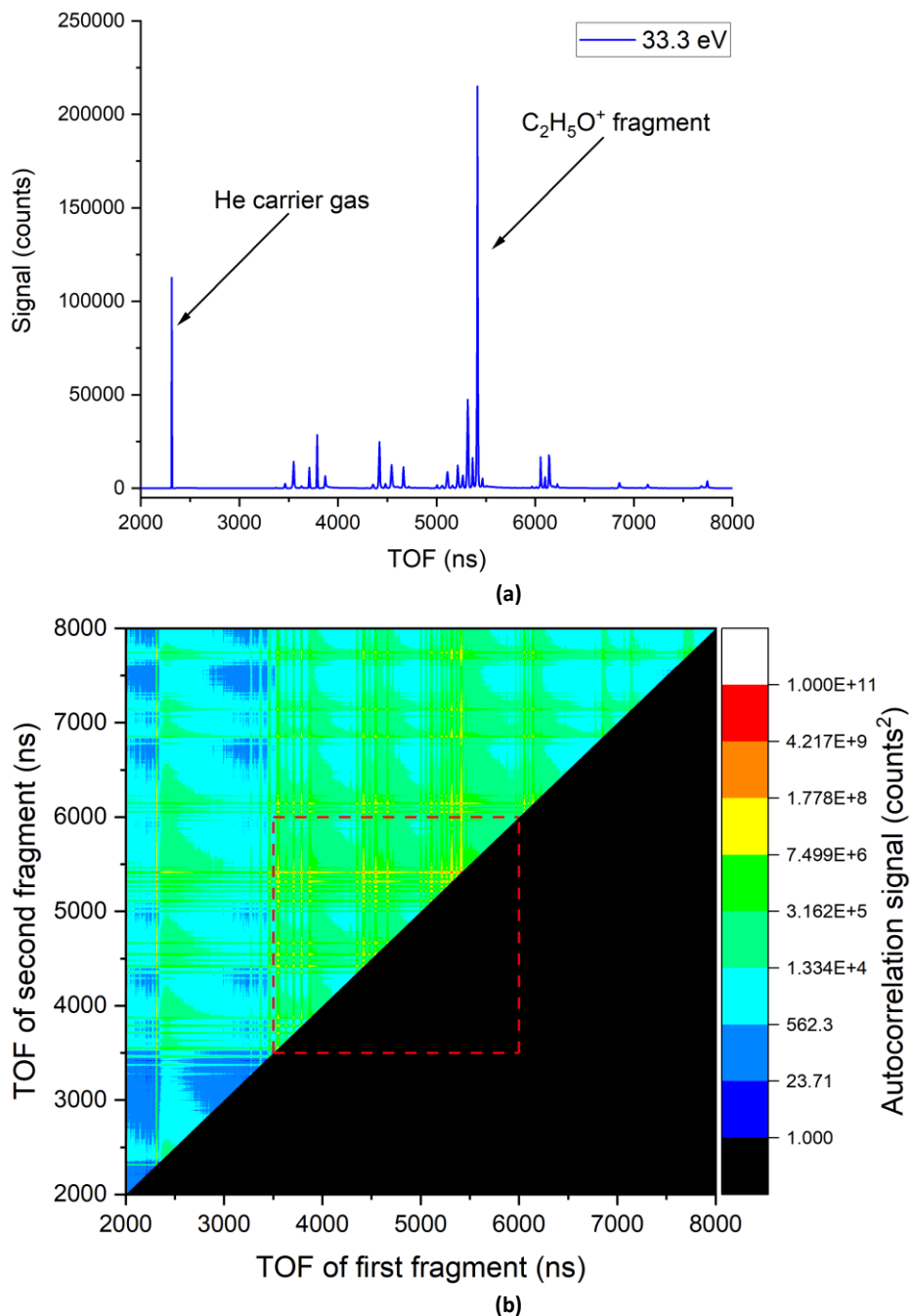
Figure 3.28: (a) Singles TOF spectrum of 2-propanol ionised at 33.3 eV. (b) Autocorrelation matrix of the singles spectrum with a logarithmic colour scale, obtained by the matrix multiplication $S \times S^T$. The area outlined in red is the region of interested highlighted in Figure 3.29.

(a)

(b)
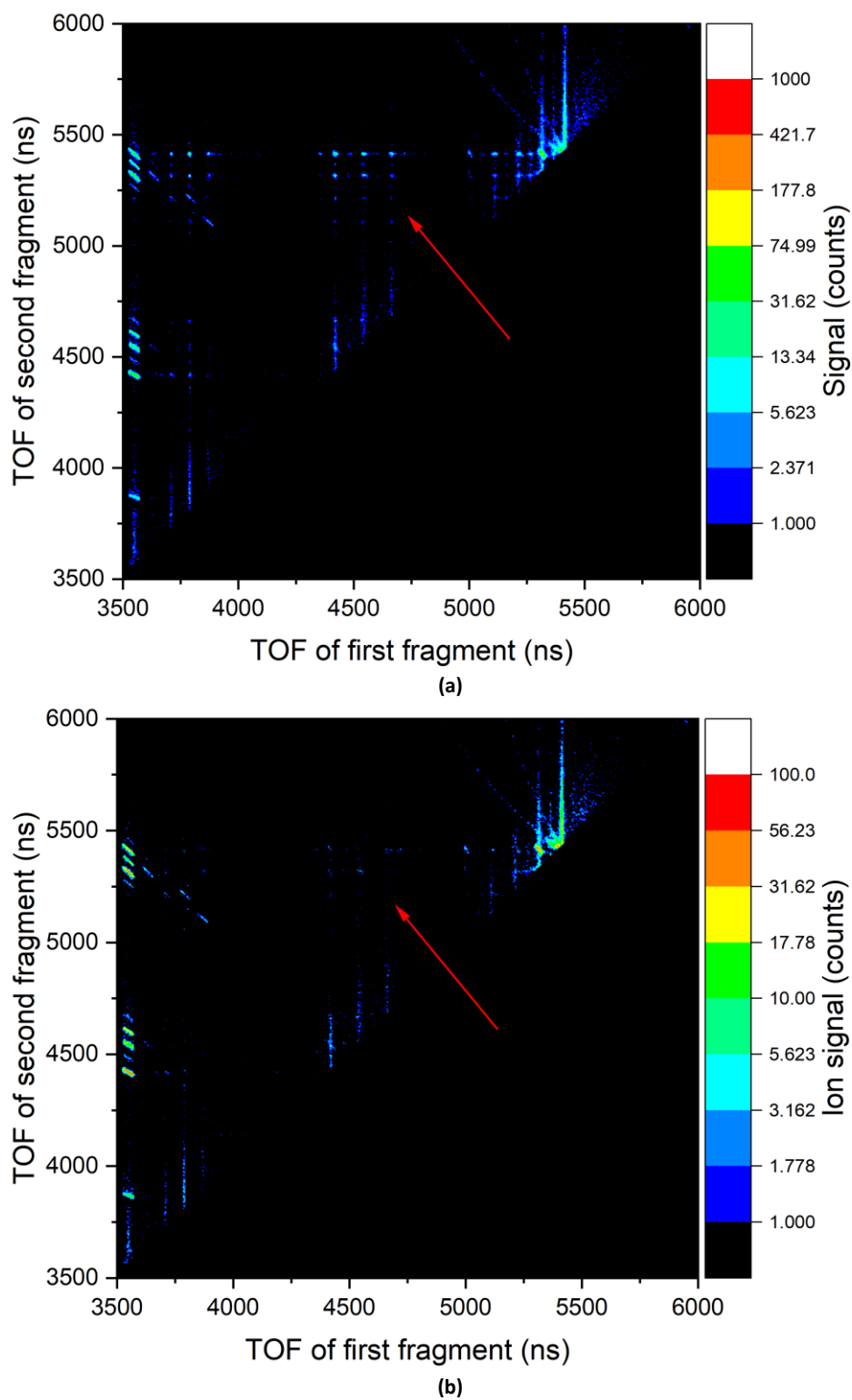
Figure 3.29: (a) Total coincidence TOF "pairs" spectrum P. (b) Pairs spectrum C after having false coincidences subtracted. Red arrows point to false coincidences that were successfully subtracted.

3.4 Summary and performance evaluation

This chapter details attempts to model the behaviour of the TOF-MS and VMI features of the constructed endstation, along with simulations and experiments to calibrate the endstation and characterise its performance in terms of resolution and operating ranges. These have been detailed for the endstation both under static voltage conditions, where the electrode potentials are held constant to image either electrons or ions, and switched voltage conditions, where the electrode potentials are switched between positive and negative values to image both electrons and ions together.

The TOF-MS has been found to have TOF resolutions up to approximately 2000 in both switched and static modes. This means the resolution in m/z is approximately 1000, allowing separation of adjacent units up to this value. It is unclear if this would be sufficient for experiments on large clusters or nanodroplets as initially planned. If controlling the size of the clusters, the degree of fine control over the number of units may be unclear, although the difference of a single mass unit is less likely to be important for larger solvent clusters, particularly when the cluster unit monomers have mass significantly larger than 1 amu e.g. if using water as a solvent cluster. It may be an issue identifying a particular molecular fragment if it is detected while still bonded to a large cluster fragment. However, this is deemed sufficient for any experiments done here using the current molecular beam source, which would be focused on small polyatomic molecules and their clusters. A model was constructed to attempt to model the relationship between TOF, m/z and voltage settings for switched voltage conditions, however the complexity of the resulting expression rendered it unusable. The standard Wiley-McLaren relation used for the static voltage conditions was found to be a suitable approximation for the switched conditions, at least for the m/z ranges sampled. A model was also constructed to attempt to model the relationship between fragment TOF and the lifetime of metastable parent ions. The simplifications in representing the electric field of the setup meant that derived lifetimes were not accurate when comparing the model to SIMION simulations, but the metastable signature traces in coincident TOF spectra were well reproduced. In the case of metastable monocation parents that dissociate to a singly-charged fragment and a neutral fragment, it is possible to use the model to isolate these particular coincidences in the dataset for analysis.

The spatial resolution of the VMI is optimally approximately 150 µm for the photoions in the molecular beam under static voltage conditions. Under switched voltage conditions, it is closer to 250-300 µm for ion-favourable conditions such as 4-1 or 3-3 switching. This can vary greatly if using harsh conditions for the photoions such as 4-1 switching. Retention of molecular ions appears reliable for m/z values at least as low as 12 when switching voltages that are optimised for low masses. Although this becomes more questionable for m/z values in the range up to 18 when using harsh switching conditions that are optimised for higher m/z values such as 4-1 $M92$ switching. Significant loss of temporal and spatial resolution also begins to occur for the lower m/z values under these conditions. This could potentially create problems if one were to try to record fast electrons in coincidence with light ions. However, this does not appear to be an issue if using 4-1 $M18$ switching. Therefore, it is proposed that if one were to do such an experiment, then optimising the ion voltages as low as possible is key to recovering them. This works in conjunction with also improving their spatial and TOF resolutions. If there is a large range of m/z values of interest in the experiment, multiple scans can be done with the ion voltages optimised for different subsections of the total region of interest.

In the HHG calibration experiments, the electron kinetic energy resolution may be limited by the photon energy resolution of the HHG source itself. Although the DLD-VMI resolution is about twice as bad as the CCD-VMI, this might be due to broadening effects in the detector itself. Potential causes of broadening in the DLD-VMI could be improperly chosen CFD parameters, or an effect from magnetic fields from the turbomolecular pumps on the electrons emitted from the back of the MCP stack before the impact on the DLD anode. The native kinetic energy resolution of the instrument is therefore not known. The DLD-VMI is capable of creating photoelectron spectra in coincidence with specific masses, which may result in cleaner spectra, however the CCD-VMI could also be used to recorded higher resolution spectra if necessary. The CCD-VMI also has the advantage of not needing to have the photoelectron VMI images recircularised. In an experiment, it is possible that both detectors may need to be used in a complementary fashion to maximise available information from

the data. The setup is therefore sufficiently energy-resolved for any experiments using the HHG either in single-photon or pump-probe experiments, but it is unknown whether the resolution would be sufficient for any experiments requiring higher resolution e.g. for resolving vibrational bands if one were to perform experiments with nanosecond lasers. A possible experiment to determine the resolution to a higher degree of accuracy is to photoionise xenon atoms and clusters using a 400 nm ATI scheme by frequency doubling the output of the Ti:sapphire fs laser. However, this experiment was unable to take place in the current time frame.

VMI of ions using the switching mode can be done for an experiment provided one is also done under the same molecular conditions (molecular beam parameters, photon energy) using static voltages to calibrate the process. There is a different calibration constant when using switching voltages from static voltages even if the ion repeller has the same potential. The calibration constant is found to depend on the kinetic energy, but has been approximated as constant here. There may be minor shifts in kinetic energy when using this simplified calibration, however these ion distributions are likely to be broad and the shifts relatively minor in importance. In such cases where they are important, the images recorded with static conditions should be used for accurate determination of kinetic energies and the images recorded with switched voltages can simply be used for additional filtering of coincident photoelectrons if necessary.

Much of the behaviour of the TOF and spatial resolutions as a function of m/z is different between the SIMION simulations and the experimental reality. Reasons for this may be poor physical construction or conditions of the VMI system causing it to be geometrically different from the nominal design; the SIMION simulations failing to account for some real-life physical effect in the experiment or the experimental ionisation region not being well-placed in the centre of the VMI setup. An additional cause may be that the molecular beam also produces higher order clusters of 2-propanol and toluene which may fragment. This means the "native" molecular beam species may have their signals significantly broadened by fragmentations from larger clusters. How this affects or causes the specific trends observed here is unclear. An in-depth ion-ion coincidence analysis involving the clusters was not performed here but could potentially reveal the causes and represents a future proposal of evaluating the instrument's performance. It may also be possible to improve upon the data shown by using molecular beam conditions that would not produce clusters, such as examining each featured chemical species individually rather than all together in the beam. This was not performed here due to the time-intensiveness of changing the molecular beam source and re-recording spectra for each species.

A model was constructed to attempt to calculate the relationship between ionisation rate, detection efficiency and false coincidence count for the DLD-VMI, given its limitation of only being able to detect one electron per laser shot. However, this model was not successful in giving physically meaningful results. A vastly simplified model was used and the absolute collection-detection efficiencies were estimated to be approximately 55% for photoelectrons and to reach a maximum of 60% for photoions when the repeller voltages is maxed at 4000 V. The analysis has some limitations due to the DLDs inability to detect multiple electrons in an event, so the figures can only be considered upper estimates. The detection efficiency is an important factor in determining the level of false coincidences in an experiment. False coincidence subtraction can be achieved for the coincident TOF spectra by using the established method of subtracting an autocorrelation matrix of the TOF of single-ion events that has been normalised. The normalisation factor is found by comparing intensities of peaks in both spectra that is known to be entirely composed of false coincidences. This method is shown to be successful in removing many false coincidences from coincident TOF data.

4 Extreme-ultraviolet photoionisation of toluene

4.1 Introduction

The ionosphere of Saturn's largest moon Titan contains many hydrocarbons C_mH_n with masses of at least 100 amu. The routes of formation of some of the heavier ions have been hypothesised to take place through reactions of smaller dications $C_mH_n^{2+}$ with the major atmospheric component methane, resulting in growth of the larger hydrocarbons [72]. Toluene (C_7H_8, methyl benzene) is a common precursor to several of these proposed dication starting reagents. Electron impact ionisation of toluene produces a series of dications $C_7H_n^{2+}$ (where n = 3 − 8) [73] corresponding to hydrogen loss. This has led to the reactive chemistry of the toluene dication being extensively studied through mass spectrometric methods [72]–[76].

Toluene is also commonly used as a calibration species for charge stripping (CS) mass spectrometry. CS is a method for determining the energetics of gas-phase multi-ionised cations where a mass-selected ion is accelerated to high kinetic energies (several keV) to impact on a stationary gas target, causing collisional ionisation before it is detected.

$$A^{n+} \rightarrow A^{(n+1)+} + e^-$$

<div align="right">4.1</div>
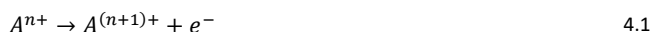
The product ion is detected with a lower kinetic energy than the incident kinetic energy, having lost some in the collision process. The vertical ionisation potential is then derived from the difference between incident and final kinetic energy. Toluene forms a stable (or metastable at higher energies) dication. The m/z value of the singly-charged cation is 92 and the dication is 46. No singly-charged ion fragment of toluene has same the m/z value as that of the dication meaning DPI can be clearly identified in a mass spectrum. The singly-charged ion is also highly abundant. These factors contribute to toluene being an ideal system as a calibration standard for the kinetic energy scale in CS, where the single and double ionisation energies were typically taken to be 8.81(3) eV [77] and 24.5(2) eV [78] respectively. The appearance potential of the $C_7H_8^{2+}$ dication using EI ionisation was determined taken to be the DIP for calibration purposes. Appearance energies of ionisation products are typically found by scanning the incident electron or photon energy and measuring the yield. Above the threshold there is often a region of linear increase in signal with excess energy which is then extrapolated to the intercept to determine the appearance potential. This was found to be incorrect in the case of toluene, because appreciable signal was observed at lower photon energies in synchrotron studies [79], [80] that could not be accounted for by the instrumental resolution or thermal population. Taking this into account along with calculating Franck-Condon factors for the transition between the neutral and lowest-lying dicationic states, the DIP was refined to 23.62(10) eV. Toluene is therefore a good example of the dangers of the common method of estimating DIPs based on fragment appearance energies from electron impact ionisation.

In initially revising the DIP, the mechanism of DPI was initially assumed to be direct. The initial assignment was based on the linear increase of dication signal with photon energy around the threshold, an indicator of good agreement with the Wannier law for direct DPI (Equation 1.4) [18], [20]. However, the Wannier law has only been verified for a few many-electron systems and later photoelectron-photoelectron measurements found that there is a substantial (indirect) autoionisation contribution [81]. This was determined in the PEPECO spectrum (Figure 4.1), where strong coincidence signals were observed between an electron at approximately 1 eV and an electron with kinetic energy directly dependent on the photon energy. The

electrons with photon energy-dependent kinetic energies are primary photoelectrons corresponding to single ionisation from a C 2s inner-valence orbital leading to population of a superexcited state of the monocation. This state lies approximately 1 eV above three low-lying dication electronic states ($^1A'$, $^3A''$ and $^1A''$) to which it then autoionises, leading to ejection of the second electron whose kinetic energy is independent of the photon energy [81]. This method also confirmed the revision of the DIP to 23.6 eV and highlights the relevance of the PEPECO technique in examining DPI mechanisms.

In this chapter the photoionisation of toluene at XUV energies around the DIP is explored as an initial test and commissioning of the CIS endstation coupled to Harmonium for a molecular sample using coincidence operation. It is also to test the feasibility of using the endstation and HHG for DPI experiments. This is done by comparing the results for photoelectron-photoion coincidences and photoion-photoion coincidences to existing literature. Toluene was chosen for this test because its high vapour pressure means it is easy to concentrate into a molecular beam and its ionisation dynamics at high ionising energies have been well studied previously [82]–[85].
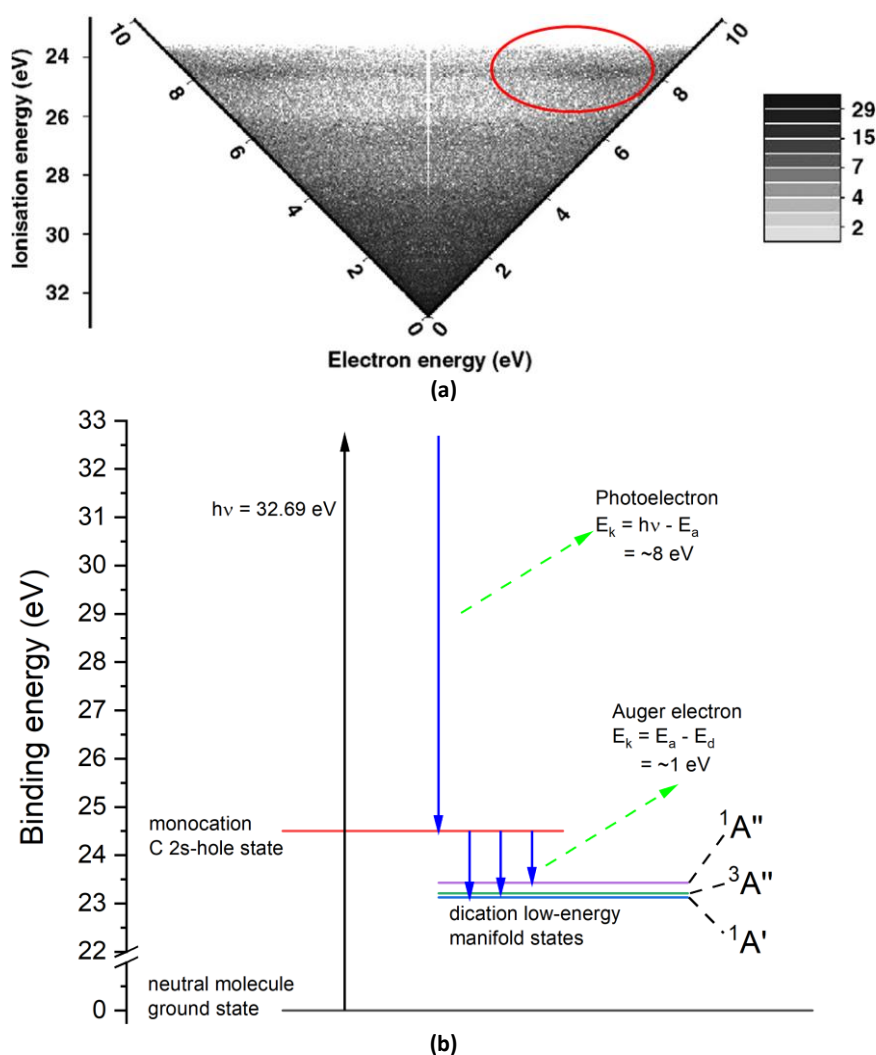
Figure 4.1: (a) PEPECO spectrum of toluene at 32.69 eV photon energy showing the autoionisation peak at the kinetic energies ~1 eV and (32.69 – DIP – 1) ≈ 8 eV in the red circle. Reproduced from [81]. (b) Energy-state diagram illustrating the autoionisation mechanism at this photon energy. The states are very broad in energy, so derived electron kinetic energies are approximate.

4.2 Experimental

Toluene was heated in the source chamber reservoir to approximately 45°C, giving a vapour pressure of approximately 0.1 bar [86]. Helium backing gas at approximately 1.7 bar so that the resulting molecular beam composition was approximately 6% toluene. The molecular beam was crossed in the detection chamber by the HHG beam at photon energies between 23 eV and 35 eV at 6000 s^{-1} repetition rate. The photon flux is approximately 2 x 10^8 pulse^{-1} [27] using the 200 gr mm^{-1} density grating on the time-preserving monochromator, giving an expected FWHM energy resolution of 0.5 – 0.6 eV (Figure 2.11) [27]. Various coincidence imaging datasets were recorded using the DLD-VMI, typically using either 4-2 M92 focusing or 4-2 M4 focusing. DLD-VMI acquisitions were typically 8 - 12 hours long. Electron and ion images were Abel inverted and calibrated for kinetic energy and TOF spectra were calibrated using a linear relationship between the TOF and $\sqrt{m/z}$. Both used constants determined from a unique fit for each dataset. Photoelectron spectra of the entire gas-phase ensemble were recorded on the CCD-VMI with 4-electrode static voltages at V_R = 4000 V – 6000 V. The CCD-VMI acquisitions were typically 30 - 60 minutes long. The ionisation rate was estimated to be approximately 14%. Air leaking into the HHG beamline meant that there was a lot of nitrogen and oxygen ions in the TOFs and their photoelectrons in the dataset.

Electron images obtained with the DLD VMI (Figure 4.2) contained artefacts borne from a DLD issue and the switching processes that produced ringing on the detector. These artefacts are horizontal and vertical stripes of low intensity across the image and might cause slight intensity discrepancies in photoelectron spectra. These defects were only fixed after this experiment and prior to the 2-propanol experiment (Chapter 5).
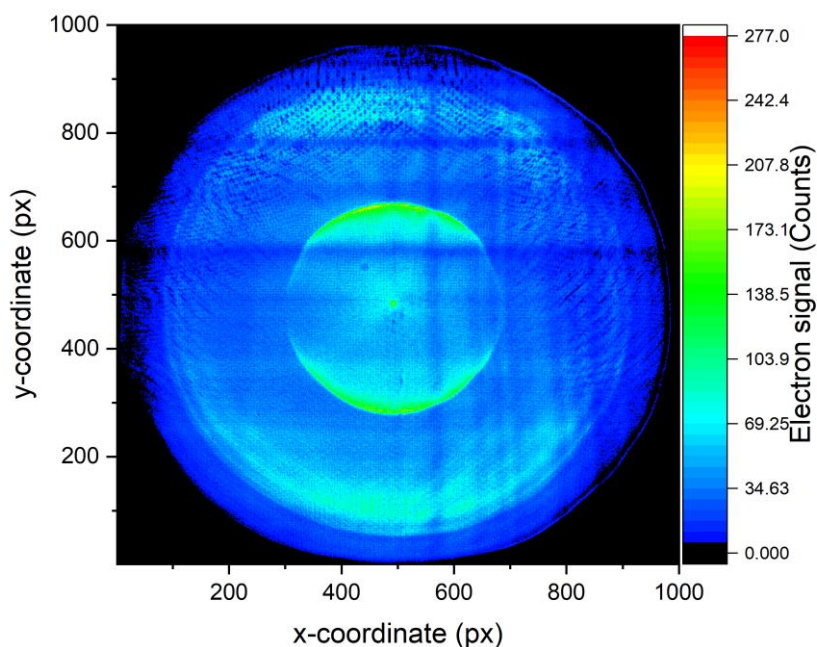
Figure 4.2: Velocity-map image of all photoelectrons from toluene molecular beam ensemble at 27.2 eV photon energy recorded on the DLD-VMI. The strongest ring is photoelectrons ionised from the helium carrier gas. The two strong signals at larger radius are photoelectrons from background nitrogen and oxygen.

The photoelectron circularisation method (Section 3.2.2.1) was not quantified until the later beamtime on 2-propanol (Chapter 5). In the meantime, arcing incidents meant that the electrode setup had to be disassembled, repaired and reassembled which might have led to small changes in the electrode geometry or alignment and the relative laser pointing. This might cause different deformations on the photoelectron

images. The circularisation method is tested for the electron images (Figure 4.4) at photon energies 23.9 eV, 27.2eV and 30.5 eV using the 3-electrode, V_R = 4000 V constants (Appendix C). The polar-coordinate images show the angular and radial variation of the electron peaks. The centre was the high-intensity spot in the middle of the Cartesian image (Figure 4.2). At 27.2 eV and 30.5 eV the peak from helium photoionisation can be seen at lower radius, while peaks at higher radius are from toluene and the background gases. θ is the anticlockwise angle with the positive Cartesian x-coordinate. The uncorrected images show deformations where the signal at 0 - 180° is at a larger radius than at 180 - 360°. The effect is greater at 90° and 270° and increases at larger radii. Circularisation partially corrects this, although it remains prominent. The procedure appears to overcompensate the correction slightly for the signals at 180 - 360°, which are now slightly further from the centre than those at 0 - 180° although higher-frequency distortions are significantly reduced.
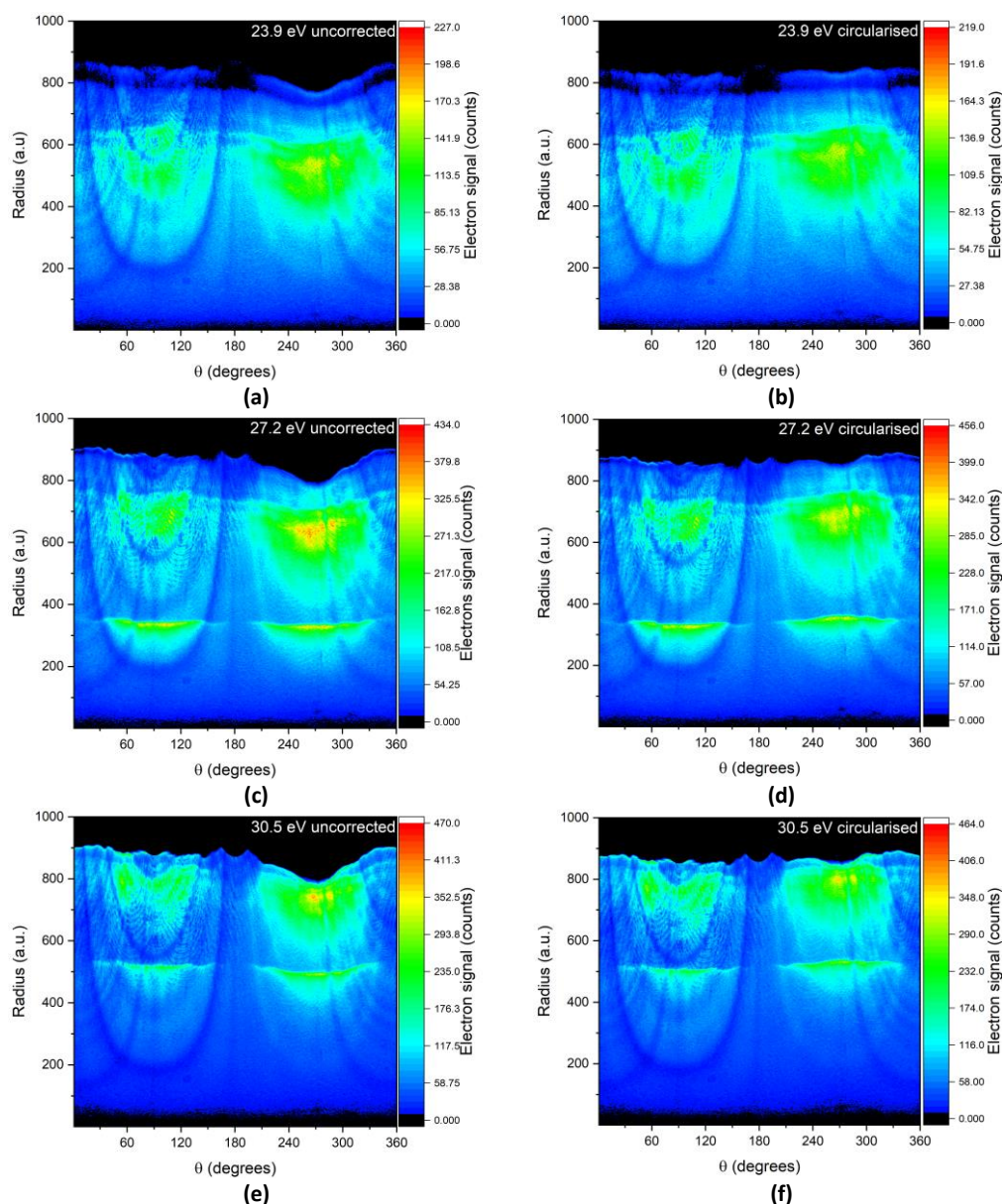
Figure 4.3: Polar coordinate images of all photoelectrons from the molecular beam ensemble. (Left column) raw uncorrected images, (right column) images after attempted circularisation. Image recorded at photon energies 23.9 eV ((a) and (b)), 27.2 eV ((c) and (d)) and 30.5 eV ((e) and (f).

89

The effect of the circularisation on the photoelectron spectra is explored (Figure 4.4). At higher kinetic energies (detected at larger radii) the resolution is unambiguously improved, with the valence structure of toluene becoming more resolved upon circularisation. At short radii the effect is more ambiguous. At 27.2 eV photon energy the helium peak at 2.6 eV kinetic energy becomes slightly broader after circularising. This appears to be due to the overcompensation of the procedure as the polar plots in Figure 4.3 (c) and (d) show that the left (0 - 180°) signal band at approximately 350 px is slightly further from the centre than the right (180 - 360°) signal band before recircularisation and that they effectively switch places after recircularisation. At 30.5 eV photon energy the deformations are extreme enough that the helium peak at 6 eV kinetic energy appears almost as a doublet due to the poor radial overlap of the two halves of polar coordinate spectrum. This is improved slightly on circularising. The circularisation method is therefore judged to improve the resolution of the spectra overall and is employed for electron analysis in this chapter. The slight broadening of the helium peak in Figure 4.4 is negligible compared to the broad featureless signals from DPI that are observed at low kinetic energy later, but may add some uncertainty to any determined values. The deviations here therefore suggest that the exact nature of the deformations described in Section 3.2.2.1 come from the flight path of the electrons through the TOF, rather than any problem with the detector itself. If the defects came from the DLD, they would likely remain consistent through different experiments. However, it is possible that dismounting and remounting changes certain properties of the DLD.
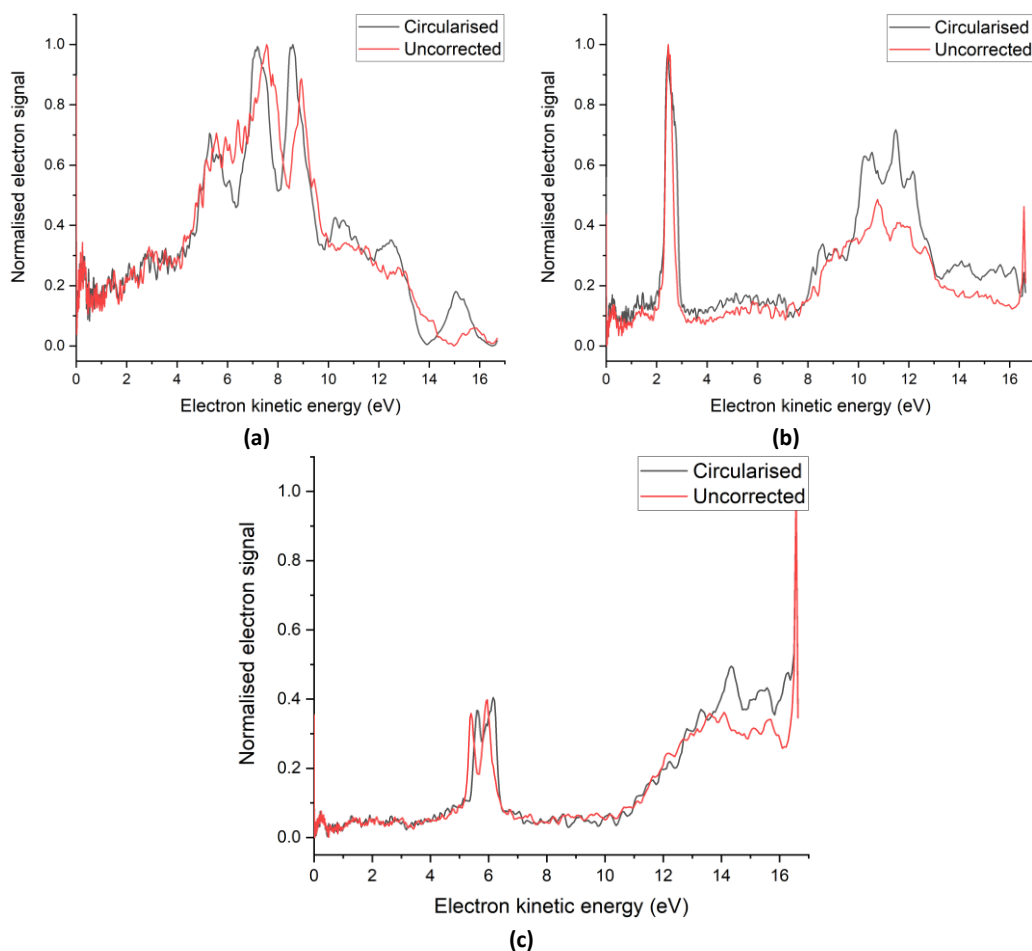
Figure 4.4: Circularised and uncorrected kinetic energy spectra on the DLD obtained at 23.9 eV (a), 27.2 eV (b) and 30.5 eV (c) photon energies

During this beamtime an improper switching technique was used where the Behlke switches were connected in series to a single output of the delay generator with unnecessarily long cables in between (over 10 ns). This results in the electrode voltages being switched in series sequentially rather than simultaneously and may produce additional broadening in the ion TOF or VMI data. The effect is likely more pronounced for lighter ions, although the analysis of such lighter ions is obscured by large amounts of background gas caused by the beamline air leak. Ions originating from background gases in the chamber, N^+, O^+, OH^+, H_2O^+, N_2^+ and O_2^+ are observed in the TOFs (Figure 4.5) as extremely broad (almost 1 m/z unit wide) "doublet" peaks, where there is a second peak at a lower m/z value and large amounts of signal in between. This distorted peak is attributed to the switching effect on the background gases, as the HHG laser can ionise these species all along the beam path, instead of just in the VMI centre. Peaks in this region belonging to toluene fragments are at m/z 15 (CH_3^+) and m/z 27 ($C_2H_3^+$). The m/z 27 peak is comparatively unaffected by these distortions, despite the m/z 28 peak suffering greatly. The effect is therefore more pronounced for the background gases. For the m/z 15 it is a bit more difficult to gauge as the peak is broadened due to fast CH_3^+ ions arising from Coulomb explosion of the toluene dication [81] and it is located in between two large background-gas peaks, of which the N^+ peak might be obscuring its "doublet" structure. The relative intensities of the summed O^+/O_2^+ signals are approximately 27% of the summed N^+/N_2^+ signal, corresponding to the ratio in air.
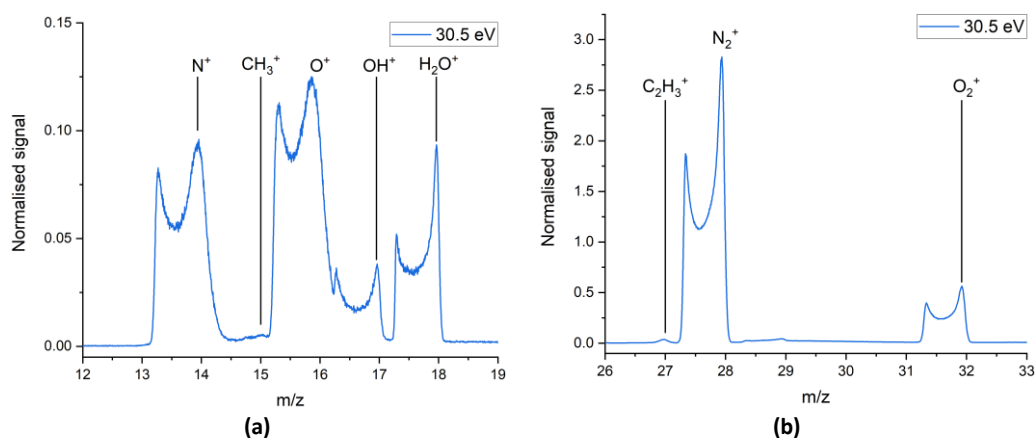
Figure 4.5: Mass spectrum peaks of some toluene fragments alongside ions from background gases in the chamber. Recorded at 30.5 eV photon energy.

4.3 Results and discussion

4.3.1 Electron-ion coincidences: toluene photoelectron spectrum and background gases

The uncorrelated photoelectron spectrum of the entire molecular beam ensemble recorded on the CCD-VMI is shown (Figure 4.6) at 34.0 eV photon energy as well as spectra from literature obtained at 21.2 eV [87]. At a quick glance it appears that the valence structure is approximately reproduced from the literature spectrum, although several significant intensity variations exist that can be due to overlap of photoelectrons from the N_2 and O_2 background gases. Additionally, the literature spectrum shows a clear structure of peaks above 18 eV binding energy that is washed out as a featureless background in the CCD-VMI spectrum. The CCD-VMI spectrum is shown because it does not require recircularisation and can image higher kinetic energy electrons than the DLD-VMI in coincidence mode.
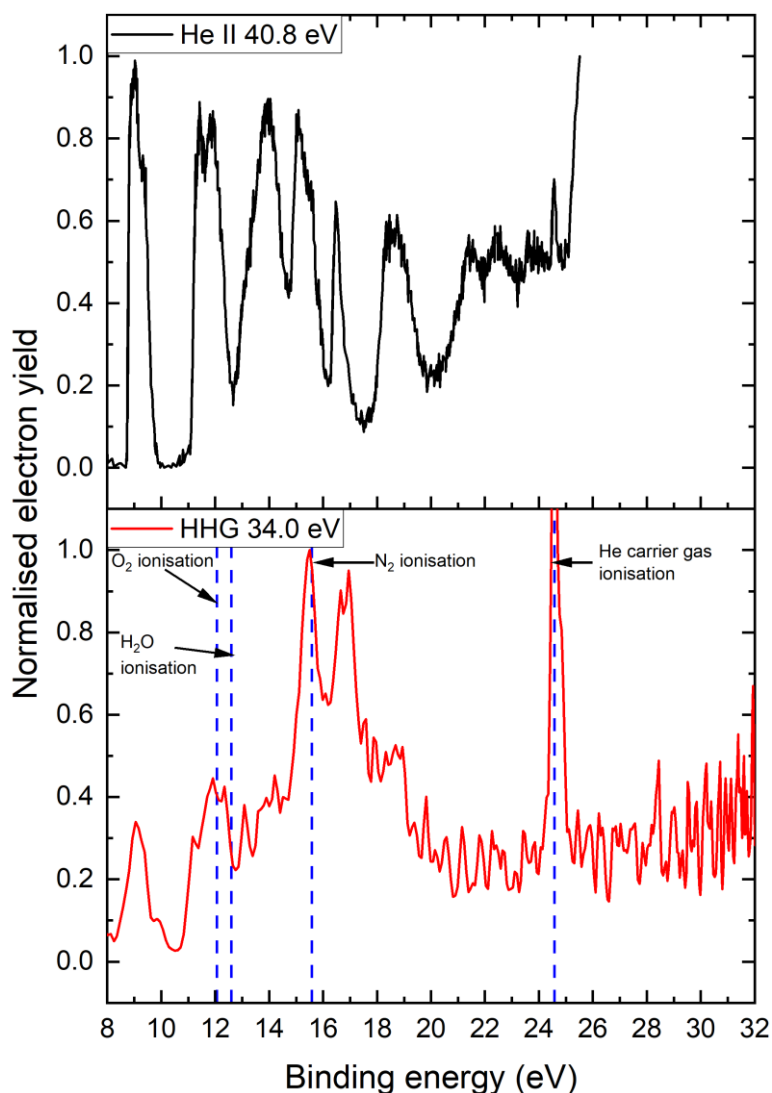
Figure 4.6: Photoelectron spectrum of toluene from ionisation with He II radiation at 40.8 eV photon energy (black) [87] and the HHG experiment at 34.0 eV photon energy (red) on the CCD-VMI.

The mass spectrum of toluene ionised at 30.5 eV photon energy is shown (Figure 4.7). As mentioned previously, nitrogen (m/z 28) and oxygen (m/z 32) are present in the mass spectra as background gases from a leak in the HHG beamline. There is also the presence of atomic oxygen ions (m/z 16), water (m/z 18) as well as atomic nitrogen ions (m/z = 14) at the higher photon energies where a pre-dissociative state of the molecular cation is populated [88],. Apart from the background gas impurities, the spectrum is largely in good agreement with literature results, particularly of photoionisation studies performed at similar photon energies [79], [89]. Compared to electron impact spectra at higher energies [90], there are a few fragments missing, primarily belonging to C_nH^+ fragments such as m/z 49 C_4H^+ and m/z 73 C_6H^+ which are already very weak in electron impact spectra. The toluene monomer $C_7H_8^+$ peak is present at m/z 92 (Figure 4.10 (a)). The strongest peak in the spectrum (excluding background gases) is the dehydrogenated monomer $C_7H_7^+$. For each fragment containing n carbons, there are multiple peaks corresponding to loss of varying numbers of hydrogen atoms. For many of the peaks, but most prominently for the parent ion, there are also peaks corresponding to the ^{13}C isotopologue.
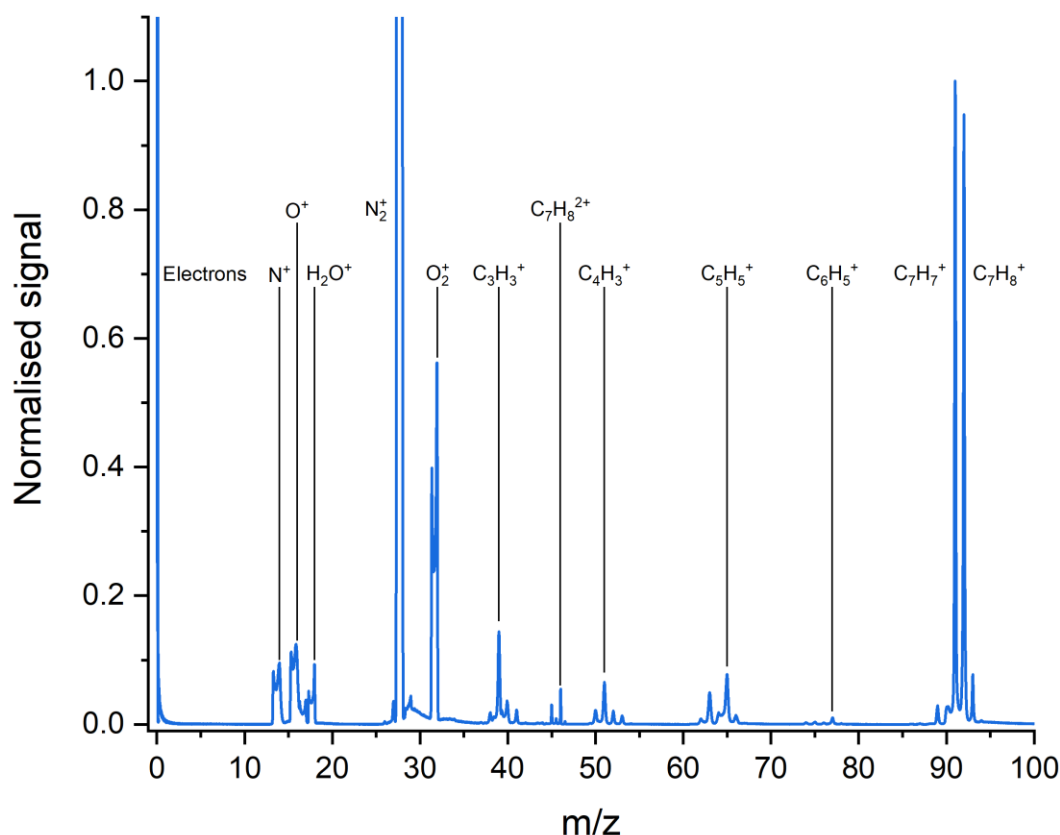
Figure 4.7: Mass spectrum of toluene recorded with 4-2 $M92$ focusing conditions at 30.5 eV photon energy. Relevant ion fragments are marked with labels. The spectrum is normalised on the $C_7H_7^+$ peak ($m/z = 91$), which is the strongest peak in the toluene spectrum at these photon energies. The spectrum also includes electrons that are detected prior to the voltage switching on the electrodes.

The discrepancies between the CCD-VMI and experimental photoelectron spectra are further investigated using the coincidence functionality of the DLD-VMI. Photoelectrons are recorded in coincidence with the various background gases and their spectra shown (Figure 4.8). The peaks are assigned based on previous photoelectrons studies of water [91], nitrogen [88], [92] and oxygen [93] with which they are in agreement, although are present at much lower resolution. This is likely due to broadening effects due to them being a background gas and not a molecular beam species, such as Doppler broadening and ionisation occurring away from the VMI centre. The nature of the experiment also reduces the resolution compared to the literature, many of which are rotationally resolved studies. At higher binding energies it can be seen that the electronic states populated lead to dissociation of the parent ion, as the peaks are now in coincidence with the fragment ion. There are also electronic states present with significant intensities other than the ground ionic states marked in Figure 4.6 which overlap with many of the other photoelectron peaks. The photoelectrons are also investigated in coincidence with the toluene ions and fragments. The peaks of $C_7H_7^+$ and $C_7H_8^+$, the most intense peaks belonging to toluene are both investigated as well the photoelectrons of all the fragments from m/z 37 to m/z 92 (Figure 4.9).
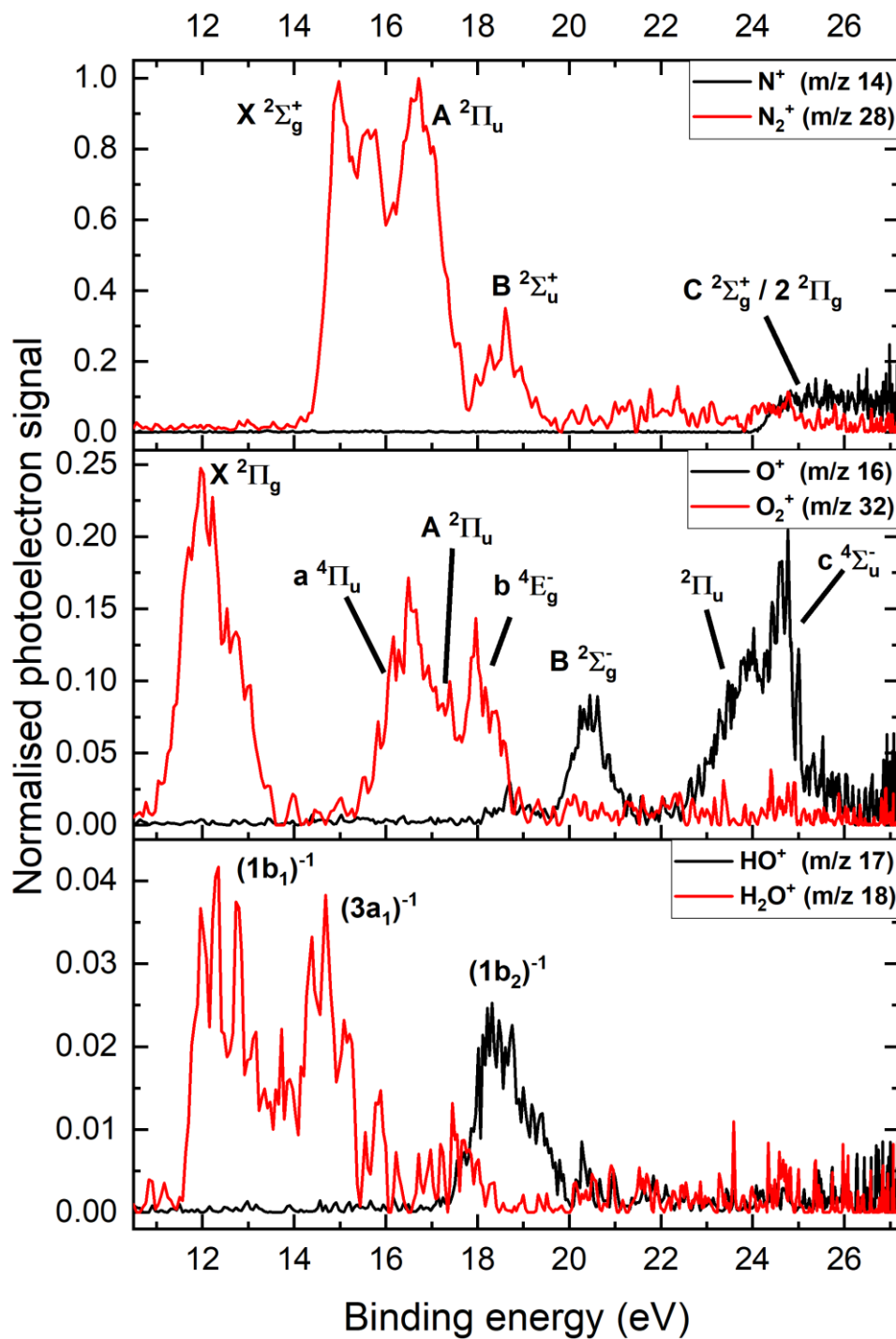
Figure 4.8: PEPICO photoelectron spectra of the various background gases present in the chamber. Recorded at 27.2 eV. All spectra are normalised against the N_2^+ peak. Refer to Figure 4.5 for the corresponding mass spectrometry peaks. The photoelectrons are selected in coincidence only with the right-most "peak" of the doublet structure, as this part corresponds to the region closest to the VMI centre.
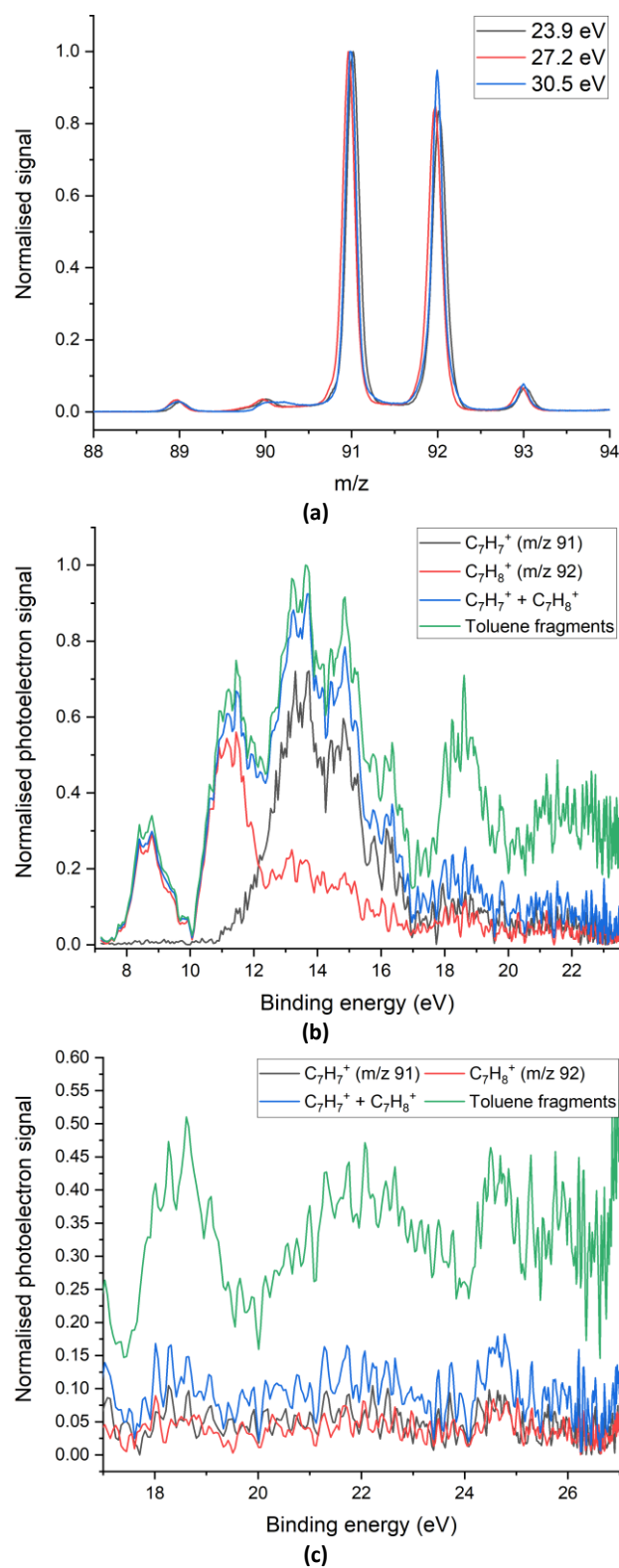
Figure 4.9: (a) MS peaks of the toluene parent ion (m/z 92), base peak $C_7H_7^+$ (m/z 91) and further dehydrogenated species. (b) Photoelectron spectrum of toluene at 23.9 eV. (c) Photoelectron spectrum at 27.2 eV. "Toluene fragments" corresponds to all fragments between m/z 37 and m/z 92.

The outer-valence photoelectron spectra show that population of the electron state at 13-14 eV results in significant deprotonation of the parent ion to form $C_7H_7^+$. This is seen from the decrease of the $C_7H_8^+$ signal and increase of the $C_7H_7^+$ at these binding energies. Population of the higher states above 18 eV results in more extensive dissociation to form many of the smaller fragments, which can be seen as the signal from both ions decreases against the total signal from all of the toluene fragments. This agrees with literature photoionisation mass spectrometry (PIMS) studies where many of the smaller fragments appear in the mass spectrum at higher photon energies [89], [94]. Many of the outer-valence peaks are better resolved after removing the background gas, however there are still different relative intensities compared to the literature spectrum, which may be due to different photoionisation cross sections for each peak. The relative intensities of the outer-valence peaks to literature spectra recorded at lower photon energies [82], [95]. Additionally, after removal of the background gas, some of the inner-valence peaks present in the literature spectrum that were hidden by background in the CCD-VMI spectrum become better resolved.

4.3.2 Electron-ion coincidences: double photoionisation of the toluene monomer

DPI of toluene is observed by the presence of the dication $C_7H_8^{2+}$ (m/z 46) in the mass spectrum at 27.2 eV photon energy (Figure 4.10). There is also a peak at m/z 46.5 which is attributed to the ^{13}C isotopologue. A peak at m/z 45 amu is attributed to H_2 loss of the dication $C_7H_6^{2+}$. Between the m/z 46 and m/z 45 peaks there is a region of increased background signal in the TOF. This is a signature of metastable decay of $C_7H_8^{2+}$ to $C_7H_6^{2+}$ [84], [96]. The m/z 45.5 peak can be a combination of the ^{13}C isotopologue $^{13}CC_6H_6^{2+}$ as well as the dication $C_7H_7^{2+}$ [73]. At 27.2 eV the intensity corresponds simply to that of the ^{13}C isotopologue (Table 4.1). However, on increasing the photon energy to 30.5 eV the relative intensity of this signal grows, suggesting formation of a new species which is likely to be $C_7H_7^{2+}$ [73].
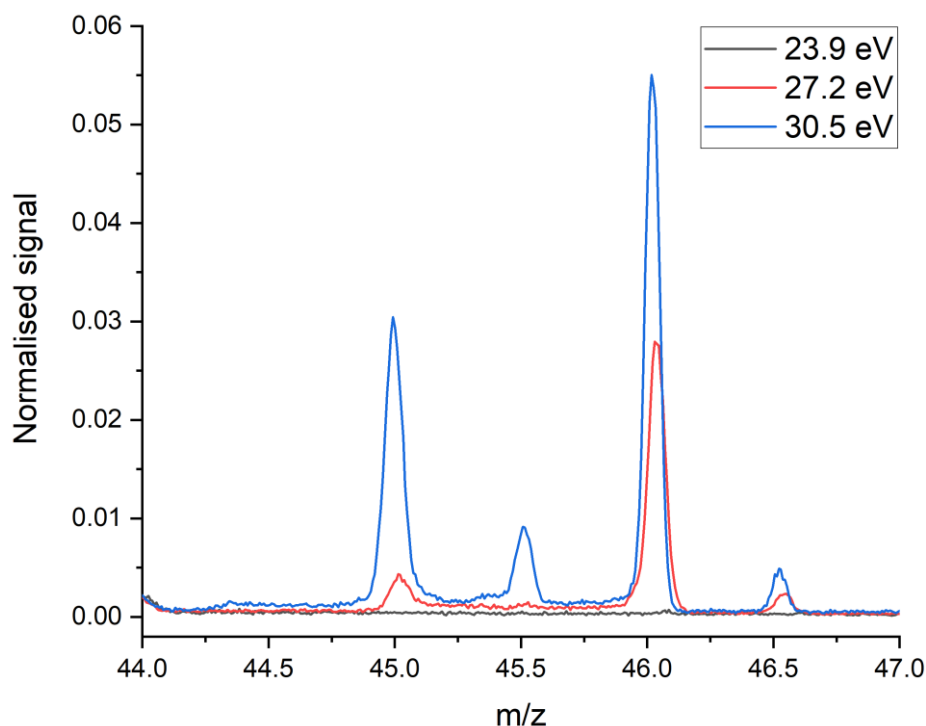
Figure 4.10: Mass spectrum of toluene monocations (a) and dications (b) along with ^{13}C isotopologues and fragments corresponding to hydrogen loss.

Peak (m/z)	Intensity ratio		
	$h\nu$ = 23.9 eV	$h\nu$ = 27.2 eV	$h\nu$ = 30.5 eV
45.5/45	-	7.4%	24.1%
46.5/46	-	6.9%	7.6%
93/92	7.8%	7.9%	7.5%

Table 4.1: Ratios of peak intensities at different photon energies. The ratio expected for the ^{13}C isotopologue of the parent ion is 7.6%
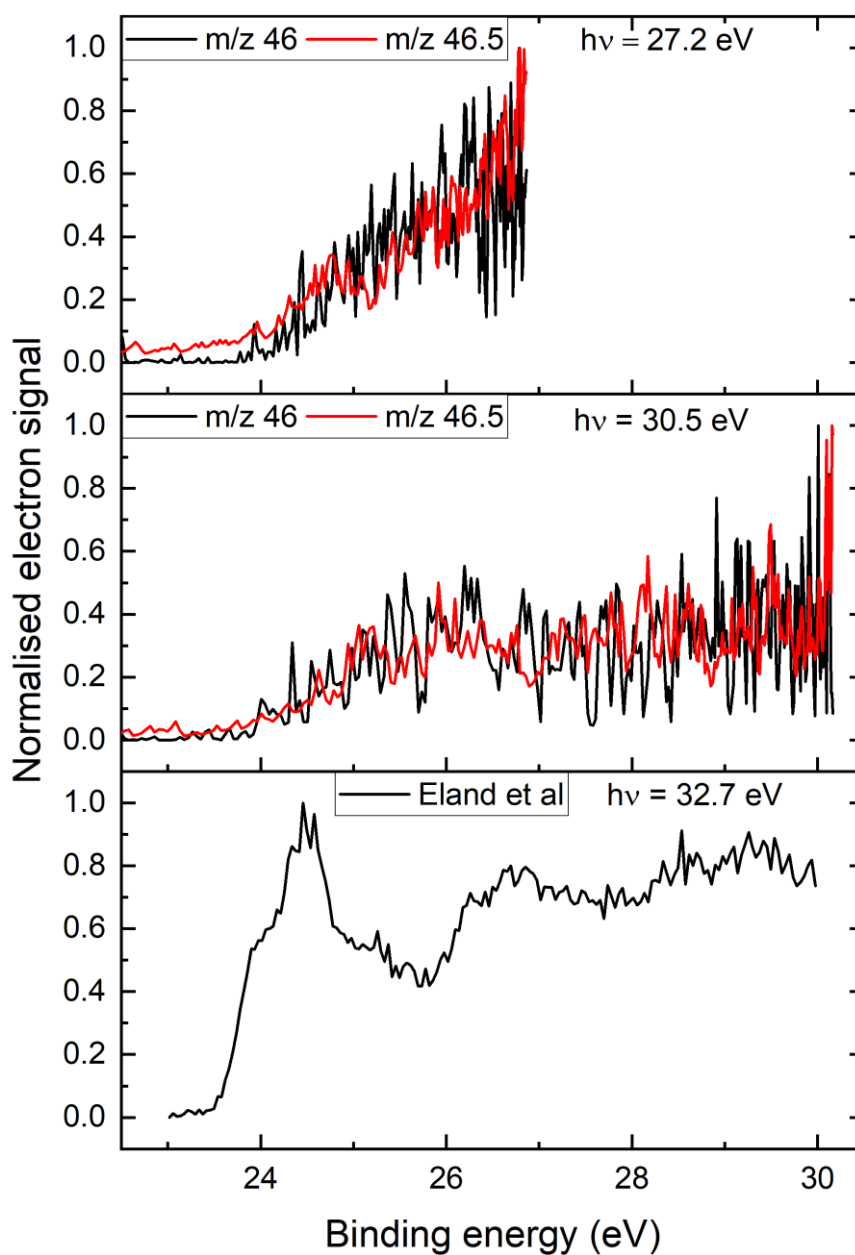
Figure 4.11: Partial DPI spectra of the toluene dications $C_7H_8^{2+}$ (m/z = 46) and $^{13}CC_6H_8^{2+}$ (m/z = 46.5), compared with the complete DPI spectrum from literature [19].

The partial DPI spectra, where only one of the electrons emitted per DPI event are recorded, for toluene (Figure 4.11) are compared to a complete DPI spectrum from literature PEPECO experiments [81]. The signal onset is at approximately 23.8 eV, in good agreement with the synchrotron studies [80] but slightly higher than was derived from PEPECO [81]. The ^{13}C isotopologue has a very similar spectrum to that of the main dication peak. The spectrum structure is also considerably more featureless than that from PEPECO, which shows the existence of several populated dication states. These deviations may be because the electron spectra recorded here include only one of the two emitted electrons, making them partial instead of complete DPI spectra. Additionally, if an Auger electron is present then $E_b = h\nu - E_k$ will not give a correct binding energy E_b. The true value of E_b would be calculated by [19]:

$$E_b = h\nu - \left(E_k^{(1)} + E_k^{(2)} \right),$$
$$\qquad\qquad\qquad\qquad\qquad\qquad\qquad\qquad\qquad\qquad\qquad\qquad 4.2$$

where $h\nu$ is the photon energy, and $E_k^{(1)}$ and $E_k^{(2)}$ are the kinetic energies of each electron in eV. This means binding energy values obtained from the partial DPI spectra are upper limits because the undetected electron must have $E_k \geq 0$ eV. They may still be accurate if the electron energy-sharing distribution is such that the fastest electrons (corresponding to lowest binding energies) are correlated with threshold electrons that have almost zero kinetic energy. This energy sharing is mainly seen for direct DPI mechanisms such as knock-out or shake-off, where the distributions tend to be continuous and concave. Indirect mechanisms such as Auger-Meitner decay via core-hole states, where the electron kinetic energies are discrete, are not likely to share such a distribution and the spectra would be inaccurate. However, these distributions are possible for Auger-Meitner decays from inner valence states, such as those based on C 2s [19], which is the case for toluene.

The partial DPI spectra of the species corresponding to hydrogen loss of the dication are shown (Figure 4.12). The onset of the photoelectron signal from $C_7H_6^{2+}$ is slightly below 26 eV, which is consistent with appearance potentials [84]. Loss of H_2 from $C_7H_8^{2+}$ is found to most favourably happen from the doubly-charged cycloheptatriene isomer, for which there is a 0.51 eV barrier to formation from the toluene dication, and the $C_7H_6^{2+}$ ion lies approximately 1.22 eV higher in energy than the toluene dication [83]. There is a manifold of electronic states approximately 2 eV above the lowest-lying dication electronic states [80], and population of these is required to overcome the barrier. The onset of the $C_7H_7^{2+}$ photoelectron signal also begins at approximately 26 eV despite there being no appreciable signal at these photon energies, however the extent to which this is genuine signal instead of background noise is questionable as it may contain contributions from the ^{13}C isotopologue $^{13}CC_6H_6^{2+}$ of the m/z 45 signal. The singly-charged cation $C_7H_7^+$ typically rearranges to either a benzyl cation or tropylium ion [97]–[99] and it is possible that something similar happens for the corresponding dication $C_7H_7^{2+}$ which merits further investigation.
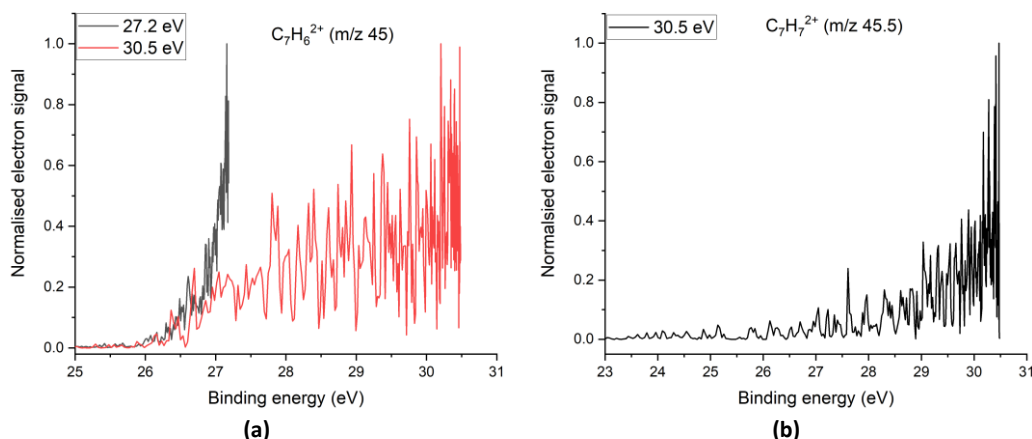
Figure 4.12: Partial DPI spectra of $C_7H_6^{2+}$ (a) and $C_7H_7^{2+}$ (b).

4.3.3 Coincidence time-of-flight spectra

The coincidence TOF spectrum recorded with 4-2 M92 settings at 30.5 eV is shown (Figure 4.13). There are several prominent features present in the spectrum. A number of diagonal peaks corresponding to Coulomb-exploding ion pairs of the toluene monomer are identified, as well as one from a cluster. Many of the monomer peaks (Table 4.2) are also present in literature [81], however some of the weaker signals are missing here. Additionally, two peaks have been observed featuring ^{13}C isotopologues. Analysis of the peak gradients is distorted by the fact that the dataset is acquired for a switching experiment and made worse by the improper switching technique described previously. The trajectories of ions propelled upwards from the Coulomb explosion are distorted differently from those propelled downwards. This is most prominent for light ions in pairs such as CH_3^+ + $C_6H_5^+$. The two fragments correspond to direct fragmentation of a monomer with no loss of a neutral: a "two-body" peak. The gradient should therefore be -1 (Section 3.1.3.2), however the measured value is -0.637(7) and the peak shape is clearly composed of two different parts, where the gradients are different on either side of the central coordinate (Figure 4.14). The effect is also observed to a lesser degree for many of the other "two-body" peaks for which the gradient should be -1, but is instead closer to -0.9. There is also a Coulomb explosion peak attributed to a tetramer cluster dication fragmenting into two singly-charged dimers, one of which decays further to a singly-charged monomer. The heavier weight of the clusters means that they are less affected by voltage-switching distortions and the measured gradient is more likely to be accurate. The gradient of this peak is interesting as it suggests the primary contribution of signal to this peak is that of a tetramer parent instead of a trimer (for which this fragmentation would give a peak gradient of -1). This is despite the lower numbers of tetramers in the mass spectrum compared to trimers (approx. 40%) and suggests that the trimer dication might be more stable than the tetramer dication.

As well as the Coulomb-explosion peaks of ion pairs, the coincidence TOF also contains signatures of both metastable monocations and metastable dications. The metastable dication fragmentation of m/z 45 to m/z 27 and m/z 63 ($C_7H_6^{2+} \rightarrow CH_3^+ + C_5H_3^+$) [81], [96] has already been discussed previously (Section 3.1.3.1). The derived model was found to well replicate the curve shape of the metastable fragmentation, albeit with an offset induced by the voltage switching effect. By adjusting this offset to make the origin of the metastable curve on the autocorrelation line match with experiment, the model was used to diagnose the metastable monocation fragmentations. This was done by adjusting the m/z value of the daughter fragment ion so that the shape of the model lines matched those in the spectra. The resulting fragmentations found are summarised (Table 4.3). Additional metastable fragmentations observed are those of $C_7H_7^+ \rightarrow C_5H_5^+ + C_2H_2$ and $C_5H_5^+ \rightarrow C_3H_3^+ + C_2H_2$ [100], as well as that of the toluene dimer decaying to the monomer.
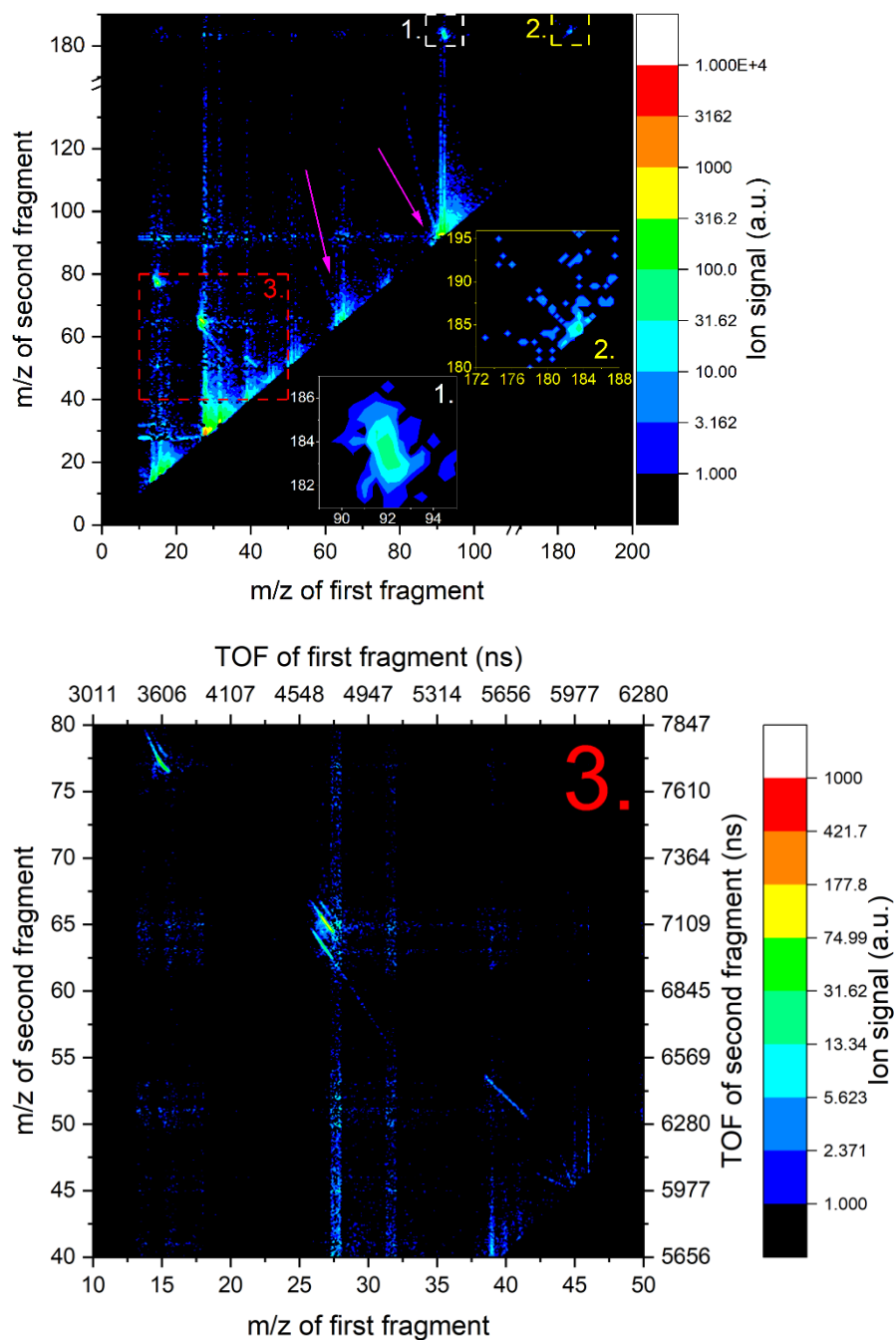
Figure 4.13: (top) Coincidence mass spectrum of toluene at 30.5 eV photon energy. Pink arrows indicate metastable monocations at m/z 65 and m/z 91. White outline (1) shows a Coulomb explosion peak at m/z (92,184). Yellow outline (2) shows a metastable monocation cluster at m/z 183. Red outline (3) is a series of Coulomb explosion peaks of monomer fragments. (Bottom) Plot of the area in the red outline (3) at a higher m/z resolution (0.1 m/z units instead of 0.5).

Ion pair (detected m/z values)	Ion pair (fragments)	Measured peak gradient	Possible mechanism (m/z values)	Possible mechanism (fragments)	Theoretical gradient of mechanism
15 + 77	$CH_3^+ + C_6H_5^+$	-0.637(7)		2-body peak	-1
15 + 78	$CH_3^+ + {}^{13}CC_5H_5^+$			2-body peak	-1
27 + 63	$C_2H_3^+ + C_5H_3^+$	-0.98979	65 → 63	$C_5H_5^+ → C_5H_3^+$	-0.969
27 + 65	$C_2H_3^+ + C_5H_5^+$	-0.896(7)		2-body peak	-1
27 + 66	$C_2H_3^+ + {}^{13}CC_4H_5^+$			2-body peak	-1
39 + 53	$C_3H_3^+ + C_4H_5^+$	-0.869(5)		2-body peak	-1
40 + 52	$C_3H_4^+ + C_4H_4^+$	-0.869(5)		2-body peak	-1
41 + 51	$C_3H_5^+ + C_4H_3^+$	-0.869(5)		2-body peak	-1
92 + 184	$C_7H_8^+ + (C_7H_8)_2^+$	-2.00(14)	184 → 92	$(C_7H_8)_2^+ → C_7H_8^+$	-2

Table 4.2: Identified ion pairs from Coulomb explosions of toluene 30.5 eV. Entries left blank are where peaks were identified but signal levels were too low to reliably fit. 2-body peaks are direct Coulomb explosion of the toluene dication with no neutral fragment generated and always have a theoretical gradient of -1.
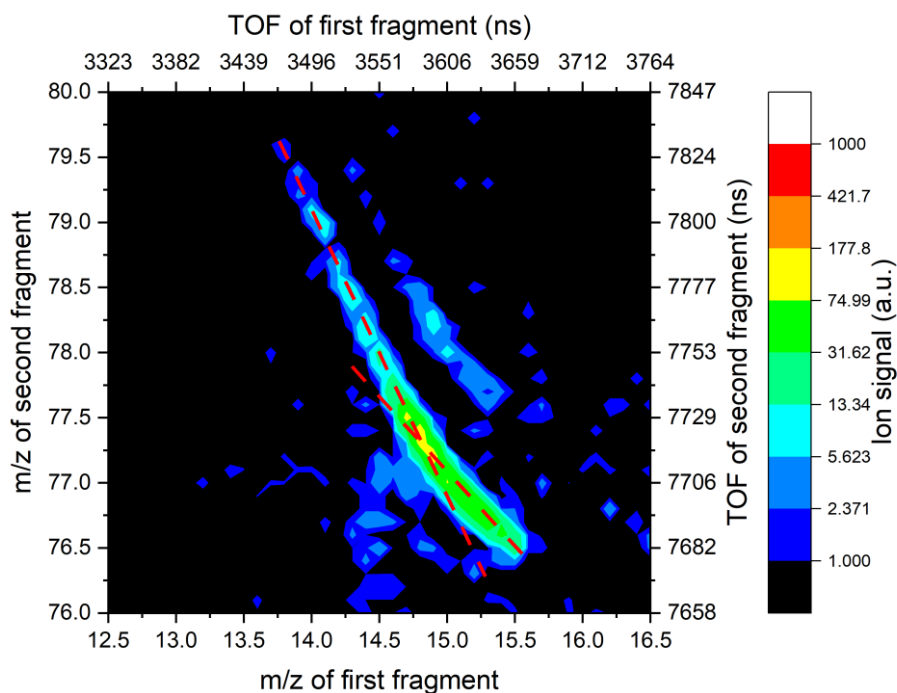
Figure 4.14: Close-up of the m/z 15 + 77 and m/z 15 + 78 ion pairs in Figure 4.13. The red lines are added to highlight the different gradients of each part of the peak.

Ion fragmentation (m/z values)	Ion fragmentation (proposed fragments)	Additional offset (ns)
45 → 27 + 63	$C_7H_6^{2+} → C_2H_3^+ + C_5H_3^+$	180
65 → 39	$C_5H_5^+ → C_3H_3^+ + C_2H_2$	220
91 → 65	$C_7H_7^+ → C_5H_5^+ + C_2H_2$	250
184 → 92	$(C_7H_8)_2^+ → C_7H_7^+ + C_7H_7$	350

Table 4.3: Observed metastable fragmentations of singly-charged 2-propanol cations at 30.5 eV. The additional offset does not include the offset that is already present in the experimental dataset (366.1 ns).

4.4 Conclusion

This chapters details the initial trials and testing of the use of the endstation in conjunction with the HHG source on a molecular sample in a supersonic beam. The XUV ionisation of toluene was examined and compared to existing literature. The initial trial of this experiment illustrated that there were several experimental issues that hampered the quality of the data. The photoelectron images showed two types of defects: radial deviations for photoelectrons emitted with the same kinetic energies emitted but at different angles, and horizontal and vertical stripes of low intensity signal across the image. The radial deviations led to the circularisation method detailed in the previous chapter being defined during the next experiment. Retroactive use of the circularisation constants that were defined proved partially successful, which suggests that the deformations are sensitive to the exact path of the electrons though the flight tube as defined by the laser pointing and electrode conditions, rather any defect with the DLD itself. Areas of low signal intensity were caused by a fault on the DLD anode wires which would be fixed before the next beamtime.

Air leaking into the HHG beamline meant that the pressure in the detection chamber was high, and that signatures of nitrogen, oxygen and water vapour were present in the dataset. When examining the total photoelectron spectrum on the CCD-VMI, these signatures obscured that of the toluene, however with the coincidence operation these contributions could be removed and the toluene photoelectron spectrum better reproduced in comparison with the literature. The toluene photoelectron spectrum showed that population of ionic states close to the threshold lead to the formation of the parent ion $C_7H_8^+$. However, population of higher lying states at approximately 13-14 eV increasingly lead to hydrogen loss and formation of $C_7H_7^+$. Population of states at 18 eV and above lead to both of these ions predominantly dissociating to the smaller fragments which make up the toluene mass spectrum

DPI of toluene was confirmed to be possible by the presence of dication ($C_7H_8^{2+}$) peaks in the TOF. Analysis of the partial DPI in coincidence with them showed reasonable agreement with literature in determining the photoelectron onset, despite the fact that only one of the two electrons per DPI event could be recorded. However, this resulted in the fine structure of the spectra being washed out. The ^{13}C isotopologue of the dication was also observed with a similar photoelectron signal. The presence of $C_7H_6^{2+}$ and $C_7H_7^{2+}$ dications, due to loss of hydrogen were also observed. $C_7H_6^{2+}$ was observed in the mass spectrum to form from metastable decay of the parent dication, which loses H_2.

The coincidence TOF spectra at 30.5 eV photon energy showed a series of ion-pair peaks corresponding to Coulomb explosions. These do not occur at lower photon energies, even when the dication is formed. Many of the ion-pair peaks corresponded to fragments previously seen in the literature, although there was also a peak which suggested Coulomb-explosion of a tetramer took place into two dimers, one of which decayed to a monomer. The analysis of the ion-pair peaks was hampered by another experimental defect. Examination of the TOFs, particularly for lighter masses, showed that there were deformations to the peaks caused by an improper switching technique where the timing signals for the Behlke switches were connected in series with long cables. This means that when switching from imaging electrons to imaging ions, the electrode voltages switch sequentially rather than simultaneously which makes it harder to image ions well under VMI conditions. This would be fixed by connecting them in parallel to separate delay generator channels and by checking the timing more precisely with a fast HV probe. This factor affected the analysis of the ion-pair peaks as it led to changes in the peak gradients from the theoretical value based on the fragmentations.

The coincidence TOF also showed signatures of both metastable dications and monocations. The model derived in Chapter 3 was used to aid diagnoses of the involved masses. Despite not accounting for voltage switching, the model curves still replicated the shape of the metastable signatures. However, an offset that was dependent on the parent ion m/z had to be added to the model to align the curves.

5 Extreme-ultraviolet photoionisation of 2-propanol molecules and clusters

5.1 Introduction

2-propanol (CH_3H_7OH, isopropanol, isopropyl alcohol or propan-2-ol) has been the subject of numerous studies taken place using electron impact ionisation [101], [102] and XUV ionisation [103]. The single ionisation potential has been determined to be around 10.18 eV [104]. DPI of 2-propanol does not yet appear to have been directly examined, however the appearance of fast methyl fragments with 2.82 eV kinetic energy following EI ionisation spectra at 30.2 eV was attributed to the dissociation of doubly charged ions [102]. This indicates that DPI does take place at this energy, however this method does not necessarily give reliable information on the vertical DIP due to indirect mechanisms allowing formation of dications far outside the Franck-Condon zone for vertical transitions [12], [80]. This chapter attempts to more closely examine DPI of the 2-propanol monomer by obtaining a closer estimate of the vertical and/or adiabatic DIPs and deducing the mechanism of DPI by investigating both ion fragmentation behaviour and partial DPI spectra in coincidence with selected ion fragments upon XUV photoionisation. It also attempts to investigate DPI behaviour in 2-propanol clusters by examining ion fragmentation behaviour and to apply the model developed in Section 3.1.3.1.

DIPs of similar alcohols, mainly methanol, ethanol and 1-propanol (Table 5.1), suggest that the rule-of-thumb for estimating DIPs (Equation 1.1) [17], [105] is well followed for the linear chain primary alcohols. This rule-of-thumb considers that the electron vacancies are located in two molecular orbitals. One orbital is located mainly on the oxygen atom and the other is delocalised over the carbon chain. In estimating the inter-vacancy distance, the rule-of-thumb then approximates the location of the carbon-chain vacancy at the centre-of-mass of the carbon atoms. For the given vertical ionisation energies of 2-propanol [102], [105], the inter-vacancy distance r_{12} is approximately 1.5 Å, slightly longer than a typical C-O bond. This appears consistent with the results in [105] for the other alcohols, considering a typical C-O bond length is approximately 1.4 Å, and the carbon chain centre-of-mass will lie close to the central carbon atom which is bonded to the oxygen. Assuming that the rule-of-thumb holds equally well for secondary alcohols, this suggests that 30.2 eV remains a plausible value for the vertical DIP despite the previously mentioned shortcomings of using fragment appearance potentials to determine these values.

The mass spectrum of 2-propanol has been investigated for both electron impact ionisation [106] and photoionisation [107]. The spectrum is dominated by the signature fragments of the m/z 45 base peak belonging to $C_2H_5O^+$ and through which the major fragmentation pathways proceed [108]. $C_2H_5O^+$ is formed by simple C-C bond breaking, resulting in CH_3 loss. Further fragmentation of $C_2H_5O^+$ can proceed by several metastable pathways resulting in a range of fragments between m/z 15 and m/z 44 [108].

VUV pump-IR probe experiments [109], [110] on phenylalanine observed ultrafast migration of the charge by probing the yield of a dication fragment with time and found the positive charge in the monocation would migrate to one end of the molecule. This inspired similar experiments in 2-propanol [111] as well as a time-resolved study [48], [112] featuring VUV pump – NIR probe measurements which suggested there is a manifold of multi-electronic states at approximately 15 eV and a higher monoelectronic state at 20 eV. Population of the latter results in comparatively higher fragmentation to smaller molecular fragments and further such studies are anticipated at photon energies close to the expected DIP [48].

Hydrogen bonding of the alcohol group allows 2-propanol to readily form clusters in a supersonic molecular beam [113]. Such clusters can be regarded as simple models from which behaviour of the intermolecular interactions can be extrapolated to the bulk liquid phase. Ionisation from molecular orbitals involved in a hydrogen bond can trigger proton transfer along the bond on a femtosecond timescale. Of the two lowest energy 2-propanol conformers, only the *gauche* isomer is found in a molecular beam of the monomers, however clusters consist of both *gauche* and *trans* conformers and have various structures. Trimers and larger clusters form cyclic structures based around shared hydrogen bonding [113]. Single ionisation of these clusters and similar alcohol clusters has previously shown that they often fragment to form smaller protonated clusters from proton transfer reactions [113]–[115].

In this chapter, the XUV ionisation of 2-propanol monomers and clusters are investigated at photon energies between 27 and 37 eV. Double ionisation is investigated by recording PIPICO and PEPIPICO coincidences to observe fragmentation patterns and photoelectron spectra. Metastable fragmentations of singly-ionised monomers and clusters are also investigated through ion-ion coincidence spectra.

Molecule	Vertical IP (eV)	DIP onset (eV)	Vertical DIP (eV)
methanol	10.83(1) [104]	30.5 [105]	32.1 [105]
ethanol	10.46(1) [104]	28.2 [105]	29.6 [105]
1-propanol	10.25(1) [104]	27.0 [105]	28.2 [105]
2-propanol	10.18(1) [104]	<30.2 [102]	

Table 5.1: Literature values of single and double ionisation potentials of 2-propanol and similar alcohols.

5.2 Experimental

2-propanol was inserted into the sample reservoir inside the source chamber and heated to 65°C, corresponding to a vapour pressure of approximately 0.5 bar [116]. Helium was used as a backing gas at approximately 2.3 bar so that the resulting molecular beam composition was approximately 20% of 2-propanol. The molecular beam was crossed in the detection chamber by the HHG beam at photon energies between 24 eV and 37 eV at 6000 s^{-1} repetition rate. The photon flux is on the order of 2 x 10^8 pulse^{-1} using the 200 gr mm^{-1} density grating on the time-preserving monochromator, giving an expected FWHM energy resolution of 0.5 – 0.6 eV (Figure 2.11) [27]. Various coincidence imaging datasets were recorded using the DLD-VMI at these photon energies, typically using either 3-3 $M20$ focusing, 3-3 $M40$ focusing for PEPIPICO datasets, or 3-electrode static voltage conditions with V_R = 3000 V for PIPICO datasets. DLD-VMI acquisitions were typically around 8 hours long. Photoelectron images were circularised using the procedure in Section 3.2.2.1. Electron and ion images were Abel inverted and calibrated for kinetic energy from Section 3.2.2.2. Switched and static TOF spectra were both calibrated using a linear relationship between the TOF and $\sqrt{m/z}$ using constants determined from a unique fit for each dataset. Photoelectron spectra of the entire molecular beam ensemble were also recorded on the CCD-VMI with 4-electrode static voltages at V_R = 5000 V – 6000 V in order to observe the fast electrons coming from single ionisation. The ionisation rate was estimated to be approximately 8%. CCD-VMI acquisitions were typically around 2 hours long.

5.3 Results and discussion

5.3.1 Double photoionisation of the 2-propanol monomer

The photoelectron spectrum of the entire molecular beam ensemble recorded on the CCD-VMI is shown (Figure 5.1) at 33.6 eV photon energy along with literature spectra obtained at 1487 eV [117] and 90 eV [48]. Peaks assignment is aided by the calculated orbital-energy diagram (Figure 5.2). The spectrum can be separated into three regions. Between 10 and 18 eV the electron is emitted from the outer-valence orbitals where there are multiple closely-packed states; between 18 and 27 eV the electron is emitted from the carbon 2s inner-valence orbitals where there are three distinct peaks; at approximately 32 eV the electron is emitted from the oxygen 2s orbital which gives a broad peak. The sharp intense peak at 24.6 eV in the HHG spectrum represents ionisation of the helium carrier gas in the molecular beam and overlaps with a C 2s peak. Signal onset can be seen around 10.2 eV, corresponding to the vertical single IP. Most of the features are reproduced between spectra except the relative peak intensities, which is likely due to different photoionisation cross-sections at each photon energy [48].
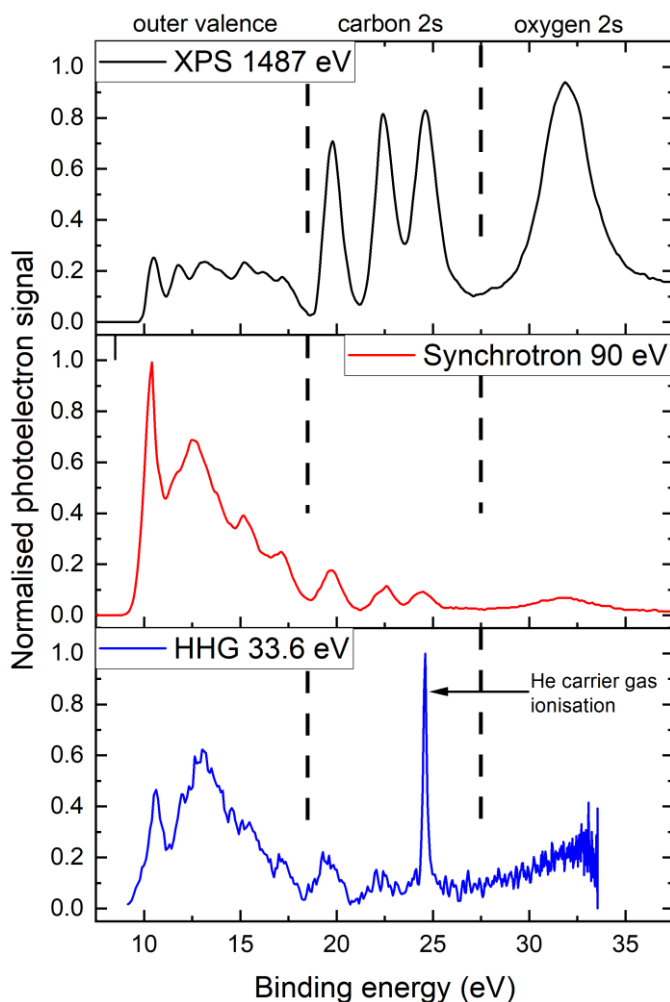
Figure 5.1: Photoelectron spectra of 2-propanol from XPS experiment [117] at 1487 eV photon energy (black), synchrotron experiment [48] at 90 eV (red) and the HHG experiment at 33.6 eV photon energy (blue). XPS and synchrotron spectra are both reproduced from [48].

The initial hypothesis for the DPI mechanism is that a photoelectron is first emitted from the O 2s orbital at 32 eV, triggering an Auger-Meitner process in which the inner-valence hole is filled by electron relaxation from a higher level and an outer-valence electron is ejected. This hypothesis is based on the notion that indirect mechanisms dominate for molecules at energies close to the DIP [19]. This corresponds with the results from [102] considering that at 30.2 eV the incident electron energy just begins to overlap with the edge of the broad electronic state created by the inner-valence hole. This should manifest in the photoelectron spectrum as two (possibly very broad) peaks: an Auger-Meitner peak with kinetic energy independent of the photon energy, and a direct photoelectron peak with kinetic energy that varies directly with photon energy.
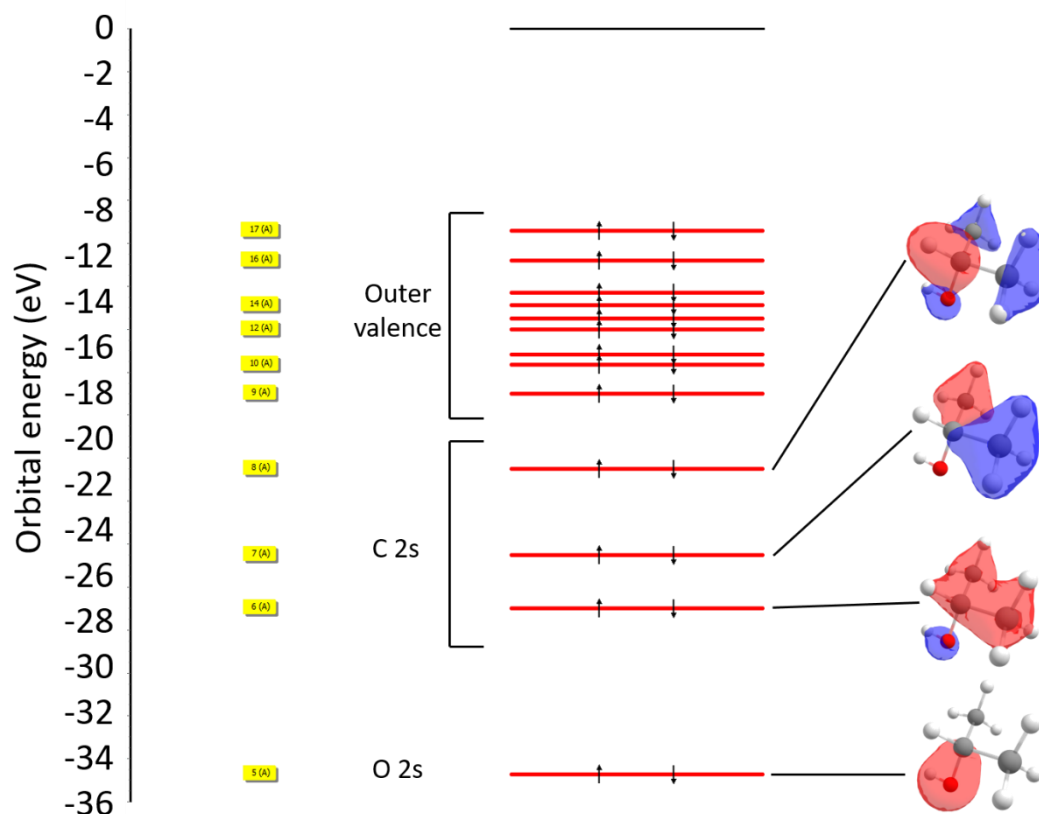
Figure 5.2: Molecular-orbital diagram of the inner- and outer-valence orbitals of 2-propanol with depictions of the inner-valence orbitals. Calculations were performed by Dr. Rebecca Ingle with Hartree-Fock theory and a minimal basis set (HF/STO-3G) on a ground-state optimised geometry.

The 2-propanol mass spectrum at 33.3 eV photon energy is shown (Figure 5.3) for masses up to the monomer (m/z 60). The most prominent fragment is at m/z 45 which is $C_2H_5O^+$ and many of the smaller fragments correspond to its dissociation [108]. Also present is hydrogen background gas and the helium carrier gas in the molecular beam. The parent ion signal at m/z 60 is weak compared to many other fragments, including the peak at m/z 61. This peak is composed mainly of the protonated monomer $C_3H_7OH_2^+$, but also of the monomer's ^{13}C isotopologue $^{13}CC_2H_7OH^+$ which should be approximately 3.3% of the m/z 60 signal. Protonation arises through cluster fragmentation and helps stabilise the ion. This spectrum includes fragments from both single and double ionisation. The 2-propanol monocation already fragments extensively and a dication peak is not expected to be easily observable. Additionally, a dication peak at m/z 30 (= 60/2) would overlap with that of the CH_2O^+ fragment which arises from dissociation of $C_3H_7O^+$ (m/z 59) [108].
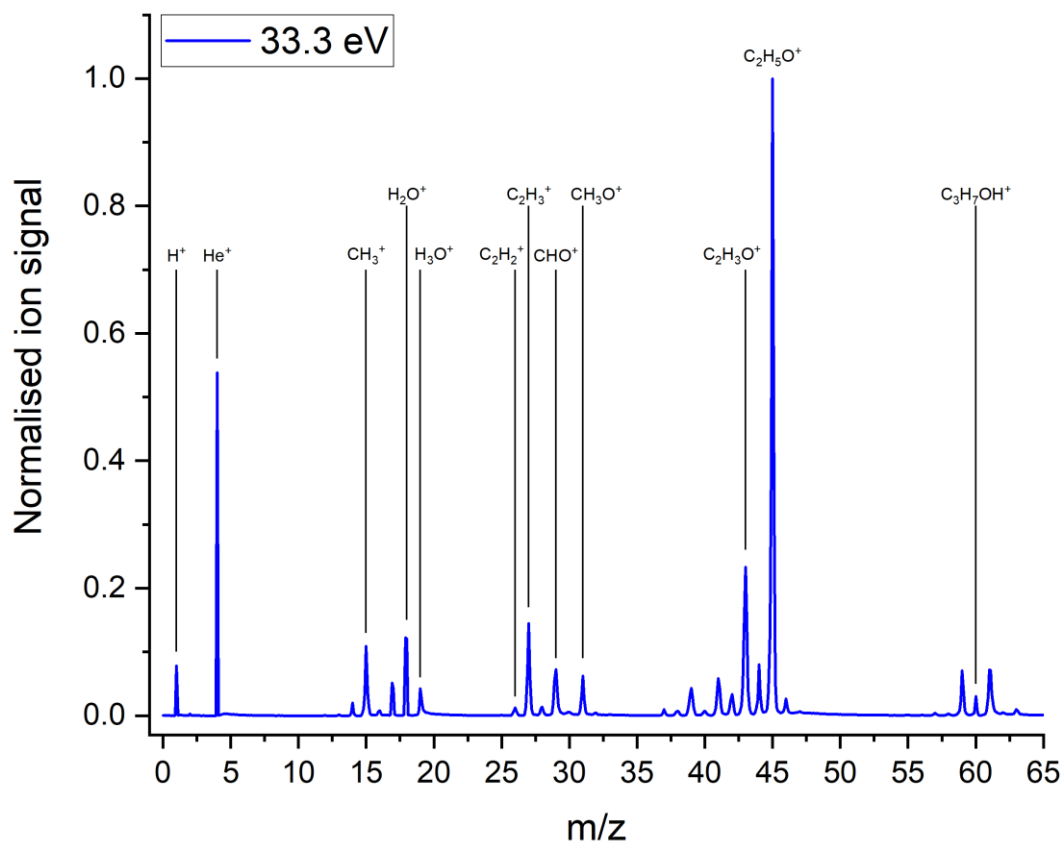
Figure 5.3: Mass spectrum of 2-propanol recorded under static voltage conditions at 33.3 eV photon energy.

DPI is observed by examining the m/z 15 TOF peak of the CH_3^+ fragment. The peak is shown at various photon energies under 3-3 M40 focusing and static voltages (Figure 5.4). On the left are the uncorrelated peaks and on the right are peaks correlated with one ion of $m/z \leq 45$, as well as one electron in the 3-3 M40 case. Many electrons from single ionisation are too fast to detect while they are slow enough when produced from DPI. Correlating the m/z 15 signal with ions of $m/z \leq 45$ should filter for DPI, since there are two ions, and suggest that the parent ion of the fragments is no larger than a monomer. It is possible that a cluster ion could fragment into two ions that then further decay to the observed masses, however this contribution should be minor due to low cluster populations in the molecular beam relative to the monomer. On increasing the photon energy, the relative CH_3^+ signal becomes stronger, suggesting increased fragmentation of larger ions, and the peaks broaden. This is more significant at higher photon energies where peak shoulders are formed on either side. The effect is significantly more pronounced in the correlated TOFs. The broadening is attributed to high TKER from a Coulomb explosion of a multiply-charged ion. Under static voltages, the peak broadening is mostly symmetric around the centre. For the switched voltages, the distribution is skewed towards the lower TOF. This may be due to TOF distortions from the switching effect, or that the fastest ions propelled away from the detector in the Coulomb explosion are lost, which decrease the intensity on the higher TOF side.
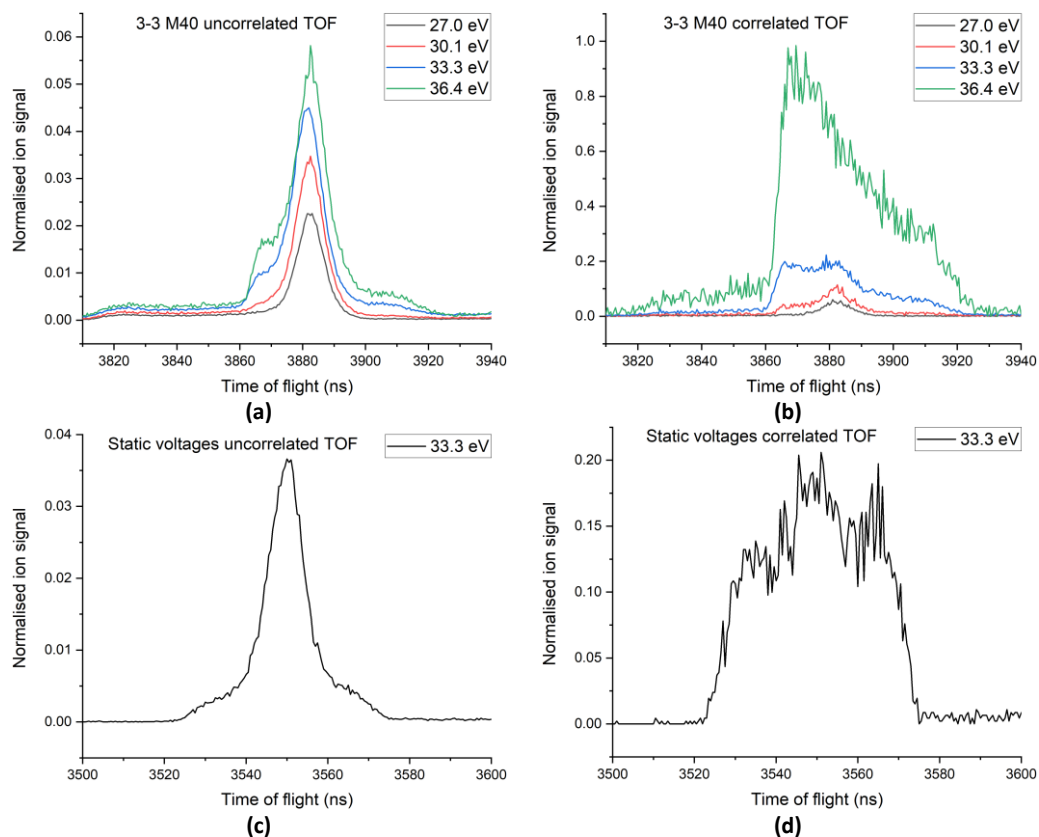
Figure 5.4: The m/z 15 ion signal in 2-propanol TOF spectra recorded with 3-3 M40 ((a) and (b)) switching conditions and static conditions ((c) and (d)). (a) and (c) show the uncorrelated peak, (b) and (d) show the peak for a PEPIPICO coincidence (b) or PIPICO coincidence (d) where the other ion has $m/z \leq 45$. Peak intensities are normalised to the most intense peak in the entire spectrum, which in most cases belongs to m/z 45. An exception is in (b) where the m/z 15 peak at 36.4 eV is the most intense.

At 27.0 eV there appears to be no Coulomb explosion occurring, as the TOF peak is not broadened like at higher energies. The effect appears to set in at 30.1 eV, suggesting that DPI has just been triggered. This is consistent with previous results [102]. While the shoulder intensities vary, the total widths are constant, from 3860 ns to 3920 ns in the M40 TOFs, suggesting the TKER is independent of photon energy. A second, flat shoulder extends from the peak to 3820 ns in the M40 spectra which is absent from the static spectrum. This is attributed to background 2-propanol signal for which the switching effect distorts the TOF. The background 2-propanol can be ionised at any point along the laser path, unlike the molecular beam molecules which are only ionised in the VMI centre.

There is a narrow central peak observed at 27.0 eV under the PEPIPICO coincidence requirements. Such a peak indicates ions with low kinetic energy such as those expected from single ionisation. If there is only single ionisation at this photon energy, then only one electron and one ion can form a true coincidence. The presence of any second ion, which these coincidence requirements filter for, would mean this must be a false coincidence. These peaks are also observed with the Coulomb explosion signatures at higher photon energies. False coincidences are likely to come from single ionisation events in a laser pulse relative to DPI events. In this case, the photoelectron is should have much higher kinetic energy than a DPI electron unless very high-energy monocation states are populated. The maximum detectable kinetic energy in these experiments is approximately 12 eV. Faster electrons which are emitted perpendicularly (or nearly so) to the TOF axis are lost. Those emitted at different angles might still be detected at a range of radii depending on the velocity component perpendicular to the TOF axis. Abel-inverting an image featuring these electrons, without those

belonging to the perpendicular "edge", should give a featureless background which slowly rises with kinetic energy. Since DPI electrons are expected to be slow there should be few prominent single ionisation features which might obfuscate the DPI spectrum.

The occurrence of Coulomb explosions is confirmed by examining the CH_3^+ images under the same coincidence requirements (Figure 5.5). The images show a broad, high-intensity ring representing fast ions and a central spot representing slower ions. Kinetic energy spectra show that the kinetic energy of the fast ions is approximately 3.20(6) eV, which is slightly higher than in [102] (2.82 eV). However, the feature is very broad ($\Delta E \approx 1.6$ eV) and the value is typical for a Coulomb explosion. The slow ion peak corresponds to the central TOF peaks in Figure 5.4 and to the 0.16 eV thermal ions in [102]. Like in Figure 5.4(b), the fast fragment signal increases with photon energy and its absence at 27.0 eV supports the diagnosis that there is no Coulomb explosion or DPI at this energy. The slow ions detected here are therefore expected to be false coincidences from single ionisation. However, it could be possible they do correspond to DPI if it takes place via the autoionisation of fragments from molecular dissociation (Equation 1.6) if the neutral fragment is stable enough to get far away from the charged fragment before autoionising to avoid any Coulomb repulsion.

These images and plots differ from those shown previously (Figure 3.23) which were not filtered for any PIPICO/PEPIPICO coincidences and would correspond to the left-side TOF peaks in Figure 5.4. The slow-ion contribution was significantly greater than shown here since the majority of events in this experiment are from single ionisation. Here the coincidence requirements restrict the available ions to mainly being from DPI.
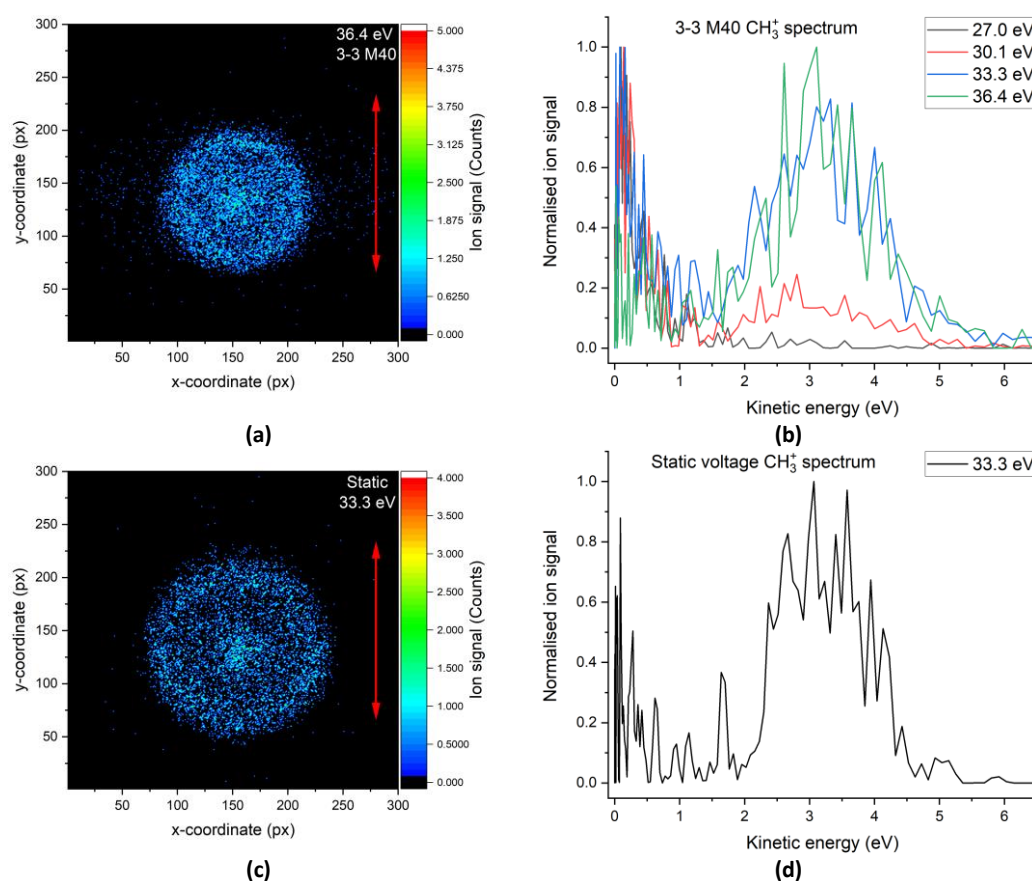
Figure 5.5: PEPIPICO ion images (left) and kinetic energy spectra (right) of CH_3^+ recorded with 3-3 M40 ((a) and (b)) and static conditions ((c) and (d)) at 27.0 eV, 30.1 eV, 33.3 eV and 36.4 eV photon energies.

DPI ionisation is investigated by examining the electrons in coincidence with these ion pairs. In most cases the signal-to-noise level is low. This could be due to the DPI cross-section possibly being much lower than the single ionisation cross-section at these photon energies. For photon energies 30.1 eV and 33.3 eV there are datasets corresponding to 3-3 $M20$ focusing and 3-3 $M40$ focusing conditions. Since the photon and electron imaging conditions are the same in both datasets, the electron data can theoretically be combined. The different m/z focusing conditions only affects the ions which should not be a problem if the relevant TOF intervals are selected correctly. It is still possible that slightly different images might be acquired due to changes in the pointing conditions caused by molecular beam or laser drift which would move the ionisation point away from the VMI centre. This is assessed by examining the raw electron images (Figure 5.6(and radial distribution plots after Abel inversion (Figure 5.7). The images show that, at least on the pixel level of the selected size (300 px x 300 px), the centre is the same as given by the region of highest intensity. The radial plots show very similar profiles, the only difference being the noise peaks. This was therefore considered sufficient to combine the electron images together before Abel-inverting.
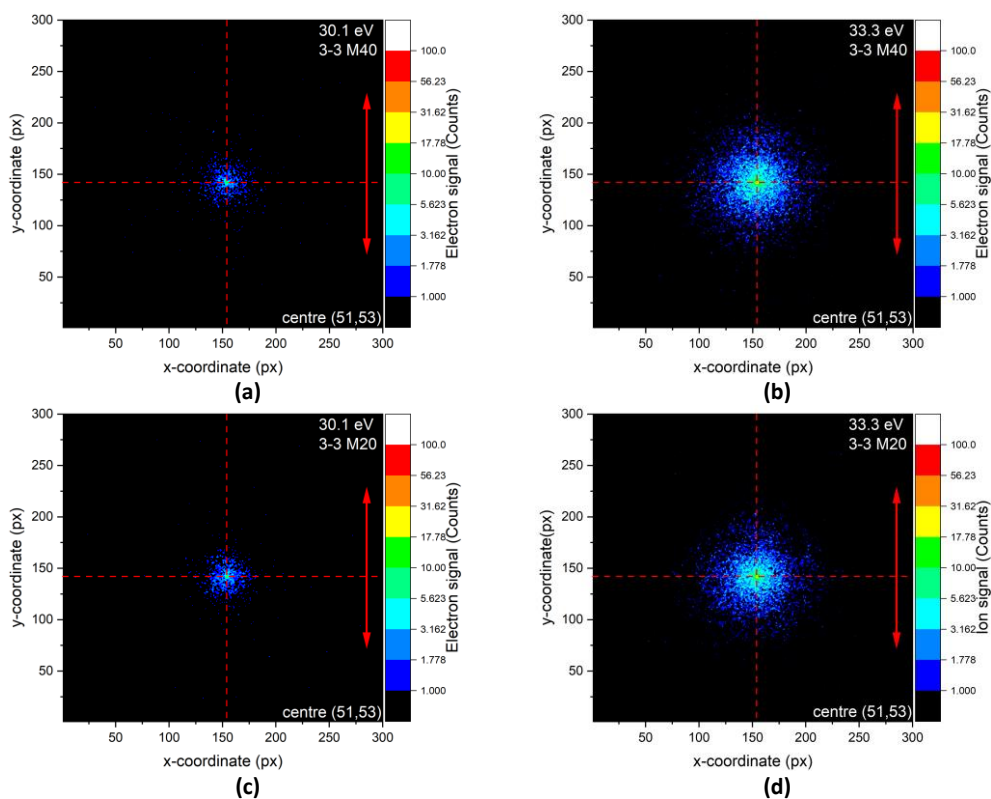
Figure 5.6: Raw electron images at 30.1 eV and 33.3 eV under $M40$ and $M20$ ion focusing in PEPIPICO coincidence with m/z 45 and m/z 15 ions.
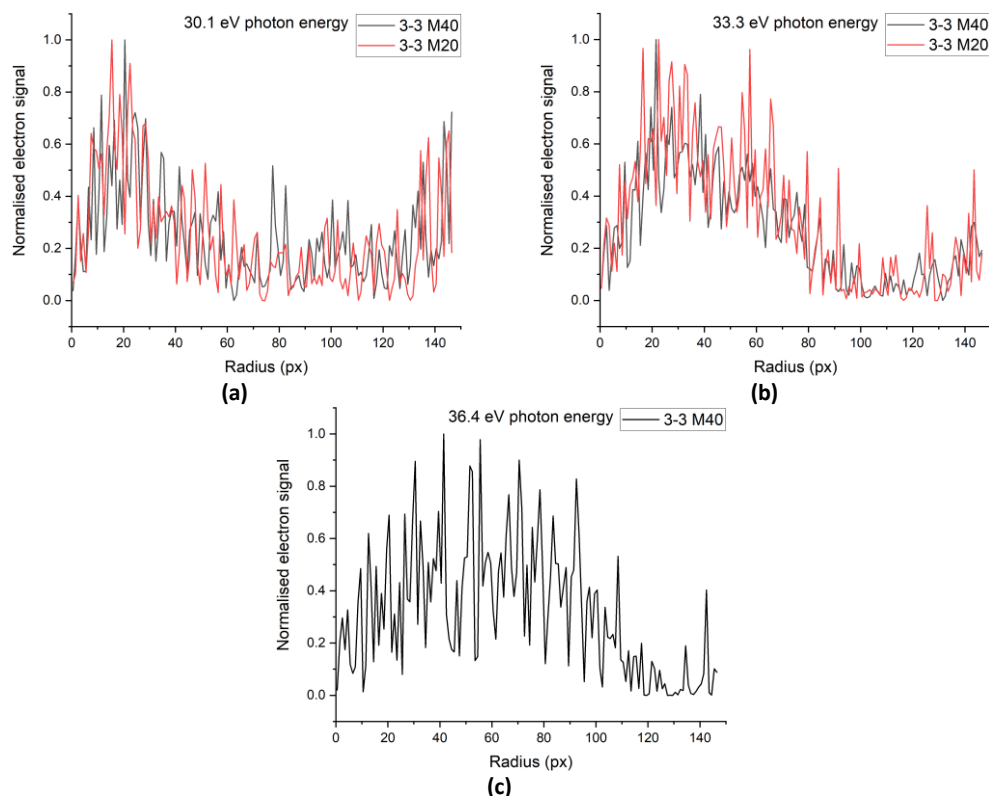
Figure 5.7: Electron radial distribution plots recorded at 30.1 eV, 33.3 eV and 36.4 eV with 3-3 $M20$ and 3-3 $M40$ voltages.

In the radial plots, there is a broad distribution at low radius before a period of comparatively low signal after which it increases with radius until the detector edge at approximately 145 px. The faster electron signals at higher radius might be from single ionisation as discussed above. This hypothesis can be explored by using the CH_3^+ signal as a filter where only electrons in coincidence with the faster ion peak are plotted. Filtering coincidences based on slow or fast particles is imperfect because the radial coordinate is the filtered property and, due to how VMI works, fast particles can arrive at smaller radial distances and contribute to signal prior to Abel inversion. This means when trying to include signal only from slow particles there will still be some coincidences from faster particles present, and when trying to include signal only from fast particles, some valid signal will be thrown away. This will result in some electrons in coincidence with valid CH_3^+ signal being discarded. The radial plot (Figure 5.8) of the electrons in coincidence with fast CH_3^+ (above 1.5 eV) ions shows that removing the slow CH_3^+ coincidences effectively removes the signal at high radii. The radial electron plots at each photon energy seem reasonably well described by two broad Gaussian peaks that overlap. Although the fit errors are quite large (Table 5.2), they are useful to highlight the structure and guide the eye to facilitate perceiving the intensity. However, at 36.4 eV the overall shape of the spectrum shows this less distinctly. As the photon energy increases both peaks move to higher radius, suggesting faster photoelectrons. This appears inconsistent with an Auger-Meitner process where the Auger-Meitner electron kinetic energy should be independent of photon energy while the primary electron increases with photon energy.
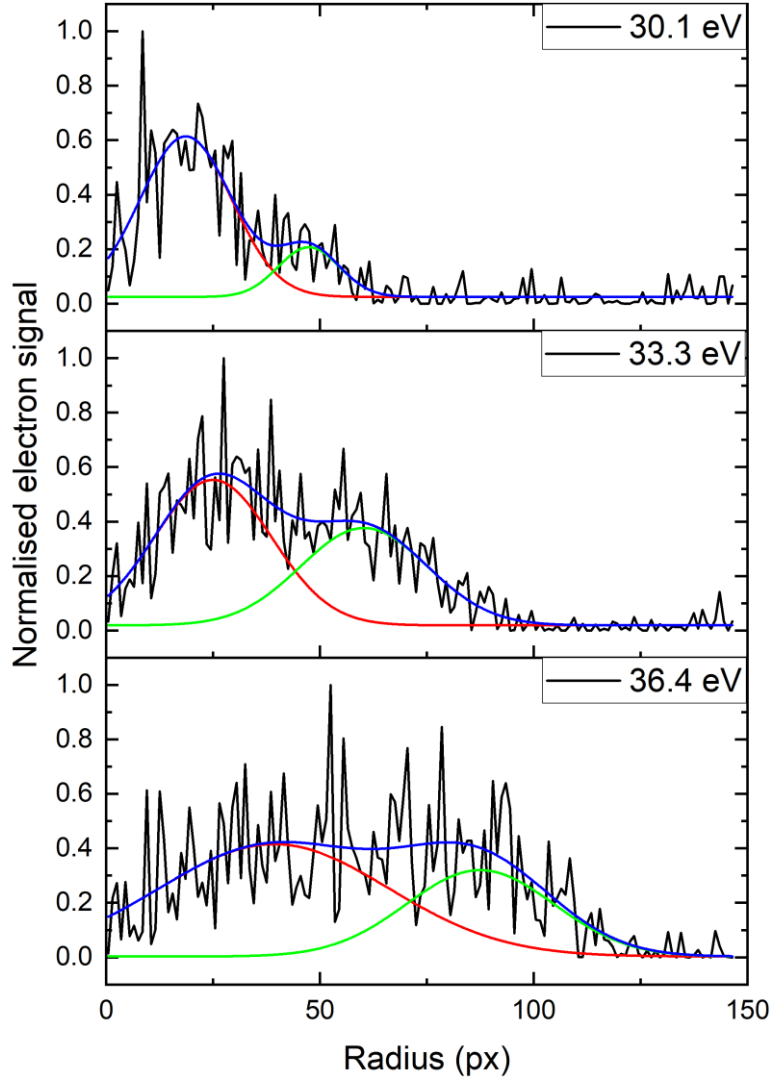
Figure 5.8: Radial photoelectron plots of PEPIPICO coincidences at 30.1 eV, 33.3 eV and 36.4 eV photon energies after being filtered for fast CH_3^+ signals with Gaussian fits of the peaks. The red and green curves are fits of the slower and faster distributions respectively, and the blue curve is the cumulative fit.

Photon energy (eV)	Peak 1 radius (px)	Peak 1 width (px)	Peak 2 radius (px)	Peak 2 width (px)
30.1 eV	18.6(7)	25(2)	47(2)	17(5)
33.3 eV	25(3)	32(5)	60(4)	35(8)
36.4 eV	39(10)	63(21)	87(7)	41(13)

Table 5.2: Parameters of the Gaussian fits to the electron radial distributions in Figure 5.8.
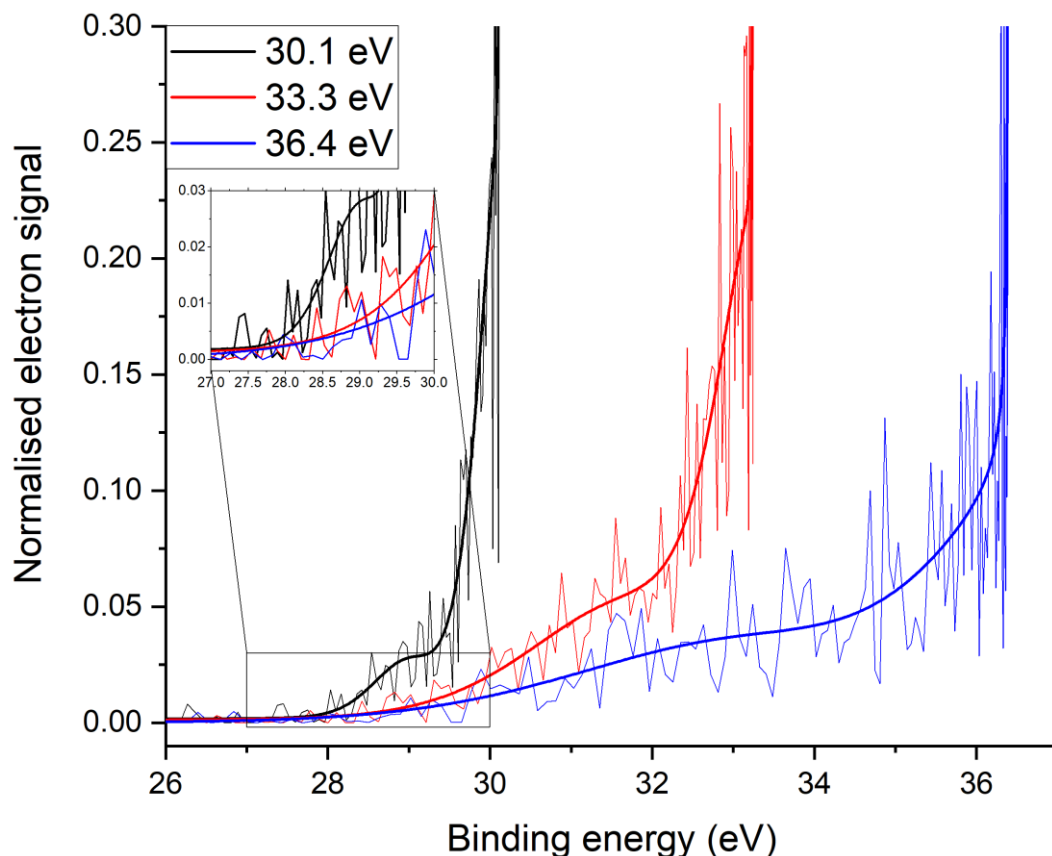
Figure 5.9: PEPIPICO partial DPI spectra filtered for fast CH₃⁺ and ion signals up to m/z 45 at 30.1 eV, 33.3 eV and 36.4 eV photon energies. The original spectra are faint lines, the bold lines show the conversion to kinetic energy of the cumulative peak fits (blue) from Figure 5.8.

With the relevant coincidences defined and photoelectron images combined, the PEPIPICO partial DPI spectra are shown at each photon energy in terms of binding energy ($E_b = hv - E_k$) (Figure 5.9). There is an onset of signal at approximately 28.0 eV for each photon energy. However, the onset is considerably slower at 33.3 eV and 36.4 eV photon energies. A lack of consistent structure in the spectra and calculations of electronic states of the 2-propanol dication make assigning the vertical ionisation energy difficult.

As discussed previously (Section 4.3.1), the spectra recorded here include only one of the two emitted electrons, making them partial instead of complete DPI spectra and resulting in a potentially incorrect binding energy. The binding energy might still be accurate if the electron energy-sharing distribution is concave, which is possible for Auger-Meitner decays from inner-valence states, such as those based on O 2s [19], and is feasible for 2-propanol. Taking a complete DPI spectrum would give a more accurate spectrum and may reveal peaks corresponding to dication electronic states. Therefore, these DPI spectra are inadequate to accurately determine the vertical DIP or adiabatic DIP at the current photon energies. The situation might be clearer at higher photon energies. With the current photon energies, both emitted electrons could have similar kinetic energies, which would result in their spectral features overlapping. Using higher photon energies might allow different features to separate in the partial DPI spectrum, particularly if there is an Auger-Meitner electron with constant kinetic energy, while the other would vary directly with the photon energy.

Recording and examining electron-electron coincidences would be the next step in examining the DPI of 2-propanol and would give more accurate DIP values and insights into the mechanism. However, this is currently impossible on the endstation as the DLD dead time of approximately 15 ns means it cannot reliably detect

both electrons because they would arrive at approximately the same time, within 1 ns, due to the VMI configuration. This could be overcome with a hexanode DLD, which uses three anodes. One of the anodes is redundant when considering only single hits, but can allow recovery of multiple hits as long as they aren't detected at both the same time and position. However, these detectors are prohibitively expensive. An alternative method is to use a fast-frame complementary metal-oxide semiconductor (CMOS) camera with the MCP-phosphor screen detector which can operate at 1000 s⁻¹ repetition rate [118]. This was a goal in the construction of the endstation that has not yet been achieved. Another alternative to deduce the second electron energy would be to apply momentum conservation to those coincidences with an electron and where the two fragment ions make up the mass of a 2-propanol monomer. This represents a potential future avenue of analysis for experiments performed with this setup. However, this would work better for a case where the dication is stable (such as toluene) to reduce uncertainties in calculated momenta.

To further discussion of the possible mechanism in the absence of complete DPI spectra, the lifetime of the inner-valence hole on the O 2s orbital is considered. If the hole lifetime is longer than the time for the primary photoelectron to leave the molecule then an Auger-Meitner decay mechanism is supported. A scattering process where the primary photoelectron knocks out the secondary electron before leaving the molecule would mean the intermediate electronic state is comparatively short-lived. The two literature spectra from Figure 5.1 are considered along with the HHG data (Figure 5.10). The first was obtained from ionisation by 1487 eV Al Kα radiation on 2-propanol in a gas cell [117], with the photoelectrons being analysed by a hemispherical electrostatic analyser [119]. The second was obtained from ionisation by 90 eV synchrotron radiation at SOLEIL on 2-propanol in an effusive molecular beam [48], with the photoelectrons being analysed by a double-toroidal analyser [120]. To determine the hole lifetime from the peak energy broadening, the instrumental broadening in each case should be determined. For the XPS spectrum, the natural linewidth of the Al Kα radiation is approximately 0.8 eV; the spectrometer has a resolution of 0.4 - 0.6 eV and the Doppler broadening is estimated to be 0.09 eV from the experimental parameters [121], [122] by:

$$\Delta E_{doppler} = 2\sqrt{\frac{m_e E_k k_B T}{m_p}},$$
5.1

where m_e is the rest mass of an electron (5.486 x 10⁻⁴ amu), E_k is the electron kinetic energy (1455 eV = 1487 eV photon energy – 32 eV binding energy), k_B is the Boltzmann constant (8.617 x 10⁻⁵ eV K⁻¹), T is the gas cell temperature (423 K) and m_P is the target 2-propanol molecular mass (60 amu). For the synchrotron spectrum, the synchrotron radiation has a specified resolution of 0.5 meV at 50 eV photon energy which was assumed not to change significantly at 90 eV, and the analyser has kinetic energy resolution of 1% of the pass energy [123], which was set to 120 eV. The 2-propanol being in an effusive molecular beam means the Doppler broadening should be negligible compared to other contributions. These broadening factors are all considered to contribute to an instrumental broadening factor $\Delta E_{instrument}$ with a Gaussian line shape:

$$\Delta E_{instrument} = \sqrt{\Delta E_{radiation}^2 + \Delta E_{analyser}^2 + \Delta E_{doppler}^2}.$$
5.2

This gives $\Delta E_{instrument}$ = 0.95 eV for the XPS data and $\Delta E_{instrument}$ = 1.2 eV for the synchrotron data. A Voigt profile is fit to the photoelectron peaks (Figure 5.10) with the FWHM of the Gaussian contribution fixed at $\Delta E_{instrument}$ and the FWHM of the Lorentzian contribution determined as the energy broadening due to the lifetime $\Delta E_{lifetime}$. The lifetime τ is calculated from the energy broadening by:

$$\tau = \frac{\hbar}{\Delta E_{lifetime}},$$
5.3

where $\hbar$ is the reduced Planck constant (6.582 x 10⁻¹⁶ eV s). A summary of the determined parameters is shown (Table 5.3). The lifetime is found to be approximately 210 as. Typical inner-valence hole lifetime values

for the O 2s orbital have not been found in the literature, however the values here are much shorter than those typically found for other types of core-hole state, such as C 1s (41 fs) [124] and O 1s (13.8 fs) [125]. Lifetimes of core-hole states are expected to normally decrease in a molecule compared to a free atom due to there being more available states into which the system can relax [126]. With the cooling from the effusive molecular beam in the synchrotron experiment, it is likely only the lowest vibrational level in the neutral molecule ground state is populated, which may partially restrict the extent of the vibrational progression. However, the width of the peak in the synchrotron spectrum is larger than that of the XPS spectrum. This suggests that, assuming that the hole lifetime itself is the same in both experiments, the synchrotron experiment has more additional broadening effects than the XPS experiment.
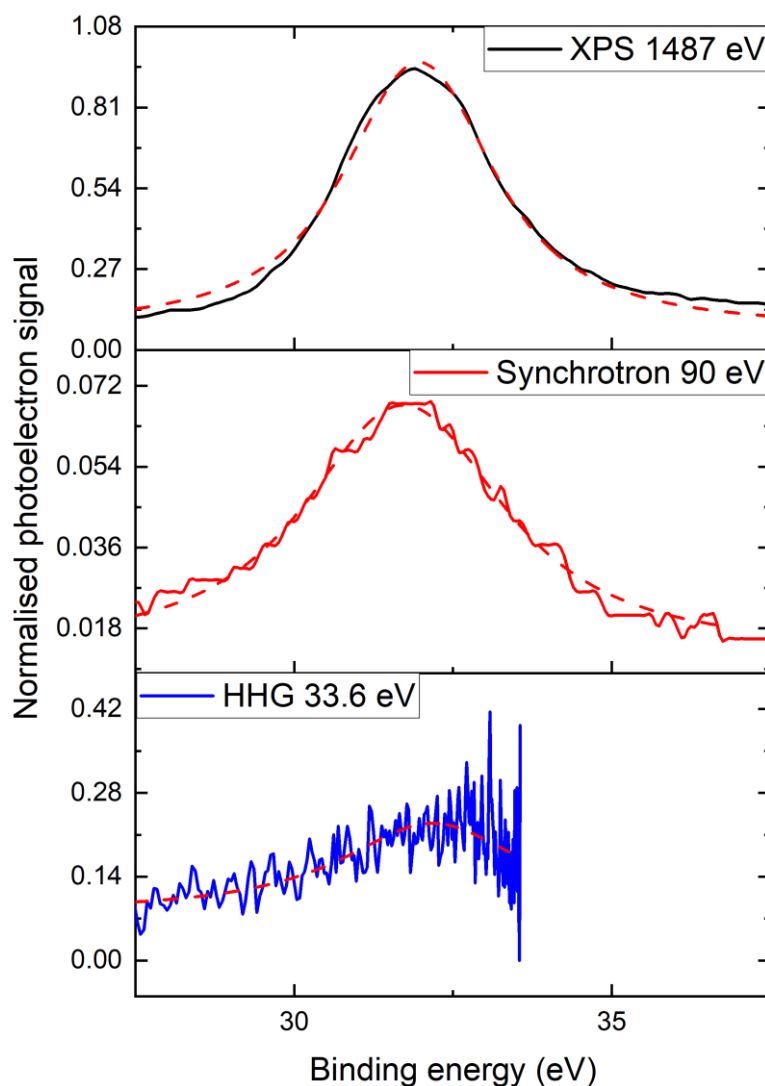
Figure 5.10: Voigt profile fits to O 2s peak for the XPS, synchrotron and HHG experiments, where the Gaussian component width is fixed to $\Delta E_{instrument}$.

Property	XPS [117]	Synchrotron [48]	HHG
$\Delta E_{radiation}$ (eV)	0.8	0.0005	-
$\Delta E_{analyser}$ (eV)	0.5(1)	1.2	-
$\Delta E_{doppler}$ (eV)	0.09	-	-
$\Delta E_{instrument}$ (eV)	0.95	1.2	0.15 (section 3.2.2.2)
$\Delta E_{lifetime}$ (eV)	2.49(5)	3.37(9)	3.5(5)
τ (as)	266(5)	187(4)	190(30)
Mean τ (as)		210(50)	

Table 5.3: Summary of parameters used in peak fitting to determine the lifetime of the oxygen 2s inner valence hole for each experiment. Known standard errors are shown in brackets.

The lifetimes estimated here should be regarded only as minimum bounds, because there are additional contributions to the broadening that were not considered in the estimation. Franck-Condon overlap of the three different electronic states involved: the ground electronic state of the neutral molecule, the inner valence hole electronic state of the monocation and the dication electronic state should result in a vibrational progression, with the lifetimes corresponding to individual vibronic peaks being able to be determined. Additionally, multiplet peaks would also feature and be able to have their lifetimes determined individually. However, at the observed energy resolutions these peaks overlap and only one peak is observed. Additionally, the noise of the HHG peak and the fact that the signal stops before the peak is "complete" means that any lifetime derived from it would be highly suspect, although it is within the same order of magnitude as those from the other experiments.

Assuming the distance between electron vacancies to be around 1.5 Å (Section 5.1), an approximate time for the primary photoelectron to travel this distance is given by a back-of-the-envelope calculation ($t = d/v$) to be 1 fs, 30 as and 6 as for the HHG, synchrotron and XPS experiments respectively. These numbers would be a lower limit on any escape times as the calculations do not include deceleration from the positively-charged nucleus. For the synchrotron and XPS experiments, the estimated lifetimes are much larger than the time for the primary electron to travel the distance and suggest the electronic state is longer-lived than would be given by a direct electron-scattering mechanism such as knock-out. For the HHG experiment this is more ambiguous as the calculated time for the electron to leave the molecule is larger than the estimated (lower bound) lifetime. Additionally, a theoretical calculation of the O 2s-hole lifetime using an *ab initio* method of second-order algebraic diagrammatic reconstruction ADC(2)x [127] suggests that it is on the order of 1-2 fs [111] which is approximately the same as the time for the primary electron to leave the molecule.

Had the experimental hole lifetime been appreciably longer than the time for the electron to leave the molecule, a strong case could be made for the mechanism being an Auger-Meitner decay. However, since the lifetime is on the order of the time for the electron to leave the molecule, and considering the limitations of the approximations used in deriving it, determination of the DPI mechanism from the photoelectron data remains uncertain.

To determine whether the mechanism of autoionisation of fragments from molecular dissociation is viable, the ion-ion coincidence mass spectrum is analysed (Figure 5.11). At the coincidence peaks between smaller masses there are diagonal lines stretching across the peaks. These peaks denote Coulomb explosions of the correlated ions. The section around the Coulomb explosions is zoomed in and represented in the ion-ion coincidence TOF spectrum.

(a)

(b)
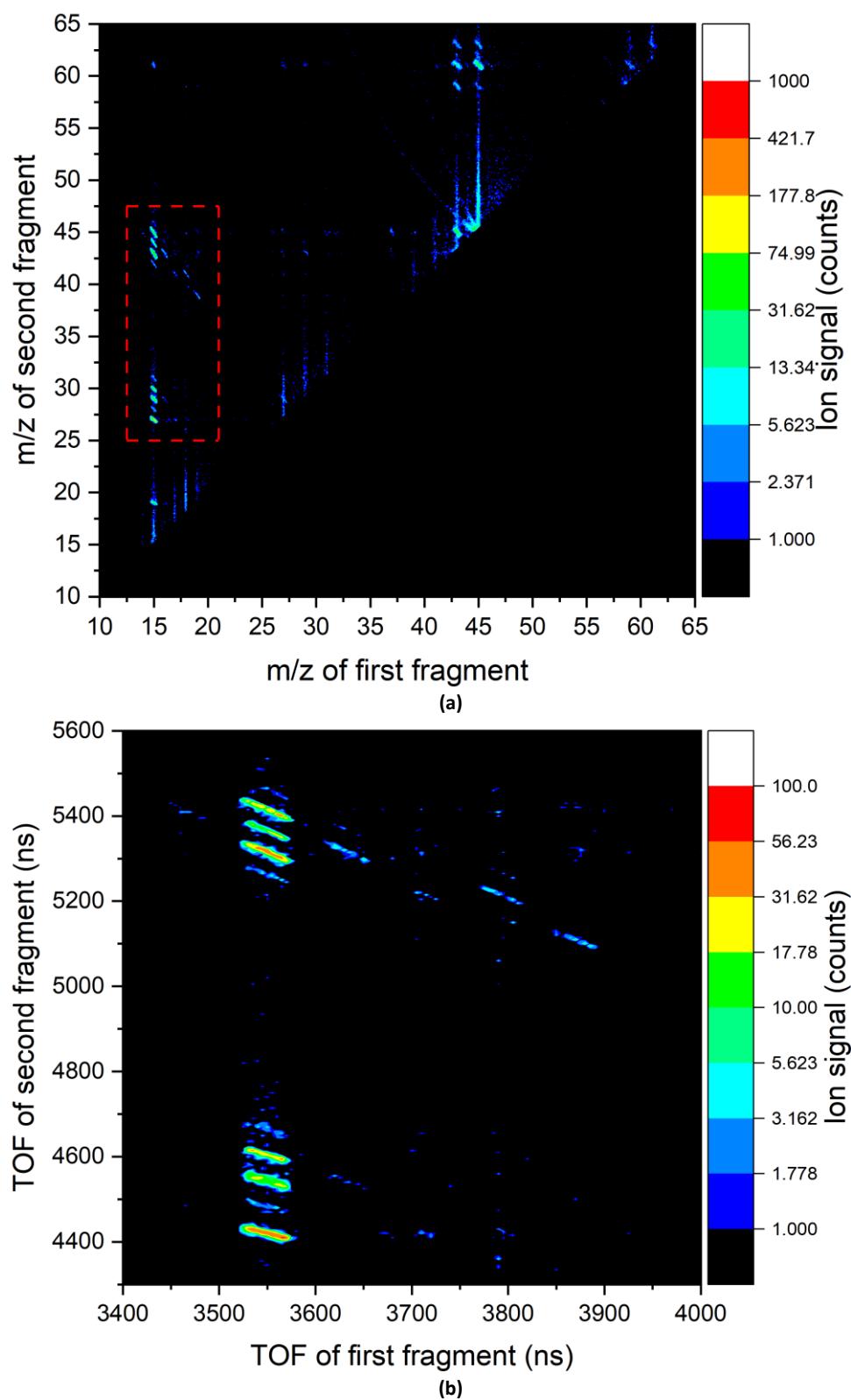
Figure 5.11: (a) Coincidence mass spectrum of 2-propanol recorded under static voltage conditions at 33.3 eV and coincidence TOF representation (b) of the area outlined in red in (a).

The gradients of the strongest diagonal peaks for each diagnosed ion pair coming from a 2-propanol monomer are calculated (Table 5.4) by fitting a rotated 2D Gaussian model. The rotated Gaussian fit is given by

$$f(t_1, t_2) = z_0 + A \exp\left\{ -\frac{1}{2}\left(\left(\frac{(t_1 - t_{1c})\cos\theta + (t_2 + t_{2c})\sin\theta}{\sigma_1} \right)^2 \right.\right.$$
$$\left.\left. + \left(\frac{(-t_1 + t_{1c})\sin\theta + (t_2 - t_{2c})\cos\theta}{\sigma_2} \right)^2 \right) \right\},$$

5.4

where t_1 and t_2 are the TOFs of the first and second fragments respectively and t_{1c} and t_{2c} are the corresponding central peak coordinates, z_0 is an intensity offset, σ_1 and σ_2 are the standard deviations along the t_1 and t_2 axes respectively and θ is the angle of rotation anticlockwise from the positive t_1 direction.

Depending on the m/z values involved in each peak, they can be categorised as either two-body peaks if the summed m/z values add up to the monomer, or multibody peaks if they sum to a lower value indicating loss of at least one neutral fragment. Two-body peaks should have gradient of -1 due to conservation of momentum in the TOF tube [12]. The measured gradients of all the multibody peaks are greater than -1. If these peaks are taken to be three-body, the simplest scenario, this suggests a secondary decay of one of the fragments after an initial Coulomb explosion of the dication:

$$M^{2+} \rightarrow m_1^+ + m_2^+$$

$$m_2^+ \rightarrow m_3^+ + m_4$$

5.5

The variation of the calculated gradients with the fragment m/z values (Figure 5.12) shows that at least for fragments correlated to m/z 15, the peak gradient varies linearly with the second fragment's m/z. A linear fit gives the variation as $-0.0239(11) \approx -1/45$. If each fragment that is correlated with m/z 15 originated from the m/z 45 fragment, then the gradient of each peak is expected to be (according to Equation 3.31):

$$-\frac{m/z(detected\ fragment)}{45}.$$

5.6

This means the linear variation of the peak gradient with m/z would be $-1/45$ for those peaks correlated with m/z 15. The observed variation therefore corresponds approximately to the second fragments coming from dissociations of m/z 45, the $C_2H_5O^+$ moiety. The m/z 15 peaks are also the most intense in the coincidence spectrum. This suggests that the main fragmentation channel of a 2-propanol dication is $C_3H_7OH^{2+}$ $\rightarrow CH_3^+ + C_2H_5O^+$, which is similar to that of the monocation ($C_3H_7OH^+ \rightarrow CH_3 + C_2H_5O^+$) [108].

A notable exception is the ion pair $CH_3^+ + CH_3O^+$, for which the calculated peak gradient significantly deviates from this relationship. Using the peak gradient to estimate the mass of a parent cation does not correspond to any fragments in an acceptable mass range. Possible m/z values from which the CH_3^+ fragment could come are m/z 16 - 19, with the only possible precursor being CH_4^+ based on known fragments. Possible m/z values from which the CH_3O^+ fragment could come from are m/z 33 - 41, a range in which there are no known fragments that could be a precursor [108]. Even if such a fragment existed it would not preserve mass conservation for a 2-propanol monomer, making the fragmentation either that of a cluster or a four-body (at least) process. However, the peak in question is comparatively weak (Figure 5.11 (b) at (3550 ns, 4700 ns)) which is reflected in the large error and a better fit might be achieved with more statistics.

This suggests that the 2-propanol monomer is doubly-ionised before it fragments, ruling out the mechanism of DPI taking place via dissociative ionisation. It also suggests that any DPI mechanism that occurs is direct enough to happen before fragmentation of any superexcited singly-charged ion that might be created as an intermediate in an indirect process.

Ion pair (detected m/z values)	Possible fragments	Measured peak gradient	Possible mechanism (m/z values)	Possible mechanism (fragments)	Theoretical gradient of mechanism
15 + 19	$CH_3^+ + H_3O^+$	-0.40(2)	45 → 19	$C_2H_5O^+ \rightarrow H_3O^+$	-0.42
15 + 27	$CH_3^+ + C_2H_3^+$	-0.594(11)	45 → 27	$C_2H_5O^+ \rightarrow C_2H_3^+$	-0.60
15 + 28	$CH_3^+ + CO^+$ $CH_3^+ + C_2H_4^+$	-0.61(5)	45 → 28	$C_2H_5O^+ \rightarrow CO^+$ $C_2H_5O^+ \rightarrow C_2H_4^+$	-0.62
15 + 29	$CH_3^+ + CHO^+$ $CH_3^+ + C_2H_5^+$	-0.72(3)	41 → 29	$C_2HO^+ \rightarrow CHO^+$ $C_3H_5^+ \rightarrow C_2H_5^+$	-0.71
15 + 30	$CH_3^+ + CH_2O^+$	-0.677(17)	45 → 30	$C_2H_5O^+ \rightarrow CH_2O^+$	-0.67
15 + 31	$CH_3^+ + CH_3O^+$	-0.86(8)			
15 + 42	$CH_3^+ + C_2H_2O^+$	-0.90(3)	45 → 42	$C_2H_5O^+ \rightarrow C_2H_2O^+$	-0.93
15 + 43	$CH_3^+ + C_2H_3O^+$	-0.990(12)	45 → 43	$C_2H_5O^+ \rightarrow C_2H_3O^+$	-0.96
15 + 44	$CH_3^+ + C_2H_4O^+$	-1.002(18)	45 → 44	$C_2H_5O^+ \rightarrow C_2H_4O^+$	-0.98
15 + 45	$CH_3^+ + C_2H_5O^+$	-1.000(15)		2-body peak	-1
16 + 29	$CH_4^+ + CHO^+$	-0.61(5)	44 → 29	$C_2H_4O^+ \rightarrow CHO^+$	-0.66
16 + 30	$CH_4^+ + CH_2O^+$				
16 + 43	$CH_4^+ + C_2H_3O^+$	-1.03(3)	44 → 43	$C_2H_4O^+ \rightarrow C_2H_3O^+$	-0.98
16 + 44	$CH_4^+ + C_2H_4O^+$			2-body peak	-1
17 + 41	$OH^+ + C_3H_5^+$				
17 + 43	$OH^+ + C_3H_7^+$			2-body peak	-1
18 + 39	$H_2O^+ + C_3H_3^+$				
18 + 40	$H_2O^+ + C_3H_4^+$				
18 + 41	$H_2O^+ + C_3H_5^+$	-1.04(4)	42 → 41	$C_3H_6^+ \rightarrow C_3H_5^+$	-0.98
18 + 42	$H_2O^+ + C_3H_6^+$			2-body peak	-1
19 + 39	$H_3O^+ + C_3H_3^+$	-1.01(5)	41 → 39	$C_3H_5^+ \rightarrow C_3H_3^+$	-0.95
19 + 41	$H_3O^+ + C_3H_5^+$				
27 + 29	$C_2H_3^+ + CHO^+$				
27 + 31	$C_2H_3^+ + CH_3O^+$				

Table 5.4: Identified ion pairs from Coulomb explosions corresponding to the 2-propanol monomer at 33.3 eV. Entries left blank are where peaks were identified but signal levels were too low to reliably fit. 2-body peaks are direct Coulomb explosion of the 2-propanol dication with no neutral fragment generated and always have a theoretical gradient of -1.
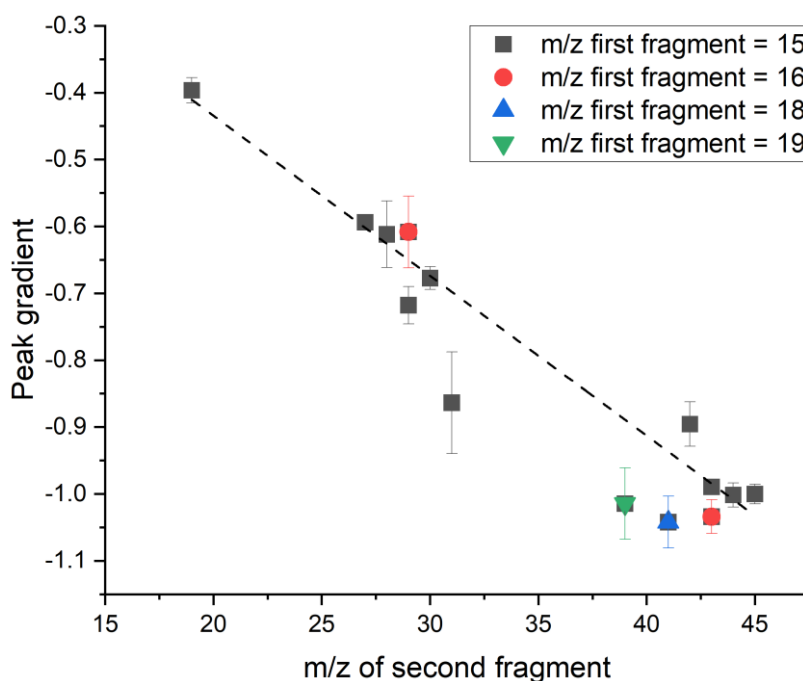
Figure 5.12: Variation of PIPICO peak gradients with the m/z value of the fragments including a linear fit of the data in which the m/z value of the first fragment is 15 (CH_3^+).

To further test this hypothesis, the kinetic energies of the ion pairs involving CH_3^+ are analysed using VMI (Figure 5.13). The CH_3^+ fragment kinetic energy varies between 2.6 and 3.6 eV, although the peaks are very broad and the signal-to-noise level is low. The kinetic energy of the observed fragment "X^+" that is correlated with the CH_3^+ shows a general trend of increasing with mass from 0.43(4) eV at m/z 19 to 1.19(1) eV at m/z 45. If the dication fragments primarily by Coulomb explosion into CH_3^+ and $C_2H_5O^+$, then the TKER should partition into the fragments in a 3:1 ratio by momentum conservation. This is confirmed in the CH_3^+ and $C_2H_5O^+$ pair, where CH_3^+ has kinetic energy 3.61(7) eV and $C_2H_5O^+$ has kinetic energy 1.19(1) eV, corresponding to a TKER of 4.80(7) eV. If the $C_2H_5O^+$ then fragments, then the kinetic energy of the X^+ will be reduced by a factor of $m_{X^+}/45$. Rescaling the kinetic energies to estimate the kinetic energy of the supposed parent ion gives an approximately constant value at 1.02(13) eV. The mean energy of the CH_3^+ fragment is 2.99(16) eV and the mean TKER is 4.0(2) eV. The CH_3^+ fragment having approximately constant kinetic energy suggests it always recoils from the same mass in the initial Coulomb explosion, and the scaling of the kinetic energy of X^+ suggests that it initially gains the kinetic energy as a $C_2H_5O^+$ ion which then further dissociates. This therefore supports the hypothesis that these fragments originally come from the $C_3H_7OH^{2+} \rightarrow CH_3^+ + C_2H_5O^+$ decay channel. This suggests that autoionisation of fragments after dissociation is unlikely to be a dominant DPI mechanism, which is consistent with previous observations that this does not often take place for molecules larger than a triatomic, or those without a terminal O atom [19], [21].

(a)

(b)

(c)
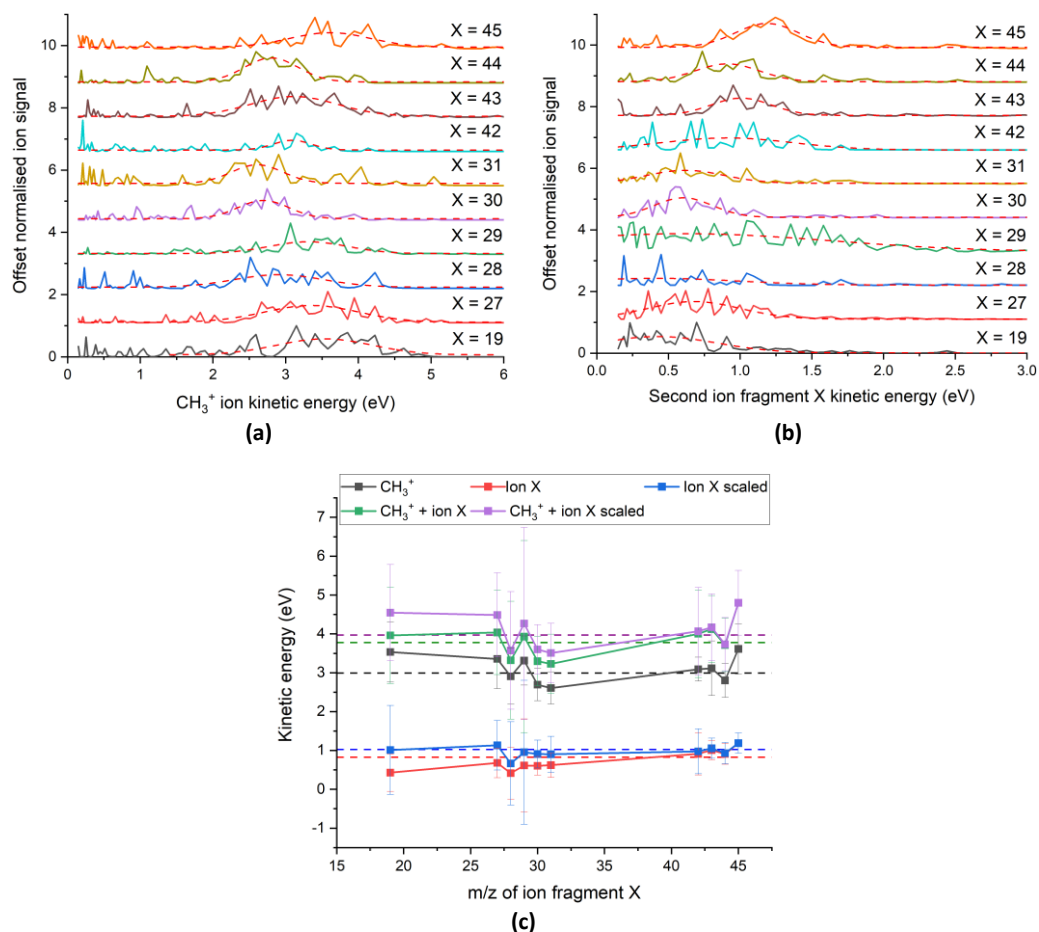
Figure 5.13: (a) Kinetic energy of CH_3^+ ions when correlated to fragment X^+ (b) Kinetic energy of X^+ when it is correlated to CH_3^+. Gaussian fits are given by the dashed lines. (c) Kinetic energy variations with m/z of X^+ given by the Gaussian peaks. Error bars are the half-width-at-half-maximum (HWHM) of the Gaussian fits. The kinetic energies of X^+ are also scaled by $m_X/45$. Dashed lines in (c) indicate weighted means.

5.3.2 Double photoionisation of 2-propanol clusters

2-propanol clusters can be seen in the uncorrelated mass spectrum (Figure 5.14), where there are fragments corresponding to dimers, trimers and tetramers. The strongest signals correspond to protonated clusters, as is common for ionised alcohol clusters [113], [128], [129], and indicates that they are fragments of larger clusters. Very weak cluster signals could be seen as high as the protonated hexamer $(IPA)_6H^+$, where IPA denotes a 2-propanol monomer unit. Other notable fragments present in the mass spectrum are those of an $(IPA)_n$ cluster bound to the $C_2H_5O^+$ ion at m/z 105, 165 and 225; the $C_2H_5O \cdot H_3O^+$ fragment [130], [131] at m/z 63, and the $(IPA) \cdot H_3O^+$ fragment at m/z 79. Additional peaks are at m/z 103, which is $[(CH_3)_2CH]_2OH^+$ formed through fragmentation of a protonated dimer, and at m/z 87 which is $C_5H_{11}O^+$ [128].
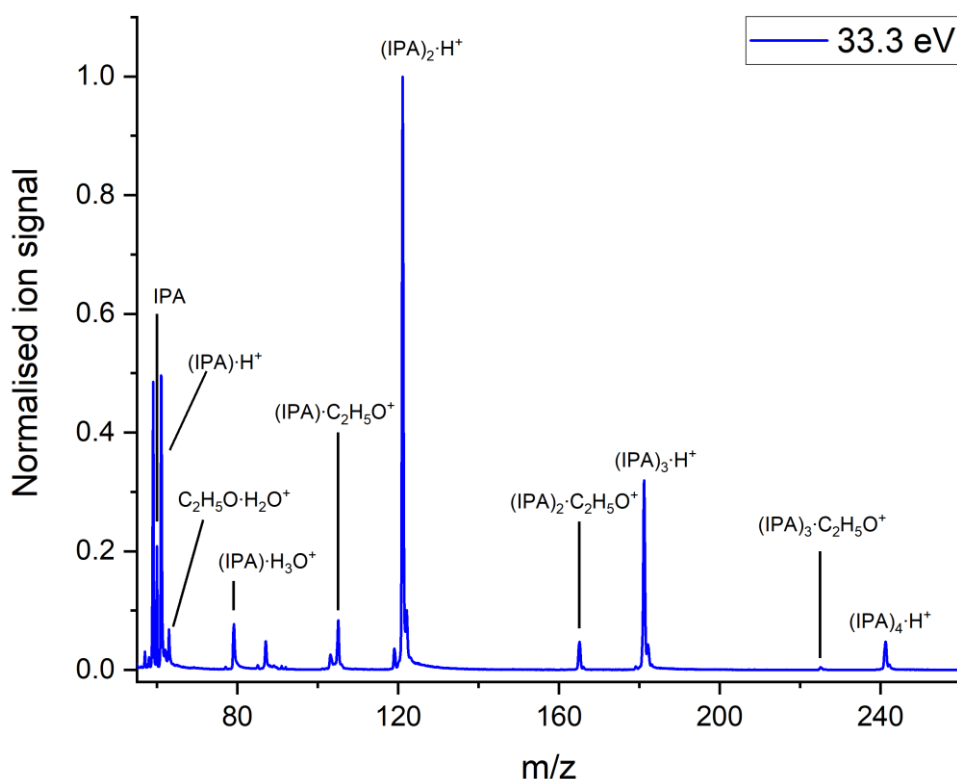
Figure 5.14: Mass spectrum of 2-propanol clusters recorded under static voltage conditions at 33.3 eV photon energy.

These fragments can also be seen in ion pair peaks in the coincidence mass spectrum (Figure 5.15). The fragment peaks are summarised (Table 5.5). Many of the clusters contain smaller "satellite" fragments hydrogen-bonded to monomer units of 2-propanol. The XUV photon is absorbed by a particular monomer unit of the cluster. If the DPI process proceeds similarly to what has been observed in the monomer, it might be expected that the irradiated monomer unit is doubly-ionised and dissociates the cluster into fragments where the satellite fragments are bonded to any remaining monomer units. The satellite fragment masses should therefore sum to a value equal or less than that of a monomer. For example, if a trimer $(IPA)_3 = (IPA)(IPA)(IPA)$ absorbs an XUV photon on the centrally marked monomer unit. This monomer might then be doubly-ionised and Coulomb explode, fragmenting the cluster. The process would be

$$(IPA)(IPA)(IPA) + h\nu \rightarrow (IPA)(IPA)^{2+}(IPA) + 2e^-$$
$$(IPA)(IPA)^{2+}(IPA) \rightarrow (IPA) \cdot CH_3^+ + C_2H_5O^+ \cdot (IPA).$$

5.7
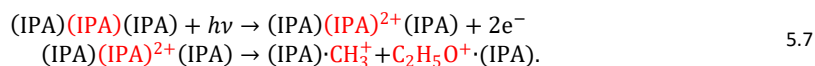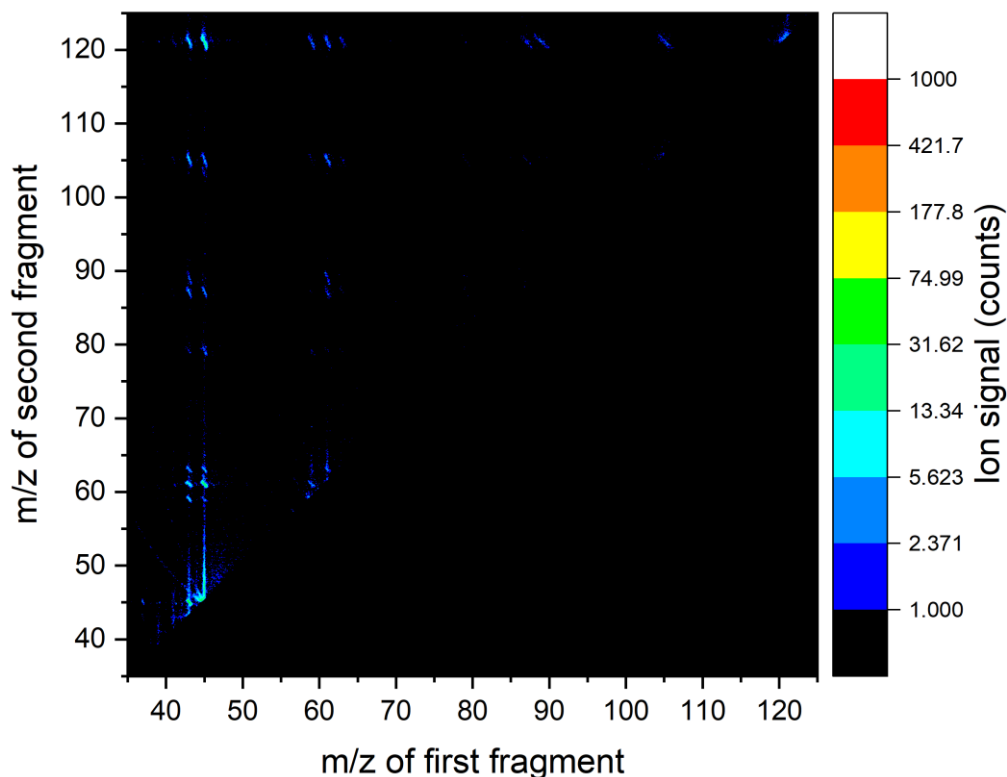
Figure 5.15: Coincidence mass spectrum of 2-propanol clusters at 33.3 eV photon energy.

In this case $(IPA)\cdot CH_3^+$ does not appear to favourably form [128] based on its absence in the mass spectrum and therefore might decay to $(IPA)\cdot H^+$, which is a prominent peak. Meanwhile the $C_2H_5O^+\cdot(IPA)$ fragment can remain stable (m/z 105). It can be seen that the CH_3^+/H^+ and $C_2H_5O^+$ satellite fragments sum to a monomer or less and therefore the two positive charges could possibly originate from the same monomer. However, many fragment pairs have satellite fragments that do not sum to less than a 2-propanol monomer. This might suggest that the positive charges could originate on different monomers. A potential explanation could be intermolecular Coulombic decay (ICD) [132]–[135], where ionisation of a monomer unit from an inner-valence orbital occurs (such as the O 2s orbital of 2-propanol), after which an outer-valence electron fills the inner-valence hole. The energy released by the relaxation then ionises a neighbouring neutral monomer, resulting in two singly-charged monomer units in the cluster. Alternatively, the electron relaxing into the vacancy can come from the neighbouring monomer, and the energy released re-ionises the original monomer unit, again resulting in two singly-charged monomer units. The cluster then Coulomb explodes and the satellite fragments do not necessarily sum to a mass of less than a monomer, since they originate from different monomer units. ICD has since come to be known as a commonplace process in weakly-bound systems [136]–[150]. Alternative explanations for the observed mass pairs might involve complex rearrangements of the cluster fragments; a knock-out mechanism where the primary photoelectron knocks a secondary electron from a different monomer unit; or a cluster absorbing two XUV photons at different monomer sites. However, the low photon density of the HHG and number density of clusters in the molecular beam make the latter explanation seem unlikely. Confirmation of this hypothesis would likely require the recording of PEPECO spectra and/or theoretical calculations. As mentioned previously for the analysis of DPI of the 2-propanol monomer, PEPECO spectra could possibly be recorded after upgrading the endstation.

Ion pair (m/z values)	Ion pair (possible fragments)	m/z sum	Summed m/z of satellite fragments	Satellite fragments possibly from same monomer unit?	Minimum possible parent cluster size (IPA units)
43 + 45	$C_2H_3O^+ + C_2H_5O^+$	88	88	✗	2
43 + 59	$C_2H_3O^+ + C_3H_7O^+$	102	102	✗	2
43 + 61	$C_2H_3O^+ + (IPA){\cdot}H^+$	104	44	✓	2
43 + 63	$C_2H_3O^+ + C_2H_5O{\cdot}H_2O^+$	106	61 or 88	✗	3
43 + 79	$C_2H_3O^+ + (IPA){\cdot}H_3O^+$	122	62	✗	3
43 + 87	$C_2H_3O^+ + C_5H_{11}O^+$	130	70	✗	3
43 + 89	$C_2H_3O^+ + (IPA){\cdot}CHO^+$	132	72	✗	3
43 + 105	$C_2H_3O^+ + (IPA){\cdot}C_2H_5O^+$	148	88	✗	3
43 + 121	$C_2H_3O^+ + (IPA)_2{\cdot}H^+$	164	44	✓	3
43 + 165	$C_2H_3O^+ + (IPA)_2{\cdot}C_2H_5O^+$	208	88	✗	4
43 + 181	$C_2H_3O^+ + (IPA)_3{\cdot}H^+$	224	44	✓	4
45 + 59	$C_2H_5O^+ + C_3H_7O^+$	104	104	✗	2
45 + 61	$C_2H_5O^+ + (IPA){\cdot}H^+$	106	46	✓	2
45 + 63	$C_2H_5O^+ + C_2H_5O{\cdot}H_2O^+$	108	63 or 90	✗	2
45 + 79	$C_2H_5O^+ + (IPA){\cdot}H_3O^+$	124	64	✗	3
45 + 87	$C_2H_5O^+ + C_5H_{11}O^+$	132	72	✗	3
45 + 103	$C_2H_5O^+ + [(CH_3)_2CH]_2OH^+$	148	88	✗	3
45 + 105	$C_2H_5O^+ + (IPA){\cdot}C_2H_5O^+$	150	90	✗	3
45 + 121	$C_2H_5O^+ + (IPA)_2{\cdot}H^+$	166	46	✓	3
45 + 165	$C_2H_5O^+ + (IPA)_2{\cdot}C_2H_5O^+$	210	90	✗	4
45 + 181	$C_2H_5O^+ + (IPA)_3{\cdot}H^+$	226	46	✓	4
59 + 61	$C_3H_7O^+ + (IPA){\cdot}H^+$	120	60	✓	2
59 + 79	$C_3H_7O^+ + (IPA){\cdot}H_3O^+$	138	78	✗	3
59 + 87	$C_3H_7O^+ + C_5H_{11}O^+$	146	86	✗	3
59 + 105	$C_3H_7O^+ + (IPA){\cdot}C_2H_5O^+$	164	104	✗	3
59 + 121	$C_3H_7O^+ + (IPA)_2{\cdot}H^+$	180	60	✓	3
61 + 63	$(IPA)H^+ + C_2H_5O{\cdot}H_2O^+$	124	19 or 46	✓	3
61 + 79	$(IPA)H^+ + (IPA){\cdot}H_3O^+$	140	20	✓	3
61 + 87	$(IPA){\cdot}H^+ + C_5H_{11}O^+$	148	28	✓	3
61 + 89	$(IPA){\cdot}H^+ + (IPA){\cdot}CHO^+$	150	30	✓	3
61 + 103	$(IPA){\cdot}H^+ + [(CH_3)_2CH]_2OH^+$	164	44	✓	3
61 + 105	$(IPA){\cdot}H^+ + (IPA){\cdot}C_2H_5O^+$	166	46	✓	3
63 + 79	$C_2H_5O{\cdot}H_2O^+ + (IPA){\cdot}H_3O^+$	142	37 or 64	✗	4
63 + 87	$C_2H_5O{\cdot}H_2O^+ + C_5H_{11}O^+$	150	45 or 72	✓/✗	3
63 + 105	$C_2H_5O{\cdot}H_2O^+ + (IPA){\cdot}C_2H_5O^+$	168	63 or 90	✗	4
63 + 121	$C_2H_5O{\cdot}H_2O^+ + (IPA)_2{\cdot}H^+$	184	19 or 46	✓	4
79 + 87	$(IPA){\cdot}H_3O^+ + C_5H_{11}O^+$	166	46	✓	3
79 + 89	$(IPA){\cdot}H_3O^+ + (IPA){\cdot}CHO^+$	168	48	✗	3
79 + 105	$(IPA){\cdot}H_3O^+ + (IPA){\cdot}C_2H_5O^+$	184	64	✗	4
87 + 103	$C_5H_{11}O^+ + [(CH_3)_2CH]_2OH^+$	190	72	✗	4
87 + 121	$C_5H_{11}O^+ + (IPA)_2{\cdot}H^+$	208	28	✓	4
89 + 121	$(IPA){\cdot}CHO^+ + (IPA)_2{\cdot}H^+$	210	30	✓	4
105 + 121	$(IPA){\cdot}C_2H_5O^+ + (IPA)_2{\cdot}H^+$	226	46	✓	4

Table 5.5: Identified Coulomb explosion ion pairs corresponding to 2-propanol clusters at 33.3 eV

5.3.3 Metastable states of singly-charged 2-propanol monomer and cluster ions

The coincidence mass spectrum of 2-propanol and its clusters ionised at 33.3 eV is shown (Figure 5.16). There are long, faint lines originating from the autocorrelation line and extending asymptotically towards a smaller m/z value along the x-axis, while proceeding to very large m/z values along the y- axis. The specific lineshapes, extending to infinite values of the second fragment m/z rather than a peak location, confirm that they are signatures of metastable monocations rather than dications. The metastable parent ion can be easily diagnosed from the tails' origins on the autocorrelation line. However, it is more difficult concerning the daughter fragments, as the tail lengths depend on detecting both the charged and neutral fragments and the neutral detection efficiency quickly decreases at low parent lifetimes. Diagnosis is done using the model developed in Section 3.1.3.1 and based on prior knowledge of metastable fragmentations in the 2-propanol monomer [108] and dimer [128].
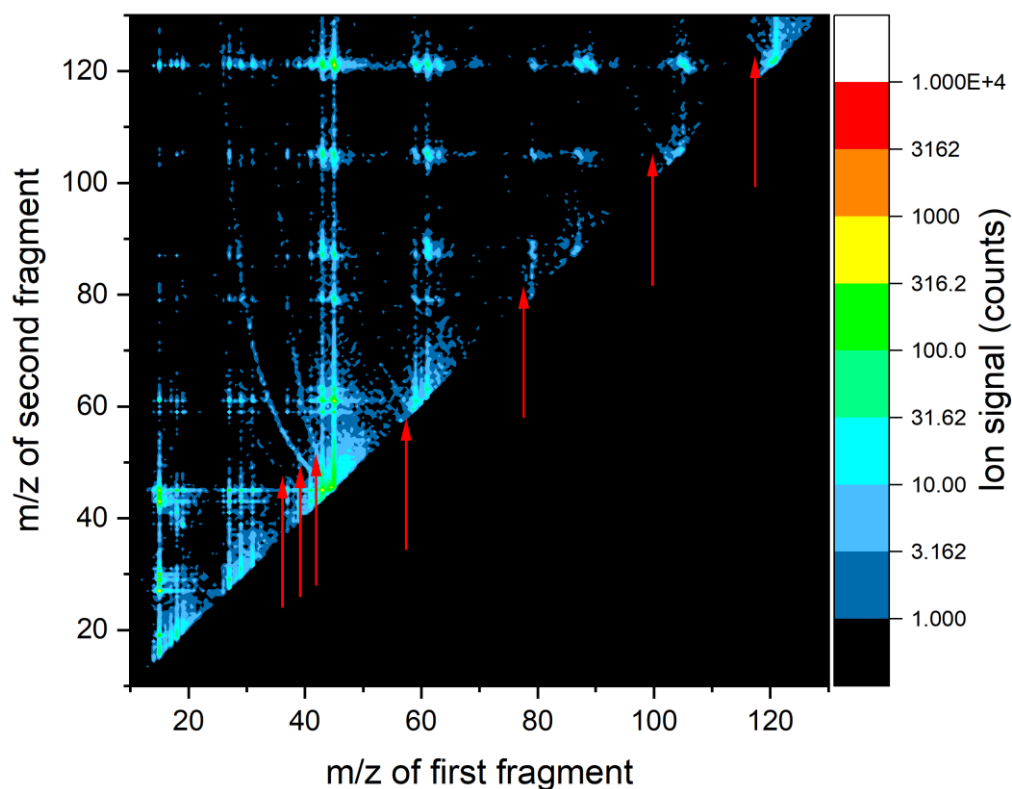
Figure 5.16: Coincidence TOF spectrum of 2-propanol monomers and clusters at 33.3 eV photon energy. Faint lines of signal marked by red arrows can be seen extending from the autocorrelation line at m/z values of 43, 45, 59, 60, 79, 103, 121. False coincidences are not removed in this spectrum (in contrast to Figure 5.15) to show how the metastable tails can overlap with them, a matter which is further discussed later in this section.

In Ref. [48], an ion-ion covariance spectrum recorded at 20 eV photon energy showed metastable signatures that were assigned to the delayed fragmentations based on a similar model as derived in Section 3.1.3.1:

$$C_2H_5O^+ \rightarrow C_2H_4 + OH^+$$

$$C_2H_5O^+ \rightarrow C_2H_4^+ + OH.$$

5.8
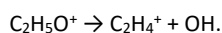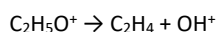
This corresponds to an ion with m/z 45 fragmenting to ions of m/z 17 and m/z 28 respectively. In contrast, the best fits of the model used here correspond to the fragmentations of an ion of m/z 45 to ions of m/z 19 and m/z 29:

$$C_2H_5O^+ \rightarrow CHO^+ + CH_4$$

$$C_2H_5O^+ \rightarrow H_3O^+ + C_2H_2$$

5.9

This is supported known by fragmentation pathways of $C_2H_5O^+$ [108] as well as by the line shapes in the 1D mass spectrum (Figure 5.17) where tails towards higher mass-to-charge ratios are visible on the peaks at m/z 19 and m/z 29. There are many additional delayed fragmentations observed at lower signal levels (Table 5.6).

(a)   **(b)**
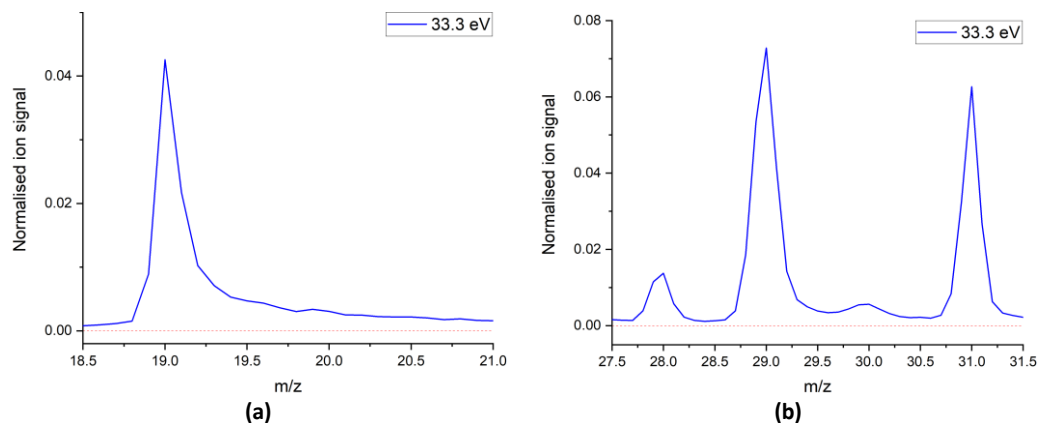
Figure 5.17: Mass spectrum peaks of metastable signature of (a) H_3O^+ (m/z 19) and (b) CHO^+ (m/z 29). The metastable signature is given by the long tails of slowly decreasing intensity to higher m/z, confirming that they are product fragments of a metastable process. It is harder to see for the m/z 29 peak due to the presence of other peaks nearby, but can be inferred by comparison of the signal levels between peaks on either side of the m/z 29 peak to the red line at zero signal.

Ion fragmentation (observed m/z values)	Ion fragmentation (proposed fragments)
43 → 15	$C_2H_3O^+ \rightarrow CH_3^+ + CO$
45 → 19	$C_2H_5O^+ \rightarrow H_3O^+ + C_2H_2$
45 → 29	$C_2H_5O^+ \rightarrow CHO^+ + CH_4$
59 → 29	$C_3H_7O^+ \rightarrow C_2H_5^+ + CH_2O$
59 → 41	$C_3H_7O^+ \rightarrow C_3H_5^+ + H_2O$
60 → 43	$C_3H_7OH^+ \rightarrow C_3H_7^+ + OH$
79 → 61	$(IPA)\cdot H_3O^+ \rightarrow (IPA)\cdot H^+ + H_2O$
103 → 61	$[(CH_3)_2CH]_2OH^+ \rightarrow (IPA)\cdot H^+ + C_3H_6$
121 → 61	$(IPA)_2\cdot H^+ \rightarrow (IPA)\cdot H^+ + IPA$
121 → 79	$(IPA)_2\cdot H^+ \rightarrow (IPA)\cdot H_3O^+ + C_3H_6$
121 → 103	$(IPA)_2\cdot H^+ \rightarrow [(CH_3)_2CH]_2OH^+ + H_2O$
165 → 121	$(IPA)_2\cdot C_2H_5O^+ \rightarrow (IPA)_2\cdot H^+ + CH_3CHO$
181 → 121	$(IPA)_3\cdot H^+ \rightarrow (IPA)_2\cdot H^+ + IPA$
241 → 181	$(IPA)_4\cdot H^+ \rightarrow (IPA)_3\cdot H^+ + IPA$

Table 5.6: Observed metastable fragmentations of singly-charged 2-propanol cations at 33.3 eV.

The model developed in Section 3.1.3.1 is used to isolate coincidences corresponding to the metastable states, and reject all others. This is shown in Figure 5.18 for the fragmentations m/z 43 → 15, 45 → 19 and 45 → 29 where the trails are seen extending from the autocorrelation line. A ± 50 ns-wide "window" is created around the model through which to show the metastable signatures. The signal is saturated at 1 count and false coincidences are not removed here in order to illustrate their presence in the lifetime variation plot (Figure 5.19). The lifetime variation shows the signal variation of the metastable fragmentations with

"lifetime" (as accurately as the model can determine it). A large spike is present at approximately 620 ns lifetime. This signal indicates fragmentations in the drift tube, which appear on the autocorrelation line in the coincidence TOF spectrum. The spike is high as all fragmentations in the drift tube arrive at this same point regardless of where in the drift tube it happens. Also, the detection efficiency is highest here as both particles have been accelerated to their highest possible velocity in the acceleration region. The signal rapidly drops off and decreases with shorter lifetimes, possibly due to the natural signal variation, but almost certainly due to reduced detection efficiency of the neutral, which is much slower with earlier fragmentations. Previous observations of such metastable tails of adenine [151] in coincidence spectra used the ratio of the signal level between parent and fragment peaks in the uncorrelated TOF spectrum, and the intensity of the tail to estimate the neutral detection efficiency at 15%. However, this would only give an average value and not a variation with lifetime. Other spikes can be seen in the variations which are false coincidences or Coulomb explosion peaks as seen in Figure 5.18 near the beginning of the tails. There is no method yet to remove false coincidence effects from these signals although one might be possible by determining the coincidence TOF histogram bins corresponding to each lifetime histogram bin and subtracting the appropriate value.
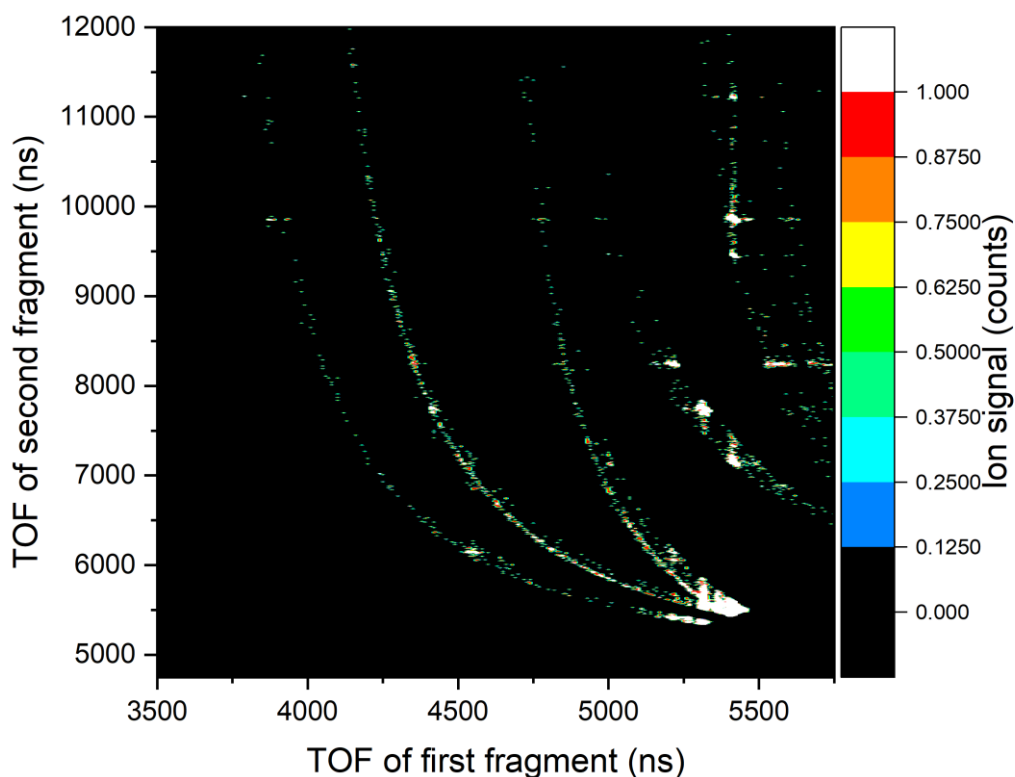
Figure 5.18 : Coincidence TOF spectrum of 2-propanol monomers and clusters at 33.3 eV photon energy with coincidence corresponding to metastable fragmentations of the first three entries in Table 5.6 isolated using a ± 50 ns wide margin. Originating from the side of the spectrum are the coincidence windows corresponding to m/z 59 $\rightarrow$ 29 and m/z 59 $\rightarrow$ 41 fragmentations.
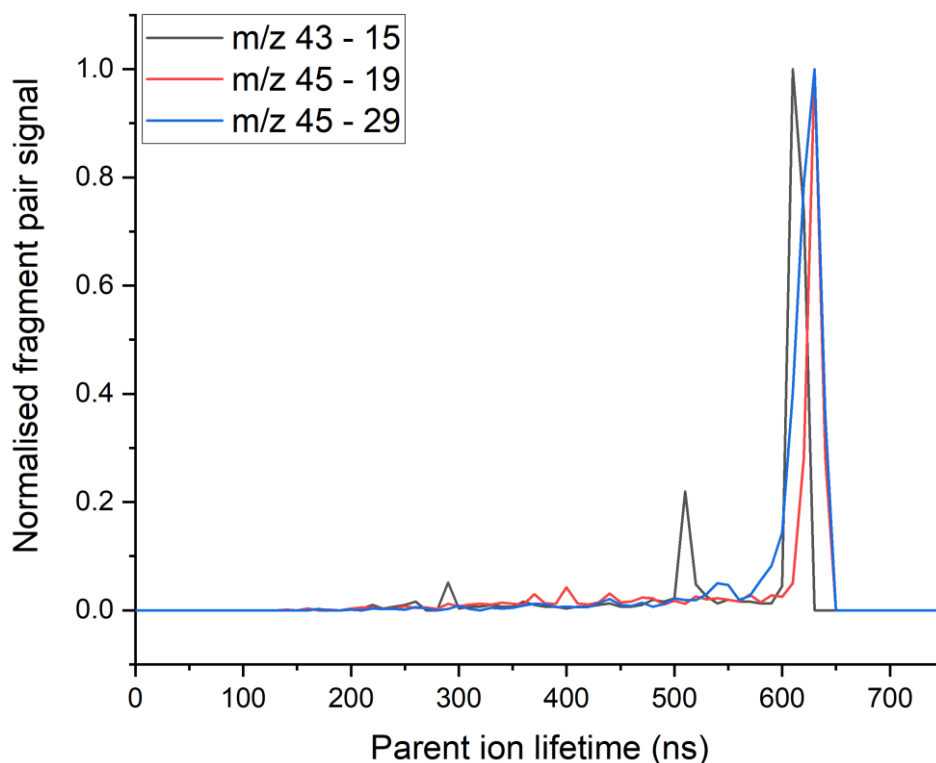
Figure 5.19: Variation of signal with lifetime of metastable fragmentations $m/z\ 43 \rightarrow 15$, $m/z\ 45 \rightarrow 19$, $m/z\ 45 \rightarrow 29$.

The lifetime variations and ion images in the metastable fragmentations could be improved by recording the spectra at photon energies below the DIP with static voltages. Not having ion-ion coincidences originating from DPI will clean up the PIPICO maps while still leaving the ion-neutral coincidences, and using the static voltages will allow for a better fit of the method to the data which will give more accurate lifetimes. Additionally, lower ionisation rates would be needed to better deal with false coincidences. While they can be removed in the coincidence TOF spectra, the results are noisy and there is no way yet to diagnose and remove false coincidences in the data file to clean up the lifetime variation plots.

The model is therefore of limited success. It is effective at diagnosing and isolating the coincidences due to metastable fragmentations. However, it can only give qualitative information on the lifetime variation as the scale is not strictly accurate (see Section 3.1.3.1) and it also requires correction for the detection efficiency of the neutral fragment. Additionally, much of the signal is "hidden" around the autocorrelation line due to fragmenting in the drift tube. This could at least be partly ameliorated in the existing setup by using weaker extraction voltages to increase the TOF, which would allow longer parent ion lifetimes to manifest before the drift tube, but this would further affect the detection efficiency. Metastable dication lifetimes can be determined by using a Monte Carlo simulation [152], [153] on the signal variation with the time difference between the two fragments and the same procedure can be done here, again assuming the neutral detection efficiency is accounted for, without the need for the model. So, it is perhaps difficult to see the benefit that the model brings in this regard. It is however effective at isolating the relevant coincidences and diagnosing certain fragmentations for which the involved m/z values might otherwise remain unclear. Isolating the metastable coincidences could be used to plot photoelectron spectra and ion VMI images uniquely belonging to these metastable states. However, in the present work the very low signal-to-noise levels of the metastable signatures meant that these images provided little to no useful information. This is further exacerbated by the fact the metastable signatures are those of single ionisation, so many of the photoelectrons in coincidence with these ion-neutral pairs will be too fast for the detector when obtained with the HHG.

5.4 Conclusion

The photoionisation of 2-propanol monomers and clusters with XUV radiation was investigated by velocity-map imaging of PEPICO, PIPICO and PEPIPICO coincidences. DPI of monomers was seen to occur at photon energies of 30.1 eV and above by examination of fast CH_3^+ fragments coming from a Coulomb explosion. The DPI of the monomer was examined by inspection of the emitted electrons detected in PEPIPICO coincidence with the fast methyl fragments and fragments up to m/z 45. The partial DPI spectra at each photon energy showed an onset of electron signal at approximately 28 eV. Since the partial DPI spectra are recorded with only one of the two emitted photons, this value remains an upper bound for the true value of the onset and DIP. It would represent a correct value if it was known that the electron sharing distribution is such that the fastest electrons are correlated with threshold electrons. Ambiguity would be resolved by detecting electron-electron coincidences with energy analysis which would allow a complete DPI spectrum to be recorded. Without complete DPI spectra or electron-electron coincidence spectra, the DPI mechanism was unclear. The results could be expanded on by extending the experiment to higher photon energies, where the two electron peaks might separate to distinct values. However, any results of this could be obscured if the higher photon energies trigger additional processes such as excitation to higher dication states. Analysis of the ion-ion coincidences after DPI suggests that most fragmentations proceed through the channel $C_3H_7OH^{2+} \rightarrow CH_3^+ + C_2H_5O^+$ by an initial Coulomb explosion before $C_2H_5O^+$ decays further. This suggests that the mechanism of autoionisation of fragments after dissociation of a singly-charged cation is unlikely, which is consistent with prior observations that this mechanism is restricted to small (diatomic or triatomic) molecules with a terminal O atom. The mechanism of DPI is therefore still uncertain but is most likely to be either a knock-out or inner-valence Auger-Meitner process.

A large number of ion pairs corresponding to Coulomb explosions of 2-propanol clusters were identified in coincidence TOF spectra. Ion pairs belonging to parent clusters at least as large as tetramers were observed. Analysis of the masses of the pairs appeared to suggest that the two positive charges created by DPI originate on different monomer units. This might suggest that a process such as ICD is taking place. Like the 2-propanol monomer, further confirmation of this would require observation of electron-electron coincidences from these ion pairs, something the endstation is currently incapable of.

Metastable fragmentations of the singly-charged monomer and clusters were observed on inspection of coincidence TOF spectra. They were diagnosed by long coincidence tails extending from the autocorrelation line. The fragmentations were identified based on known fragmentation pathways of 2-propanol from literature and aided using the theoretical model developed in Chapter 3 for this purpose. The model allows isolation of coincidences specifically belonging to the metastable fragment pairs from the data file and the signal variation with parent ion lifetime to be determined. However, the calculated lifetime has previously been seen to be inaccurate and any quantitative analysis must also consider the variation of the MCP detection efficiency of the neutral fragment for which the incident velocity on the detector varies greatly with the lifetime. The model can allow photoelectron spectra coincident to the metastable fragmentations to be plotted as well as ion images of the neutral and ionic fragments. However, in the present work these images were not of sufficient quality to provide any useful information.

6 Conclusion

The details of an experimental endstation for investigating microsolvation effects on time-resolved excited state dynamics in polyatomic molecules has been described. The endstation was designed, simulated, constructed, characterised and coupled to an HHG facility during the work of this thesis. The endstation was originally planned to perform time-resolved CIS experiments on molecules doped in size-controlled clusters and nanodroplets in which photoelectrons and photoions would be imaged onto two opposite detectors. Currently it can perform static CIS experiments on molecules and small, undoped clusters by imaging the photoelectrons and photoions onto the same detector.

The endstation is currently capable of being used for several variations of photoionisation experiments and was extensively characterised accordingly. Fixing the electrode potentials at positive values allowed detection of ions and gave TOF and VMI information. This mode also allows observation of PIPICO coincidences, or ion-neutral coincidences if the parent ion is sufficiently metastable. Fixing the electrode potentials at negative values allowed detection of electrons and gave VMI information. The last mode of operation involved initially holding the electrode potentials at negative values to detect the electrons before using HV Behlke switches to change them to positive values and detect the ion before it left the interaction region. This operating mode allowed detection of electrons and ions together, allowing observation of PEPICO and PEPIPICO coincidences. The limitations of the DLD meant that a maximum of only one electron could be detected per laser shot, while the phosphor screen arcing problems prevented it from obtaining coincidence information. These factors mean that PEPECO coincidences could not be observed in this work. For operating modes where the voltages are held at fixed values; 2, 3 or 4 electrodes could be used. For the switched-voltage operating mode, the number of available power supplies meant that only 2 or 3 electrodes could be used.

The endstation performance of TOF-MS experiments on photoions for mass analysis was investigated. The relationship between TOF and m/z was calibrated and the m/z-dependent resolution characterised for two of the operating modes: where the voltages were fixed at positive values, and when they were switched from negative to positive values. A gas-phase molecular beam mixture composed of water, oxygen, 2-propanol and toluene was photoionised using 780 nm femtosecond pulses in an ATI scheme. This allowed characterisation of the instrument performance across the range from m/z 18 to m/z 92. The TOF operation was found to be capable of resolving mass units up to approximately 1000 amu using static 2- or 3-electrode operation, and 2500 for static 4-electrode operation. This was more than adequate for the experiments performed here, but it is uncertain if that would be the case for the initially planned experiments on large, doped clusters. The switched-voltage operation resulted in large, m/z-dependent perturbations to the ion flight trajectories. This is due to ions of different m/z value travelling different distances away from the interaction region during the time when the electrode potentials are negative and imaging the electrons. The ions must then be turned around when being imaged by the positive voltages. This meant that multiple switched-voltage schemes were available, depending on both the electron-imaging conditions and ion-imaging conditions. Using high, negative voltages, which is necessary to image fast electrons, would increase the distance the ions travelled in the wrong direction. The current limits of the HV switches would also limit how high the positive voltages could be to recover the ions when high negative voltages are used. Conversely, using low negative voltages is minimally perturbative and allows high positive voltages to effectively recover the ions. The m/z-dependence of the ion trajectory perturbations means that the exact voltage conditions can optimised for ions of a single m/z value, with the resolution of the TOF peaks of other ions subsequently suffering. The 3-electrode switching schemes were characterised for the ions and found that the TOF resolution could be as low as 100 if detecting m/z 18 when the voltages are optimised for m/z 92 and strong negative potentials are used for electron imaging. Heavier ions tend to suffer less, and the TOF resolution can be up to 2800 for m/z 92 if detected under optimal voltage conditions. This means that effectively performing switched-voltage

experiments requires careful consideration of the electron kinetic energy range and the particular ions of interest. Detecting fast electrons (such as those created by photoionisation with the HHG) in coincidence with light ions can be difficult. Multiple datasets could be required, with the voltages optimised for different ions each time, if there is a wide enough range of ions of interest or the resolution requirements are stringent enough. These factors could be ameliorated if the MCP-VMI is successfully commissioned for coincidence detection because imaging the electrons and ions onto different detectors means that the ions do not travel the wrong way when the electrode voltages are negative and therefore do not need to be recovered in the same way. Additionally, the switching scheme would change so that high voltages can be used to image both electrons and ions more effectively.

The ion VMI performance was investigated by examining the spatial focusing of the ions of the four species in the molecular beam for both static- and switched-voltage schemes. The FWHM resolution varies from 150 µm at high voltage to 300 µm at low voltage for the static scheme. Like the TOF resolution, the ion spatial resolution using switched voltages varies strongly with m/z and the specific voltage scheme. Detecting ions under favourable conditions gives spatial resolution of approximately 250 µm, while unfavourable conditions can give extremely large spot widths. For example, detecting light ions when the voltages are optimised for heavy ions and strong electron-imaging settings are used can give spot widths over 10,000 µm wide. As already suggested by the TOF example, this means care must be taken when considering imaging fast electrons in coincidence with light ions. Calibration of the VMI in terms of the relationship between radial distance and kinetic energy was based on observing slow (approximately 0.2 eV) and fast (approximately 3.2 eV) CH_3^+ ions arising from XUV photoionisation of 2-propanol. The slow ions are from dissociation of the 2-propanol monocation, while the fast ions come from Coulomb explosion of the 2-propanol dication. The calibration shows that there is a dependence on both m/z and the kinetic energy of the detected ion when switching the voltages. This is because both parameters affect the distance the ion travels from the interaction region before the voltages are switched to image it.

The electron VMI performance was investigated using the HHG source for single-photon ionisation on an atomic beam mixture composed of helium, neon and argon. The relationship between radial distance and kinetic energy was calibrated and the kinetic energy-dependent resolution was characterised. Photoelectron VMI performance is the same regardless of whether they are detected alone or in coincidence with photoions as the voltage switching does not take place until after the electrons are detected. These experiments were performed on both the DLD-VMI and the CCD-VMI. The kinetic energy resolution gets worse with increasing kinetic energy, as is expected in VMI, but generally goes from approximately 0.2 eV FWHM of the photoelectron peak for 1 eV electrons to 0.7 eV FWHM at 15 eV for the DLD-VMI and 0.2 eV FWHM at 1 eV to 0.4 eV FWHM at 15 eV for the CCD-VMI. The nominal energy resolution of the HHG setup is approximately 0.2 eV. Analysis of the photoelectron VMI images from the DLD-VMI showed that they were distorted, as the kinetic energy rings were not circular but appeared to contain both elliptical and higher order deformations. This may arise from the presence of stray magnetic fields, noise from other equipment such as turbopumps, or an artefact of the DLD itself. The images were repaired using a recircularisation procedure before calibration and resolution characterisation.

The DPI of toluene was investigated and compared with existing literature. DPI was confirmed to occur at photon energies higher than 23.9 eV by the presence of a dication peak of toluene. The partial DPI spectrum was recorded by detecting one of the electrons in coincidence with this fragment. From this spectrum the DIP was estimated to be at 23.8 eV, in agreement with literature. This was despite the fact that only one of the two electrons emitted in any single DPI event could be detected per laser shot, which prevented complete DPI spectra from being recorded. The agreement is attributed to the mechanism proceeding via Auger decay of an inner valence-hole state, which can give concave electron pair distributions, where the fastest electrons in a pair are often correlated with a threshold electron. Observation was also made of a dication peak corresponding to molecular hydrogen loss and a dication peak corresponding to atomic hydrogen loss.

Signatures of a metastable toluene dication were seen in the 1D TOF. Coincidence TOF spectra revealed further metastable signatures of both the dication and monocation parent fragmentations. Numerous ion-pair peaks corresponding to Coulomb explosion of dication parents were observed at 30.5 eV photon energies. Most of these indicated 2-body fragmentations of the toluene monomer, but one peak suggested a 3-body fragmentation of a toluene tetramer. This experiment was an initial trial of the coincidence capabilities of the endstation coupled with the HHG source and revealed several experimental issues in the setup that negatively affected the quality of the data and required addressing before the next experiments.

The DPI of 2-propanol monomers was investigated. DPI was determined to have occurred through the observation of fast CH_3^+ fragments, which is attributed to coming from Coulomb explosions of a dication. The onset of signal corresponding to the DIP was estimated to be approximately 28 eV by recording PEPIPICO coincidences and analysing the partial DPI spectrum in coincidence with the fast CH_3^+ fragments and a second fragment that has an m/z of 45 or less. However, the details of the DPI mechanism remained ambiguous from the electron analysis. Recording PEPECO spectra would better determine the threshold and possibly also elucidate the mechanism, however this experiment requires the CCD-VMI arcing issues to be resolved and the setup to be upgraded. Analysis of the ion-ion coincidences suggests that the dication is formed and primarily decays via the $C_2H_7OH^{2+} \rightarrow CH_3^+ + C_2H_5O^+$ channel in a Coulomb explosion. The $C_2H_5O^+$ ion then may decay further. This suggests the DPI mechanism does not proceed via autoionisation of fragments after dissociation of an excited monocation state and is more likely to be either Auger-Meitner decay of an inner valence-hole state or a knock-out mechanism.

DPI was also determined to have occurred in 2-propanol clusters at least as large as the tetramer by observation of specific ion pairs in coincidence with high kinetic energies. Analysis of the ion-ion coincidences from these clusters suggest that the two positive charges created by DPI are born on different monomer units. This is due to the observation that many of the ion pairs are composed of 2-propanol fragments hydrogen-bonded to a larger cluster and that these fragment pairs often do not follow mass or element conservation for a 2-propanol monomer. A potential mechanism proposed is that of ICD, which would result in each positive charge being created on a different monomer unit in the original parent cluster. Other potential mechanisms include a knock-out process similar to that possible for the monomer. Like the monomer case, further analysis to determine this mechanism would benefit greatly from the ability to perform PEPECO experiments on an upgraded endstation

Long-lived metastable states of the singly-charged ion were determined to have occurred through the observation of long "tailing" of ion-neutral fragment coincidence signals going from TOF values corresponding to immediate fragmentation to very high TOF values. An attempt was made at developing a model that would allow determination of the lifetimes of the parent ions. However, it fell short in two areas: the approximation of a uniform electric field in the acceleration region resulted in the calculated lifetimes being underestimated compared to SIMION simulations, and it does not account for the variation of neutral fragment detection efficiency. The model was however accurate at reproducing the shapes of the metastable tails in coincidence TOF spectra.

By the end of this thesis work, the endstation was capable of being used for CIS experiments, but not to the specifications initially planned. The cryogenic source required for generating large clusters and nanodroplets, and the crucible oven for doping them, were not constructed. The source was also intended to use a piezo cantilever valve which would produce a high-intensity pulsed molecular or cluster beam. However, this was not installed. Instead, the source was only able to create continuous room-temperature or heated beams of isolated molecules or small clusters. CIS was also only achieved on one of the two detectors, the DLD-VMI, because the MCP with phosphor screen detector had arcing problems that were never resolved. This meant that the CCD-VMI was able to acquire velocity-map images, but could give no TOF or coincidence information. This restricted the capabilities of the endstation when being used with the HHG laser because the high photon

energy creates fast electrons which are difficult to image in coincidence with light ion masses. Additionally, while the endstation was coupled with the HHG laser and a Ti:sapphire femtosecond laser individually for separate experiments, the synchronisation of the two light sources for use in time-resolved pump-probe experiments was never performed. This means only singe-laser experiments could be performed in this work. The culmination of the part of the work in this thesis based on endstation construction therefore represents a project that is essentially unfinished. Future work prospects regarding reaching the endstation's original purpose are therefore clear. Absent ambitions to reach the project's original goal, the uncertainties regarding the 2-propanol DPI in terms of both its potential and mechanism can be most effectively explored via the observation of electron-electron coincidences, which could potentially be achieved by upgrading the CCD-VMI.

A.   Time-of-flight derivations

This appendix contains more detailed versions of the derivations for the TOF equations given in Chapter 3.

a. Static voltages ion time-of-flight

The TOF operation of the detector can be described as having three categories of components (Figure A.6.1): The extraction region, labelled $N = 0$, where the charged particles are first generated and accelerated towards the detector; the intermediate acceleration region(s), labelled $N = 1,2,3 \dots$, where particles continue to be accelerated; and the field-free drift tube, where the particles travel towards the detector with a constant final velocity. Depending on whether a lens electrode is used in this setup, there can be one or two intermediate acceleration regions, with the effective length of the drift tube changing accordingly.

4-electrode mode

2- and 3-electrode modes
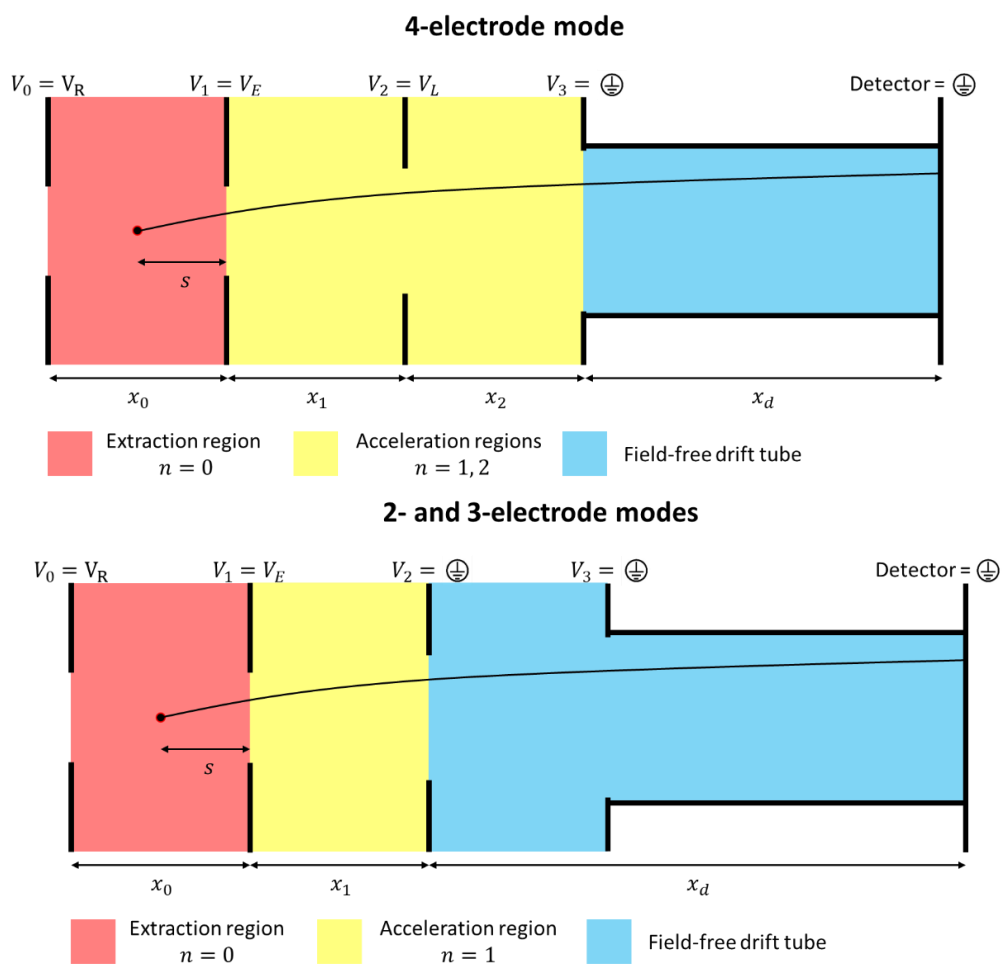
Figure A.6.1: Schematic of the TOF operation on the DLD-VMI for static voltages showing the flight path of the ions or electrons through the different regions. The different regions are colour-coded. Top: 4-electrode mode, where there are two intermediate acceleration regions coloured yellow. Bottom: 2- and 3-electrode modes, where there is one acceleration region due to the lens electrode being grounded and so the effective length of the field-free drift tube x_d is increased. In all operation modes, the repeller electrodes $V_0 = V_R$ are graphically represented here as a single solid electrode for simplicity.

In determining the relationship between time of flight and mass, the particle is assumed to begin with zero initial velocity u_0 in the direction of the TOF axis, as the molecular beam travels in a direction perpendicular to this axis, and transverse spread is minimal. All electric fields are approximated to be uniform, which will give constant acceleration values.

The acceleration a_N of a charged particle in a TOF-MS region N with a uniform electric field E_N is

$$a_N = -\frac{z}{m}E_N = \frac{z}{m}\frac{V_N - V_{N+1}}{x_N} = \frac{z}{m}\frac{\Delta V_N}{x_N}, \tag{A.1}$$

where z is the particle's charge in C, m is the particle's mass in kg, V_N is the initial electrode potential in region N in volts, V_{N+1} is the final electrode potential in region N in volts, ΔV_N is the potential difference across the region N and x_N is the length of the region N along the TOF axis in metres.

Extraction region

In the extraction region ($N = 0$), the particle gains kinetic energy corresponding to a final velocity v_0 given by:

$$v_0 = \sqrt{u_0 + 2a_0s} = \sqrt{2\frac{z}{m}\frac{\Delta V_0 s}{x_0}}, \tag{A.2}$$

where s is the distance travelled by the particle through the region from its origin point where the photoionisation occurs. The time spent by the particle in this region t_0 is given by

$$t_0 = \frac{v_0 - u_0}{a_0} = \sqrt{2\frac{m}{z}\frac{x_0 s}{\Delta V_0}}. \tag{A.3}$$

Acceleration regions

In an intermediate acceleration region N, the velocity the particle gains depends on the configuration of the region as well as the initial velocity upon entering the region, which is equal to the final velocity from the previous region v_{N-1}:

$$v_N = \sqrt{v_{N-1}^2 + 2a_N x_N} = \sqrt{v_{N-1}^2 + 2\frac{z}{m}\Delta V_N}. \tag{A.4}$$

This can be generalised to give the final velocity of region N in terms of all the preceding intermediate regions and the initial extraction region:

$$v_N = \sqrt{v_0^2 + 2\frac{z}{m}\sum_{i=1}^{N}\Delta V_i}, $$

$$= \sqrt{2\frac{z}{m}\left(\frac{\Delta V_0 s}{x_0} + \sum_{i=1}^{N}\Delta V_i\right)}. \tag{A.5}$$

The time spent in the Nth acceleration region t_N is

$$t_N = \frac{v_N - v_{N-1}}{a_N},$$

$$= \sqrt{2\frac{m}{z}\frac{x_N}{\Delta V_N}}\left(\sqrt{\frac{\Delta V_0 s}{x_0} + \sum_{i=1}^{N}\Delta V_i} - \sqrt{\frac{\Delta V_0 s}{x_0} + \sum_{i=1}^{N-1}\Delta V_i}\right). \qquad \text{A.6}$$

The total time of flight T_N of the particle in all N intermediate regions is therefore

$$T_N = \sum_{i=1}^{N} t_i,$$

$$= \sqrt{2\frac{m}{z}}\sum_{i=1}^{N}\frac{x_i}{\Delta V_i}\left(\sqrt{\frac{\Delta V_0 s}{x_0} + \sum_{i=1}^{N}\Delta V_i} - \sqrt{\frac{\Delta V_0 s}{x_0} + \sum_{i=1}^{N-1}\Delta V_i}\right). \qquad \text{A.7}$$

Field-free drift tube

In the field-free drift tube region, there is no electric field or further acceleration on the ion, the time of flight in this region t_d is therefore simply

$$t_d = \frac{x_d}{v_N},$$

$$= \sqrt{\frac{m}{z}}\frac{x_d}{\sqrt{2\left(\frac{\Delta V_0 s}{x_0} + \sum_{i=1}^{N}\Delta V_i\right)}}. \qquad \text{A.8}$$

Total

The total time of flight t of an ion in the setup is therefore the sum of the times of flight of the ion in each individual region:

$$t = t_0 + T_N + t_d,$$

$$= \sqrt{2\frac{m}{z}\frac{x_0 s}{\Delta V_0}} + \sqrt{2\frac{m}{z}}\sum_{i=1}^{N}\sqrt{\frac{x_i}{\Delta V_i}}\left(\sqrt{\frac{\Delta V_0 s}{x_0} + \sum_{i=1}^{N}\Delta V_i} - \sqrt{\frac{\Delta V_0 s}{x_0} + \sum_{i=1}^{N-1}\Delta V_i}\right)$$

$$+ \sqrt{\frac{m}{z}}\frac{x_d}{\sqrt{2\left(\frac{\Delta V_0 s}{x_0} + \sum_{i=1}^{N}\Delta V_i\right)}}, \qquad \text{A.9}$$

$$= \sqrt{2\frac{m}{z}}\left(\sqrt{\frac{x_0 s}{\Delta V_0}} + \sum_{i=1}^{N}\frac{x_i}{\Delta V_i}\left(\sqrt{\frac{\Delta V_0 s}{x_0} + \sum_{i=1}^{N}\Delta V_i} - \sqrt{\frac{\Delta V_0 s}{x_0} + \sum_{i=1}^{N-1}\Delta V_i}\right) + \frac{x_d}{2\sqrt{\frac{\Delta V_0 s}{x_0} + \sum_{i=1}^{N}\Delta V_i}}\right).$$

b. Switched voltages ion time-of-flight

When performing PEPICO, the voltages are first set to image electrons onto the delay-line detector. For the duration that the voltages are set this way, the ions will move in the opposite direction to the electrons, away from the detector, before the voltages are switched to image the ions on the detector (Figure A.6.2). For a fixed time between ionisation and switching, lighter ions will move farther from the interaction region than heavier ions, resulting in a longer total flight distance and may subsequently affect the mass dependence of the TOF signal. It is also possible that they move too far from the region for the ion potentials to successfully image them and they are lost. These factors are more significant when imaging fast electrons. Fast electrons require stronger negative voltages to image, and the limit of switching different voltages with the Behlke switches introduces a cap on the how strong the field can be to recover the ions. This limit is set by the maximum current (20 mA) of the HV power supplies used by the switches. This results in ions being accelerated far in the wrong direction by a strong negative field, that then need to be recovered by a comparatively weak positive field. Considering the opposite case, if imaging slow electrons, a weak negative field may be used which will perturb the ions less, and a strong ion imaging field can be used to easily overcome the distortion. This is more likely to closely resemble static TOF operation. Subsequently the TOF-M relationship may be significantly different from that of the static operation and may also vary significantly between different potential settings within PEPICO operation.

For simplicity, the switching of the potentials is assumed to be instantaneous, with no significant rise time, and all electric fields are approximated to be uniform and defined only by the two most local electrode potentials. The ions are again assumed to start with zero velocity along the TOF axis.

Before switching: electron settings

$V_0 = -V_R$ $V_1 = -V_E$ $V_2 = \oplus$ $V_3 = \oplus$ Detector $= \oplus$

$-\Delta s$ s

x_0 x_1 x_d

Extraction region electrons
$n = 0$

Acceleration region electrons
$n = 1$

Field-free drift tube

After switching: ion settings

$V_0 = V_R$ $V_1 = V_E$ $V_2 = \oplus$ $V_3 = \oplus$ Detector $= \oplus$

$s - \Delta s$

x_0 x_1 x_d

Extraction region ions
$n = 0$

Acceleration region ions
$n = 1$

Field-free drift tube
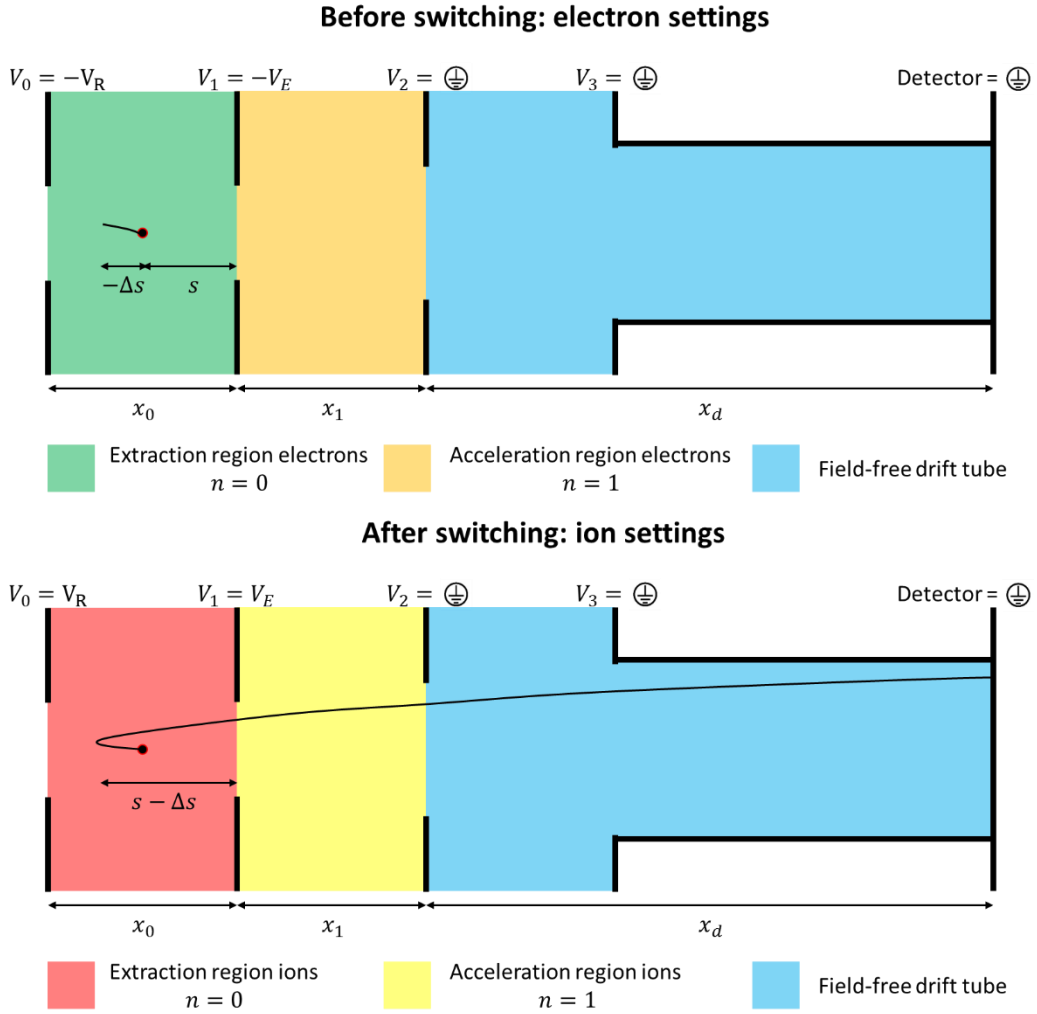
Figure A.6.2: Schematic of the TOF operation on the DLD-VMI for switched voltages. Only the flight path of the ions is shown. The extraction and acceleration regions are colour-coded differently when imaging the electrons and ions. Top: flight path of the ions when the potentials are set to negative values for imaging electrons. The distances s and Δs are displacement vectors from the particle's origin point where the positive direction is taken as going towards the detector and is therefore negative when going the other way. The ion trajectory before switching is assumed to only be affected by the conditions in the extraction region, not the acceleration region. Bottom: flight path of the ions after switching the voltages to positive value to image the ions. Only 2- or 3-electrode modes are used when switching, so there is only one intermediate acceleration region.

Extraction region: before switching

The potentials for the electrons are set for a fixed period of time t_s after the generation of the photoproduct, the velocity gained v_e by the ion in this time is

$$v_e = u_0 + a_{el}t_s = \frac{z}{m}\frac{\Delta V_{el}}{x_0}t_s,$$ A.10

where ΔV_{el} is the potential difference in the extraction when set to image the electrons and a_{el} is the acceleration experienced under these conditions. The distance travelled by the ion Δs in the wrong direction during this time is given by

$$\Delta s = u_0 t_s + \frac{1}{2} a_{el} t_s^2 = \frac{1}{2} \frac{z}{m} \frac{\Delta V_{el}}{x_0} t_s^2. \tag{A.11}$$

Extraction region: after switching

Upon switching the potentials to image ions ΔV_{ion}, the particle must now travel a longer distance $s - \Delta s$ in the extraction region starting from an initial velocity v_e in the opposite direction. The final velocity from this region v_0 is given by

$$v_0 = \sqrt{v_{el}^2 + 2 \frac{z}{m} \frac{\Delta V_{ion}}{x_0} (s - \Delta s)},$$

$$= \sqrt{\left(\frac{z}{m}\right)^2 \frac{\Delta V_{el}(\Delta V_{el} - \Delta V_{ion})}{x_0^2} t_s^2 + 2 \frac{z}{m} \frac{\Delta V_{ion}}{x_0} s}, \tag{A.12}$$

and the time spent by the ion after the switch in traversing the region is

$$t_{ion} = \sqrt{\frac{\Delta V_{el}^2 - \Delta V_{el}\Delta V_{ion}}{\Delta V_{ion}^2} t_s^2 + 2 \frac{m}{z} \frac{x_0 s}{\Delta V_{ion}}} - \frac{\Delta V_{el}}{\Delta V_{ion}} t_s \tag{A.13}$$

where ΔV_{el} and ΔV_{ion} always have opposite signs. The total time in the extraction region t_0 is then the sum of the time prior to switching and the time required to traverse the region

$$t_0 = t_{ion} + t_s$$

$$= \sqrt{\frac{(\Delta V_{el}^2 - \Delta V_{el}\Delta V_{ion})t_s^2}{\Delta V_{ion}^2} + 2 \frac{m}{z} \frac{x_0 s}{\Delta V_{ion}}} + t_s \left(1 - \frac{\Delta V_{el}}{\Delta V_{ion}}\right) \tag{A.14}$$

The second term within the radical is the same as the time of flight of the ion if there was no switching. Outside of the radical, the contributions to the TOF are the value of t_s which is simply added, and a term which is voltage-dependent that can be interpreted as a deceleration time. This is because the ion has already been given a certain velocity in the wrong direction which must be reversed, a process that adds time. It is independent of m/z because light (heavy) ions will have a higher (lower) initial velocity in the wrong direction, but this is compensated by faster (slower) deceleration according to Equation A.1. The first term in the radical is a fixed offset depending only the voltage differences and switching time. This describes the time the ion takes to travel back along the additional distance Δs as well as the distance gained while being decelerated. This is independent of m/z because light (heavy) ions will have travelled a longer (shorter) distance in the wrong direction, but this is compensated by higher (lower) velocity induced by the ion electrode settings. As t_s approaches zero, the TOF approximates to that of the static conditions Equation A.3. As t_s becomes very large, so too does the TOF until eventually the ion is lost and the TOF becomes effectively infinite.

Acceleration regions

In the intermediate acceleration regions, in calculating the final velocity it is possible to start from Equation A.4, the same as the static case. However, the initial velocity into the acceleration regions v_0 is no longer directly proportional to $\sqrt{z/m}$ and leads to a much more complicated expression. In the setup, only 2- or 3-

electrode mode is used, so there is no lens electrode and therefore only one acceleration region $N = 1$. The final velocity from the acceleration regions v_1 for the switched TOF is

$$v_1 = \sqrt{v_0^2 + 2\frac{z}{m}\Delta V_1}$$

$$= \frac{z}{m}\sqrt{\frac{(\Delta V_{el}^2 - \Delta V_{el}\Delta V_{ion})t_s^2}{x_0^2} + 2\frac{m}{z}\left(\frac{\Delta V_{ion}}{x_0}s + \Delta V_1\right)} \qquad \text{A.15}$$

The time spent in the acceleration region t_1 is

$$t_1 = \frac{x_1}{\Delta V_1}\left(\sqrt{\frac{(\Delta V_{el}^2 - \Delta V_{el}\Delta V_{ion})t_s^2}{x_0^2} + 2\frac{m}{z}\left(\frac{\Delta V_{ion}}{x_0}s + \Delta V_1\right)}\right.$$

$$\left. - \sqrt{\frac{(\Delta V_{el}^2 - \Delta V_{el}\Delta V_{ion})t_s^2}{x_0^2} + 2\frac{m}{z}\frac{\Delta V_{ion}}{x_0}s}\right) \qquad \text{A.16}$$

Field-free drift tube

The time spent in field free drift tube t_d is simply

$$t_d = \frac{x_d}{v_1},$$

$$= \frac{m}{z}\frac{x_d}{\sqrt{\frac{(\Delta V_{el}^2 - \Delta V_{el}\Delta V_{ion})t_s^2}{x_0^2} + 2\frac{m}{z}\left(\frac{\Delta V_{ion}}{x_0}s + \Delta V_1\right)}}. \qquad \text{A.17}$$

The total time of flight of an ion in the setup t is therefore the sum of the times of flight of the ion in each individual region:

$$t = t_0 + t_1 + t_d,$$

$$= \sqrt{A + B\frac{m}{z}} + \sqrt{C + D\frac{m}{z}} - \sqrt{C + E\frac{m}{z}} + \frac{\frac{m}{z}}{\sqrt{F + G\frac{m}{z}}} + z_, \qquad \text{A.18}$$

where the geometric factors are:

$$A = \frac{\left(\Delta V_{el}^2 - \Delta V_{el}\Delta V_{ion}\right)}{\Delta V_{ion}^2} t_s^2, \tag{A.19}$$

$$B = 2\frac{x_0 s}{\Delta V_{ion}}, \tag{A.20}$$

$$C = \frac{x_1^2}{\Delta V_1^2}\frac{\left(\Delta V_{el}^2 - \Delta V_{el}\Delta V_{ion}\right)}{x_0^2} t_s^2, \tag{A.21}$$

$$D = 2s\frac{\Delta V_{ion}x_1^2}{\Delta V_1^2 x_0} + \frac{x_1^2}{\Delta V_1}, \tag{A.22}$$

$$E = 2s\frac{\Delta V_{ion}x_1^2}{\Delta V_1^2 x_0}, \tag{A.23}$$

$$F = \frac{1}{x_d^2}\frac{\left(\Delta V_{el}^2 - \Delta V_{el}\Delta V_{ion}\right)}{x_0^2} t_s^2, \tag{A.24}$$

$$G = \frac{2}{x_d^2}\left(\frac{\Delta V_{ion}}{x_0}s + \Delta V_1\right), \tag{A.25}$$

$$z = t_s\left(1 - \frac{\Delta V_{el}}{\Delta V_{ion}}\right). \tag{A.26}$$

B. False coincidences of double ionisation

Here is an attempt to extend the DLD false coincidence model in Section 3.3.1 to double ionisation.

a. Single ionisation vs. double ionisation

In double ionisation experiments the issue of false coincidences can be complicated by the competing processes of single and double ionisation. Although single ionisation experiments have their own competing processes in terms of the electrons having a specific kinetic energy and the ions fragmenting to a certain mass, the above methods approximate that the detection efficiency is independent of the electron kinetic energy and the ion mass and a single Poisson distribution can be used. Additionally, the number of charged particle products to detect remains the same (one photoelectron and one photoion per ionisation event).

Double ionisation processes change the number of charged particles to detect. Double ionisation produces two electrons and either one or two ions depending on whether the dication fragments or remains stable. One possible way of reducing false coincidences is to use knowledge of the dataset signatures of double and single ionisation to identify which coincidences are true. The kinetic energy of the electrons in a double ionisation event is usually much lower than for a single ionisation event. The available kinetic energy is lower due to the significantly higher double ionisation threshold that must be overcome and it must be shared between two electrons. False coincidences in double ionisation PEPICO and PEPIPICO spectra can therefore be reduced by filtering for slow electrons. If the dication fragments, the monocation m/z values might be the same as fragments arising from single ionisation, but are likely to have their TOF or VMI information distorted by a large kinetic energy release resulting from Coulomb repulsion between the two positive charges. False coincidences in PEPIPICO and PIPICO spectra could therefore also be reduced by filtering for fast ions.

At photon energies around the double ionisation threshold, the cross section is typically much greater for single ionisation than for double ionisation. The probability of singly ionising n_1 times and doubly ionising n_2 times in a given pulse are each given as separate Poisson distributions that are treated independently:

$$p(n_1) = \frac{\overline{n_1}^{n_1}}{n_1!} e^{-\overline{n_1}},$$

$$p(n_2) = \frac{\overline{n_2}^{n_2}}{n_2!} e^{-\overline{n_2}},$$

B.1

where $\overline{n_1}$ and $\overline{n_2}$ are the single and double ionisation rates respectively. The number of electrons n_e generated in a pulse is

$$n_e = n_1 + 2n_2$$

B.2

The number of ions when the dication is stable $n_i^{(s)}$ is

$$n_i^{(s)} = n_1 + n_2.$$

B.3

The number of ions when the dication fragments $n_i^{(f)}$ is

$$n_i^{(f)} = n_1 + 2n_2 \qquad \text{B.4}$$

The false coincidences for double ionisation are compared for one-electron-one-ion coincidences when the dication is stable (PEPICO) and one-electron-two-ion when the dication fragments (PEPIPICO) and two-ion coincidences when the dication fragments (PIPICO). The scenarios of the dication either remaining stable or fragmenting are treated here as separate experiments. This is not fully realistic as if there are multiple dications created in a laser shot, some might remain stable and some might fragment with some probability dependent on the molecule and photon energy. Here the assumption is made that the probability of there being more than one double ionisation in a single laser shot is extremely small due to a small cross section compared to single ionisation. If there is a dataset featuring both stable dications and monocation fragments, any given analysis will only look at them separately.

The probability to detect a single electron on the DLD is calculated similarly to before:

$$\begin{aligned}
p_e(n_e, 1) &= 1 - p_e(n_e, 0) \\
&= 1 - (1 - \xi_e)^{n_1 + 2n_2}
\end{aligned} \qquad \text{B.5}$$

The probability to detect an intact dication is:

$$\begin{aligned}
p_i\left(n_i^{(s)}, 1\right) &= \binom{n_i^{(s)}}{1} \xi_i^1 (1 - \xi_i)^{n_i^{(s)} - 1} \\
&= (n_1 + n_2) \xi_i (1 - \xi_i)^{n_1 + n_2 - 1}
\end{aligned} \qquad \text{B.6}$$

When the dication fragments, the probability to detect two fragments is.

$$\begin{aligned}
p_i\left(n_i^{(f)}, 2\right) &= \binom{n_i^{(f)}}{2} \xi_i^2 (1 - \xi_i)^{n_i^{(f)} - 2} \\
&= \binom{n_1 + 2n_2}{2} \xi_i^2 (1 - \xi_i)^{n_1 + 2n_2 - 2}
\end{aligned} \qquad \text{B.7}$$

In any experiment the average number of ionisation events per laser shot depends on several experimental parameters, including the molecular beam density; molecular beam sample composition; energy-dependent photoionisation cross sections; photon energy; laser power and laser pulse length. In single ionisation, the average number of ionisation events per laser shot can be estimated from the experimental data with no prior knowledge of these parameters. There may be a number of different species in the molecular beam (e.g. the sample of interest, impurities or the carrier gas) which will affect the resultant spectra. There may also be different competing processes triggered on photon absorption. However, the only process detected, photoionisation, always results in the generation of a single photoelectron and photoion. This allows the above method to be used to calculate the fraction of false coincidences no matter the experimental conditions. It is only necessary in this context to consider the experimental parameters if the false coincidence level must be changed during the experiment itself.

In a double ionisation experiment with two different average ionisation rates $\bar{n}_1$ and $\bar{n}_2$ it is difficult to estimate both from the experimental data. Knowledge of the experimental parameters can be used to estimate these quantities relative to each other. In the double ionisation experiments performed here, the two species in the molecular beam are the carrier gas (usually helium) and the sample molecule of interest.

The presence of impurities is neglected. The sample may undergo single or double ionisation while the helium will only be singly ionised at the photon energies used. In this context, the competing processes to consider are single ionisation versus double ionisation, *not* ionisation of helium versus ionisation of the sample.

For a sample molecule X. The single (double) ionisation probability per laser pulse $p_{1(2)}^{(X)}$ is

$$p_{1(2)}^{(X)} = \sigma_{1(2)}^{(X)} F\tau, \tag{B.8}$$

where $\sigma_{1(2)}^{(X)}$ is the single (double) ionisation cross section in cm²; F is the laser intensity in cm⁻² s⁻¹ and τ is the laser pulse length in s. F and τ are the same for all species and processes in the interaction. The number of molecules of X singly (doubly) ionised per pulse $\bar{n}_{1(2)}^{X}$ is therefore

$$\bar{n}_{1(2)}^{(X)} = p_{1(2)}^{(X)} N^{(X)}, \tag{B.9}$$

where N_X is the number of molecules of X present in the interaction region. N_X is the same for both single and double ionisation of X, so the ratio of single to double ionisation of X is

$$\frac{\bar{n}_1^{(X)}}{\bar{n}_2^{(X)}} = \frac{p_1^{(X)}}{p_2^{(X)}}. \tag{B.10}$$

The relative numbers of single and double ionisations can therefore be simply estimated from the single and double photoionisation cross sections. This can be expanded to include the presence of the carrier gas by considering the source conditions of the molecular beam. The approximation is made that the relative composition of the molecular beam species in the interaction region is the same as at the molecular beam source, although this does not hold for clusters. So, the number of molecules in the interaction region is

$$N_{interaction}^{(X)} = k N_{source}^{(X)}, \tag{B.11}$$

where k is some scaling factor to account for the difference in molecular beam density between the source and interaction region. $N_{source}^{(X)}$ is approximately calculated by considering the ideal gas law:

$$N_{source}^{(X)} = \frac{P^{(X)} V}{k_B T} \tag{B.12}$$

Here $P^{(X)}$ is the partial pressure of species X in the molecular beam source, V is the volume in the molecular beam source, k_B is the Boltzmann constant and T is the source temperature. The number of molecules of X ionised per pulse is therefore

$$\bar{n}_{1(2)}^{(X)} = \frac{\sigma_{1(2)}^{(X)} F\tau k P^{(X)} V}{k_B T} \tag{B.13}$$

The total single ionisation rate is the sum of the single ionisation rates of each species present. For helium and X it is

$$\begin{aligned} \bar{n}_1 &= \bar{n}_1^{(He)} + \bar{n}_1^{(X)} \\ &= \frac{F\tau kV}{k_B T}\left(\sigma_1^{(He)}P^{(He)} + \sigma_1^{(X)}P^{(X)}\right) \end{aligned}$$

<div align="right">B.14</div>

While the total double ionisation rate is only the double ionisation rate of X :

$$\begin{aligned} \bar{n}_2 &= \bar{n}_2^{(X)} \\ &= \frac{F\tau kV}{k_B T}\left(\sigma_2^{(X)}P^{(X)}\right) \end{aligned}$$

<div align="right">B.15</div>

The ratio of single to double ionisation events is therefore

$$\frac{\bar{n}_1^{(X)}}{\bar{n}_2^{(X)}} = \frac{\sigma_1^{(He)}P^{(He)} + \sigma_1^{(X)}P^{(X)}}{\sigma_2^{(X)}P^{(X)}}$$

<div align="right">B.16</div>

b. Double ionisation electron-ion coincidences

The probability ω_{11} of detecting a PEPICO coincidence when double ionisation occurs is

$$\begin{aligned} \omega_{11} &= \sum_{n_1=0}^{\infty}\sum_{n_2=0}^{\infty} p_e(n_1+2n_2,1)p_i(n_1+n_2,1)p(n_1)p(n_2) \\ &= \xi_i\left((1-\xi_e)\big((\xi_e-1)\overline{n_2}-\overline{n_1}\big)e^{-\xi_i(\overline{n_1}+\overline{n_2})-(1-\xi_e)(n_2\xi_i^2-(\overline{n_1}+\overline{n_2})\xi_e)} + e^{-\xi_i(\overline{n_1}+\overline{n_2})}(\overline{n_1}+\overline{n_2})\right) \end{aligned}$$

<div align="right">B.17</div>

Out of n_1 single ionisations and n_2 double ionisations in a given laser pulse, the total number of possible coincidences N_{11} is

$$\begin{aligned} N_{11} &= n_e n_i \\ &= (n_1+2n_2)(n_1+n_2). \end{aligned}$$

<div align="right">B.18</div>

In the case of a stable dication, each electron from a double ionisation can only be truly correlated to one possible ion. This is also true for the single ionisation events, so the number of true coincidences in a given laser pulse $N_{11}^{(t)}$ is the number of electrons generated:

$$\begin{aligned} N_{11}^{(t)} &= n_e, \\ &= n_1 + 2n_2. \end{aligned}$$

<div align="right">B.19</div>

The fraction of true coincidences in a given laser pulse is therefore

$$\frac{N_{11}^{(t)}}{N_{11}} = \frac{1}{n_1+n_2}.$$

<div align="right">B.20</div>

The probability of detecting a true PEPICO coincidence is therefore

$$\omega_{11}^t = \sum_{n_1=0}^{\infty} \sum_{n_2=0}^{\infty} \frac{p_e(n_1 + 2n_2, 1)p_i(n_1 + n_2, 1)p(n_1)p(n_2)}{n_1 + n_2}$$

$$= \frac{\xi_i\left(e^{-\xi_i(\overline{n_1}+\overline{n_2})} - e^{-\overline{n_2}(\xi_i-1)\xi_e^2 + (\overline{n_1}+2\overline{n_2})(\xi_i-1)\xi_e - \xi_i(\overline{n_1}+\overline{n_2})}\right)}{1 - \xi_i}$$

B.21

The true coincidence ratio is therefore

$$\frac{\omega_{11}^{(t)}}{\omega_{11}} = \frac{\dfrac{\left(e^{-\xi_i(\overline{n_1}+\overline{n_2})} - e^{-\overline{n_2}(\xi_i-1)\xi_e^2 + (\overline{n_1}+2\overline{n_2})(\xi_i-1)\xi_e - \xi_i(\overline{n_1}+\overline{n_2})}\right)}{1 - \xi_i}}{(1-\xi_e)\left((\xi_e-1)\overline{n_2} - \overline{n_1}\right)e^{-\xi_i(\overline{n_1}+\overline{n_2}) - (1-\xi_e)\left(n_2\xi_i^2 - (\overline{n_1}+\overline{n_2})\xi_e\right)} + e^{-\xi_i(\overline{n_1}+\overline{n_2})}(\overline{n_1} + \overline{n_2})}$$

B.22

c. **Double ionisation ion-ion coincidences**

The probability ω_{02} of detecting a PIPICO coincidence is

$$\omega_{02} = \sum_{n_1=0}^{\infty} \sum_{n_2=0}^{\infty} p_i(n_1 + 2n_2, 2)p(n_1)p(n_2)$$

$$= \sum_{n_1=0}^{\infty} \sum_{n_2=0}^{\infty} \binom{n_1 + 2n_2}{2} \xi_i^2 (1-\xi_i)^{n_1+2n_2-2} \frac{\overline{n_1}^{n_1}\overline{n_2}^{n_2}}{n_1! \, n_2!} e^{-(\overline{n_1}+\overline{n_2})}$$

B.23

The total number of possible coincidences in a given laser pulse is known from choosing any two ions from those generated

$$N_{all} = \binom{n_i}{2}$$

$$= \binom{n_1 + 2n_2}{2}$$

B.24

The number of true coincidences possible is simply the number of double ionisation events.

$$N_{true} = n_2$$

B.25

The probability of detecting a true PIPICO coincidence is

$$\omega_{02}^t = \sum_{n_1=0}^{\infty} \sum_{n_2=0}^{\infty} p_i(n_1 + 2n_2, 2)p(n_1)p(n_2) \times \frac{n_2}{\binom{n_1+2n_2}{2}}$$

$$= \sum_{n_1=0}^{\infty} \sum_{n_2=0}^{\infty} n_2 \xi_i^2 (1-\xi_i)^{n_1+2n_2-2} \frac{\overline{n_1}^{n_1}\overline{n_2}^{n_2}}{n_1! \, n_2!} e^{-(\overline{n_1}+\overline{n_2})}$$

B.26

d. **Double ionisation electron-ion-ion coincidences**

The probability ω_{12} of detecting a PEPIPICO coincidence is this given by

$$\omega_{12} = \sum_{n_1=0}^{\infty} \sum_{n_2=0}^{\infty} p_e(n_1 + 2n_2, 1) p_i(n_1 + 2n_2, 2) p(n_1) p(n_2) \qquad \text{B.27}$$

For the 3-fold PEPIPICO coincidences, for each electron there is the possibility to choose any two ions from those present. The total number of possible coincidences possible is therefore

$$N_{all} = n_e \binom{n_i}{2}$$
$$= (n_1 + 2n_2) \binom{n_1 + 2n_2}{2} \qquad \text{B.28}$$

The number of true coincidences is given by the number of electrons that come solely from double ionisation events $2n_2$. Any electron from a single ionisation event can only have a true coincidence with a single ion. Any coincidences of these electrons with multiple ions are necessarily false.

$$N_{true} = 2n_2 \qquad \text{B.29}$$

The fraction of true PEPIPICO coincidences in a laser pulse is therefore

$$\frac{N_{true}}{N_{all}} = \frac{2n_2}{(n_1 + 2n_2)\binom{n_1+2n_2}{2}} \qquad \text{B.30}$$

The probability of a detecting a true PEPIPICO coincidence is nominally given by the expression:

$$\omega_{12}^t = \sum_{n_1=0}^{\infty} \sum_{n_2=0}^{\infty} p_e(n_1 + 2n_2, 1) p_i(n_1 + 2n_2, 2) p(n_1) p(n_2) \times \frac{2n_2}{(n_1 + 2n_2)\binom{n_1+2n_2}{2}}$$

$$= \sum_{n_1=0}^{\infty} \sum_{n_2=0}^{\infty} \frac{2n_2 [1 - (1 - \xi_e)^{n_1+2n_2}] \xi_i^2 (1 - \xi_i)^{n_1+2n_2-2} \overline{n_1}^{n_1} \overline{n_2}^{n_2} e^{-(\overline{n_1}+\overline{n_2})}}{(n_1 + 2n_2) n_1! n_2!} \qquad \text{B.31}$$

However, this could not be solved by the Maple software program after a week of running.

C. Delay-line detector recircularisation constants

a. 2 electrodes

Repeller voltage (V)	Centre x	Centre y	A1	A2	A3	B1	B2	B3
2000	124.4	-146.27	0.045636	0.0024503	-0.0055417	0.0051572	0.025946	0.0029836
3000	120.29	-145.72	0.047018	0.0026209	-0.0074507	0.0035385	0.027235	0.00301
4000	123.84	-153.28	0.050111	0.0020852	-0.007234	0.00021211	0.026366	0.0028063
5000	104.94	-124.22	0.036746	0.0017166	-0.0042544	0.0081663	0.021631	0.002414

b. 3 electrodes

Repeller voltage (V)	Centre x	Centre y	A1	A2	A3	B1	B2	B3
2000	63.225	-125.25	0.042299	0.0010302	-0.0037746	0.0088059	0.022851	0.0022654
3000	93.356	-146.79	0.051617	0.00071004	-0.0075874	-0.0032088	0.025901	0.002339
4000	84.65	-135.52	0.045316	0.00043559	-0.0056805	0.003386	0.022747	0.0026259
5000	83.076	-128.48	0.041472	0.0003993	-0.0048639	0.0044514	0.020388	0.0023355

c. 4 electrodes

Repeller voltage (V)	Centre x	Centre y	A1	A2	A3	B1	B2	B3
2000	82.211	-158.59	0.044997	0.0021537	-0.0058313	0.0060311	0.025474	0.0026307
3000	82.916	-150.95	0.043122	0.0018066	-0.0041995	0.0065365	0.022122	0.0020465
4000	87.658	-142.78	0.039996	0.0016633	-0.00408	0.005915	0.02	0.0024176
5000	85.574	-139.75	0.03956	0.0018161	-0.0038672	0.0078359	0.019533	0.0020369

References

[1]   K. C. Prince, P. Bolognesi, V. Feyer, O. Plekan, and L. Avaldi, "Study of complex molecules of biological interest with synchrotron radiation," *Journal of Electron Spectroscopy and Related Phenomena*, doi: 10.1016/j.elspec.2015.08.010.

[2]   M. S. de Vries and P. Hobza, "Gas-phase spectroscopy of biomolecular building blocks," *Annu Rev Phys Chem*, vol. 58, pp. 585–612, 2007, doi: 10.1146/annurev.physchem.57.032905.104722.

[3]   H. H. Hammud, K. H. Bouhadir, M. S. Masoud, A. M. Ghannoum, and S. A. Assi, "Solvent Effect on the Absorption and Fluorescence Emission Spectra of Some Purine Derivatives: Spectrofluorometric Quantitative Studies," *Journal of Solution Chemistry*, vol. 37, no. 7, pp. 895–917, Jul. 2008, doi: 10.1007/s10953-008-9289-8.

[4]   J. C. Owrutsky, D. Raftery, and R. M. Hochstrasser, "Vibrational Relaxation Dynamics in Solutions," *Annu. Rev. Phys. Chem.*, vol. 45, no. 1, pp. 519–555, Oct. 1994, doi: 10.1146/annurev.pc.45.100194.002511.

[5]   N. S. Bayliss and E. G. McRae, "Solvent Effects in the Spectra of Acetone, Crotonaldehyde, Nitromethane and Nitrobenzene," *J. Phys. Chem.*, vol. 58, no. 11, pp. 1006–1011, Nov. 1954, doi: 10.1021/j150521a018.

[6]   R. Knochenmuss and S. Leutwyler, "Proton transfer from 1-naphthol to water: Small clusters to the bulk," *J. Chem. Phys.*, vol. 91, no. 2, pp. 1268–1278, Jul. 1989, doi: 10.1063/1.457202.

[7]   P. A. Hatherly, D. M. Smith, and R. P. Tuckett, "Non-Statistical Effects in the Fragmentation of Electronic States of Gas-Phase Polyatomic Molecular Ions," *Zeitschrift für Physikalische Chemie*, vol. 195, no. 1–2, pp. 97–136, Jan. 1996, doi: 10.1524/zpch.1996.195.Part_1_2.097.

[8]   A. Shahi, Y. Albeck, and D. Strasser, "Simultaneous 3D coincidence imaging of cationic, anionic, and neutral photo-fragments," *Review of Scientific Instruments*, vol. 89, no. 1, p. 013303, Jan. 2018, doi: 10.1063/1.5004523.

[9]   C. Stråhlman, R. Sankari, A. Kivimäki, R. Richter, M. Coreno, and R. Nyholm, "Negative-ion/positive-ion coincidence spectroscopy with a novel spectrometer," *J. Phys.: Conf. Ser.*, vol. 635, no. 11, p. 112123, 2015, doi: 10.1088/1742-6596/635/11/112123.

[10]   A. T. J. B. Eppink and D. H. Parker, "Velocity map imaging of ions and electrons using electrostatic lenses: Application in photoelectron and photofragment ion imaging of molecular oxygen," *Review of Scientific Instruments*, vol. 68, no. 9, pp. 3477–3484, Sep. 1997, doi: 10.1063/1.1148310.

[11]   D. W. Chandler and P. L. Houston, "Two-dimensional imaging of state-selected photodissociation products detected by multiphoton ionization," *J. Chem. Phys.*, vol. 87, no. 2, pp. 1445–1447, Jul. 1987, doi: 10.1063/1.453276.

[12]   J. H. D. Eland, "Coincidence studies of multiionized molecules," in *Vacuum Ultraviolet Photoionization and Photodissociation of Molecules and Clusters*, 0 vols., WORLD SCIENTIFIC, 1991, pp. 297–343. doi: 10.1142/9789812814821_0006.

[13]   T. J. Millar, E. Roueff, S. B. Charnley, and S. D. Rodgers, "The chemistry of complex molecules in interstellar clouds," *International Journal of Mass Spectrometry and Ion Processes*, vol. 149–150, pp. 389–402, Nov. 1995, doi: 10.1016/0168-1176(95)04270-U.

[14]   R. Thissen, O. Witasse, O. Dutuit, C. S. Wedlund, G. Gronoff, and J. Lilensten, "Doubly-charged ions in the planetary ionospheres: a review," *Phys. Chem. Chem. Phys.*, vol. 13, no. 41, pp. 18264–18287, Oct. 2011, doi: 10.1039/C1CP21957J.

[15]   S. Falcinelli *et al.*, "Molecular Dications in Planetary Atmospheric Escape," *Atmosphere*, vol. 7, no. 9, Art. no. 9, Sep. 2016, doi: 10.3390/atmos7090112.

[16]   R. Wehlitz, "Double photoionization of hydrocarbons and aromatic molecules," *J. Phys. B: At. Mol. Opt. Phys.*, vol. 49, no. 22, p. 222004, Nov. 2016, doi: 10.1088/0953-4075/49/22/222004.

[17]   R. D. Molloy, A. Danielsson, L. Karlsson, and J. H. D. Eland, "Double photoionisation spectra of small molecules and a new empirical rule for double ionisation energies," *Chemical Physics*, vol. 335, no. 1, pp. 49–54, May 2007, doi: 10.1016/j.chemphys.2007.03.016.

[18]   G. H. Wannier, "The Threshold Law for Single Ionization of Atoms or Ions by Electrons," *Phys. Rev.*, vol. 90, no. 5, pp. 817–825, Jun. 1953, doi: 10.1103/PhysRev.90.817.

[19]   J. H. D. Eland and R. Feifel, *Double Photoionisation Spectra of Molecules*. Oxford University Press, 2018.

[20] G. H. Wannier, "Threshold Law for Multiple Ionization," *Phys. Rev.*, vol. 100, no. 4, pp. 1180–1180, Nov. 1955, doi: 10.1103/PhysRev.100.1180.

[21] J. H. D. Eland, "Dynamics of Double Photoionization in Molecules and Atoms," in *Advances in Chemical Physics*, John Wiley & Sons, Ltd, 2009, pp. 103–151. doi: 10.1002/9780470431917.ch3.

[22] W. Kuhn, B. Feuerstein, and W. Mehlhorn, "Post-collision interaction after inner-shell ionization by electron impact: the shape of Auger lines," *J. Phys. B: At. Mol. Opt. Phys.*, vol. 34, no. 14, pp. 2835–2850, Jul. 2001, doi: 10.1088/0953-4075/34/14/306.

[23] R. Dörner *et al.*, "Cold Target Recoil Ion Momentum Spectroscopy: a 'momentum microscope' to view atomic collision dynamics," *Physics Reports*, vol. 330, no. 2, pp. 95–192, Jun. 2000, doi: 10.1016/S0370-1573(99)00109-X.

[24] J. Ullrich, R. Moshammer, A. Dorn, R. Dörner, L. P. H. Schmidt, and H. Schmidt-Böcking, "Recoil-ion and electron momentum spectroscopy: reaction-microscopes," *Rep. Prog. Phys.*, vol. 66, no. 9, p. 1463, Sep. 2003, doi: 10.1088/0034-4885/66/9/203.

[25] G. C. King and L. Avaldi, "Double-excitation and double-escape processes studied by photoelectron spectroscopy near threshold," *J. Phys. B: At. Mol. Opt. Phys.*, vol. 33, no. 16, pp. R215–R284, Aug. 2000, doi: 10.1088/0953-4075/33/16/201.

[26] J. H. D. Eland, F. S. Wort, and R. N. Royds, "A photoelectron-ion-ion triple coincidence technique for the study of double photoionization and its consequences," *Journal of Electron Spectroscopy and Related Phenomena*, vol. 41, no. 2, pp. 297–309, Jan. 1986, doi: 10.1016/0368-2048(86)85010-1.

[27] J. Ojeda *et al.*, "Harmonium: A pulse preserving source of monochromatic extreme ultraviolet (30–110 eV) radiation for ultrafast photoelectron spectroscopy of liquids," *Structural Dynamics*, vol. 3, no. 2, p. 023602, Mar. 2016, doi: 10.1063/1.4933008.

[28] P. B. Corkum, "Plasma perspective on strong field multiphoton ionization," *Phys. Rev. Lett.*, vol. 71, no. 13, pp. 1994–1997, Sep. 1993, doi: 10.1103/PhysRevLett.71.1994.

[29] T. Horio, R. Spesyvtsev, and T. Suzuki, "Generation of sub-17 fs vacuum ultraviolet pulses at 133 nm using cascaded four-wave mixing through filamentation in Ne," *Opt. Lett., OL*, vol. 39, no. 20, pp. 6021–6024, Oct. 2014, doi: 10.1364/OL.39.006021.

[30] S. Adachi and T. Suzuki, "UV-Driven Harmonic Generation for Time-Resolved Photoelectron Spectroscopy of Polyatomic Molecules," *Applied Sciences*, vol. 8, no. 10, p. 1784, Oct. 2018, doi: 10.3390/app8101784.

[31] S. Jin, F. Fan, M. Guo, Y. Zhang, Z. Feng, and C. Li, "Note: Deep ultraviolet Raman spectrograph with the laser excitation line down to 177.3 nm and its application," *Review of Scientific Instruments*, vol. 85, no. 4, p. 046105, Apr. 2014, doi: 10.1063/1.4870444.

[32] D. H. Mordaunt *et al.*, "Primary product channels in the photodissociation of methane at 121.6 nm," *J. Chem. Phys.*, vol. 98, no. 3, pp. 2054–2065, Feb. 1993, doi: 10.1063/1.464237.

[33] D. H. Mordaunt, M. N. R. Ashfold, and R. N. Dixon, "Dissociation dynamics of $H_2O(D_2O)$ following photoexcitation at the Lyman-α wavelength (121.6 nm)," *J. Chem. Phys.*, vol. 100, no. 10, pp. 7360–7375, May 1994, doi: 10.1063/1.466880.

[34] G. P. Morley, I. R. Lambert, M. N. R. Ashfold, K. N. Rosser, and C. M. Western, "Dissociation dynamics of HCN(DCN) following photoexcitation at 121.6 nm," *J. Chem. Phys.*, vol. 97, no. 5, pp. 3157–3165, Sep. 1992, doi: 10.1063/1.463002.

[35] M. A. Parkes, K. M. Douglas, and S. D. Price, "Ionization of acetonitrile," *International Journal of Mass Spectrometry*, vol. 438, pp. 97–106, Apr. 2019, doi: 10.1016/j.ijms.2018.12.012.

[36] L. Young *et al.*, "Roadmap of ultrafast x-ray atomic and molecular physics," *J. Phys. B: At. Mol. Opt. Phys.*, vol. 51, no. 3, p. 032003, Jan. 2018, doi: 10.1088/1361-6455/aa9735.

[37] A. Braun, "Photodissociation studies of CH_3I and CF_3I in fluid ^{4}Helium nanodroplets," *Infoscience*, 2004. https://infoscience.epfl.ch/record/33440 (accessed Oct. 14, 2019).

[38] E. Loginov, "Photoexcitation and photoionization dynamics of doped liquid helium-4 nanodroplets," *Infoscience*, 2008. https://infoscience.epfl.ch/record/126132 (accessed Oct. 14, 2019).

[39] V. Lyamayev *et al.*, "A modular end-station for atomic, molecular, and cluster science at the low-density matter beamline of FERMI@Elettra," *J. Phys. B: At. Mol. Opt. Phys.*, vol. 46, no. 16, p. 164007, Aug. 2013, doi: 10.1088/0953-4075/46/16/164007.

[40] A. Vredenborg, W. G. Roeterdink, and M. H. M. Janssen, "A photoelectron-photoion coincidence imaging apparatus for femtosecond time-resolved molecular dynamics with electron time-of-flight resolution of σ=18ps and energy resolution ΔE/E=3.5%," *Review of Scientific Instruments*, vol. 79, no. 6, p. 063108, Jun. 2008, doi: 10.1063/1.2949142.

[41] C. S. Lehmann, N. B. Ram, and M. H. M. Janssen, "Velocity map photoelectron-photoion coincidence imaging on a single detector," *Review of Scientific Instruments*, vol. 83, no. 9, p. 093103, Sep. 2012, doi: 10.1063/1.4749843.

[42] A. Vredenborg, C. S. Lehmann, D. Irimia, W. G. Roeterdink, and M. H. M. Janssen, "The Reaction Microscope: Imaging and Pulse Shaping Control in Photodynamics," *ChemPhysChem*, vol. 12, no. 8, pp. 1459–1473, Jun. 2011, doi: 10.1002/cphc.201100107.

[43] J. J. P. Ojeda Andara, "Ultrafast Photoelectron Spectroscopy of Liquid Samples," EPFL, Lausanne, 2016. doi: 10.5075/epfl-thesis-7122.

[44] C. A. Arrell *et al.*, "Harmonium: An Ultrafast Vacuum Ultraviolet Facility," *Chimia (Aarau)*, vol. 71, no. 5, pp. 268–272, May 2017, doi: 10.2533/chimia.2017.268.

[45] W. C. Wiley and I. H. McLaren, "Time-of-Flight Mass Spectrometer with Improved Resolution," *Review of Scientific Instruments*, vol. 26, no. 12, pp. 1150–1157, Dec. 1955, doi: 10.1063/1.1715212.

[46] U. Boesl, "Time-of-flight mass spectrometry: Introduction to the basics," *Mass Spectrometry Reviews*, vol. 36, no. 1, pp. 86–109, 2017, doi: 10.1002/mas.21520.

[47] J. Mooney and P. Kambhampati, "Get the Basics Right: Jacobian Conversion of Wavelength and Energy Scales for Quantitative Analysis of Emission Spectra," *J. Phys. Chem. Lett.*, vol. 4, no. 19, pp. 3316–3318, Oct. 2013, doi: 10.1021/jz401508t.

[48] P. Matía Hernando, "Attosecond pump-probe methods for measurement of molecular hole dynamics," Mar. 2017, doi: 10.25560/50155.

[49] N. A. Love, "Studies of electron ioization," University of London, 2005.

[50] S. J. King, "Studies of the dissociation and energetics of gaseous ions," University of London, 2008.

[51] L. Montgomery Smith, D. R. Keefer, and S. I. Sudharsanan, "Abel inversion using transform techniques," *Journal of Quantitative Spectroscopy and Radiative Transfer*, vol. 39, no. 5, pp. 367–373, May 1988, doi: 10.1016/0022-4073(88)90101-X.

[52] M. J. J. Vrakking, "An iterative procedure for the inversion of two-dimensional ion/photoelectron imaging experiments," *Review of Scientific Instruments*, vol. 72, no. 11, pp. 4084–4089, Oct. 2001, doi: 10.1063/1.1406923.

[53] V. Dribinski, A. Ossadtchi, V. A. Mandelshtam, and H. Reisler, "Reconstruction of Abel-transformable images: The Gaussian basis-set expansion Abel transform method," *Review of Scientific Instruments*, vol. 73, no. 7, pp. 2634–2642, Jun. 2002, doi: 10.1063/1.1482156.

[54] G. A. Garcia, L. Nahon, and I. Powis, "Two-dimensional charged particle image inversion using a polar basis function expansion," *Review of Scientific Instruments*, vol. 75, no. 11, pp. 4989–4996, Nov. 2004, doi: 10.1063/1.1807578.

[55] A. Braun and M. Drabbels, "Simple procedure to extract speed distributions from ion images with a large background contribution," *Review of Scientific Instruments*, vol. 76, no. 11, p. 113103, Nov. 2005, doi: 10.1063/1.2130941.

[56] B. Dick, "Inverting ion images without Abel inversion: maximum entropy reconstruction of velocity maps," *Phys. Chem. Chem. Phys.*, vol. 16, no. 2, pp. 570–580, 2014, doi: 10.1039/C3CP53673D.

[57] curtis.suplee@nist.gov, "Atomic Spectra Database," *NIST*, Jul. 21, 2009. https://www.nist.gov/pml/atomic-spectra-database (accessed Nov. 06, 2020).

[58] J. R. Gascooke, S. T. Gibson, and W. D. Lawrance, "A 'circularisation' method to repair deformations and determine the centre of velocity map images," *J. Chem. Phys.*, vol. 147, no. 1, p. 013924, May 2017, doi: 10.1063/1.4981024.

[59] J. R. Gascooke and W. D. Lawrance, *FITS Viewer and VMI Analysis: A program for analysing and circularising VMI images*. [Online]. Available: 10.4226/86/59278ab872838

[60] E. W. Hansen and P.-L. Law, "Recursive methods for computing the Abel transform and its inverse," *J. Opt. Soc. Am. A, JOSAA*, vol. 2, no. 4, pp. 510–520, Apr. 1985, doi: 10.1364/JOSAA.2.000510.

[61] E. Hansen, "Fast Hankel transform algorithm," *IEEE Transactions on Acoustics, Speech, and Signal Processing*, vol. 33, no. 3, pp. 666–671, Jun. 1985, doi: 10.1109/TASSP.1985.1164579.

[62] D. L. Osborn, C. C. Hayden, P. Hemberger, A. Bodi, K. Voronova, and B. Sztáray, "Breaking through the false coincidence barrier in electron–ion coincidence experiments," *J. Chem. Phys.*, vol. 145, no. 16, p. 164202, Oct. 2016, doi: 10.1063/1.4965428.

[63] P. Heim, M. Rumetshofer, B. Thaler, W. E. Ernst, W. von der Linden, and M. Koch, "Bayesian probability theory to identify false coincidences in coincidence experiments," *EPJ Web Conf.*, vol. 205, p. 09025, 2019, doi: 10.1051/epjconf/201920509025.

[64] P. Heim *et al.*, "Bayesian Analysis of Femtosecond Pump-Probe Photoelectron-Photoion Coincidence Spectra with Fluctuating Laser Intensities," *Entropy*, vol. 21, no. 1, Art. no. 1, Jan. 2019, doi: 10.3390/e21010093.

[65] M. Rumetshofer, P. Heim, B. Thaler, W. E. Ernst, M. Koch, and W. von der Linden, "Analysis of femtosecond pump-probe photoelectron-photoion coincidence measurements applying Bayesian probability theory," *Phys. Rev. A*, vol. 97, no. 6, p. 062503, Jun. 2018, doi: 10.1103/PhysRevA.97.062503.

[66] M. R. Bruce, C. Ma, and R. A. Bonham, "Positive ion pair production by electron impact dissociative ionization of CF_4," *Chemical Physics Letters*, vol. 190, no. 3, pp. 285–290, Mar. 1992, doi: 10.1016/0009-2614(92)85340-G.

[67] M. R. Bruce, L. Mi, C. R. Sporleder, and R. A. Bonham, "Covariance mapping mass spectroscopy using a pulsed electron ionizing source: application to CF_4," *J. Phys. B: At. Mol. Opt. Phys.*, vol. 27, no. 23, pp. 5773–5794, Dec. 1994, doi: 10.1088/0953-4075/27/23/019.

[68] V. Stert, W. Radloff, C. P. Schulz, and I. V. Hertel, "Ultrafast photoelectron spectroscopy: Femtosecond pump-probe coincidence detection of ammonia cluster ions and electrons," *Eur. Phys. J. D*, vol. 5, no. 1, pp. 97–106, Jan. 1999, doi: 10.1007/PL00021590.

[69] J. Mikosch and S. Patchkovskii, "Coincidence and covariance data acquisition in photoelectron and -ion spectroscopy. I. Formal theory," *Journal of Modern Optics*, vol. 60, no. 17, pp. 1426–1438, Oct. 2013, doi: 10.1080/09500340.2013.839837.

[70] J. Mikosch and S. Patchkovskii, "Coincidence and covariance data acquisition in photoelectron and -ion spectroscopy. II. Analysis and applications," *Journal of Modern Optics*, vol. 60, no. 17, pp. 1439–1451, Oct. 2013, doi: 10.1080/09500340.2013.839840.

[71] L. J. Frasinski, M. Stankiewicz, P. A. Hatherly, and K. Codling, "Removal of false coincidences in triple coincidence experiments employing continuous excitation," *Meas. Sci. Technol.*, vol. 3, no. 12, pp. 1188–1191, Dec. 1992, doi: 10.1088/0957-0233/3/12/012.

[72] C. L. Ricketts, D. Schröder, C. Alcaraz, and J. Roithová, "Growth of Larger Hydrocarbons in the Ionosphere of Titan," *Chemistry – A European Journal*, vol. 14, no. 16, pp. 4779–4783, 2008, doi: 10.1002/chem.200800524.

[73] E.-L. Zins *et al.*, "Formation of Organoxenon Dications in the Reactions of Xenon with Dications Derived from Toluene," *Chemistry – A European Journal*, vol. 17, no. 14, pp. 4012–4020, 2011, doi: 10.1002/chem.201002556.

[74] J. Roithová and D. Schröder, "Bond-Forming Reactions of Molecular Dications as a New Route to Polyaromatic Hydrocarbons," *J. Am. Chem. Soc.*, vol. 128, no. 13, pp. 4208–4209, Apr. 2006, doi: 10.1021/ja0600429.

[75] J. Roithová and D. Schröder, "On a Possible Growth Mechanism for Polycyclic Aromatic Hydrocarbon Dications: $C_7H_6^{2+}+C_2H_2$," *Chemistry – A European Journal*, vol. 13, no. 10, pp. 2893–2902, 2007, doi: 10.1002/chem.200600913.

[76] J. Roithová, C. L. Ricketts, and D. Schröder, "Reactions of the dications $C_7H_6^{2+}$, $C_7H_7^{2+}$, and $C_7H_8^{2+}$ with methane: Predominance of doubly charged intermediates," *International Journal of Mass Spectrometry*, vol. 280, no. 1, pp. 32–37, Feb. 2009, doi: 10.1016/j.ijms.2008.07.017.

[77] K. T. Lu, G. C. Eiden, and J. C. Weisshaar, "Toluene cation: nearly free rotation of the methyl group," *J. Phys. Chem.*, vol. 96, no. 24, pp. 9742–9748, Nov. 1992, doi: 10.1021/j100203a032.

[78] F. H. Dorman and J. D. Morrison, "Double and Triple Ionization in Molecules Induced by Electron Impact," *J. Chem. Phys.*, vol. 35, no. 2, pp. 575–581, Aug. 1961, doi: 10.1063/1.1731972.

[79] D. A. Shaw *et al.*, "An experimental and theoretical study of the spectroscopic and thermodynamic properties of toluene," *Chemical Physics*, vol. 230, no. 1, pp. 97–116, Apr. 1998, doi: 10.1016/S0301-0104(98)00031-7.

[80] J. Roithová *et al.*, "Revision of the second ionization energy of toluene," *The Journal of Chemical Physics*, vol. 122, no. 9, p. 094306, Feb. 2005, doi: 10.1063/1.1856916.

[81] R. D. Molloy and J. H. D. Eland, "Double photoionisation of toluene," *Chemical Physics Letters*, vol. 421, no. 1, pp. 31–35, Apr. 2006, doi: 10.1016/j.cplett.2006.01.051.

[82] A. D. Baker, D. P. May, and D. W. Turner, "Molecular photoelectron spectroscopy. Part VII. The vertical ionisation potentials of benzene and some of its monosubstituted and 1,4-disubstituted derivatives," *J. Chem. Soc. B*, vol. 0, no. 0, pp. 22–34, Jan. 1968, doi: 10.1039/J29680000022.

[83] J. Roithová, D. Schröder, P. Gruene, T. Weiske, and H. Schwarz, "Structural Aspects of Long-Lived $C_7H_8^{2+}$ Dications Generated by the Electron Ionization of Toluene," *J. Phys. Chem. A*, vol. 110, no. 9, pp. 2970–2978, Mar. 2006, doi: 10.1021/jp0545288.

[84]   C. Shaffer, D. Schröder, E.-L. Zins, C. Alcaraz, J. Žabka, and J. Roithová, "Unimolecular dissociation of doubly ionized toluene and electron transfer between neutral toluene and its dication," *Chemical Physics Letters*, vol. 534, pp. 8–12, May 2012, doi: 10.1016/j.cplett.2012.03.014.

[85]   T. P. Debies and J. W. Rabalais, "Photoelectron spectra of substituted benzenes: II. Seven valence electron substituents," *Journal of Electron Spectroscopy and Related Phenomena*, vol. 1, no. 4, pp. 355–370, Jan. 1972, doi: 10.1016/0368-2048(72)80037-9.

[86]   C. Jr. Gould, G. Holzman, and C. Niemann, "Determination of Vapor Pressure of Liquids on a Milligram Scale," *Anal. Chem.*, vol. 19, pp. 204–206, 1947.

[87]   L. Åsbrink, C. Fridh, and E. Lindholm, "Electronic structure of toluene from photoelectron spectroscopy and a spindo calculation," *Chemical Physics Letters*, vol. 15, no. 4, pp. 567–570, Sep. 1972, doi: 10.1016/0009-2614(72)80373-7.

[88]   P. Baltzer, M. Larsson, L. Karlsson, B. Wannberg, and M. Carlsson Göthe, "Inner-valence states of N_2 studied by uv photoelectron spectroscopy and configuration-interaction calculations," *Phys. Rev. A*, vol. 46, no. 9, pp. 5545–5553, Nov. 1992, doi: 10.1103/PhysRevA.46.5545.

[89]   M. Schwell *et al.*, "Photoionization mass spectrometry of six isomers of C_7H_8 in the 7–22 eV photon energy range," *Chemical Physics*, vol. 260, no. 1, pp. 261–279, Oct. 2000, doi: 10.1016/S0301-0104(00)00174-9.

[90]   "Toluene." https://webbook.nist.gov/cgi/cbook.cgi?ID=C108883&Mask=200#Mass-Spec (accessed Oct. 19, 2021).

[91]   S. Y. Truong, A. J. Yencha, A. M. Juarez, S. J. Cavanagh, P. Bolognesi, and G. C. King, "Threshold photoelectron spectroscopy of H_2O and D_2O over the photon energy range 12–40eV," *Chemical Physics*, vol. 355, no. 2, pp. 183–193, Jan. 2009, doi: 10.1016/j.chemphys.2008.12.009.

[92]   J. L. Gardner and J. A. R. Samson, "Photoion and photoelectron spectroscopy of CO and N_2," *J. Chem. Phys.*, vol. 62, no. 4, pp. 1447–1452, Feb. 1975, doi: 10.1063/1.430603.

[93]   O. Edqvist, E. Lindholm, L. E. Selin, and L. Åsbrink, "On the Photoelectron Spectrum of O_2," *Phys. Scr.*, vol. 1, no. 1, pp. 25–30, Jan. 1970, doi: 10.1088/0031-8949/1/1/004.

[94]   "Vacuum ultraviolet photoionization and dissociative photoionization of toluene: Experimental and theoretical insights - Yujie Zhao, Pei Huang, Li Li, Yousheng Zhan, Ke Wang, Haohang Yang, Jianhui Jin, Yuqian Chen, Yibao Liu, Liusi Sheng, Jun Chen, Maoqi Cao, 2021." https://journals.sagepub.com/doi/abs/10.1177/14690667211042707 (accessed Oct. 27, 2021).

[95]   L. Klasinc, B. Kovac, and H. Gusten, "Photoelectron spectra of acenes. Electronic structure and substituent effects," *Pure and Applied Chemistry*, vol. 55, no. 2, pp. 289–298, Jan. 1983, doi: 10.1351/pac198855020289.

[96]   S. Feil *et al.*, "Metastable dissociation of doubly charged ions produced from toluene: Kinetic energy release upon charge separation and H2 elimination," *Chemical Physics Letters*, vol. 411, no. 4, pp. 366–372, Aug. 2005, doi: 10.1016/j.cplett.2005.06.051.

[97]   K. G. Torma, K. Voronova, B. Sztáray, and A. Bodi, "Dissociative Photoionization of the C_7H_8 Isomers Cycloheptatriene and Toluene: Looking at Two Sides of the Same Coin Simultaneously," *J. Phys. Chem. A*, vol. 123, no. 16, pp. 3454–3463, Apr. 2019, doi: 10.1021/acs.jpca.9b00936.

[98]   U. Jacovella, G. da Silva, and E. J. Bieske, "Unveiling New Isomers and Rearrangement Routes on the C7H8+ Potential Energy Surface," *J. Phys. Chem. A*, vol. 123, no. 4, pp. 823–830, Jan. 2019, doi: 10.1021/acs.jpca.8b10642.

[99]   J. C. Choe, "Dissociation of Toluene Cation: A New Potential Energy Surface," *J. Phys. Chem. A*, vol. 110, no. 24, pp. 7655–7662, Jun. 2006, doi: 10.1021/jp0612782.

[100]   K. R. Jennings, "Consecutive metastable transitions in a double-focussing mass spectrometer," *Chem. Commun. (London)*, no. 9, pp. 283–284, Jan. 1966, doi: 10.1039/C19660000283.

[101]   J. R. Vacher, F. Jorand, N. Blin-Simiand, and S. Pasquiers, "Partial ionisation cross-sections of 2-propanol and ethanal," *Chemical Physics*, vol. 323, no. 2, pp. 587–594, Apr. 2006, doi: 10.1016/j.chemphys.2005.10.027.

[102]   J. Olmsted, K. Street, and A. S. Newton, "Excess-Kinetic-Energy Ions in Organic Mass Spectra," *J. Chem. Phys.*, vol. 40, no. 8, pp. 2114–2122, Apr. 1964, doi: 10.1063/1.1725480.

[103]   K. J. Covert, A. Bodi, K. G. Torma, K. Voronova, T. Baer, and B. Sztáray, "To roam or not to Roam, That is the question for the methyl group in isopropanol cations," *International Journal of Mass Spectrometry*, p. 116469, Nov. 2020, doi: 10.1016/j.ijms.2020.116469.

[104]   M. J. S. Dewar and S. D. Worley, "Photoelectron Spectra of Molecules. I. Ionization Potentials of Some Organic Molecules and Their Interpretation," *J. Chem. Phys.*, vol. 50, no. 2, pp. 654–667, Jan. 1969, doi: 10.1063/1.1671114.

[105] P. Linusson *et al.*, "Double photoionization of alcohol molecules," *Phys. Rev. A*, vol. 80, no. 3, p. 032516, Sep. 2009, doi: 10.1103/PhysRevA.80.032516.

[106] L. Friedman, F. A. Long, and M. Wolfsberg, "Study of the Mass Spectra of the Lower Aliphatic Alcohols," *J. Chem. Phys.*, vol. 27, no. 3, pp. 613–622, Sep. 1957, doi: 10.1063/1.1743799.

[107] K. M. A. Refaey and W. A. Chupka, "Photoionization of the Lower Aliphatic Alcohols with Mass Analysis," *J. Chem. Phys.*, vol. 48, no. 11, pp. 5205–5219, Jun. 1968, doi: 10.1063/1.1668196.

[108] B. G. Keyes and A. G. Harrison, "Structure and mechanism of fragmentation of $[C_2H_5O]^+$," *Organic Mass Spectrometry*, vol. 9, no. 2, pp. 221–246, 1974, doi: 10.1002/oms.1210090210.

[109] L. Belshaw *et al.*, "Observation of Ultrafast Charge Migration in an Amino Acid," *J. Phys. Chem. Lett.*, vol. 3, no. 24, pp. 3751–3754, Dec. 2012, doi: 10.1021/jz3016028.

[110] F. Calegari *et al.*, "Ultrafast electron dynamics in phenylalanine initiated by attosecond pulses," *Science*, vol. 346, no. 6207, pp. 336–339, Oct. 2014, doi: 10.1126/science.1254061.

[111] T. Barillot *et al.*, "Correlation-Driven Transient Hole Dynamics Resolved in Space and Time in the Isopropanol Molecule," *Phys. Rev. X*, vol. 11, no. 3, p. 031048, Sep. 2021, doi: 10.1103/PhysRevX.11.031048.

[112] D. J. Walke, "New instrumentation and methods for ultrafast pump-probe spectroscopy," Sep. 2016, doi: 10.25560/48040.

[113] J.-W. Shin and E. R. Bernstein, "Experimental and theoretical studies of isolated neutral and ionic 2-propanol and their clusters," *J. Chem. Phys.*, vol. 130, no. 21, p. 214306, Jun. 2009, doi: 10.1063/1.3148378.

[114] Y. J. Shi, S. Consta, A. K. Das, B. Mallik, D. Lacey, and R. H. Lipson, "A 118 nm vacuum ultraviolet laser/time-of-flight mass spectroscopic study of methanol and ethanol clusters in the vapor phase," *J. Chem. Phys.*, vol. 116, no. 16, pp. 6990–6999, Apr. 2002, doi: 10.1063/1.1466467.

[115] S.-T. Tsai, J.-C. Jiang, M.-F. Lin, Y. T. Lee, and C.-K. Ni, "Carbon–carbon bond cleavage in the photoionization of ethanol and 1-propanol clusters," *J. Chem. Phys.*, vol. 120, no. 19, pp. 8979–8984, May 2004, doi: 10.1063/1.1704637.

[116] T. E. Daubert, J. W. Jalowka, and V. Goren, "Vapour Pressure of 22 Pure Industrial Chemicals," in *AIChE Symposium Series*, 1987, vol. 83, pp. 128–156.

[117] D. Nordfors, A. Nilsson, N. Mortensson, S. Svensson, U. Gelius, and H. Ågren, "X-ray excited photoelectron spectra of free molecules containing oxygen," *Journal of Electron Spectroscopy and Related Phenomena*, vol. 56, no. 2, pp. 117–164, May 1991, doi: 10.1016/0368-2048(91)80009-J.

[118] Y. F. Lin *et al.*, "Note: An improved 3D imaging system for electron-electron coincidence measurements," *Review of Scientific Instruments*, vol. 86, no. 9, p. 096110, Sep. 2015, doi: 10.1063/1.4931684.

[119] U. Gelius, L. Asplund, E. Basilier, S. Hedman, K. Helenelund, and K. Siegbahn, "A high resolution multipurpose ESCA instrument with X-ray monochromator," *Nuclear Instruments and Methods in Physics Research Section B: Beam Interactions with Materials and Atoms*, vol. 1, no. 1, pp. 85–117, Jan. 1984, doi: 10.1016/0168-583X(84)90482-8.

[120] C. Miron, M. Simon, N. Leclercq, and P. Morin, "New high luminosity 'double toroidal' electron spectrometer," *Review of Scientific Instruments*, vol. 68, no. 10, pp. 3728–3737, Oct. 1997, doi: 10.1063/1.1148017.

[121] P. Baltzer, L. Karlsson, M. Lundqvist, and B. Wannberg, "Resolution and signal-to-background enhancement in gas-phase electron spectroscopy," *Review of Scientific Instruments*, vol. 64, no. 8, pp. 2179–2189, Aug. 1993, doi: 10.1063/1.1143957.

[122] J. A. R. Samson, "Line Broadening in Photoelectron Spectroscopy," *Review of Scientific Instruments*, vol. 40, no. 9, pp. 1174–1177, Sep. 1969, doi: 10.1063/1.1684192.

[123] K. Le Guen *et al.*, "Development of a four-element conical electron lens dedicated to high resolution Auger electron–ion(s) coincidence experiments," *Review of Scientific Instruments*, vol. 73, no. 11, pp. 3885–3894, Oct. 2002, doi: 10.1063/1.1511799.

[124] T. X. Carroll *et al.*, "Carbon 1s core-hole lifetime in CO_2," *Phys. Rev. A*, vol. 61, no. 4, p. 042503, Mar. 2000, doi: 10.1103/PhysRevA.61.042503.

[125] F. Frati, M. O. J. Y. Hunault, and F. M. F. de Groot, "Oxygen K-edge X-ray Absorption Spectra," *Chem. Rev.*, vol. 120, no. 9, pp. 4056–4110, May 2020, doi: 10.1021/acs.chemrev.9b00439.

[126] C. Nicolas and C. Miron, "Lifetime broadening of core-excited and -ionized states," *Journal of Electron Spectroscopy and Related Phenomena*, vol. 185, no. 8, pp. 267–272, Sep. 2012, doi: 10.1016/j.elspec.2012.05.008.

[127] A. B. Trofimov and J. Schirmer, "Molecular ionization energies and ground- and ionic-state properties using a non-Dyson electron propagator approach," *J. Chem. Phys.*, vol. 123, no. 14, p. 144115, Oct. 2005, doi: 10.1063/1.2047550.

[128] A. K. Shukla and A. J. Stace, "Intermolecular ion-molecule reactions in clusters: the reactions of aliphatic alcohols," *J. Phys. Chem.*, vol. 92, no. 9, pp. 2579–2583, May 1988, doi: 10.1021/j100320a036.

[129] A. Fujii *et al.*, "Hydrogen bond network structures of protonated short-chain alcohol clusters," *Phys. Chem. Chem. Phys.*, vol. 20, no. 22, pp. 14971–14991, Jun. 2018, doi: 10.1039/C7CP08072G.

[130] H.-T. Kim, J. Liu, and S. L. Anderson, "Reaction of acetaldehyde cations with water: The effects of CH_3CHO^+ vibrational mode and impact parameter on reactivity and product branching," *J. Chem. Phys.*, vol. 115, no. 3, pp. 1274–1286, Jul. 2001, doi: 10.1063/1.1378816.

[131] O. Kostko, T. P. Troy, B. Bandyopadhyay, and M. Ahmed, "Proton transfer in acetaldehyde–water clusters mediated by a single water molecule," *Phys. Chem. Chem. Phys.*, vol. 18, no. 36, pp. 25569–25573, Sep. 2016, doi: 10.1039/C6CP04916H.

[132] L. S. Cederbaum, J. Zobeley, and F. Tarantelli, "Giant Intermolecular Decay and Fragmentation of Clusters," *Phys. Rev. Lett.*, vol. 79, no. 24, pp. 4778–4781, Dec. 1997, doi: 10.1103/PhysRevLett.79.4778.

[133] U. Hergenhahn, "Interatomic and intermolecular coulombic decay: The early years," *Journal of Electron Spectroscopy and Related Phenomena*, vol. 184, no. 3, pp. 78–90, Apr. 2011, doi: 10.1016/j.elspec.2010.12.020.

[134] T. Jahnke, "Interatomic and intermolecular Coulombic decay: the coming of age story," *J. Phys. B: At. Mol. Opt. Phys.*, vol. 48, no. 8, p. 082001, Mar. 2015, doi: 10.1088/0953-4075/48/8/082001.

[135] T. Jahnke *et al.*, "Interatomic and Intermolecular Coulombic Decay," *Chem. Rev.*, vol. 120, no. 20, pp. 11295–11369, Oct. 2020, doi: 10.1021/acs.chemrev.0c00106.

[136] M. Mucke *et al.*, "A hitherto unrecognized source of low-energy electrons in water," *Nature Phys*, vol. 6, no. 2, pp. 143–146, Feb. 2010, doi: 10.1038/nphys1500.

[137] C. Richter *et al.*, "Competition between proton transfer and intermolecular Coulombic decay in water," *Nature Communications*, vol. 9, no. 1, Art. no. 1, Nov. 2018, doi: 10.1038/s41467-018-07501-6.

[138] H.-K. Kim *et al.*, "Enhanced production of low energy electrons by alpha particle impact," *PNAS*, vol. 108, no. 29, pp. 11821–11824, Jul. 2011, doi: 10.1073/pnas.1104382108.

[139] T. Jahnke *et al.*, "Experimental Separation of Virtual Photon Exchange and Electron Transfer in Interatomic Coulombic Decay of Neon Dimers," *Phys. Rev. Lett.*, vol. 99, no. 15, p. 153401, Oct. 2007, doi: 10.1103/PhysRevLett.99.153401.

[140] A. C. LaForge *et al.*, "Highly efficient double ionization of mixed alkali dimers by intermolecular Coulombic decay," *Nat. Phys.*, vol. 15, no. 3, pp. 247–250, Mar. 2019, doi: 10.1038/s41567-018-0376-5.

[141] K. Ueda *et al.*, "Interatomic Coulombic decay following the Auger decay: Experimental evidence in rare-gas dimers," *Journal of Electron Spectroscopy and Related Phenomena*, vol. 166–167, pp. 3–10, Nov. 2008, doi: 10.1016/j.elspec.2008.03.002.

[142] G. A. Grieves and T. M. Orlando, "Intermolecular Coulomb Decay at Weakly Coupled Heterogeneous Interfaces," *Phys. Rev. Lett.*, vol. 107, no. 1, p. 016104, Jul. 2011, doi: 10.1103/PhysRevLett.107.016104.

[143] R. Obaid *et al.*, "Intermolecular Coulombic Decay in Endohedral Fullerene at the $4d\ensuremath{\rightarrow}4f$ Resonance," *Phys. Rev. Lett.*, vol. 124, no. 11, p. 113002, Mar. 2020, doi: 10.1103/PhysRevLett.124.113002.

[144] P. Zhang, C. Perry, T. T. Luu, D. Matselyukh, and H. J. Wörner, "Observation of intermolecular Coulombic decay in liquid water," Mar. 2021, Accessed: Oct. 12, 2021. [Online]. Available: https://arxiv.org/abs/2103.15014v1

[145] T. Aoto, K. Ito, Y. Hikosaka, E. Shigemasa, F. Penent, and P. Lablanquie, "Properties of Resonant Interatomic Coulombic Decay in Ne Dimers," *Phys. Rev. Lett.*, vol. 97, no. 24, p. 243401, Dec. 2006, doi: 10.1103/PhysRevLett.97.243401.

[146] S. Barth *et al.*, "Observation of resonant Interatomic Coulombic Decay in Ne clusters," *J. Chem. Phys.*, vol. 122, no. 24, p. 241102, Jun. 2005, doi: 10.1063/1.1937395.

[147] F. Trinter *et al.*, "Resonant Auger decay driving intermolecular Coulombic decay in molecular dimers," *Nature*, vol. 505, no. 7485, pp. 664–666, Jan. 2014, doi: 10.1038/nature12927.

[148] W. Iskandar *et al.*, "Tracing intermolecular Coulombic decay of carbon-dioxide dimers and oxygen dimers after valence photoionization," *Phys. Rev. A*, vol. 99, no. 4, p. 043414, Apr. 2019, doi: 10.1103/PhysRevA.99.043414.

[149] T. Jahnke *et al.*, "Ultrafast energy transfer between water molecules," *Nature Phys*, vol. 6, no. 2, pp. 139–142, Feb. 2010, doi: 10.1038/nphys1498.

[150] N. B. Bejoy, N. K. Singh, S. Mishra, B. Pananghat, and G. N. Patwari, "Outer Valence Intermolecular Coulombic Decay in Hydrogen-Bonded Complexes Induced by Resonant Two-Photon Excitation by 4.4 eV Photons," *arXiv:2010.06494 [physics]*, Oct. 2020, Accessed: Oct. 12, 2021. [Online]. Available: http://arxiv.org/abs/2010.06494

[151] S. Martin *et al.*, "Coincidence method for measuring the mass of neutral fragments emitted in a delayed fragmentation process from a singly charged molecule: Fragmentation pathway of adenine," *Phys. Rev. A*, vol. 77, no. 6, p. 062513, Jun. 2008, doi: 10.1103/PhysRevA.77.062513.

[152] M. Alagia *et al.*, "Angular and energy distribution of fragment ions in dissociative double photoionization of acetylene molecules at 39 eV," *J. Chem. Phys.*, vol. 136, no. 20, p. 204302, May 2012, doi: 10.1063/1.4720350.

[153] T. A. Field and J. H. D. Eland, "Lifetimes of metastable molecular doubly charged ions," *Chemical Physics Letters*, vol. 211, no. 4, pp. 436–442, Aug. 1993, doi: 10.1016/0009-2614(93)87087-J.

Abbreviations and acronyms

AEPIPICO	Auger-Meitner electron-photoion-photoion coincidence spectroscopy
ARPES	Angle-resolved photoelectron spectroscopy
ATI	Above-threshold ionisation
CCD	Charge-coupled device
Ce:YAG	Cerium doped yttrium aluminium garnet
CFD	Constant fraction discriminator
CIS	Coincidence imaging spectroscopy
DIP	Double ionisation potential
DLD	Delay line detector
DPI	Double photoionisation
EI	Electron impact
FWHM	Full width at half maximum
HHG	High-harmonic generation
HV	High-voltage
HWHM	Half width at half maximum
I(2)-PEPICO	(Double) imaging photoelectron-photoion coincidence
IP	(Single) ionisation potential
IPA	2-propanol (Isopropanol)
IR	Infrared
LACUS	Lausanne Centre for Ultrafast Science
LCPM	Laboratory of Molecular Physical Chemistry
LDM	Low-Density Matter endstation
LSU	Laboratory of Ultrafast Spectroscopy
(T)KER	(Total) kinetic energy release
MCP	Micro-channel plate
MPI	Multi-photon ionisation
MS	Mass spectrometry
Nd:YAG	Neodymium-doped yttrium-aluminium-garnet
Nd:YLF	Neodymium doped yttrium lithium fluoride
NIM	Nuclear Instrument Module
OFHC	Oxygen-free high conductivity
PAD	Photoelectron angular distribution
PEPECO	Photoelectron-photoelectron coincidence
PEPICO	Photoelectron-photoion coincidence
PEPIPICO	Photoelectron-photoion-photoion coincidence spectroscopy
PES	Photoelectron spectroscopy
PIPICO	Photoion-photoion coincidence
PS	Phosphor screen
QMS	Quadrupole mass spectrometer
ROI	Region of interest
TOF	Time of flight
TPEPICO	Threshold photoelectron-photoion coincidence
TPEsCO	Threshold photoelectrons coincidence
TR	Time-resolved
TTL	Transistor-Transistor Logic
UHV	Ultra-high vacuum
VUV	Vacuum ultraviolet
VMI	Velocity-map imaging
XFEL	X-ray free electron laser
XUV	Extreme ultraviolet

List of tables

List of figures

Acknowledgements

I have been lucky enough in my time at EPFL to have been heavily involved with as many as three different laboratories, each filled with the special kind of people that made my degree not only possible, but enjoyable. As a result, there are many I have to thank for dragging me kicking and screaming to the end of my studies.

The first and foremost is my supervisor, Prof. Marcel Drabbels for the faith shown to me when he accepted me as his student onto a project building a machine when I had no idea on how to do such a thing; for the constant support and guidance during my time here, helpfully facilitated by two always-open doors; for his expertise in the lab, always being able to find unexpected and obscure solutions to problems and for kicking me into gear when I needed to be kicked.

I would like to thank the members of my thesis committee, Prof. Maurice Janssen, Dr. Robert Richter, Prof. Christoph Bostedt and Prof. Majed Chergui for reading this thesis and their valuable feedback and questions as well making the private defence of the thesis nothing like the nightmare I thought it would be. A very special thank you is also extended to Majed who allowed me to squat in his lab space and was astonishingly supportive and patient with how long it took to get results on the CIS endstation.

In LCPM, the first lab of which I was a member, I want to thank Prof. Thomas Rizzo for accepting me into his lab and providing a fantastically friendly community environment. During my time in his group (and even after I switched groups) he has given me endless kindness and scientific and pastoral support; hosted many amazing barbeques with Karen (who kept me well-fed with many amazing chocolate brownies), and literally saved my PhD by generously extending my contract and allowing me to get the results I needed to graduate.

I also owe my eternal gratitude to Dr. Thomas Barillot and Dr. Rebecca Ingle for VMI expertise, data analysis expertise, thesis-checking expertise and fighting for me and being responsible for my first successful beamtime and getting the results which allowed me to finish my thesis. Like Tom, you both literally saved my PhD.

My closest friends in EPFL have undoubtedly been Dr. Verónica Oliver Álvarez de Lara, Dr. Valeriu Scutelnic and Miriam Pougin. I am lucky to have had Vero as my long-suffering officemate and constant companion in the Helium crew almost from the start. Vero has been the foremost victim of my untidiness, disorganisation, mood swings and aptitude for "borrowing" lab equipment, yet somehow found the patience and fortitude to not only not murder me, but actively keep me alive with a steady supply of cakes, biscuits, support, perspective and banana liquor. It has been a highlight to inhabit this office with her and discuss science and gossip; share ice creams and patatas; argue about opening or closing the window; complain about the printer going all day; invent projectile-based games and to extend the Art of the Experiment from the lab to the pizza oven. Sometimes we even did work. Val has been my friend ever since we both started our PhDs in LCPM on the same day and has shared with me many good times of scientific discussions over vending machine panini dinners, running sessions, flange-bolting and weasel-baiting. Miriam came in to my office soon after the heart-breaking departure of Vero and quickly proved herself just as wonderful a companion with whom I shared many enjoyable moments including Friday Beers, lakeside chats, cakes (I gained so much weight in my PhD and I blame everyone feeding me cakes) and late-night and weekend writing sessions. My time at EPFL would have been far less enjoyable without the three of you.

In LCPM I thank Prof. Rainer Beck, Prof. Oleg Boyarkine, Dr. Andreas Osterwalder, Dr. Mike Kamrath, Dr. Aleksandra Zabuga, Dr. Maarten van Reijzen, Dr. Lucy Voronina, Dr. Helen Chadwick, Dr. Chiara Masellis, Dr. Jörn Werdecker, Dr. Natalia Yalovenko, Dr. Robert Pellegrinelli, Dr. Ana Gutiérrez González, Bo-jung Chen,

Curriculum vitae

Education

2014 - 2021   PhD in physical chemistry at École polytechnique fédérale de Lausanne, Switzerland.

Supervisor: Prof. Marcel Drabbels.
Thesis title: *Coincidence imaging spectroscopy of extreme-ultraviolet photoionisation processes in molecules and clusters*

2009 - 2014   MChem in chemistry and materials chemistry at University of Edinburgh, United Kingdom.

Supervisor: Dr. Adam Kirrander
Thesis title: *Resonances and wavefunctions of heavy Rydberg states of lithium fluoride*

2012 - 2013   Exchange year for undergraduate research project in chemistry at University of Hong Kong, Hong Kong.

Supervisor: Prof. Allan Shi-Chung Cheung
Thesis title: *Optical-optical double resonance spectroscopy of yttrium oxide: transitions in the ultraviolet region*

2011   Summer research stay in solid-state physics laboratory at Konkuk University, Republic of Korea.

Supervisor: Prof. Jung-Ho Park
Research topic: *Synthesis of zinc oxide nanowires*

Publications

T. Barillot, O. Alexander, B. Cooper, T. Driver, D. Garratt, S. Li, A. Al Haddad, A. Sanchez-Gonzalez, M. Agåker, C. Arrell, M. J. Bearpark, N. Berrah, C. Bostedt, J. Bozek, C. Brahms, P. H. Bucksbaum, A. Clark, G. Doumy, R. Feifel, L. J. Frasinski, S. Jarosch, A. S. Johnson, L. Kjellsson, P. Kolorenč, Y. Kumagai, E. W. Larsen, P. Matía-Hernando, M. Robb, J.-E. Rubensson, M. Ruberti, C. Sathe, R. J. Squibb, A. Tan, J. W. G. Tisch, M. Vacher, D. J. Walke, T. J. A. Wolf, D. Wood, V. Zhaunerchyk, P. Walter, T. Osipov, A. Marinelli, T. J. Maxwell, R. Coffee, A. A. Lutman, V. Averbukh, K. Ueda, J. P. Cryan, J. P. Marangos. "Correlation-Driven Transient Hole Dynamics Resolved in Space and Time", *Physical Review X* (2021), **11**, 031048

A. C. LaForge, R. Michiels, Y. Ovcharenko, A. Ngai, J. M. Escartín, N. Berrah, C. Callegari, A. Clark, M. Coreno, R. Cucini, M. Di Fraia, M. Drabbels, E. Fasshauer, P. Finetti, L. Giannessi, C. Grazioli, D. Iablonskyi, B. Langbehn, T. Nishiyama, V. Oliver, P. Piseri, O. Plekan. K. C. Prince, D. Rupp, S. Stranges, K. Ueda, N. Sisourat, J. Eloranta, M. Pi, M. Barranco, F. Stienkemeier, T. Möller, M. Mudrich, "Ultrafast Resonant Interatomic Coulombic Decay Induced by Quantum Fluid Dynamics", *Physical Review X* (2021), **11**, 021011

R. Michiels, A. C. LaForge, M. Bohlen, C. Callegari, A. Clark, A. von Conta, M. Coreno, M. Di Fraia, M. Drabbels, P. Finetti, M. Huppert, V. Oliver, O. Plekan, K. C. Prince, S. Stranges, H. J. Wörner, F. Stienkemeier, "Evolution and ion kinetics of a XUV-induced nanoplasma in ammonia clusters", *Journal of Physics B: Atomic, Molecular and Optical Physics* (2021), **54**, 024002

R. Michiels, A. C. LaForge, M. Bohlen, C. Callegari, A. Clark, A. von Conta, M. Coreno, M. Di Fraia, M. Drabbels, P. Finetti, M. Huppert, V. Oliver, O. Plekan, K. C. Prince, S. Stranges, V. Svoboda, H. J. Wörner, F. Stienkemeier, "Time-resolved formation of excited atomic and molecular states in XUV-induced nanoplasmas in ammona clusters", *Physical Chemistry Chemical Physics* (2020), **22**, 7828-7834

A. C. LaForge, R. Michiels, M. Bohlen, C. Callegari, A. Clark, A. von Conta, M. Coreno, M. Di Fraia, M. Drabbels, M. Huppert, P. Finetti, J. Ma, M. Mudrich, V. Oliver, O. Plekan, K. C. Prince, M. Shcherbinin, S. Stranges, V. Svoboda, H. J. Wörner, F. Stienkemeier, "Real-Time Dynamics of the Formation of Hydrated Electrons upon Irradiation of Water Clusters with Extreme Ultraviolet Light", *Physical Review Letters* (2019), **122**, 133001

B. Langbehn, K. Sander, Y. Ovcharenko, C. Peltz, A. Clark, M. Coreno, R. Cucini, M. Drabbels, P. Finetti, M. Di Fraia, L. Giannessi, C. Grazioli, D. Iablonskyi, A. C. LaForge, T. Nishiyama, V. Oliver Álvarez de Lara, P. Piseri, O. Plekan, K. Ueda, J. Zimmermann, K. C. Prince, F. Stienkemeier, C. Callegari, T. Fennel, D. Rupp, T. Möller, "Three-Dimensional Shapes of Spinning Helium Nanodroplets", *Physical Review Letters* (2018), **121**, 255301

C. A. Arrell, J. Ojeda, L. Longetti, A. Crepaldi, S. Roth, G. Gatti, A. Clark, F. van Mourik, M. Drabbels, M. Grioni, M. Chergui, "Harmonium: An Ultrafast Vacuum Ultraviolet Facility", *CHIMIA* (2017), **71**, 268-272

Poster Presentations

Perspectives on Photonics Summer School (2016), Gstaad, "A TR-CIS spectrometer to investigate microsolvation effects on molecular excited state dynamics".

Lausanne Center for Ultrafast Science (LACUS) Inauguration Symposium (2016), EPFL Rolex Center, "Technique development for studying spectroscopy and dynamics of doped clusters and helium nanodroplets".